



T.C.
MANİSA CELAL BAYAR ÜNİVERSİTESİ
FEN BİLİMLERİ ENSTİTÜSÜ

MANİSA CELAL BAYAR UNIVERSITY
INSTITUTE OF NATURAL&APPLIED
SCIENCE

CİLT:18 SAYI :2 YIL:2022
VOLUME:18 ISSUE:2 YEAR:2022

ISSN: 1305-130X
e-ISSN: 1305-1385

**CELAL BAYAR ÜNİVERSİTESİ
FEN BİLİMLERİ DERGİSİ**

**CELAL BAYAR UNIVERSITY
JOURNAL OF SCIENCE**

**CELAL BAYAR
ÜNİVERSİTESİ**



Journal of Science

Volume: 18, Issue: 2, Year: 2022

Contact

Manisa Celal Bayar University
Institute of Natural and Applied Sciences
Campus of Şehit Prof Dr İlhan Varank 45140 Yunusmre – MANİSA, TURKEY
Tel: (00 90) 236 201 27 05
Fax: (00 90) 236 241 21 49
e-mail: cbujos@gmail.com
Web: <https://dergipark.org.tr/tr/pub/cbayarfb>

“CBU Journal of Science is indexed by ULAKBIM-TUBITAK TR-DIZIN”



ISSN 1305-130X

E-ISSN 1305-1385

CBUJOS is published quarterly at Manisa Celal Bayar University Printing House

“CBU Journal of Science is a refereed scientific journal”



Celal Bayar University Journal of Science

Owner

Manisa Celal Bayar University,

Editors : Assoc. Prof. Dr. Kamil ŞİRİN

Assoc. Prof. Dr. Emine KEMİKLİOĞLU

Assistant Editor: Assoc. Prof. Dr. Mustafa AKYOL

Layout Editor & Secretary

Dr. İlker Çetin KESKİN

International Scientific Advisory Board

Prof. Dr. Arianit REKA; State University of Tetova, Macedonia

Prof. Dr. Tomasz NIEMIEC; Warsaw University of Life Sciences, Poland

Prof. Dr. Alyani ISMAIL; Universiti Putra, Malaysia

Prof. Dr. Iuliana APRODU; Dunarea de Jos University, Romania

Assoc. Prof. Dr. Johanan Christian PRASANNA; Madras Christian College, South India

Assoc. Prof. Dr. Noureddine ISSAOUI; Université de Monastir, Tunisie.

Assoc. Dr. Edward Albert UECKERMANN; North-West University, South Africa

Assoc. Dr. Zhi-Qiang ZHANG; The University of Auckland, Holland

Assist. Prof. Dr. Young Ki KIM; Pohang University of Science and Technology, South Korea

Assist. Prof. Can BAYRAM; University of Illinois, USA

Assist. Prof. Dr. Mona MIRHEYDARI; Rutgers University, USA

Assist. Prof. Dr. Donatella ALBANESE; Università Degli Studi Di Salerno, Italy

Assist. Prof. Dr. Jinghua JIANG; The University of Memphis, USA

Assist. Prof. Dr. Jens OLDELAND; University of Hamburg, Germany

Dr. Cheng CHENG; Apple Inc., USA

Dr. Sajedah AFGHAH; Microsoft Corporation, USA

Dr. Jinghua JIANG; The University of Memphis

National Scientific Advisory Board

Prof. Dr. Mustafa Ersöz; Selçuk University

Prof. Dr. Oğuz Gürsoy; Mehmet Akif University

Prof. Dr. Mehmet Çevik; İzmir Katip Çelebi University

Prof. Dr. Sezgin Çelik; Yıldız Teknik University

Prof. Dr. Osman Dayan; Çanakkale Onsekiz Mart University

Prof. Dr. Serdar İplikçi; Pamukkale University

Prof. Dr. Yasin Üst; Yıldız Teknik University

Prof. Dr. Mahmut Kuş; Konya Teknik University

Prof. Dr. Ertunç Gündüz; Hacettepe University

Prof. Dr. Tülin Aydemir; Manisa Celal Bayar University

Prof. Dr. Sezai Taşkın; Manisa Celal Bayar University

Prof. Dr. Fatma Şaşmaz Ören; Manisa Celal Bayar University

Prof. Dr. Fatih Selimefendigil; Manisa Celal Bayar University

Prof. Dr. Osman Çulha; Manisa Celal Bayar University

Prof. Dr. Ali Konuralp; Manisa Celal Bayar University

Prof. Dr. Ali Demir; Manisa Celal Bayar University

Assoc. Prof. Dr. Fatih Doğan; Çanakkale Onsekiz Mart University

Assoc. Prof. Dr. Erol Akpınar; Abant İzzet Baysal University

Assoc. Prof. Dr. Yeliz Yıldırım; Ege University

Assoc. Prof. Dr. Serap Derman; Yıldız Teknik University

Assoc. Prof. Dr. Hayati Mamur; Manisa Celal Bayar University

Assoc. Prof. Dr. Özlem Çağındı; Manisa Celal Bayar University

Assoc. Prof. Dr. Mehmet Söylemez; Adıyaman University

Assoc. Prof. Dr. Nil Mansuroğlu; Ahi Evran University

Assist. Prof. Dr. Zeynep Çipiloğlu Yıldız; Manisa Celal Bayar University



CBU Journal of Science

Celal Bayar University Journal of Science (CBUJOS) covers scientific studies in the fields of Engineering and Science and publishes accounts of original research articles concerned with all aspects of experimental and theoretical studies. CBU Journal of Science is a refereed scientific journal published four times annually (March, June, September and December) by Institute of Natural and Applied Sciences of Manisa Celal Bayar University. CBU Journal of Science considers the original research articles written in English for evaluation.

CBU Journal of Science is indexed by TUBİTAK ULAKBİM TR-DİZİN, and also is included in DOAJ, Cite Factor, Journal TOCS, Advanced Science Index and OAJI databases. Digital Object Identifier (DOI) number will be assigned for all the articles being published in CBU Journal of Science.

Instructions for Authors and Article Template can be found on the main page of MCBU Institute of Natural and Applied Sciences (<http://fbe.cbu.edu.tr>)





Vol: 18, Issue: 2, Year: 2022

Contents

Research Article

Pages

- The Effect of Strain Rate and Initial Grain Size on Deformation Behavior of OFHC Copper at Elevated Temperatures
DOI: 10.18466/cbayarfbe.1009553
Selim Yıldırım, Mustafa Merih Arıkan 119-127
- The Evaluation of the Non-Toxic Ferrous Matrix Based WC Reinforced Composites: A Review
DOI: 10.18466/cbayarfbe.1020170
Esad Kaya, Mustafa Ulutan 129-139
- Development of Salt Core Use as an Alternative in Aluminum Alloy Castings
DOI: 10.18466/cbayarfbe.1033177
Tülay Hançerlioğlu 141-147
- Tension Field Performance of GFRP Plate Shear Walls
DOI: 10.18466/cbayarfbe.1015437
Tuna Ülger 149-160
- An Investigation on the Flexural and Thermo-mechanical Properties of CaCO₃/Epoxy Composites
DOI: 10.18466/cbayarfbe.1015351
S. Bahar Baştürk 161-167
- Adventitious and Normal Respiratory Sound Analysis with Machine Learning Methods
DOI: 10.18466/cbayarfbe.1002917
Burcu Acar Demirci, Yücel Koçyiğit, Deniz Kızıllırmak, Yavuz Havlucu 169-180
- Log-normal and Negative Binomial Distributions of DONUT Data
DOI: 10.18466/cbayarfbe.986699
Çağın Kamışcıoğlu 181-184
- Synthesis of Poly(azomethine) Containing Sulfonic Acid Unit Oxygen and Sulphur Bridged: Investigation of Its Thermal, Optical and Electrochemical Properties
DOI: 10.18466/cbayarfbe.1070592
Elif Karacan Yeldir 185-191
- Phylogenetic Analysis of Mosquito (Diptera: Culicidae) Species with Mitochondrial Cytochrome Oxidase Subunit 1 Gene Distributed in Kocaeli
DOI: 10.18466/cbayarfbe.1007398
Fikriye Polat, Serkan Dede 193-202
- The Quasi Parallel Curve of a Space Curve
DOI: 10.18466/cbayarfbe.955974
Fatma Güler 203-206



- Effects of Zinc oxide Nanoparticles (ZnO NPs) on Hemocyte Types of *Galleria mellonella* 207-212
DOI: 10.18466/cbayarfbe.989240
Ata Eskin
- The Anatomical Characteristics of *Salvia* (section *Aethiopsis*) From Mardin and Their Taxonomic Implications 213-224
DOI: 10.18466/cbayarfbe.1018553
Fatma Mungan Kılıç, Murat Kılıç
- Chemical Inferences Drawn From Basalt Volcanic Pumice 225-231
DOI: 10.18466/cbayarfbe.993131
Ruhan Benlikaya, Mehmet Kahrıman

The Effect of Strain Rate and Initial Grain Size on Deformation Behavior of OFHC Copper at Elevated Temperatures

Selim Yıldırım¹ , Mustafa Merih Arıkan^{2*} 

¹ Dept. of Metallurgical and Materials Engineering, İstanbul University-Cerrahpaşa, Avcılar-İstanbul, Türkiye

^{2*} Arıkan Engineering and Consultancy, 07400 Oba-Alanya-Antalya, Türkiye

* meriharikan@yahoo.com

* Orcid No:0000-0002-5820-1871

Received: 14 October 2021

Accepted: 27 May 2022

DOI: 10.18466/cbayarfbe.1009553

Abstract

Understanding of plastic deformation mechanisms and/or microstructural changes of metals and alloys at elevated temperatures makes possible to control their hot working behavior and final mechanical properties. The aim of the present work is to optimize the conditions to achieve maximum ductility in terms of initial grain size, process temperature and deformation rate. In this study, the OFHC (oxygen-free high conductivity) copper samples of different initial grain sizes (25, 50, 100 and 150 μm) were subjected to tensile tests at temperatures 300, 405, 500 and 700 $^{\circ}\text{C}$ ($0.42 - 0.75 T_m$) and cross-head speeds of 1, 2, 5, 10, 20 and 50 mm/min (strain rates of $5.6 \times 10^{-4} - 2.8 \times 10^{-2} \text{ s}^{-1}$). Experimental results indicated that particular conditions (initial grain size of 50 μm ; 700 $^{\circ}\text{C}$ of working temperature and $5.6 \times 10^{-3} \text{ s}^{-1}$ of strain rate) should be provided in terms of process temperature and deformation rate depending upon initial grain size for dynamic recrystallization and also maximum ductility.

Keywords: OFHC copper; strain rate; elevated temperature; tensile test

1. Introduction

Various types of forming methods of metallic materials are used in technology and material acquires some properties depending on the applied method. Processes such as rolling, deep drawing, extrusion, pressing, forging in the manufacturing of flat products, wires and pipes are carried out in cold or hot conditions. Since cold forming processes of metallic materials are limited, hot forming processes are applied in a wide variety. Hot forming also homogenizes the material and provides reaching the final desired properties by controlling the microstructure [1-6]. Therefore, it should be known how the behavior at the elevated temperatures of the materials is dependent on the parameters such as material microstructure, working temperature and strain rate. This information helps us increasing the production speed and obtaining both higher ductility and strength in the product during the production step [7-8].

Hot forming is the oldest method before forming by casting in the history of technology. Research on archeological findings showed that natural copper was formed with primitive tools by forging in the hot conditions in Anatolia since Acheramic Neolithic times (BC 8000) [9, 10].

High temperature generally decreases material's strength and increases the ductility. Weakening of the bonds among the atoms at elevated temperatures and thus increasing the possibility of movements of the atoms and movement of dislocations by the possibility of substitution especially the possibility of the climbing movement are the reasons for this situation. Atomic vacancies formed at the elevated temperatures also accelerate the diffusion. In addition, slip systems can change by temperature and this eases the deformation. Slip occurs at the grain boundaries due to weakening of the grain boundaries at high temperatures. On the other hand, other diffusion-controlled phenomena can also happen and microstructure changes [11-15].

A lot of research has been made for understanding the complex deformation behavior of the materials at elevated temperatures and studies continue with a great acceleration at present. Various mechanisms were claimed regarding the behavior of the materials at elevated temperatures, mechanism maps were prepared and empirical relationships were developed. Research results put forward that different deformation mechanisms occur at certain temperature and strain rate intervals at high temperature deformations such as hot working, creep and superplastic deformation [16-23].

In the recent years, it has been observed that some fluctuations occurred in the tensile diagrams of some important engineering materials and ductility increased. It has been detected that this was related to the dynamic recrystallization and dynamic grain growth [24-32]. The critical strain for dynamic recrystallization depends on the composition of the material, grain size prior to deformation and deformation temperature and strain rate [33,34].

The purpose of this study is to optimize the conditions to reach at the maximum ductility in the OFHC copper due to the requirements for determination of load during the forming processes, estimation of the metal flow pattern to represent the plastic flow behavior of the material from the point of view of initial grain size, working temperature and strain rate.

2. Materials and Methods

In this study, cold drawn OFHC copper rods (in the purity of 99.99%) were used to investigate the effect of initial grain size, strain rate and deformation temperature on elevated temperature deformation behavior.

High temperature tensile tests were performed at elevated temperatures to investigate the hot working behavior and the final mechanical properties of OFHC copper. High temperature tensile test rods were prepared from cold drawn copper rods in the original diameter of 10 mm by lathe. Tensile test rods had initial grain size of 25 μm and were annealed for 0.5 hours at the temperatures of 300, 700 and 900 $^{\circ}\text{C}$ to obtain

specimens with initial grain sizes of 50, 100 and 150 μm respectively. The specimens were etched by the solution including 5 g of FeCl_3 and 95 ml of methanol and 2 ml of HCl (concentrated) after metallographic polishing methods. Initial grain sizes of the copper specimens were measured by an image analysis method. For this purpose, linear interception method was used excluding annealing twins and 10 mm^2 of area were considered on the specimens.

The surfaces of the high temperature tensile test rods were ground by 1200 grit sandpaper and smooth and clear surfaces were obtained. High temperature tensile tests were performed at the temperatures of 300, 405, 500, 700 and 750 $^{\circ}\text{C}$, and at the strain rates of 1, 2, 5, 10, 20, 50 mm/min by the tensile testing machine (Instron 1195, High Wycombe, England) under atmospheric conditions. Temperatures and strain rates were determined by considering the ductility values obtained from the tests which were carried out to examine the region where optimum results were obtained in more detail. Test temperatures correspond to absolute temperature values of 573 - 1023 $^{\circ}\text{K}$ ($0.42 - 0.75 T/T_m$) and cross-head speeds correspond engineering strain rates of $0.5 - 30 \times 10^{-3} \text{ s}^{-1}$. Engineering stress-strain diagrams were recorded with a plotter. The reduction in area was calculated by measuring the diameter on the fracture zone of the broken specimens. High temperature tensile tests conducted at different temperatures and strain rates on OFHC copper are summarized in Table 1.

Table 1. Experimental program for high temperature tensile tests conducted at different temperatures and strain rates on OFHC copper. (IGS is initial grain size, T is temperature).

IGS (μm)	T ($^{\circ}\text{C}$)	Cross-head speed (mm/min)					
		1	2	5	10	20	50
25	500		X		X		X
25	700		X		X		X
50	-		X		X		X
50	300		X		X		X
50	405				X		
50	500		X		X		X
50	700	X	X	X	X	X	X
100	-				X		
100	500		X	X	X	X	X
100	700	X	X	X	X	X	X
100	750		X		X		X
150	700		X		X		

Rupture zones of elevated temperature specimens which are pre-investigated by stereo microscope (Leica Mz 125, Heerbrugg, Switzerland) were investigated by

SEM (Jeol Jsm T-330, Tokyo, Japan) at high magnifications. SEM investigations contributed to the determination of fracture type.

3. Results and Discussion

High temperature tensile behavior of copper materials which have different initial grain sizes is shown in Figure 1. The local stress increases observed after necking at the curves 500-2, 700-10, 700-2 and 700-1 in Figure 1 (b) could be caused by the effects of dynamic recrystallization and grain refinement. Strain hardening covering the dislocation generation, multiplication and intersection are significant as the strain increases in the early stages of deformation. The flow stress quickly increases since the dynamic softening caused by cross-

slip is not enough to overcome the effect of strain hardening. Dynamic recrystallization usually takes place due to the buildup of stored energy sufficiently after the critical strain is exceeded. Hence the increasing rate of flow stress decreases rapidly up to the peak value. The softening occurs due to the dislocation climb and dynamic recrystallization beyond the peak flow stress, during which the softening effect dominates: the flow curve decreases continuously until the dynamic balance between strain hardening and dynamic softening is achieved [35].

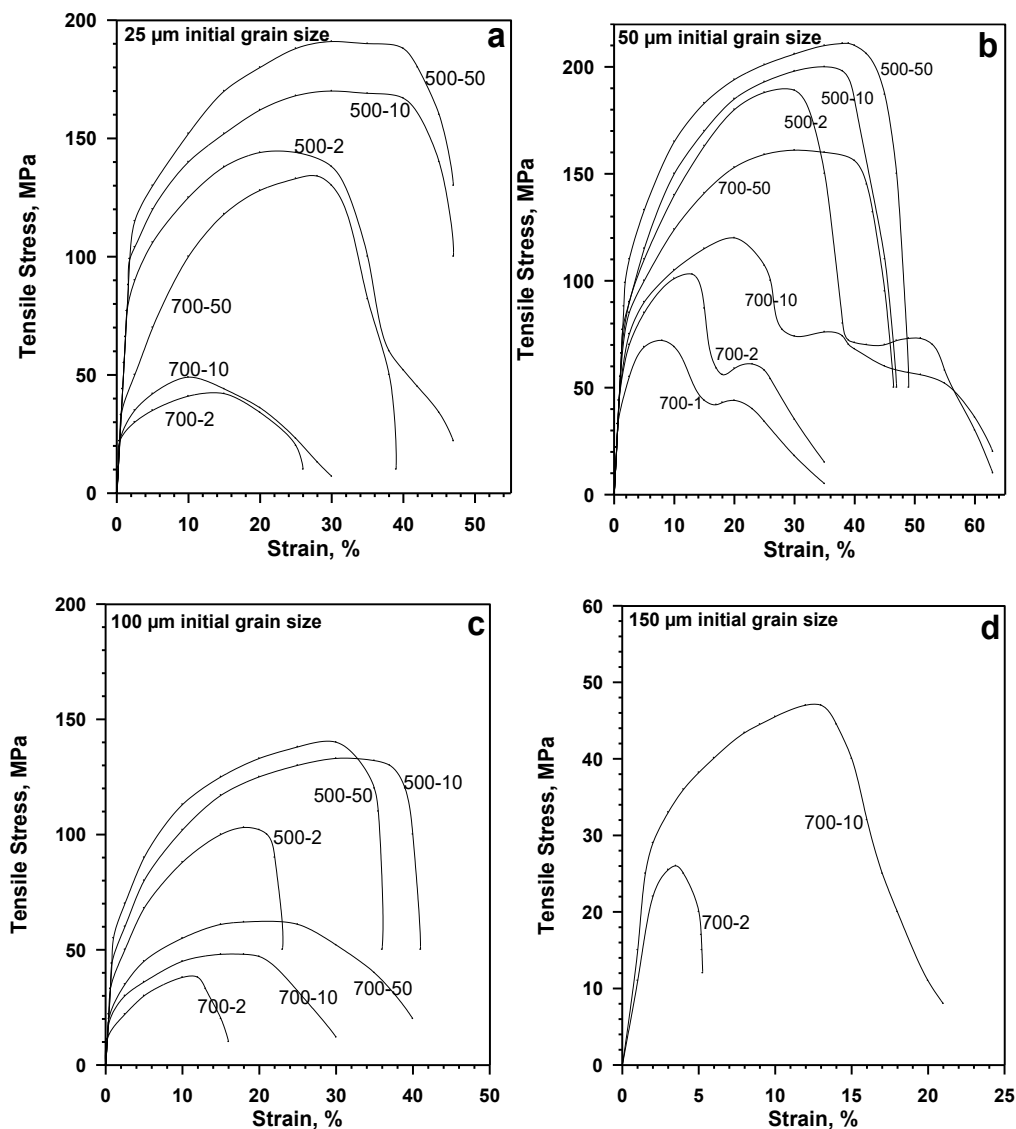


Figure 1. High temperature engineering tensile behavior of copper materials which have different initial grain sizes. Test temperatures ($^{\circ}\text{C}$) and cross-head speeds (mm/min) are given on the curves.

Shear strain is often produced by dislocation slip and/or deformation twinning, especially when a metal or alloy is plastically deformed at low temperatures and strain rates. Grain rotation, grain boundary sliding, and diffusion are other deformation mechanisms, but these

mechanisms only become important at relatively high temperatures, especially when the grain sizes are relatively large [20].

It is reported that one grain layer slides relative to the other and produces a shear stress in the process: plastic deformation has occurred due to the upper layers displaced to the right with respect to the lower layer of the grains [21]. This requires grain boundary sliding and is the basic mechanism in super plasticity.

It is also reported in another study on nanocrystalline materials that the dominant mode of superplasticity is grain-boundary sliding. Van Swygenhoven et al. demonstrated by molecular-dynamics simulations that grain-boundary sliding is the primary deformation mechanism in nanocrystalline materials [36].

Some models about the parameters such as the grain size, grain boundaries, slip bands and dislocation movements have been developed. A widely used model as an explanation for the empirical Hall–Petch relationship relating the yield strength of a polycrystalline material to its grains reports that the pile-up of dislocations against grain boundaries can lead to localized high-intensity stress concentrations, especially in planar slip materials. [37].

3.1. Effect of Grain Size

Initial grain size has a strong influence on the flow stress behavior and the recrystallization kinetics [38]. The flow stress tends to oscillate if $D_0 < 2 D_{rex}$, since there are sufficient grain boundaries for nucleation as suggested by Sakai and Jonas [39].

Grain boundaries are the source and sink of dislocations in a wide range of grain sizes. Particularly in nanocrystalline FCC metals, the emission of partial dislocations from grain boundaries is important. This leads to stacking faults and the formation of deformation twins. When the grain sizes decrease, grain rotation and grain boundary sliding becomes dominant, which can be supported by diffusion and dislocation activities [20].

The effect of grain size on reduction in area and tensile strength at 500 and 700 °C is seen in Figures 2 and 3 respectively. Effect of grain size on reduction in area was investigated in three different regions (Figure 2). Reduction in area is high on the specimens which have initial grain sizes of 25 and 50 μm corresponding the region I. Ductility is not dependent on temperature and strain rate in this region. Ductility decreases with the increasing grain size in region II which is a transition region. Ductility is influenced significantly by the temperature and strain rate in this region. Ductility is low in region III which the grain size increases (150 μm) and is not influenced by the strain rate too much [40].

Strength of the OFHC copper specimens decreases as the initial grain size increases on the deformation at 500 and 700 °C for all strain rates as can be seen from Figure 3. But a peak value at the strengths of the

specimens is seen for initial grain size of 50 μm . This peak value is more obvious for 700 °C than the one for 500 °C especially for lower strain rates.

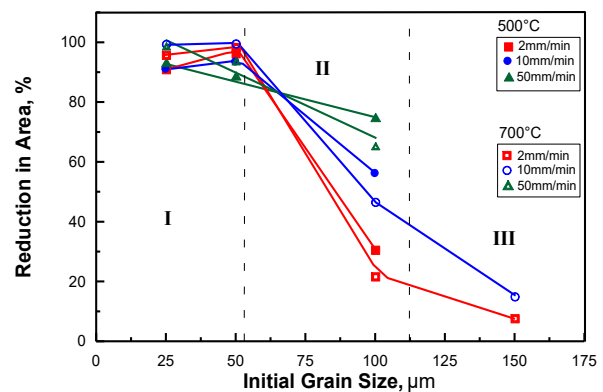


Figure 2. Variation of reduction in area with the initial grain size in the OFHC copper specimens.

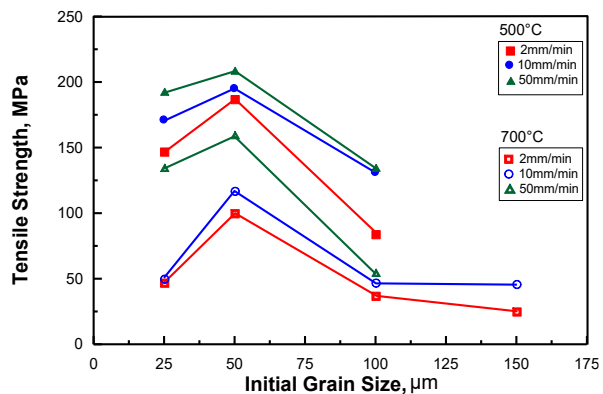


Figure 3. Variation of tensile strength with initial grain size in OFHC copper specimens.

Strength of the OFHC copper specimens decreases as the initial grain size increases on the deformation at 500 and 700 °C for all strain rates as can be seen from Figure 3. But a peak value in the strengths of the specimens is observed for the initial grain size of 50 μm . This peak value is more obvious for 700 °C than the one for 500 °C especially for lower strain rates.

Dynamic recrystallization occurs more easily with increasing temperature [41]. Ductility is high at all strain rates since the dynamic recrystallization ratio is high on the specimens having fine grain sizes at the strain rates at 500 and 700 °C. In the case of large grain sizes, it can be assumed that vacancies formed at the grain boundaries, due to the grain boundary sliding, caused the material to be fractured intergranularly and ductility decreased. Grain boundary sliding occurrence is mentioned in a study on OFHC copper: stress concentrations which can cause cracks and cavities arose in boundary irregularities such as triple points or at grain boundary particles [42]. As the grain size increases, the magnitude of stress concentrations increases.

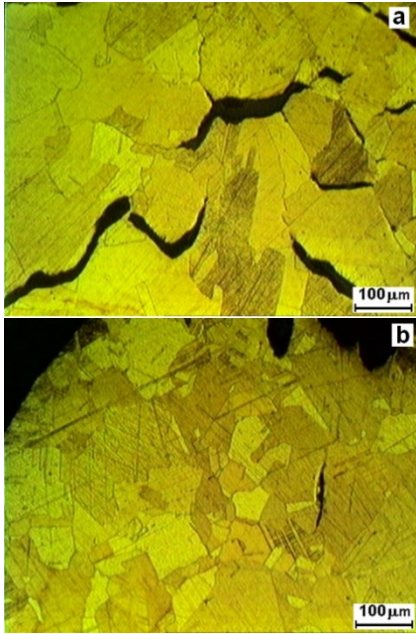


Figure 4. Microstructures of OFHC copper having an initial grain size of 100 μm tested at 750 $^{\circ}\text{C}$ (a) a strain rate of 2 mm/min, (b) a strain rate of 50 mm/min.

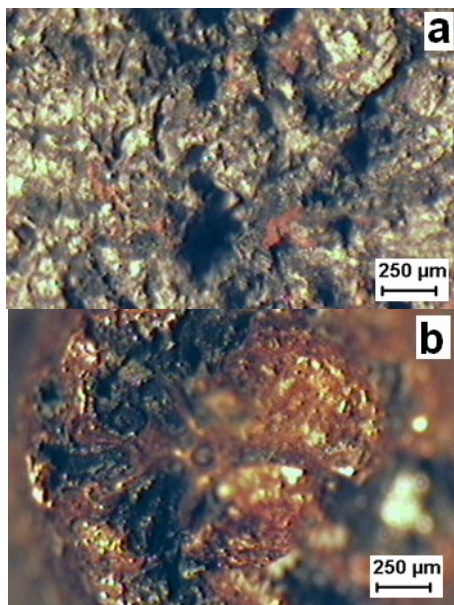


Figure 5. Fracture surfaces of OFHC copper having an initial grain size of 100 μm tested at 750 $^{\circ}\text{C}$ (a) a strain rate of 2 mm/min, (b) a strain rate of 50 mm/min.

Microstructures and fracture surfaces of OFHC copper having an initial grain size of 100 μm tested at 750 $^{\circ}\text{C}$ (a) a strain rate of 2 mm/min, (b) a strain rate of 50 mm/min are seen in Figures 4 and 5 respectively. It is seen that cavities are formed and intergranular fracture occurs due to grain boundary sliding at a strain rate of 2 mm/min (Figure 4 (a) and Figure 5 (a)); the amount of grain boundary sliding slightly decreases as the dynamic recrystallization increases for higher strain rates (Figure

4 (b) and Figure 5 (b)). The intercrystalline brittleness was investigated in the tin bronzes [43] and this brittleness was found to be mainly due to the grain boundary sliding mechanism, which generates a tensile stresses concentration at the grain boundary.

3.2. Effect of Temperature

The effect of temperature on ductility and tensile strength is seen in Figures 6 and 7 respectively. As can be seen from Figure 6, the values of reduction in area of OFHC copper specimens which have initial grain sizes of 50 μm are high and not influenced by the increasing temperature. Ductility is preserved at higher temperatures (500 $^{\circ}\text{C}$ - 0.57 T_m and 700 $^{\circ}\text{C}$ - 0.72 T_m) as a result of the occurrence of dynamic recrystallization. An evaluation of potential mechanisms responsible for low ductility at high temperatures indicates that grain boundary sliding is the dominant deformation mode in CuNiBe alloy at intermediate temperatures due to the high matrix strength associated with the high density of semi-coherent precipitates [22].

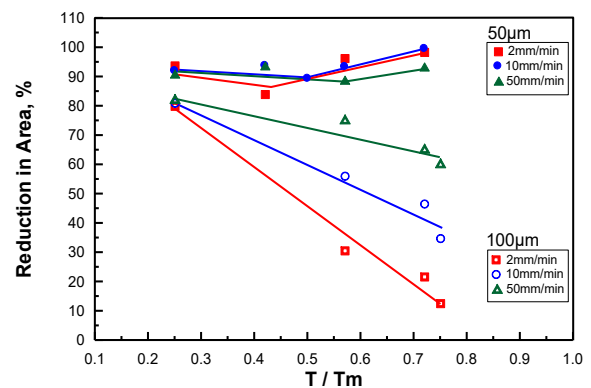


Figure 6. Variation of reduction in area with temperature in OFHC copper specimens.

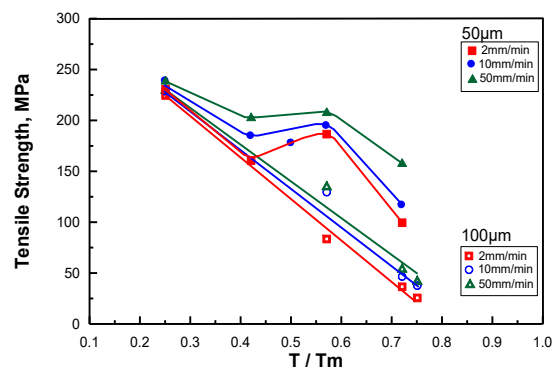


Figure 7. Variation of strength with temperature in OFHC copper specimens.

The reduction in area of specimens which have initial grain sizes of 100 μm decreases quickly by the increase in temperature. Increasing temperature and grain size increase the effect of intergranular fracture by grain boundary sliding. It is understood that the decrease in ductility is very sensitive against the strain rate.

Ductility increases with increasing strain rate. Possible causes are the increase in dynamic recrystallization ratio with the increasing strain rate and more difficult intergranular fracture behavior. Tensile strength decreases when temperature increases as can be seen from Figure 7. Tensile strength of copper specimens decreases with the increasing temperature for initial grain size of 100 μm but there is a slower decrease at the tensile strength of copper specimens having an initial grain size of 50 μm .

3.3. Effect of Strain Rate

The effect of strain rate and temperature has also been investigated in copper: a decreasing strain rate reduces ductility at a constant temperature. An increase in temperature up to 400 or 500 $^{\circ}\text{C}$ also causes a decrease in ductility [42].

The effect of strain rate on reduction in area and strength at 700 $^{\circ}\text{C}$ is shown in Figures 8 and 9 respectively. It is known that decreasing the strain rate decreases the equicohesive temperature and thus increases the tendency of intergranular fracture [44]. Effect of strain rate on reduction in area was studied in three regions for 700 $^{\circ}\text{C}$ and initial grain size of 100 μm by Lim and Lu [27]. In region I, grain boundary sliding and intergranular fracture is dominant in lower strain rates; ductility is low and not dependent on the strain rate. Region II is the transition region; ductility increases with the increasing strain rate by the influence of the dynamic recrystallization. In region III, dynamic recrystallization is the dominant mechanism; ductility is high and not dependent on the strain rate. As can be seen from Figure 6, the ductility values of the specimens having initial grain sizes of 25 and 50 μm are high and not dependent on the strain rate. Ductility increases with the increasing strain rate on the specimens having initial grain sizes of 100 μm . Ductility values of the specimens having initial grain sizes of 150 μm are low and not dependent on the strain rate.

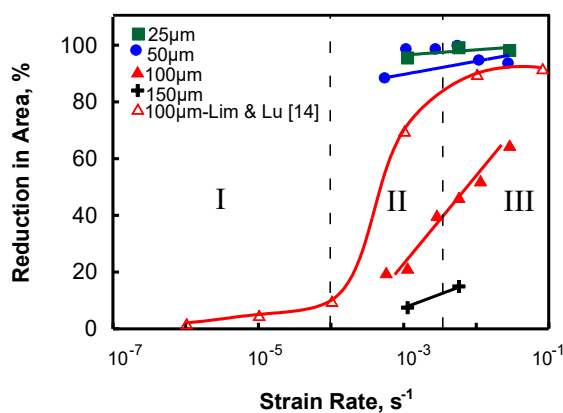


Figure 8. Variation of reduction in area with strain rate at 700 $^{\circ}\text{C}$ in OFHC copper specimens.

The effect of strain rate on tensile deformation was also investigated for the materials except for the copper. The high micro-shear banding frequency seen at low strain rates was found to be associated with an increased incidence of grain boundary sliding for an ultrafine-grained aluminum alloy. An increased slip level is required at higher strain rates since grain boundary sliding is limited. Micro-shear bands produced under these conditions quickly turn into macro-shear bands leading to failure [45].

According to Figure 8, the ductility does not change with the increasing strain rates for the lower initial grain sizes, but the ductility increases as the strain rate increases for the higher initial grain sizes. The slopes of the strength-strain rate curves seen in Figure 9, showing the increasing trend of tensile strength of copper specimens with the increasing strain rate, are consistent with the study of Lim and Lu [27].

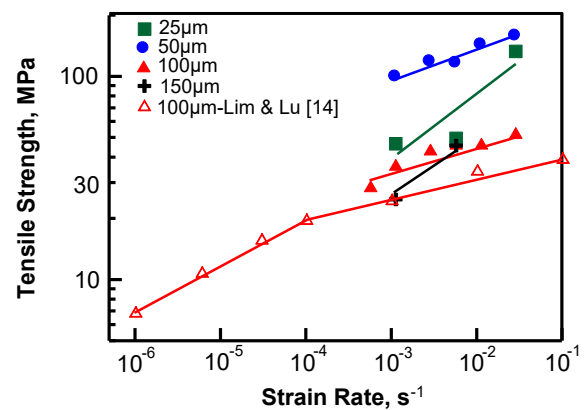


Figure 9. Variation of tensile strength with strain rate at 700 $^{\circ}\text{C}$ in OFHC copper specimens.

Fracture mechanism comes out as a result of hot deformation behavior of material. Ductile fracture occurs at low temperatures in FCC materials. Typical ductile fracture was seen on the specimens in which dynamic recrystallization occurred at the studied temperatures (Figure 10), but intergranular fracture was detected on the coarse grained specimens due to grain boundary sliding (Figure 11). In a 3N copper material, tested at 600 $^{\circ}\text{C}$, intergranular fracture was observed at the fractured surface: a lot of small dimples were observed on the grain boundaries. Many intergranular failures were also observed in the microstructure of this copper. The cavities first nucleate at the grain boundaries and become enlarged and chained together during deformation [41].

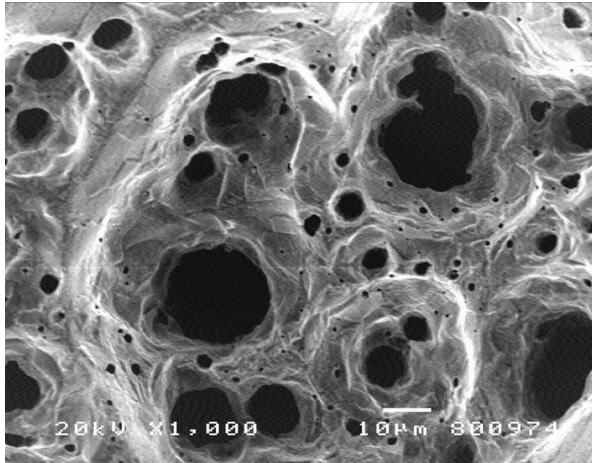


Figure 10. SEM image of a copper specimen which is broken in a ductile manner due to dynamic recrystallization; 700 °C (0.72 T_m), initial grain size: 50 μm , cross-head speed: 10 mm/min.

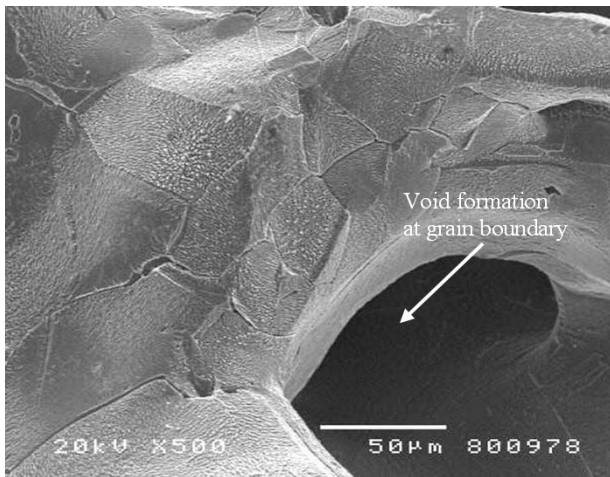


Figure 11. Void formation at the grain boundaries as a result of intergranular fracture at elevated temperatures; fracture surface of tensile specimen; 750 °C (0.75 T_m), initial grain size: 100 μm , cross-head speed: 2 mm/min.

4. Conclusion

Samples of different initial grain sizes were subjected to tensile tests at different temperatures and cross-head speeds to optimize the conditions to achieve maximum ductility in terms of initial grain size, process temperature and deformation rate in OFHC copper.

The optimum initial grain size is 50 μm , from the viewpoint of dynamic recrystallization, which can be responsible for the increase of strength and ductility at the temperatures and strain rates studied. The highest ductility for the initial grain size of 50 μm was obtained at 700 °C and a strain rate of $5.6 \times 10^{-3} \text{ s}^{-1}$ (62.4% strain and 99.6% reduction in area).

Fracture mechanism in OFHC copper is dependent on the parameters such as temperature, strain rate and grain size. Ductile fracture was observed at room temperature and it is the dominant fracture mechanism at elevated temperatures which have the conditions that dynamic recrystallization to occur. Intergranular fracture was observed under the conditions when dynamic recrystallization did not occur.

Working at temperatures and strain rates in which the dynamic recrystallization is the effective mechanism provides the easier production of the parts which are hard to be shaped in the real application conditions. This observed ductility increase for copper may also be used as a model for the other metals especially having face centered cubic (FCC) structure.

Author's Contributions

Selim Yıldırım: Conceptualized the methodology, made investigations, performed the experiments and helped in manuscript preparation.

Mustafa Merih Arkan: Made investigations, wrote and edited the manuscript, interpreted the results.

Ethics

There are no ethical issues after the publication of this manuscript.

References

- [1]. Karbasian, H, Tekkaya, AE. 2010. A review on hot stamping. *Journal of Materials Processing Technology*; 210: 2103-2118.
- [2]. Huang, F, Chen, Q, Ding, H, Wang, Y, Mou X, Chen, J. 2021. Automotive steel with a high product of strength and elongation used for cold and hot forming simultaneously. *Materials*; 14: 1121.
- [3]. Jeswiet, J, Geiger, M, Engel, U, Kleiner, M, Schikorra, M, Duflou, J, Neugebauer, R, Bariani, P, Bruschi, S. 2008. Metal forming progress since 2000. *CIRP Journal of Manufacturing Science and Technology*; 1: 2-17.
- [4]. Hu, P., Ma, N., Liu, Lz., Zhu, YG. Hot forming process. Theories, methods and numerical technology of sheet metal cold and hot forming. Springer series in advanced manufacturing. Springer, London, U.K., 2013.
- [5]. Kumar, F.B., Sharma, A., Oraon, M. Future research potentials of hot rolling process: a review. In: Chattopadhyay, J., Singh, R., Prakash, O. (eds) *Innovation in Materials Science and Engineering*. Springer, Singapore, 2019.
- [6]. Bhojar, V, Umredkar, S. 2020. Manufacturing processes part II: a brief review on rolling & extrusion, *International Journal of Innovations in Engineering and Science*, 5: 33-37.
- [7]. Blum, W, Li, YJ, Durst, K. 2009. Stability of ultrafine-grained Cu to subgrain coarsening and recrystallization in annealing and deformation at elevated temperatures. *Acta Materialia*; 57: 5207-5217.
- [8]. Li, X, Xia, W, Yan, H, Chen, J, Su, B, Song, M, Li, Z, Lu, Y. 2020. High strength and large ductility of a fine-grained Al-Mg alloy processed by high strain rate hot rolling and cold Rolling. *Materials Science and Engineering A*; 787: 139481

- [9]. Muhly, JD. The beginning of metallurgy in the old world, the beginning of the use of metals and alloys, MIT Press: Cambridge MA, USA, 1988.
- [10]. Yener, KA, Geçkinli, AE, Özbal, H. A brief survey of Anatolian metallurgy prior 500 BC, Proceedings of 29th Int. Symp. on Archaeom., İstanbul, Turkey, 1994, pp 375-391.
- [11]. Hajkazemi, J, Zarei-Hanzaki, A, Sabet, M, Khoddam, S. 2011. Double-hit compression behavior of TWIP steels. *Materials Science and Engineering A*; 530: 233-238.
- [12]. Hallberg, H, Wallin, M, Ristinmaa, M. 2010. Simulation of discontinuous dynamic recrystallization in pure Cu using a probabilistic cellular automaton. *Computational Materials Science*; 49: 25-34.
- [13]. Zhang, H, Zhang, H, Li, L. 2009. Hot deformation behavior of Cu-Fe-P alloys during compression at elevated temperatures. *Journal of Materials Processing Technology*; 209: 2892-2896.
- [14]. Lv, J, Zheng, J-H, Yardley, VA, Shi Z, Lin, J. 2020. A review of microstructural evolution and modelling of aluminium alloys under hot forming conditions. *Metals*; 10: 1516.
- [15]. Churyumov, AY, Pozdniakov, AV. 2020. Simulation of microstructure evolution in metal materials under hot plastic deformation and heat treatment. *Physics Metals and Metallography*; 121: 1064-1086.
- [16]. Gao, W, Belyakov, A, Miura, H, Sakai, T. 1999. Dynamic recrystallization of copper polycrystals with different purities. *Materials Science and Engineering A*, 265: 233-239.
- [17]. Favre, J, Fabre` Gue, D, Piot, D, Tang, N, Koizumi, Y, Maire, E, Chiba, A. 2013. Modeling grain boundary motion and dynamic recrystallization in pure metals. *Metallurgical and Materials Transactions A*; 44: 5861-5875.
- [18]. Vöse, M, Otto, F, Fedelich, B, Eggeler, G. 2014. Micromechanical investigations and modelling of a Copper-Antimony-Alloy under creep conditions. *Mechanics of Materials*; 69: 41-62.
- [19]. Srivastava, V, Mcnee, KR, Jones, H, Greenwood, GW. 2003. The effect of low stresses on creep and surface profiles of thin copper wires. *Acta Materialia*; 51: 4611-4619.
- [20]. Zhu, YT, Liao, XZ, Wu, XL. 2012. Deformation twinning in nanocrystalline materials. *Progress in Materials Science*; 57: 1-62.
- [21]. Meyers, MA, Mishra, A, Benson, DJ. 2006. Mechanical properties of nanocrystalline materials. *Progress in Materials Science*; 51: 427-556.
- [22]. Zinkle, SJ. 2014. Evaluation of high strength, high conductivity CuNiBe alloys for fusion energy applications. *Journal of Nuclear Materials*; 449: 277-289.
- [23]. Zhang, H, Zhang, H-Gang, Peng, D. 2006. Hot deformation behavior of KFC copper alloy during compression at elevated temperatures. *Transactions of Nonferrous Metals Society of China*; 16: 562-566.
- [24]. Jonas, JJ, Toth, LS, Urabe, T. 1994. Modelling the effects of static and dynamic recrystallization on texture development. *Materials Science Forum*; 157: 1713-1730.
- [25]. Belyakov, A, Miura, H, Sakai, T. 1998. Dynamic recrystallization under warm deformation of polycrystalline copper. *ISIJ International*; 38: 595-601.
- [26]. Yamagata, H. 1995. Dynamic recrystallization and dynamic recovery in pure aluminum at 583 K. *Acta Metallurgica et Materialia*; 43: 723-729.
- [27]. Lim, LC, Lu, HH. 1994. Dynamic grain growth and ductility enhancement at intermediate temperature. *Materials Science and Engineering A*; 176: 439-446.
- [28]. Hamed, AA, Blaz, L. 1998. Microstructure of hot-deformed Cu-3.45 wt.% Ti alloy. *Materials Science and Engineering A*; 254: 83-89.
- [29]. Manonukul, A, Dunne, FPE. 1999. Initiation of dynamic recrystallization under inhomogeneous stress states in pure copper. *Acta Materialia*; 47: 4339-4354.
- [30]. Lin, J, Cheng, J. 1999. Dynamic recrystallization during hot torsion of Al-9Mg alloy. *Transactions of Nonferrous Metals Society of China*; 9: 799-805.
- [31]. Muto, A, Kawagishi, S, Tagami, M. 1999. Effects of grain size and strain rate on ductility of Cu-30 mass % Zn alloy at 673 K. *Journal of the Japan Institute of Metals*; 63: 1062-1068.
- [32]. Yagi, H, Tsuji, N, Saito, Y. 2000. Dynamic recrystallization in 18%Cr ferritic steel. *ISIJ International*; 86: 349-356.
- [33]. Mejia, I, Bedolla-Jacuinde, A, Maldonado, C, Cabrera, JM. 2011. Determination of the critical conditions for the initiation of dynamic recrystallization in boron microalloyed steels. *Materials Science and Engineering A*; 528: 4133-4140.
- [34]. Quan, G, Li, G, Chen, T, Wang, Y, Zhang, Y, Zhou, J. 2011. Dynamic recrystallization kinetics of 42CrMo steel during compression at different temperatures and strain rates. *Materials Science and Engineering A*; 528: 4643-4651.
- [35]. Wu, B, Li, MQ, Ma, DW. 2012. The flow behavior and constitutive equations in isothermal compression of 7050 aluminum alloy. *Materials Science and Engineering A*; 54: 279-287.
- [36]. Pande, CS, Cooper, KP. 2009. Nanomechanics of Hall-Petch relationship in nanocrystalline materials. *Progress in Materials Science*; 54: 689-706.
- [37]. Guo, Y, Britton, TB, Wilkinson, AJ. 2014. Slip band-grain boundary interactions in commercial-purity titanium. *Acta Materialia*; 76: 1-12.
- [38]. Fan, XG, Yang, H, Sun, ZC, Zhang, DW. 2010. Quantitative analysis of dynamic recrystallization behavior using a grain boundary evolution based kinetic model. *Materials Science and Engineering A*; 527: 5368-5377.
- [39]. Sakai, T, Jonas, JJ. 1984. Dynamic recrystallization: Mechanical and microstructural considerations. *Acta Metallurgica*; 32: 189-209.
- [40]. Yıldırım, S. Mechanical behavior of pure copper at elevated temperatures: dynamic recrystallization and dynamic grain growth. PhD. thesis, İstanbul Technical University, Institute of Science and Technology, 2001.
- [41]. Fujiwara, S, Abiko, K. 1995. Ductility of ultra-high purity copper. *Le Journal de Physique IV*; 05 C7: C7-295-C7-300.
- [42]. Henderson, PJ, Sandström, R. 1998. Low temperature creep ductility of OFHC copper. *Materials Science and Engineering A*; 246: 143-150.
- [43]. Ozgovicz, W. 2005. The relationship between hot ductility and intergranular fracture in a CuSn6P alloy at elevated temperatures. *Journal of Materials Processing Technology*; 162-163: 392-401.



[44]. Dieter G E. Mechanical metallurgy (SI metric edition), adapted by David Bacon; McGraw-Hill Book Company, London, U.K., 1988.

[45]. Sabirov, I, Estrin, Y, Barnett, MR, Timokhina, I, Hodgson, PD. 2008. Tensile deformation of an ultrafine-grained aluminium alloy: Micro shear banding and grain boundary sliding. *Acta Materialia*; 56: 2223-2230.

The Evaluation of the Non-Toxic Ferrous Matrix Based WC Reinforced Composites: A Review

Esad Kaya^{1*} , Mustafa Ulutan¹ 

¹ Eskisehir Osmangazi University, Department of Mechanical Engineering, Eskisehir, Turkey:

* esatkaya@ogu.edu.tr

* Orcid No: 0000-0002-7332-6154

Received: 7 November 2021

Accepted: 27 May 2022

DOI: 10.18466/cbayarfbe.1020170

Abstract

Metal matrix composites are mainly used as a cutting tool insert material. These types of materials are essential to maintain desired mechanical and microstructure properties at elevated temperatures due to friction and wear. Nano sized Tungsten Carbide reinforced composites are mostly used for these conditions. The production of sintered nano sized Tungsten Carbide reinforced composites are done by using powder metallurgy. The different mass ratios of elements including mostly Cobalt and the others could be added as binder phase. The binder phase provides to metal matrix composite superior features including high elasticity, good solubility, similar thermal conduction coefficient and, effective liquid phase sintering mechanism. Cobalt is one of the base elements of high-performance superalloys and rechargeable battery technology. Also, 40% of global need supplied by a single country makes itself higher-priced. It is also known that Cobalt is a high skin allergen and carcinogenic. Together with these obstacles, the investigations of low-cost, non-toxic, or reduced-toxicity materials are always needed. In this study, the related current literature has been investigated in detail. The studies focus on an alternative matrix that providing mentioned conditions explained with pros and cons.

Keywords: Non-Toxic Materials; Powder Metallurgy; Sintered Carbides; The Carbon Window

1. Introduction

MMC structures are newly formed materials by mixing different elements or alloys with a mass or volume scale. The primary purpose of making MMC materials is to bring and unite the best properties of components in the microstructure [1, 2]. MMC materials have two components. These are matrix and reinforcement phases.

The matrix phase covers the reinforcement phase and ensures homogeneous dispersion within the microstructure. On the other hand, reinforcement materials reveal their unique properties to develop the newly formed composite material. As a result of this combination variety, the newly formed materials have unique mechanical and microstructural properties which not found on both sides. MMC can be produced by many production methods include casting and powder metallurgy (PM) technique [2].

The cutting inserts are composed of multiple compounds and elements as MMC structures. The inserts are usually produced mainly from carbide and

nitrides as reinforcing materials (TiC, WC, TiN, CrN, etc.). Such compounds that are ionic or covalently bonded have ultra-high melting temperatures and hardness. Lean carbide or nitride are brittle and difficult to manufacture in complex shapes [3]. For this reason, the binder must be added. The PM technique is used mainly in the production of cutting tool inserts. In this method, parts are made of metal powders. The Traditional PM process is followed; the powders are pre-molded to the desired shape, pressed compactly, and sintered to create a chemical bond. Sintering is usually done at a temperature nearly above the melting temperature of the binder. One of the essential factors in the sintering process is the wetting capability of the binder phase. The binder material is expected to fill the gaps in the microstructure well, wet the main reinforcing phase, and dissolve in it [2].

Different researchers have carried out experimental and theoretical studies on W-Fe-C systems. The focus of the studies was on the C ratio, austenite (Fe- γ) ratio, and Fe-containing carbide structures. Uhrenius, Forsén [4], studied the carbide, ferrite, and austenite ratios in the structure at 1000°C. They reported that the C ratios in

W-Mo-Fe-C, W-Fe-C, and Mo-Fe-C systems varied between 0.012 and 0.097. In the ternary W-Fe-C system, they observed ferrite (Fe- α), M_6C , Fe_3C , and austenite.

Kirchner, Harvig [5], investigated carbide and austenite formation kinetics in the W-Fe-Cr-C system. The studies were carried out at three temperatures, 900°C, 1000°C, and 1100°C. They reported that as the ratio of W and Cr in the structure increased, $M_{23}C_6$ type carbide lost its stability compared to M_6C type carbides. They also reported that $M_{23}C_6$ type carbides for W-Fe-C systems are metastable at these temperature ranges. This occasion has been confirmed by other studies as well [6, 7]. In another study, Upadhyaya [8] investigated the formation kinetics of Fe-containing MC, M_6C , and $M_{12}C$ carbides in metal matrix composites. He found that carbide formations containing lean Fe were metastable and brittle in his study. This occasion indicates that Fe alone cannot show sufficient binder performance. Ni also exhibits good corrosion resistance due to its similarity to Co in terms of microstructural properties. Researchers consider it an alternative binder due to the proximity of melting points to Co [8]. The fact that the lattice structure is face-centered cubic also ensures that it has a ductile character. However, the main reason why Ni or any element cannot be used directly alternative to Co in a pure state is that it has high stacking fault energy [9]. The high stack faulting energy reduces the strength of the material. This situation causes lower hardenability in the materials to be formed. Ni can wet and dissolve WC well. But it is insufficient to perform on its own.

Hard carbides such as WC are the most commonly used cutting tool reinforcement phase in MMC materials. Due to high hardness and chemical stability at elevated temperatures, WC advances rapidly among them. Co is an essential element that makes WC a cutting tool material. Due to having a similar thermal conductivity coefficient and excellent wettability in WC, Co provides superior toughness, elasticity, and liquid phase sintering occurrence [10]. However, Co is one of the base elements of high-performance superalloys, and rechargeable battery technology increases its production cost [11]. It is also a severe skin allergen and cancer trigger [12]. Due to these reasons, the search for non-hazardous alternative binder materials continues.

In this study, the microstructural and mechanical properties of nonhazardous and economical elements and compounds, which can be an alternative to the toxic Co element in sintered WC materials, were investigated as literature data. Within the scope of the article, applied alternative binding matrix materials in the literature was investigated. Identified candidate material were divided into groups and are presented to the readers with their pros and cons.

2. Materials and Methods

2.1. WC Reinforced Metal Matrix Composites

MMC materials are one of the most successful produced engineering materials. Sintered carbides, mainly composed of WC bonded with Co or the other elements and alloys, are also MMC materials. In the English technical literature, sintered carbides are known as "Cemented Carbides." The term "cement" is given because the binder acts like a "cement" among hard carbide grains. For sintered carbide materials, the binding capacity of the binder is an essential factor. Fig. 1 represents the main components of sintered carbides consisting of WC and binder matrix. WC phase is exhibited as grey layers, while the binder exhibits black layers. The role of the binder is of great importance for these materials. Fig. 2 shows the mechanical properties of carbide structure based on research. One can be implied that WC has superior mechanical properties among the carbides.

The first produced Co content sintered WC carbides goes back to the 1920s in history. It has been used in wire production and defense industry applications [13]. Over time, it has begun to be used as a cutting tool in the manufacturing industry by replacing high-speed steel due to its high mechanical properties. When today's manufacturing industry cutting tool materials are examined, it is noteworthy that MMC materials still form a vital part of the tool materials industry [14, 15]. For many years, the Co element has been under surveying about the substitution with nontoxic and economical candidates. Among the reasons for change is the price fluctuation of Co and especially for hazardous effects [16]. Co powder is known to be carcinogenic and skin allergen [17]. It is known that approximately 90% of the WC tools used in the industry are Co-based due to their high hardness and wear resistance [18].

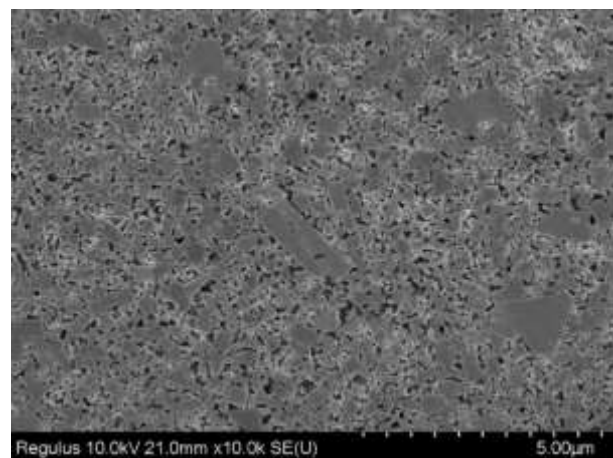


Figure 1. Typical nano-sized WC reinforced MMC containing 10% binder (wt)

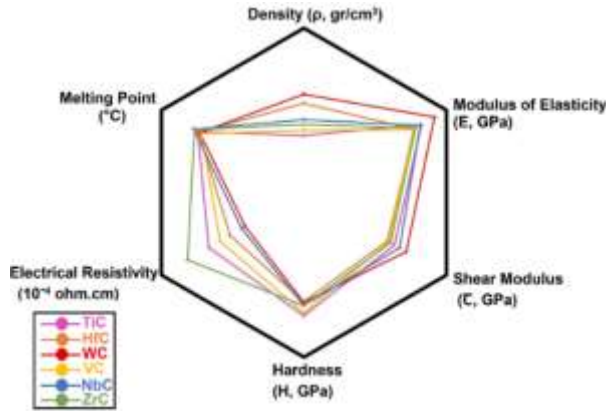


Figure 2. Mechanical performance of carbides. The figure was created by authors based on the data of Bauccio [19]

WC-based sintered carbides are the most important among the cutting tool materials.

So, superior material performance, price fluctuation, and hazardous effects of Co element enhance the efforts to seek alternative binders even more.

The WC phase provides the necessary strength and wears resistance to the MMC for the sintered carbides, while the Co contributes to the toughness and ductility. Different elements and compounds can also be added to the structure to prevent abnormal grain growth and increase the microstructure's mechanical properties. For example, VC can also be added to the microstructure as a WC grain inhibitor even though it enhances the mechanical properties of the material, increasing processing costs [20].

Sintered WC – Co is typically used in drilling or cutting tools and manufacturing wear-resistant materials due to its superior hardness and wear resistance. The main usage areas are turning, milling operations, glass cutting tools, and plastic deformation applications such as forging-drawing dies and mining operations tools [15].

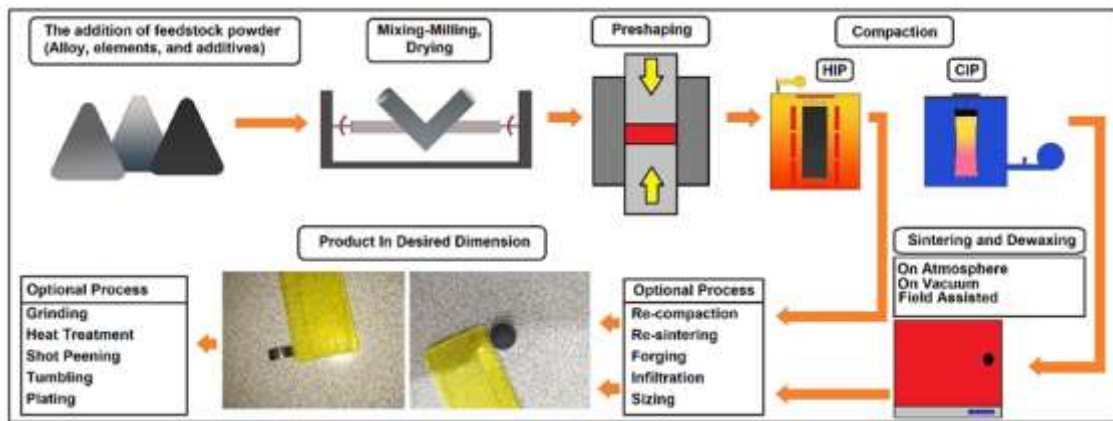


Figure 3. The basic production schema of MMC

Fig. 3 shows the basic production techniques of sintered carbide for powder metallurgy. The powders are mixed and pressed, then sintered at temperatures around 1300°C -1500°C, where the binder transforms the liquid phase. Due to the differences in thermal expansion coefficients, carbide grains are forced to compaction, while the binder phase forces the microstructure to the tension, and both phases equalize each other. Thus, homogeneous stress-free structures are obtained [21].

2.2. The importance of WC as a Reinforcement Material

Within the scope of the current research, WC preserves its rigidity, hardness, and chemical stability at elevated temperatures. Three intermediate compounds are presented for WC formations. These are W_2C , WC_{1-x} , and WC. The W_2C compound can exist in three different crystal structures. These are α - W_2C in the orthorhombic crystal structure, β - W_2C in an irregular hexagonal structure, and γ - W_2C in a hexagonal

structure. The most stable structure at room temperature is α -WC in a hexagonal structure. This structure has no solid resolution up to 2538°C.

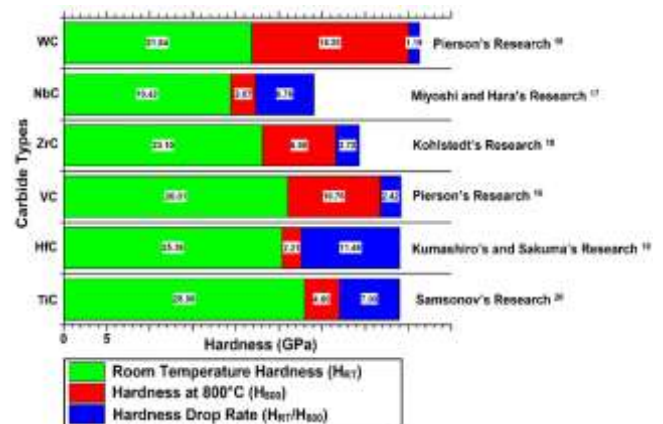


Figure 3. The hardness derivation of the metal carbides

W_2C overreacts with the C binder, causing brittleness, while the amount of C reduces toughness and stiffness. In another alloy, $WC + C$, the amount of carbon reduces hardness but does not affect toughness and sintering conditions [22].

Fig. 4 exhibits the hardness behavior of the different carbides upon the increasing temperature. It is observed that WC maintains its strength at 800°C compared to other carbide types. It is seen that WC has the lowest hardness drop ratio at elevated temperatures. These conditions make WC relatively more featured than other carbides [22].

3. Results and Discussion

3.1. Binder Materials

Today, many metals, compounds, and alloys are on trial as matrix materials for WC reinforced MMC. The most significant feature expected from the matrix material should improve inter-reinforcing bonding and overall structural strength. In this context, the general properties of the most common metals and alloys used as matrix material are summarized below.

Many studies have been conducted on carbide materials with sintered WC-Co content, including different binders. It is observed that current studies have been limited to experimental studies on the coating of the sintered carbides. This study focused on determining the properties required to select the best binder combination to replace Co by using literature. In the scope of the study, the microstructural, mechanical, and tribological properties of the materials were considered in the selection of binders. The literature research on the current topic has been expressed under seven main sections, including Co, Ni, Fe, Fe-Mn, Fe-Al, FeAl-B, and Fe-Ni binder content. Related literature topics were researched, and the studies were summarized according to the determining criterion.

3.2. Co-Based Binder Systems

The composition of the sintered WC-Co determines the microstructure and mechanical properties significantly. WC-Co binary phase combinations contain graphite and carbide phases called eta (η , which can be seen in Fig. 5 as black zones) that are not desired to form in the microstructure. These phases cause a significant deterioration of both the mechanical properties and the tribological properties of the composite. This pernicious situation is prevented by C control at the stoichiometric level in WC. Therefore, the carbon content must be kept within a narrow limit to obtain the desired compound with optimum properties.

Besides, some Co-containing carbides have negative effects on the mechanical properties of the microstructure. Co-containing carbides are formed in

compositions in the range of W_2C_4 (MC_2 type) and $Co_{3.2}W_{2.8}C$ (M_6C type) and are nucleated and grown during the sintering process.

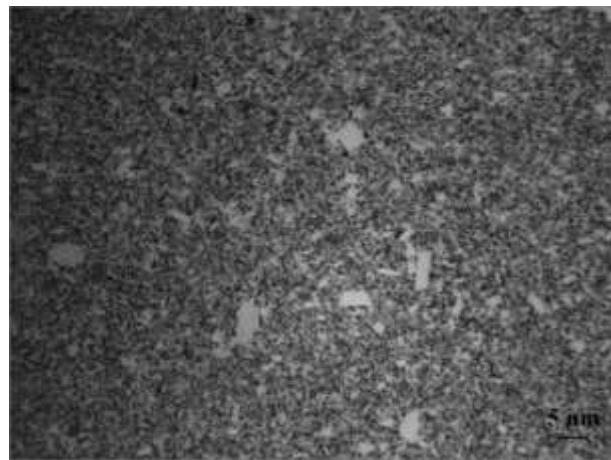


Figure 5. Typical microstructure of sintered carbides contain eta (η) type carbides and graphite

Co-containing M_6C carbides interact less with the binder, loosening the microstructure and reducing WC's contribution to the strength of the MMC material. This causes the general microstructure to become brittle. Two types of phases, M_6C and $M_{12}C$, are formed during sintering. Of the two types of phases, M_6C occurs in compositions in the range of W_2C_4 to $Co_{3.2}W_{2.8}C$, while $M_{12}C$ occurs in the form of Co_6W_6C . The M_6C is in equilibrium with the liquid phase during the sintering process. The M_6C interacts less with the binder phase to loosen up the bondings of the microstructure. It also reduces the contribution of WC to the strength of the composite material and causes the overall bulk material to become brittle. Conversely, in the $M_{12}C$ type, it occurs in the form of small grains scattered all over the matrix when cooling after solidification. Due to the increased grain limit, it provides high strength and less brittleness [28-30].

3.3. Ni-Based Binder Systems

Co is the most commonly used traditional binder metal for WC reinforced composite materials. Ni is thought to be the most likely candidate to replace Co to the research. However, Ni's high ductility and low tribological properties prevented its commercial applicability [30-32]. Bonny, De Baets [33], examined the abrasive wear resistance of WC reinforced composite material with four different Ni phase contents at different wear load and sliding speeds. As a result of their experiments, they found that the hardness and wear resistance increased as the amount of the binder phase decreased. The highest wear resistance was observed in the group containing 10% Ni with Cr_3Cr_2 addition compared to the lean Co phase. Even if the Ni ratio increased in all samples, the wear resistance did not perform higher than the reference group.

Ni's high ductility also provides higher mechanical properties. Tarragó, Ferrari [9], produced WC-reinforced MMC materials with Ni matrix. They compared the mechanical properties of the produced materials with the WC-Co material. They found that composites with Ni matrix exhibit similar fatigue strength. The crack propagation tests reported that Ni-containing material showed more stable crack propagation.

Besides the production cost of Co, it adds composite higher mechanical properties, making it a superior and more preferred binder than Ni. Also, the resolutions of Co and Ni in WC are pretty different from each other. Co can solve more WC at higher temperatures than Ni [31]. At low temperatures, it was found that the situation reversed [4]. However, this situation cannot provide the necessary contribution in cases where liquid phase formation is desired. In the case of compositions containing excessive C at high temperatures, the solubility of Ni and Co was found to be almost the same [34]. This indicates that Ni will increase its effectiveness when used with different elements. Also, the Ni element forms $Ni_xW_yC_z$ type carbides in the Ni-W-C system like Co. Different studies have determined that this type of carbide formed is more ductile than Co-containing carbides [31, 35].

Ni exhibits good corrosion resistance due to its similarity to Co in terms of microstructural properties. Due to the similar melting points to Co, researchers thought it to be an alternative binder [8]. Penrice [36], made a theoretical study on alternative binder matrix materials to Co. He studied Ni, Re, Ru, Mo, and Cr elements. He observed that although Re and Ru have similar effects as Co. Due to their unit cost and rare earth elements status, these elements aren't attractive as potential candidates. He also stated that Cr and Mo additives provide higher strength but have low corrosion resistance compared to Co. The author also reported that Ni is an austenitic binder due to its face-centered cubic structure and that it can also turn into a body-centered cubic structure in alloys if it can be used with other elements such as Fe, C, Cr, Mo. He reported that Ni's austenitic structure was also suitable for heat treatment.

Some studies are using one or more Co, Mo, Cr, V, and Mn elements to increase the hardness and strength of Ni alloys. The results of numerically computational phase methods (CALPHAD) determined that the phase would be stable in binders with different contents. Also, it has been observed that Ni performs better hardness and toughness properties in comparison to Co ingredients [37-39]. Guo, Xiong [8], produced Ni-WC-TiC-Mo₂C composite materials in different proportions and grain sizes. They applied bending and hardness tests to the produced MMC. It has been determined that the bending strength decreases with the decrease of the Ni ratio. Also, the strength of the reinforcing phase

increases with decreasing grain size. It is known that Mo₂C is a well-known grain growth inhibitor. It was observed that with the increase of Mo₂C additive, the WC grain structure shrank, and the hardness and bending strength increased.

The fact that the crystallographic structure of the Ni element is a face-centered cubic provides a ductile behavior. But the main reason Ni or any element cannot be used directly instead of Co is stacking fault energy. [9]. High stacking error energy reduces the strength of the material. This situation caused the lower hardenability of the MMC materials. The inadequate performance of the alternative binders forces the industry to use Co-Ni-containing compositions. The development of non-toxic material is a need.

3.4. Fe-Based Binder Systems

Different researchers carried out experimental and theoretical studies on W-Fe-C systems. The orientation of most of the studies was on the C ratio, austenite (Fe- γ) ratio, and Fe-containing carbide compound in the microstructure. Uhrenius, Forsén [4], researched to determine the carbide, ferrite, and austenite ratios in the microstructure at 1000°C. They reported that C ratios in W-Mo-Fe-C, W-Fe-C, and Mo-Fe-C systems ranged from 0.012 to 0.97. The balance between ferrite (Fe- α), M₆C, Fe₃C, and austenite was observed in the triple W-Fe-C system. Kirchner, Harvig [5], investigated carbide and austenite formation kinetics in the W-Fe-Cr-C system. The studies were carried out at three temperatures: 900°C, 1000°C, and 1100°C. They reported that as the ratio of W and Cr in the structure increases, M₂₃C₆ type carbide loses its stability compared to M₆C type carbides. They also reported that M₂₃C₆ type carbides for W-F-C systems were metastable at these temperature ranges. This situation was confirmed by different studies. [6, 7]. Hou, Linder [16], and C. B. Pollock [40] investigated the variations of the stoichiometric composition of Fe matrix composites. Both papers reported homogeneous formation gaps for M₁₂C and a smaller composition gap for M₆C than other binder types. In terms of formation kinetics, it was determined by these studies that it provides a more homogeneous microstructure. To evaluate mechanical properties, Moskowicz, J. [41] produced WC-Fe composites. They investigated the amount of brittle η phase (Fe₃W₃C) formed in materials produced in different ratio. They examined the mechanical (bending test) and tribological (abrasive wear) properties of the produced MMC. In the tests carried out, they determined that relatively close results were obtained for Co alloys.

Upadhyaya [21], investigated the formation kinetics of Fe-containing M₁₂C carbides in MMC. He found that Fe content M₁₂C carbide formation was not observed. This indicates that Fe alone does not have sufficient binding

performance. Schubert, Fugger [42], examined the WC-Fe structures. They found that the WC phase prevents grain growth due to the high affinity of Fe compared to Co. They also found that this condition provides high hardness after sintering. However, they found that high C affinity triggered the formation of M_6C phases known to be hard and brittle. They reported that using only the Fe element as a binder material shows low corrosion resistance and that single Fe use is insufficient for WC reinforced composite materials.

3.5. Fe-Mn Based Binder Systems

Another system considered as an alternative to the Co element is Fe-Mn alloys. It can be considered an advantage that the Mn element is an austenite trigger. It is also known that Mn increases the strength of the steel. Besides, having a body-centered cubic lattice structure makes Mn easy to form like Ni. However, the low melting temperature makes drawbacks for use as a matrix phase. Schubert, Fugger [42], produced a WC-(FeMn) content MMC. Because of the low melting temperature of the Mn element, they could not use high sintering temperatures to reach the melting of Fe. They observed that after the sintering process, which was performed at 1380°C for 1 hour, 16% of Mn remained in the microstructure. Mn mass losses were observed. The evaporated Mn particles caused high porosity in the microstructure. Therefore, Fe-Mn cannot be used effectively for cutting insert material.

3.6. Fe-Al Based Binder Systems

Fe-Al is a good alternative to Co due to its excellent physical and mechanical properties. It has been researched by many researchers for making composites containing Fe-Al and WC. It was found that the Fe-Al content composites have performed equivalent wear resistance, hardness, and oxidation resistance as WC-Co [43-45]. In general, the corrosion resistance of Fe-Al is known to perform better than that of the Co metal [46]. This situation indicates that Fe-Al content composites have the potential for use in corrosive environments. Apart from that, Fe-Al has some disadvantages. In terms of thermodynamic calculations, it has been calculated that the ability to solve WC is lower compared to Co (2% at 1450°C). While the spark plasma sintering (SPS) technique provides performance equivalent to Co, the conventional PM has been found to exhibit lower tribological and mechanical properties [46]. This situation concerns economic costs.

3.7. FeAl-B Based Binder Systems

The potential use of Boron (B_2) content FeAl structures in high-temperature applications has been investigated by many researchers for the last 20 years [43, 47-49]. Adding (FeAl) B_2 alloys performs better oxidation, corrosion, wear-resistance, and strength. The enhancing

microstructural mechanism for this situation is work hardening [43]. Ahmadian, Wexler [50], produced the hot-pressed WC-FeAl-B composite to observe the B_2 effect. Their study observed that a small amount of B_2 additives (500ppm) could increase the toughness and prevent WC grain growth. They also found that B_2 additive composites perform higher abrasive wear resistance. This situation makes B_2 content intermetallics potential candidates for WC reinforced MMC.

3.8. Fe-Ni Based Binder Systems

Fe-Ni compositions are currently being studied by many researchers to replace the conventional Co binding phase or to reduce the Co ratio due to a pretty low production cost. When the results are evaluated in microstructural and mechanical properties, chemical composition, and process conditions are well determined, these alloy systems could achieve comparable or even superior properties to Co-containing binders. [29]. Also, by carefully controlling the Fe-Ni composition ratio, carbon content, and thermodynamic processes, the desired degree of stability of the binding phase could be achieved. Thanks to the stable phase presence provided, it is predicted that with the transformation toughening seen in the Fe-Ni binder, higher toughness will be obtained without loss of hardness compared to the classical WC-Co composition [51].

There are studies about the PM method and various sintering techniques under different Fe and Ni binding ratios. A literature survey was carried out regarding the mechanical and microstructural behaviors. The studies that are found are summarized below:

Cramer, Preston [31], examined the production and mechanical properties of WC- (Fe-Ni) composite materials containing Fe-Ni in situ forms. Ni powders were melted on Fe-WC material which was pre-shaped differently. As a result of the study, 97% theoretical density and 6.72 GPa hardness was observed on WC-(FeNi) pellet composite material. They reported that Fe-Ni could be an alternative to WC-Co materials after proper sharpening operations for machining. Hou, Linder [16], investigated the effect of C ratio in materials on Curie temperature and binding content of carbides formed in WC-(Fe-Ni) composite. They found that Ni was austenitic, and it changed the paramagnetic specialty based on the content of carbides. Increasing the C ratio from 5.72% to 5.83% increased the curie temperature from 200°C to 572°C. They determined by XRD methods that even the slightly varying C ratio, the dramatic variation of the Curie temperature was due to the formation of Ni-rich carbides. De Oro Calderon, Agna [52], produced MMC materials consisting of WC and AISI 360L. Experimental studies examined the microstructural and mechanical properties in terms of

four different matrix phase ratios. They reported that the binder material does not retain its stainless steel property and shows an austenitic behavior even at increasing sintering temperatures. In addition, they found that $M_{23}C_6$ and M_7C_3 type carbide formation kinetics are high due to the Cr-rich stainless steel binder. Because of the high C range, undesired metastable η type carbides were observed in all control group samples.

Fernandes, Puga [53], formed a compound by applying high-energy grinding technique with different parameters to nano-sized WC-AISI 304 powder containing 12% stainless steel by mass. As a result of the dilatometry analysis, they observed that M_6C type carbides, which are known to have low mechanical and microstructural properties. Besides, it was determined that nano-sized powders perform better binding and activation energy in solid-state sintering than micron-sized powders. Tarraste, Kübarsepp [54], used AISI 430L ferritic stainless steel to produce WC-reinforced composite material. They examined microstructural properties for produced MMC at constant sintering temperature at five different binder chemical ratios and six different sintering temperatures. They found that the practical density increases as the sintering temperature decreases. The liquid phase formed between high sintering temperatures (1100°C -1200°C). They also found that the increased binder phase ratio enhances the fracture toughness. They stated that this situation was related to the binder phase ratio, increasing C value, and correspondingly decreasing η phase ratio in the microstructure.

It has been confirmed by many studies that, the ratio of the liquid phase in the structure is very critical. In the liquid phase sintering process, the matrix is melted and bonds to the reinforcement, followed by cooling and solidification. It is recommended that the matrix ratio should not be more than 25% for liquid phase sintering processes in the industry. [2].

Cacciamani [55], obtained a binary Fe-Ni diagram numerically and experimentally in his study. As a result, they showed that melting temperatures for the Fe-Ni mixture state containing 10-20% Ni are in the 1400°C band while Co can solve them WC amount in ranges are around 1900°C. This shows that the binders with Fe-Ni content can provide sintering at much lower temperatures. This occasion would decrease the thermal distortion of bulk composite material. Also, these temperatures are lower for Ni alloys that are predicted to exhibit similar mechanical properties. Fe-Ni alloys can provide lower temperatures for sintering. Liquid phase sintering temperatures are around 1400°C in Fe-Ni containing nearly 20% Ni. They exhibited that Ni alloys would provide the desired hardness and strength by adding the Fe element to the structure.

Fernandes, Senos [56], produced composite materials using the SPS technique with WC-AISI 304 stainless steel powder. They examined the effect of sintering at different temperatures on material density, brittle η phase formation, and liquid phase occurring formation temperature. They found that sintering at high temperatures reduced the density but increased the liquid phase ratio. They reported that the used alloy composition caused the formation of eutectic structures at 1100°C.

Wittmann, Schubert [57], produced composite materials containing WC-Fe-Ni content. They reported that the formation of the brittle Fe_3W_3C phase can be prevented by lowering the carbon density. But more importantly, they reported that with the addition of Ni or a similar austenite phase formation trigger element, the alloy exhibits equivalent bending strength comparison to Co. Besides, with the optimum addition amount of Ni, it has been observed that the structure transformed into the austenitic state. They also reported that the heat treatments can improve the Fe-Ni matrix due to the austenitic structure.

Gonzalez, Echeberria [58], produced WC-Fe-Ni-C composite materials with a PM technique. They applied different heat treatments to the produced specimens. Microstructures and mechanical properties of heat-treated materials were investigated. It has been determined that the highest fracture toughness occurs in the bainitic transformed matrix, which is also equivalent to the traditional WC-Co reference group. They reported that it would be beneficial in terms of K_{Ic} to transform the binder phase into a bainitic or martensitic microstructure by heat treatment. They also emphasized that this would improve dynamic toughness without any loss in hardness.

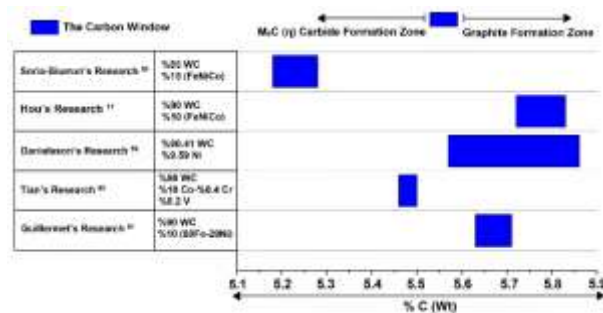


Figure 6. The carbon window of different compositions

Fig. 6 shows researchers' carbon content research of different WC- % 10 compositions. When the diagram is examined, it is seen that a large part of the composition consists of M_6C and Graphite structures. M_6C carbides and graphite structure are known to be brittle. The reason for the formation of these structures can be seen from the diagram, which depends on the C ratio by mass.

Therefore, the C ratio in the microstructure of MMC is critical and needs to be adjusted correctly. The amount of C contained in the composition should be optimized to prevent the formation of Graphite and M_6C . The critical carbon content region must be determined correctly after choosing the Fe: Ni ratio to achieve satisfactory results. In the literature, this situation is referred to as a carbon window.

The lower and upper values of the carbon window vary according to the elements and their proportions in the matrix alloy. According to the studies to be carried out, the matrix ratio included in mass should be well computed [62]. Carbon windows should be calculated using either experimental or CALPHAD methods for matrix combinations for different ratios. This situation also occurs in Fe-Ni compositions. Fig. 6 shows the carbon window ranges for a different compositions. As shown in Fig. 6, the carbon range of the Co content alloys is narrower than Ferrous based alloys. Thus, it is

known that the Ni element cannot be a matrix material alone due to high stack faulting energy and health issues [63]. Therefore, the Fe-Ni alloy mixture is more appropriate as a potential candidate.

There is also research evaluating the martensitic transformation of Fe-Ni and Co binders [64, 65]. Acet, Schneider [65] showed that the compositions containing up to 30% Ni are suitable for martensitic transformation. Therefore, it appears that the properties of the Fe-Ni content matrix in this range can be improved by cryogenic or conventional heat treatment [66].

Table 1 emphasizes the critical alteration in the use of different matrix for WC-reinforced MMC materials. It is seen that the lean alternative binder matrix materials as Fe and Ni cannot provide the requirements as lean Co performs.

Table 1. Significant changes due to the use of different binder matrix in composites

Matrix Type	Comparison to Co Binder Matrix	Author
Fe Matrix	<ul style="list-style-type: none"> • Grain growth inhibition • Lower oxidation resistance due to C affinity • Brittle η phase formation • Higher average hardness • Lower atmospheric corrosion resistance 	[36, 41, 57]
Fe-Co-Ni	<ul style="list-style-type: none"> • Higher fracture toughness • Higher abrasive wear resistance • More free C in the microstructure 	[67]
Fe₃Al-B	<ul style="list-style-type: none"> • Fine-grain structure • Equivalent fracture toughness and wear resistance 	[68]
Fe-Mn	<ul style="list-style-type: none"> • Higher porosity • Evaporation of Mn element during the sintering process • Very low fracture toughness • Equivalent hardness • Lower wear resistance 	[42]
Ni Matrix	<ul style="list-style-type: none"> • Higher corrosion resistance • Lower hardness and wear resistance 	[8, 9, 36]
Ni₃Al, NiAl	<ul style="list-style-type: none"> • Higher corrosion resistance • Lower bending strength and wear resistance • Equivalent hardness 	[43, 68-70]
Ni-Cr-Mo	<ul style="list-style-type: none"> • Equivalent toughness and hardness 	[71]
Ni-Si	<ul style="list-style-type: none"> • Lower hardness • Higher bending strength 	[72]
Ni-Cr	<ul style="list-style-type: none"> • Higher porosity ratio in the microstructure • Equivalent toughness • Higher sintering temperature requirement • Lower electrical conductivity 	[30]

4. Conclusion

When the comparative literature was carefully examined, it was seen that the use of different matrix materials in WC reinforced composites had essential effects on mechanical and tribological properties. The using effects of the different elements and alloys as an alternative matrix are explained by different mechanisms, including sintering type and temperature, grain growth preventing, and forming a new compound. Under the influence of the mechanisms mentioned above, Fe-Ni, Fe-Ni-Co, and Fe₃Al-B alloys could provide equivalent or higher mechanical and microstructural performance than plain Co elements. It is reasonable to use Fe-Ni-based materials suitable for heat treatment, such as cryogenic heat treatment, which is also cheap and reduced toxicity situation, would provide equivalent or higher contributions comparison to Co variants.

Acknowledgement

This work was supported by the Scientific Research Council of Eskisehir Osmangazi University under Grant [201915036]

Author's Contributions

Esad Kaya: Drafted and wrote the manuscript.

Mustafa Ulutan: Assisted and supervised the planning progress. He also revised interpretation and helped in manuscript preparation.

Ethics

There are no ethical issues after the publication of this manuscript.

References

1. Eliasson, J. and Sandström, R., 1995 Applications of Aluminium Matrix Composites. *Key Engineering Materials*, 104-107: 3-36.
2. German, R.M., *Powder Metallurgy and Particulate Materials Processing*. 2007, Princeton, New Jersey: Metal Powder Industry.
3. Pierson, H.O., *Handbook of Carbon, Graphite, Diamond and Fullerenes*. 1993, Park Ridge: Noyes Publications.
4. Uhrenius, B., Forsén, K., Haglund, B.O., and Andersson, I., 1995 Phase equilibria and phase diagrams in carbide systems. *Journal of Phase Equilibria*, 16(5): 430-440.
5. Kirchner, G., Harvig, H., and Uhrenius, B., 1973 Experimental and thermodynamic study of the equilibria between ferrite, austenite and intermediate phases in the Fe-Mo, Fe-W, and Fe-Mo-W systems. *Metallurgical Transactions*, 4(4): 1059-1067.
6. Glasson, D.R. and Jones, J.A., 2007 Formation and reactivity of borides, carbides and silicides. I. Review and introduction. *Journal of Applied Chemistry*, 19(5): 125-137.
7. Tyagi, A.K. and Banerjee, S., *Materials under extreme conditions : recent trends and future prospects*. 2017, Amsterdam: Elsevier.
8. Guo, Z., Xiong, J., Yang, M., and Jiang, C., 2008 WC-TiC-Ni cemented carbide with enhanced properties. *Journal of Alloys and Compounds*, 465(1-2): 157-162.
9. Tarragó, J.M., Ferrari, C., Reig, B., Coureaux, D., Schneider, L., and Llanes, L., 2015 Mechanics and mechanisms of fatigue in a WC-Ni hardmetal and a comparative study with respect to WC-Co hardmetals. *International Journal of Fatigue*, 70: 252-257.
10. Davis, J.R., *Alloying: Understanding the Basics*. 2001, Ohio: ASM International.
11. Patricia, A.P. and Thomas, S.J., *Metal Prices in the United States Through 1998*. 1999, Reston: United States Government Printing Office.
12. Fischer, T. and Rystedt, I., 1983 Cobalt allergy in hard metal workers. *Contact Dermatitis*, 9(2): 115-121.
13. Chen, J., Hou, G., Chen, J., An, Y., Zhou, H., Zhao, X., and Yang, J., 2012 Composition versus friction and wear behavior of plasma sprayed WC-(W,Cr)₂C-Ni/Ag/BaF₂-CaF₂ self-lubricating composite coatings for use up to 600°C. *Applied Surface Science*, 261(15): 584-592.
14. Fernandes, C.M. and Senos, A.M.R., 2011 Cemented carbide phase diagrams: A review. *International Journal of Refractory Metals and Hard Materials*, 29(4): 405-418.
15. Norgren, S. and García, J., 2018 On gradient formation in alternative binder cemented carbides. *International Journal of Refractory Metals and Hard Materials*, 73.
16. Hou, Z., Linder, D., Hedström, P., Borgenstam, A., Holmström, E., and Ström, V., 2019 Effect of carbon content on the Curie temperature of WC-NiFe cemented carbides. *International Journal of Refractory Metals and Hard Materials*, 78: 27-31.
17. Behl, M., Stout, M.D., Herbert, R.A., Dill, J.A., Baker, G.L., Hayden, B.K., Roycroft, J.H., Bucher, J.R., and Hooth, M.J., 2015 Comparative toxicity and carcinogenicity of soluble and insoluble cobalt compounds. *Toxicology*, 333(3): 195-205.
18. Bhaumik, S.K., Upadhyaya, G.S., and Vaidya, M.L., 2013 Properties and microstructure of WC-TiC-Co and WC-TiC-MO₂C-Co(Ni) cemented carbides. *Materials Science and Technology*, 7(8): 723-727.
19. Baucchio, M., *ASM Engineered Materials Reference Book*. 1994, Ohio: ASM International.
20. Luyckx, S., Osborne, C., Cornish, L.A., and Whitefield, D., 2013 Fine Grained WC-VC-Co Hardmetal. *Powder Metallurgy*, 39(3): 210-212.
21. Upadhyaya, G.S., *Cemented tungsten carbides production, properties, and testing*. 2003, Westwood: Noyes Publications.
22. Pierson, H.O., *Handbook of Refractory Carbides and Nitrides: Properties Characteristics, Processing and Application*. 1996, Park Ridge: Noyes Publications.
23. Miyoshi, A. and Hara, A., 1965 High Temperature Hardness of WC, TiC, TaC, NbC and Their Mixed Carbides. *Journal of the Japan Society of Powder and Powder Metallurgy*, 12(2): 78-84.
24. Kohlstedt, D.L., 1973 The temperature dependence of microhardness of the transition-metal carbides. *Journal of Materials Science*, 8(6): 777-786.



25. Kumashiro, Y. and Sakuma, E., 1980 The Vickers micro-hardness of non-stoichiometric niobium carbide and vanadium carbide single crystals up to 1500 C. *Journal of Materials Science*, 15(5): 1321-1324.
26. Samsonov, G.V., Kovalchenko, M.S., Dzemelinskii, V.V., and Upadyaya, G.S., 1970 Temperature dependence of hardness of titanium carbide in the homogeneity range. *Physica Status Solidi (a)*, 1(2): 327-331.
27. Soria-Biurrun, T., Lozada-Cabezas, L., Ibarreta-Lopez, F., Martinez-Pampliega, R., and Sanchez-Moreno, J.M., 2020 Effect of chromium and carbon contents on the sintering of WC-Fe-Ni-Co-Cr multicomponent alloys. *International Journal of Refractory Metals and Hard Materials*, 92.
28. Yang, J., Roa, J.J., Schwind, M., Odén, M., Johansson-Jøesaar, M.P., and Llanes, L., 2017 Grinding-induced metallurgical alterations in the binder phase of WC-Co cemented carbides. *Materials Characterization*, 134.
29. Buchegger, C., Lengauer, W., Bernardi, J., Gruber, J., Ntaflos, T., Kiraly, F., and Langlade, J., 2015 Diffusion parameters of grain-growth inhibitors in WC based hardmetals with Co, Fe/Ni and Fe/Co/Ni binder alloys. *International Journal of Refractory Metals and Hard Materials*, 49: 67-74.
30. Tracey, V.A., 1992 Nickel in hardmetals. *International Journal of Refractory Metals and Hard Materials*, 11(3): 137-149.
31. Cramer, C.L., Preston, A.D., Elliott, A.M., and Lowden, R.A., 2019 Highly dense, inexpensive composites via melt infiltration of Ni into WC/Fe preforms. *International Journal of Refractory Metals and Hard Materials*, 82: 255-258.
32. Upadhyaya, G.S. and Bhaumik, S.K., 1988 Sintering of submicron WC-10wt.%Co hard metals containing nickel and iron. *Materials Science and Engineering: A*, 105-106: 249-256.
33. Bonny, K., De Baets, P., Vleugels, J., Huang, S., and Lauwers, B., 2009 Tribological Characteristics of WC-Ni and WC-Co Cemented Carbide in Dry Reciprocating Sliding Contact. *Tribology Transactions*, 52(4): 481-491.
34. Bratberg, J. and Jansson, B., 2006 Thermodynamic evaluation of the C-Co-W-Hf-Zr system for cemented carbides applications. *Journal of Phase Equilibria and Diffusion*, 27(3): 213-219.
35. Voitovich, V.B., Sverdel, V.V., Voitovich, R.F., and Golovko, E.I., 1996 Oxidation of WC-Co, WC-Ni and WC-Co-Ni hard metals in the temperature range 500–800 °C. *International Journal of Refractory Metals and Hard Materials*, 14(4): 289-295.
36. Penrice, T.W., 1987 Alternative binders for hard metals. *Journal of Materials Shaping Technology*, 5(1): 35-39.
37. Kakeshita, T. and Wayman, C.M., 1991 Martensitic transformations in cermets with a metastable austenitic binder I: WC (Fe Ni C). *Materials Science and Engineering: A*, 141(2): 209-219.
38. Kakeshita, T. and Wayman, C.M., 1991 Martensitic transformation in cermets with metastable austenitic binder: II. TiC (Fe Ni C). *Materials Science and Engineering: A*, 147(1): 85-92.
39. Kumi, D.O., *A Study Of WC-X Systems For Potential Binders For WC*. 2011, University of the Witwatersrand: Johannesburg.
40. C. B. Pollock, H.H.S., 1970 The eta carbides in the Fe-W-C and Co-W-C systems. *Metallurgical Transactions*, 1(4): 767-770.
41. Moskowitz, D., J., F.M., and Humenik, J.s.M., *High-Strength Tungsten Carbides*. 1971, Michigan: Metal Powder Industries Federation.
42. Schubert, W.D., Fugger, M., Wittmann, B., and Useldinger, R., 2015 Aspects of sintering of cemented carbides with Fe-based binders. *International Journal of Refractory Metals and Hard Materials*, 49: 110-123.
43. Mosbah, A.Y., Wexler, D., and Calka, A., 2005 Abrasive wear of WC-FeAl composites. *Wear*, 258(9): 1337-1341.
44. Alman, D.E., Tylczak, J.H., Hawk, J.A., and Schneibel, J.H., 2002 An assessment of the erosion resistance of iron-aluminide cermets at room and elevated temperatures. *Materials Science and Engineering: A*, 329-331: 602-609.
45. Karimi, H., Hadi, M., Ebrahimzadeh, I., Farhang, M.R., and Sadeghi, M., 2018 High-temperature oxidation behaviour of WC-FeAl composite fabricated by spark plasma sintering. *Ceramics International*, 44(14): 17147-17153.
46. Karimi, H. and Hadi, M., 2020 Effect of sintering techniques on the structure and dry sliding wear behavior of WC-FeAl composite. *Ceramics International*, 46(11).
47. Baker, I. and Munroe, P.R., 2013 Mechanical properties of FeAl. *International Materials Reviews*, 42(5): 181-205.
48. Schneibel, J.H., Carmichael, C.A., Specht, E.D., and Subramanian, R., 1997 Liquid-phase sintered iron aluminide-ceramic composites. *Intermetallics*, 5(1): 61-67.
49. Kim, S.-E., Hong, S.-H., and Shon, I.-J., 2020 Mechanical Properties and Rapid Sintering of WC-BN-Al Composites. *Korean Journal of Metals and Materials*, 58(7): 453-458.
50. Ahmadian, M., Wexler, D., Calka, A., and Chandra, T., 2003 Liquid Phase Sintering of WC-FeAl and WC-Ni₃Al Composites with and without Boron. *Materials Science Forum*, 426-432: 1951-1956.
51. Walbrühl, M., Linder, D., Ågren, J., and Borgenstam, A., 2018 Alternative Ni-based cemented carbide binder – Hardness characterization by nano-indentation and focused ion beam. *International Journal of Refractory Metals and Hard Materials*, 73: 204-209.
52. De Oro Calderon, R., Agna, A., Gomes, U.U., and Schubert, W.-D., 2019 Phase formation in cemented carbides prepared from WC and stainless steel powder – An experimental study combined with thermodynamic calculations. *International Journal of Refractory Metals and Hard Materials*, 80: 225-237.
53. Fernandes, C.M., Puga, J., and Senos, A.M.R., 2019 Nanometric WC-12 wt% AISI 304 powders obtained by high energy ball milling. *Advanced Powder Technology*, 30(5): 1018-1024.
54. Tarraste, M., Kübarsepp, J., Juhani, K., Mere, A., Kolnes, M., Viljus, M., and Maaten, B., 2018 Ferritic chromium steel as binder metal for WC cemented carbides. *International Journal of Refractory Metals and Hard Materials*, 73: 183-191.
55. Cacciamani, G., 2016 An Introduction to the Calphad Method and the Compound Energy Formalism (Cef). *Tecnologia em Metalurgia Materiais e Mineração*, 13(1): 16-24.
56. Fernandes, C.M., Senos, A.M.R., and Vieira, M.T., 2003 Sintering of tungsten carbide particles sputter-deposited with stainless steel. *International Journal of Refractory Metals and Hard Materials*, 21(3-4): 147-154.
57. Wittmann, B., Schubert, W.-D., and Lux, B., 2002 WC grain growth and grain growth inhibition in nickel and iron binder



hardmetals. *International Journal of Refractory Metals and Hard Materials*, 20(1): 51-60.

58. Gonzalez, R., Echeberria, J., Sanchez, J.M., and Castro, F., 1995 WC-(Fe,Ni,C) hardmetals with improved toughness through isothermal heat treatments. *Journal of Materials Science*, 30(13): 3435-3439.

59. Danielsson, O., *Effect of carbon activity on microstructure evolution in WC-Ni cemented carbides*, in *Materials Science and Engineering*. 2018, KTH Royal Institute of Technology: Stockholm. p. 72.

60. Tian, H., Chen, J., Zhu, G., Du, Y., and Peng, Y., 2019 Investigation of WC-Co alloy properties based on thermodynamic calculation and Weibull distribution. *Materials Science and Technology*, 35(18): 2269-2274.

61. Guillermet, A.F., 1987 Assessment Of The Fe-Ni-W-C Phase Diagram. *Zeitschrift fuer Metallkunde/Materials Research and Advanced Techniques*, 78(3): 165-171.

62. Shi, X., Yang, H., Wang, S., Shao, G., and Duan, X., 2007 Influences of carbon content on the properties and microstructure of ultrafine WC-10Co cemented carbide. *Journal of Wuhan University of Technology-Mater. Sci. Ed.*, 22(3): 473-477.

63. Upadhyaya, G.S., 1994 Electronic mechanism of sintering: Some case studies on real systems. *Bulletin of Materials Science*, 17(6): 921-934.

64. Kalsi, N.S., Sehgal, R., and Sharma, V.S., 2014 Effect of tempering after cryogenic treatment of tungsten carbide-cobalt bounded inserts. *Bulletin of Materials Science*, 37(2): 327-335.

65. Acet, M., Schneider, T., and Wassermann, E.F., 1995 Magnetic Aspects of Martensitic Transformations in FeNi Alloys. *Le Journal de Physique IV*, 05(C2): 105-109.

66. Li, B., Zhang, S., Zhang, T., and Zhang, J., 2018 Effect of deep cryogenic treatment on microstructure, mechanical properties and machining performances of coated carbide tool. *Journal of the Brazilian Society of Mechanical Sciences and Engineering*, 41(1).

67. Prakash, L.J., *Development of tungsten carbide hardmetals using iron-based binder alloys*. 1980, Virginia National Technical Reports Library. 221.

68. Ahmadian, M., Wexler, D., Chandra, T., and Calka, A., 2005 Abrasive wear of WC-FeAl-B and WC-Ni₃Al-B composites. *International Journal of Refractory Metals and Hard Materials*, 23(3): 155-159.

69. Long, J.-z., Zhang, Z.-j., Xu, T., Peng, W., Wei, X.-y., Lu, B.-z., and Li, R.-q., 2012 WC-Ni₃Al-B composites prepared through Ni+Al elemental powder route. *Transactions of Nonferrous Metals Society of China*, 22(4): 847-852.

70. Shon, I.-J., Na, K.-I., Ko, I.-Y., Doh, J.-M., and Yoon, J.-K., 2012 Effect of FeAl₃ on properties of (W,Ti)C-FeAl₃ hard materials consolidated by a pulsed current activated sintering method. *Ceramics International*, 38(6): 5133-5138.

71. Almond, E.A. and Roebuck, B., 1988 Identification of optimum binder phase compositions for improved WC hard metals. *Materials Science and Engineering: A*, 105-106(Part 1): 237-248.

72. Correa, E.O., Santos, J.N., and Klein, A.N., 2010 Microstructure and mechanical properties of WC Ni-Si based cemented carbides developed by powder metallurgy. *International Journal of Refractory Metals and Hard Materials*, 28(5): 572-575.

Development of Salt Core Use as an Alternative in Aluminum Alloy Castings

Tülay Hançerlioğlu^{1*} 

¹ R&D Department Nemak İzmir Döküm San.A.Ş.

* tulay.hancerlioglu@nemek.com

* Orcid: 0000-0003-2373-4405

Received: 6 December 2021

Accepted: 1 June 2022

DOI: 10.18466/cbayarfbe.1033177

Abstract

For creating complex geometric shapes in the cast part, salt was used to produce core instead of sand which is thermo-chemical or chemical process using resin as a binder. In salt core casting, the efficiency will be increased by reducing the core gas-induced errors in the part. The harmful effect on the environment will be reduced with the absence of odor and smoke from the core gas. Using water in salt core breaking instead of mechanical impact and vibration during sand core breaking will bring benefits such as eliminating the noise source and using less energy. By eliminating the dust generated during sand core breaking, its harmful effects on the environment will be reduced. Since the salt core can be dissolved in water and removed from the piece without any residue, there will be no problem of sand remaining in the sand core from time to time.

Keywords: Core gas, sand core, salt core.

1. Introduction

The geometries of casting parts used in the automotive industry are quite complex. In casting molds of complex parts, steel cores (sliders) are often not sufficient in terms of both castability and casting quality [1,2]. Sand cores are generally used in the production of parts with complex structures and internal cavities, where steel cores cannot be used. Sand cores are produced by cold-box (polyurethanes as binders) or hot box (alkali silicates) method [2]. The use of salt cores instead of sand cores has been known and developed since the end of the 20th century, especially in the field of gravity and low pressure die casting work continues [3-9]. Better mechanical properties, easy removal from the part by dissolving in water without using any chemicals and reduction of waste after casting have made the development studies of using salt cores instead of sand in aluminum alloy castings important [10]. In the literature review, there are studies on the strength of salt cores [11]. The use of salt cores in high pressure casting has also been observed to have positive effects on the solubility and environment of these cores [12].

There are various methods of producing salt cores. It is one of the methods of producing salt in core molds made of metal, wood by turning it into a slurry with fast-hardening mixers [4]. In addition, salt cores are produced by injection casting method using melted salt (from the liquid phase) [13]. The important advantage of being produced from the liquid phase is that it gives a high level of mechanical and thermal stability [13]. Its high strength allowed it to be used in injection molding. In addition to high strength, it has advantages such as very smooth surface quality, no gas escape in the casting, no casting faults due to this, easily dissolving from the part with pressurized water and removing it without residue. In terms of the casting mold used, easy cleaning without residue and not causing any wear such as sand are among its advantages. The fact that it does not have any negative effects on human health or the environment, and that it is recyclable, is also one of the advantages of salt cores over sand cores. The first automatic salt core production facility in the world is Bühler's technology center in Uzwil. It was established as a pilot plant for small series production parts [13].

2. Materials and Methods

The trials were carried out with the pump body part, which was poured into a gravity mold by tilting (Figure 1). Due to the structure of the part, it is a part that is difficult to discharge sand core and evacuation of core gas in the current process.

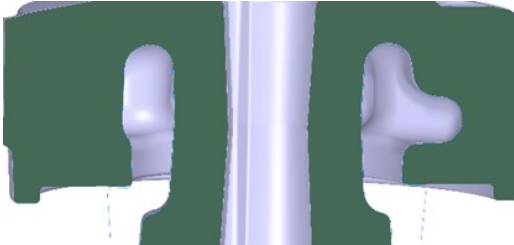


Figure 1. Sectional view of the pump body.

The internal cavities of this casting part are formed with sand cores in the current mass production. In order to use high pressure casting method for the production of salt cores to be used instead of sand cores, an injection mold with one chamber was designed for the salt core. The runner and air evacuation pockets were made using injection filling calculations according to the core geometry. Since the existing tilting casting mold will be used, the reference and fixation points, namely the core heads, are designed to have the same geometry in the salt core. Cooling channels are opened in the upper and lower holders of the mold.

There are also steel cores on both sides of the mold. Injection mold manufacturing was done according to the design (Figure 2.1, Figure 2.2).

Imported raw materials and casting facilities provided by the company within the scope of the cooperation agreement were used in the trials. The melting point of the salt (NaCl) used is ~ 800 °C, its density is ~ 2.165 kg/m³. Its appearance is crystalline solid and white in color.

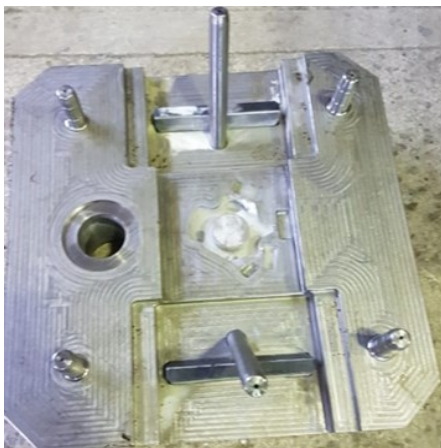


Figure 2.1. Injection mold movable side manufactured for salt core



Figure 2.2. Injection mold fixed side manufactured for salt core.

The salt was melted in the crucible, and the molten salt was poured into the steel mold, which was poured with a piston, on the casting bench, as in the casting process (Figure 3).



Figure 3. Salt core injection molding

Initially, a standard general value was given as the shrinkage margin. Salt core laser scanning was done with Faro Edge Scan Arm HD and compared with 3D data model (Figure 4). According to the core scans and the measurement results after the first trial core casting, it was observed that the shrinkage varies in the thick and thin parts of the inner and outer figures of the core, as in metal injection molding. Since the shape and thickness of the core affects the shrinkage, different values of scales are given on the core geometry and the core geometry is created. In the second trial, results were obtained with appropriate measurement values.

In the experiment, it was seen that the cooling in the mold was also very important. It has been observed that temperature change affects the surface quality, scale and core strength of the core.

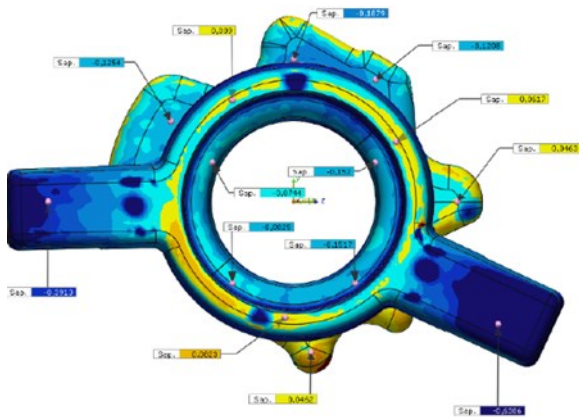


Figure 4. Salt core laser scanning compared with 3D data model.

The temperature change in solidification should not be sudden. As a result of unsuitable temperature change, it formed a fracture due to sudden shrinkage (Figure 5). Shrinkage was more in the thick mass regions.



Figure 5. Salt core exterior surface crack.

Initially, the existing cooling channels in the lower and upper holders of the mold were used. During the trials, cracks occurred in the inner diameter figure of the core (Figure 6).



Figure 6. Salt core inner diameter surface crack visible with eye control.

In order to achieve a more balanced cooling, cooling was added to the core area, which was inserted in the mold, and a separate cooling line was operated (Figure 7). Cracks formed in the inner diameter region were healed by the addition of cooling.



Figure 7. Mold inner diameter core insertion

Surface roughness of salt core and sand core compared. In the salt core, the outer most surfaces solidify rapidly and form a surface film layer, and the roughness value of the core surface was found to be smoother than that of the sand core (Figure 8). Although the grain size of the sand core small, the casting part surface the roughness of the casting is rough compared to the salt core (Figure 8.1).

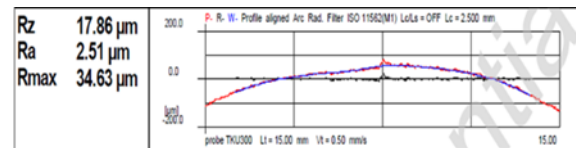


Figure 8. Roughness value measure from the casting part with a salt core.

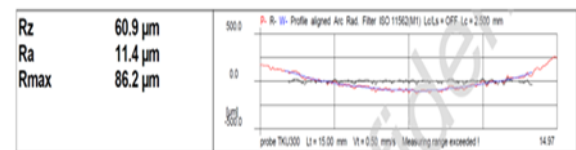


Figure 8.1. Roughness value measure from the casting part with a 60 AFS sand core.

The solidification of the salt core did not reach the inner regions at the same rate. The inner surfaces solidify later as a result of the film layer formed outside (Figure 9).

In addition, the color of the core varies according to the temperature and the residence time in the mold. The salt core produced at low temperature and in a short time is light in color (Figure 10.1). The salt core produced at high temperature and long time is dark in color (Figure 10.2).



Figure 9. Inside view of salt core.



Figure 10.1. Salt core produced in low temperature and short time.



Figure 10.2. Salt core produced in high temperature and long time.

Instead of sand, a salt core was placed in the existing tilting casting mold and a casting tilt was carried out in the same way as the casting conditions in the standard series casting machine (Figure 11.1). The aluminum alloy is robotically filled into the casting ladle (Figure 11.2).



Figure 11.1. Tilt casting machine.



Figure 11.2. Tilt casting ladle.



Figure 11.3. The tilt casting machine rotates 180 degrees.

The tilt casting machine rotates 180 degrees and fills the aluminum alloy steel mold (Figure 11.3). Trial casting cycle time with salt core is equal to casting using sand core used in series conditions.



Figure 12. The casting part with salt core that comes out of the casting mold.

After solidification, the casting machine returns to the flat position. The mold opens when casting machine is in flat position.

The casting part came out of the mold, it was left in a water-filled couldron.

The salt was dissolved in the core in a short time and was removed from the part without leaving any residue (Figure 13). The salt that settles to the bottom of the boiler can be used for recycling.



Figure 13. The salt that starts to dissolve, the core and the cast part.

The cast part was cut to see its inner surfaces. No salt core residue was found in the indentation areas on the inner surfaces. The salt core dissolved was completely (Figure 14).

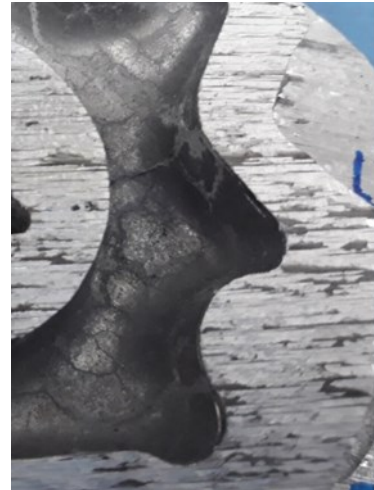


Figure 14. Casting part cross section.

For the cast part, measurements were made and appropriate results were seen. Visually, traces were seen on the surfaces coming out of the salt core on the cast part. The part was cut and polished, traces were examined, it was seen that it did not cause leaks and similar errors as it did not go inside (Figure 15, Figure 16).



Figure 15. Polished cast part cross-section.



Figure 16. Cast part zoomed images.

3. Results and Discussion

Core gas formed due to resin burning in casting with sand core match was not seen in casting with salt core. During the part casting with sand core resins stack in the steel mold. Resin blocks air filters. Core gas cannot be removed from the mold by blocking the air filters. Therefore the mold is cleaned periodically. Since there is no resin in salt core casting, core gas is not released. After casting, the mold was inspected and no resin stack and air filter blocks were observed.

The use of salt cores instead of sand cores resulted in a reduction in the waste rate by eliminating / minimizing the errors that may occur in the part due to core gas, energy savings resulting from processes such as recycling and recycling and less emission gains. During the casting process, the harmful effects on the environment are minimized by minimizing the emission of core gas and smoke.

Since the salt core can be removed from the cast part without residue, there has been no sand residue and related problems in the production with sand cores, where the sand does not completely remove from the part.

In the core breaking process, it is one of the advantages of dissolving salt in water with low/zero noise level, which does not require mechanical energy, instead of mechanical methods that require energy consumption and high noise. The sound level, which is 92dB in the pulsed method used to remove the sand from the core, has disappeared since the salt core is dissolved with water.

It is observed that salt cores can remain intact for a long time in humid environments.

Disadvantages are the difficulty in determining the shrinkage value and the increase in the cycle time due to the longer salt solidification time compared to the sand core. In order for the solidification to be homogeneous and to prevent cracks on the core surface, the cooling system and cooling parameters optimization in the mold, used for the core production are the aspects that need attention and improvement.

4. Conclusion

It has been seen that the appropriate results obtained and what has been learned about the salt core process can be a reference to the use of salt cores by injection casting or low pressure die casting method from now on.

Experimental studies examining the mechanical and thermal properties of salt core and comparison with sand core can be done in the next studies.

The possibilities of recycling salt collected in the cauldron and using local alternative supplier can be developed for cost reduction studies.

Acknowledgement

We would like to thank our colleagues of Nematik İzmir Döküm Sanayi A.Ş., especially Ferhat Güzelırmak, Yalçın Dođan and Egemen Avşar who helped us in our work. And the company we cooperated with their help on production of sand cores.

Author's Contributions

Tülay Hañçerliođlu: Drafted and wrote the manuscript, performed the experiment and result analysis.

Ethics

There are no ethical issues after the publication of this manuscript.

References

- [1]. Brůna, M., Sládek, A. & Kucharčík, L. (2012). Formation of porosity in Al-Si alloys. Archives of Foundry Engineering. 12(1), 5-8. DOI: 10.2478/v10266-012-0001-5.
- [2]. Lichý, P., Bednářová, V. & Elbel, T. (2012). Casting routes for porous metals production. Archives of Foundry Engineering. 12(1), 71-74. DOI: 10.2478/v10266-012-0014-0.
- [3]. Daňko, J., Daňko, R. (2009). Theoretical and technological aspects of the production processes of foundry cores blown In 50. Konferencji i Krystalizacja Metali (pp. 71-86). Katowice – Gliwice, Poland: Polska ademia Nauk, Komisja Odlewnictwa. ISBN: 978-83-929266-0-3. (in Polish).
- [4]. Fuchs, B., Eibisch, H. & Kömer, C. (2013). Core viability simulation for salt core technology in high – pressure die casting. International Journal of Metalcasting. 7(3), 39-45. ISSN: 1939-5981
- [5]. Stingl, P., & Shiller, G. (2009). Gichte und rückstandsfreie Entkernung – Salzkerne für den Aluminiumguss. Giesserei-Erfahrungsaustausch. 6, 4-8.
- [6]. Adámková, E., Jelínek, P., & Študentová, S. (2013). Application of cooking salts in manufacture of water soluble cores for high pressure die. Materials and technology. 61(11-12), 689-693. ISSN: 1580-2949, 1580-3414.
- [7]. P. Jelínek, E. Adámková “ Lost Cores for High-Pressure Die Casting” Department of Metallurgy and Foundry Engineering, VŠB-Technical University of Ostrava DOI:10.2478/afe-2014-0045.
- [8]. P. Jelínek, E. Adámková , F. Mikšovský, J. Beňo Advance in Technology of Soluble Cores for Die Castings, Department of Metallurgy and Foundry, VŠB – Technical University of Ostrava ISSN (1897-3310) Volume 15 Issue 2/2015 29-34.
- [9]. Eliska Adámková, Petr Jelínek, Jaroslav Beňo Frantiěk Mikšovský, Water-Soluble Cores-Verifying Development Trends, V[B-Technical University of Ostrava, Faculty of Metallurgy and Materials Engineering, Department of Metallurgy and Foundry, ISSN 1580-2949 MTAEC9,49(1)61(2015).



[10]. Mr. Vijaykumar A. Radadiya, Dr. Komal G. Dave, Mr. Kalpeshkumar R. Patel, Design and Analysis of Salt Core for a Casting of Aluminium Alloys Core casting, *International Journal Of Advance Engineering and Research Development*, Volume 2, Issue 3-2015.

[11]. Jun Yaoka wa, Daisuke Miura, Koichi Anzai, Youji Yamada and Hiroshi Yoshii, "Strength of Salt Core Composed of Alkali Carbonate and Alkali Chloride Mixtures Made by Casting" *Journal of Technique Materials Transactions*, Vol. 48, No. 5 (2007) pp. 1034 to 1041, Japan Foundry Engineering Society.

[12]. Petr Jelinek, Frantisek Miksovsky, Jaroslav Beoo, Eliska Adamkova, "Development of Foundry Cores Based On Inorganic Salts" *MTAEC9*, 47(6)689(2013), ISSN 1580-2949.

[13]. Bühler AG: Lost Core - An Industrial Process Path for High-Quality Salt Cores. <https://www.foundry-planet.com> (Date of access: 25.06.2021).

Tension Field Performance of GFRP Plate Shear Walls

Tuna Ülger^{1*} 

¹ Department of Civil Engineering, Zonguldak Bülent Ecevit University, Zonguldak, Türkiye

* tunaulger@beun.edu.tr

* Orcid: 0000-0002-1758-8299

Received: 27 October 2021

Accepted: 1 June 2022

DOI: 10.18466/cbayarfbe.1015437

Abstract

Fiber reinforced polymer (FRP) composites are alternative to the conventional materials for many civil applications because of their prominent properties. The advanced production technology allows standardized structural FRP sections, which plays an important role in progress of the structural engineering. Different fiber types can be rowed in these sections to improve the structural performance of these members. One of the most widely used FRP type is glass FRP (GFRP) in the market for structural use. The plate performance of GFRP materials as a lateral load resisting member within the moment frames was investigated in this study similar to the steel plate shear walls or timber shear walls. Post buckling performance of the GFRP plates including the experimental fracture values and different fiber orientations were studied. The tension field action was considered for the GFRP plates after the post buckling of the moment frame, and it was found that the gain for initial stiffness and story drifts gradually reduced from flexible to rigid moment frames. The least lateral load capacity gain was about 16% when the fiber main direction is oriented 0° angle within the most rigid moment frame. When the fiber orientation aligned within the tension field angle, the load capacity and the initial stiffness was reached to the ultimate values. Finally, analytical load capacity calculations were carried to verify the numerical results of the FRP plate shear walls employing the equivalent truss member approach, then plate thickness and panel aspect ratio effects on were investigated for the GFRP shear walls.

Keywords: FRP plate; FRP fracture; GFRP; lateral stiffness; shear wall; tension field

1. Introduction

The civil structures and construction technologies have been evolved by introducing new techniques, materials, and products. The use of fiber reinforced polymer (FRP) composite materials in rise during recent years. The advances in manufacturing technologies have been playing an important role to the transition from conventional materials to the new advanced materials in structural engineering [1]. Some research efforts are mainly focusing on the use of composite materials with the conventional structures for strengthening, stiffening, retrofitting or restoration applications. The use of fabric FRP materials to enhance the concrete column performance [2–5], and to enhance the flexural and shear capacity of the beams [6–8] were some typical examples in literature and investigated the performance of the structural members considering the effective design parameters such as; fiber orientation, number of composite layers, adhesive types etc. In addition to those interests, new structures and members can be

composed of fully FRP composite members [9–12]. Pedestrian bridges, cooling towers, bridge decks are today's pioneering composite structures. Pultruded FRP structural shapes are common in the market due to advanced manufacturing technologies. The pultruded FRP plates are commonly designed for the flexural properties like composite deck systems [13–15]. Some research efforts on the other hand are investigated the shear resistance of the steel plates sandwiched between the FRP laminates or fabrics and the load capacity and energy dissipation of FRP bonded steel plates are investigated with various FRP configurations [16–18]. Repair of fatigue cracks by patching FRP on shear plates are studied [19]. Lateral load resistance of the FRP plates by itself can be analogical to the steel plate shear walls (SPSWs) where the slender plate buckles before the full shear resistance, and the tension field actions develops at the post buckling phase of the lateral loadings [20,21]. The studies show that SPSWs can achieve reliable seismic performance with cyclic hysteretic behavior during the post buckling phase [22–27]. The stiffness of the surrounding frame of SPSWs plays an important role in development of the tension

field action [28]. The SPSWs have been effectively utilized in steel buildings with a moment frame to control the story drifts against an earthquake or a wind load which can be named a dual lateral load resisting system. Laminated wood plates are another analogical form of a dual system for timber structures [29,30]. It was reported that the cost of the construction can be reduced up to 50% by including the SPSWs in design of the moment frame systems [29]. Considering the prominent properties of composites, FRP plate shear wall system can be preferred instead of steel plate shear wall systems. Even though the initial cost of FRP composites is relatively higher than the cost of steel, the total weight of the structure and the required maintenance cost can be significantly reduced with the proposed FRP shear wall system. Therefore, an adequate lateral performance can be achieved, and the initial cost of FRP can be compensated during the life cycle of the structure [31].

In this study, the flexural fracture of Glass FRP (GFRP) laminates is first determined experimentally to develop an acceptable GFRP fracture mechanism for future analysis. The experimental properties of the tested GFRP laminates were used in numerical modeling and analytical load capacity calculations as well. Then, the lateral performance of three-bare moment frames with various lateral stiffness values are numerically studied with elastic-plastic material properties. The lateral performance of the bare moment frames is enhanced with including infill GFRP plates. The initial stiffness calculations, peak loads and initial fracture mechanisms are presented in the following sections. Finally, the analytical load deflection curves of the GFRP plated moment frames are calculated considering the equivalent truss method. The lateral load-deflection curves are drawn by an iterative method using parallel springs.

2. Experimental Flexural Test of GFRP Specimens

Flexural properties of GFRP strips were determined by using the three-point bending test results and one of the tested specimens at rupture is shown in Figure 1. The average cross section was 9.5 mm x 30.2 mm, and the specimen length was 304.8 mm for the tested five GFRP specimens. In addition to the experimental results, manufacturer's data sheet was provided for the definition of GFRP materials [32]. The purpose of the experimental tests was the determination of GFRP fracture mechanism and employ similar behavior in latter numerical models. It was calculated for example that the experimentally obtained lengthwise (LW) flexural elastic modulus and fracture stress were about 10% and 88% larger than those provided by the manufacturer's data sheet, respectively. This discrepancy can be attributed to several factors, but the author believes that this does not the scope of this study. Nevertheless, the lengthwise flexural properties of

GFRP plates were adopted from the experimental three-point bending tests, and they were included in the numerical models.

The experimental bending test results of five specimens were presented in this section. FE element model was developed with the averaged geometrical and mechanical properties to simulate the similar FRP bending and fracture behavior. The experimental results showed that all the specimens had a linear load deflection curve until the load reaches to the fracture load. It was noted that the fracture was initiated at the bottom layers and there was not a visual sign of a compression failure at the top layers as can be seen in Figure 1. The compression failure stress was assumed to be same as the tension failure stress in FE element models. The fracture stress and strain values were included in FE models to start the damage initiation of GFRP plates. Different fracture models can be chosen from ANSYS Mechanical APDL's [33] material library to simulate the GFRP rupture for the failure simulations; however, the maximum stress fracture model was found in good agreement with the observed fracture behavior, and the results are presented in following sections.

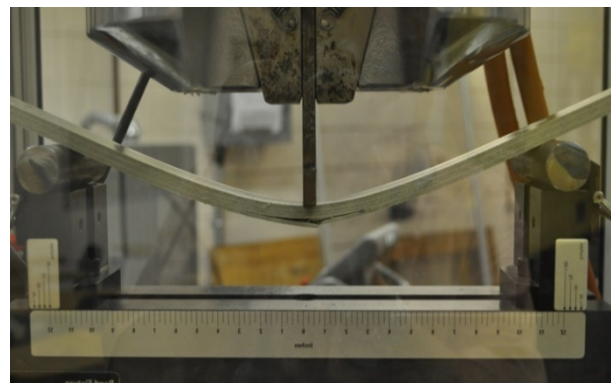


Figure 1. Three-point flexural loading tests of an GFRP strip.

The tipping loads and deflections at the midspan were used to extract elastic modulus and rupture stresses following the procedures given in ASTM D790 [34]. The minimum and maximum elastic modulus can be calculated 18100 MPa and 23500 MPa from the experimental tests, respectively. The average elastic modulus was calculated 21100 MPa for the FE Model simulations. The minimum and maximum peak stresses were calculated 332 MPa and 432 MPa from the experimental tests, respectively. The average of these peak stresses, 389 MPa, was assigned as the maximum failure stress into the GFRP material models. When the maximum stress criterion was satisfied, an assumed stiffness reduction factor, 0.80, was multiplied by the stiffness of the corresponding element; therefore, progressive delamination of GFRP layers was achieved without convergence problems. Load-deflection curves of the GFRP specimens are presented in Figure 2. The red dashed curve in Figure 2

shows the FE model results in where the averaged experimental properties were assigned. In the FE analysis, the peak load capacity was recorded at 2.64 kN which was about 14% above experimentally obtained average peak load, 2.32 kN. The maximum deflection before the initiation of fracture was 34 mm in the FE analysis which was 13% more than the experimentally obtained average maximum deflection, 30 mm. FE modelling approach and damage propagation were validated with this study, and the measured numerical differences were assumed to be within the acceptable engineering error limits; therefore, GFRP plate shear wall system was modelled using the similar layered material model and mechanical properties, and material fracture model for the rest of the study.

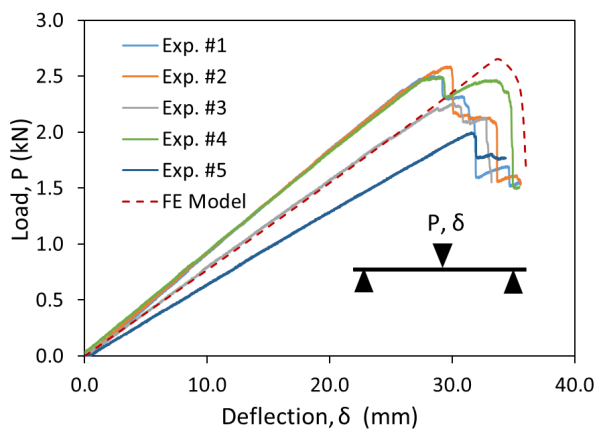


Figure 2. Experimental flexural tests with a FE model simulation.

3. Analytical Formulation of the GFRP Plate Shear Walls

Lateral load capacity of the moment frames which were stiffened with the GFRP plates were approximated using a parallel spring model. The stiffness of the GFRP plate and the steel moment frame were included in capacity calculations before the yield of steel. The stiffness of the moment frame and the deflection at yielding can be easily determined from statics; however, the coupled stiffness of the GFRP plate was not easy to extract from statics for the tension field action. Therefore, the GFRP plate was assumed to be an equivalent truss member where the equivalent truss area was defined by Thorburn *et al.* [28] and given in Equation (3.1). The tension field angle, α , and panel diagonal angle, θ , can be determined using Equations (3.2) and (3.3), respectively, and substituted in Equation (3.1) to find the equivalent truss area, A_{eq} . In these calculations, it was assumed that the columns provide enough rigidity to develop the fully tension field action; therefore, the beam and columns were contributed to the equivalent area of the plate. Also, the shear resistance of the GFRP plate was neglected and only the tension field resistance was accounted in the formulations. Once the

equivalent area of the GFRP plate was determined, the equivalent uniaxial stiffness of the GFRP plate in the tension field was approximated as a truss member. The elastic properties of the GFRP plate were different in lengthwise (LW) and crosswise (CW) directions which required an additional angle to define effective elastic modulus using the combination of orthogonal properties. Simply the effective elastic modulus, $E_{F_{eq}}$, was defined as a function of elastic properties and GFRP plate orientation as given in E Equation (3.4). The important part of analytical load capacity calculation was the definition of the failure criteria in the model. Complex failure modes develop in the buckled plate. The first mode is caused by the uniaxial stresses due to tension field and the second is the combination of bending and compression stresses due to plate compression and plate wrinkle in the buckled zones. It should be noted that the GFRP plate had five layers of fibers; therefore, the related stiffness of the section was updated at failure of each fiber layer. The compressive and tensile capacities were assumed equal at those failure limits. Once the extreme fiber reaches the maximum strain limit, the equivalent truss area and related stiffness were recalculated, and the load capacities were calculated by an iterative stiffness updating approach in that spring model. In these calculations, the critical loads were calculated with two-step fracture iterations. In other words, extreme fibers failed two times and equivalent area of the GFRP plate was updated two times for the calculation of analytical load capacities. The numerical results and approximate analytical results are presented in the following result section.

$$A_{eq} = \frac{1/2 t_F L \sin^2 2\alpha}{\sin\theta \sin 2\theta} \quad (3.1)$$

$$\tan^4 \alpha = \frac{t_F L / 2A_c + 1}{t_F H / 2A_b + 1} \quad (3.2)$$

$$\theta = \tan^{-1}(L/H) \quad (3.3)$$

$$E_{F_{eq}} = \sqrt{(E_{LW} \cos\beta)^2 + (E_{CW} \sin\beta)^2} \quad (3.4)$$

4. Numerical Modelling of the Plate Wall Systems

The lateral load capacity of a moment frame with an infill GFRP plates were determined from a single-story moment frame which was subjected to a lateral shear force. The lateral load is applied at the upper beam as a story drift and the total shear forces were recorded at the column bases. The analysis model was sketched in Figure 3, and it shows all the components of the

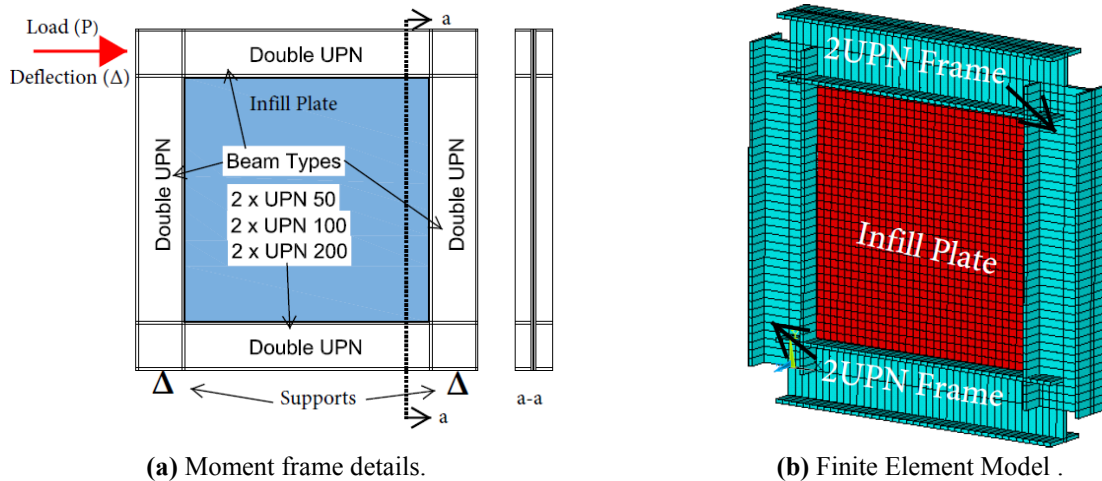


Figure 3. Single story frame and infill plate models.

moment frame. The moment frame was modeled as a steel moment frame and can resist lateral loads without infill plates by the assumed fully rigid joints. The total stiffness of the frame exists due to stiffness of the beams and columns only. Therefore, lateral deflections due to flexibility of the panel zones at the beam-column joints were not included in the total stiffness of the frames. FE model representation of the steel moment frame with infill plate is shown in Figure 3b. The initial stiffness of the moment frames was first determined without the infill GFRP plates to form the base FE model. Then, the GFRP plates were connected to the columns and beams of the surrounding moment frames without allowing the friction losses between the frame and plate. The relative strength and stiffness gain for the base frame with infill GFRP plates were determined in this study.

In the first part of this study, only one panel aspect ratio (plate height divided by width), 1/1 with one slenderness ratio (plate height divided by thickness), 315, is considered. The analytical verification of the FE model results was completed using the equivalent truss beam model and presented with the numerical results. In addition to the GFRP plate shear panels, hypothetical steel plate shear panels were modeled within the same moment frames to compare the performance of steel and GFRP plates. Steel plates were commonly used in the field and research applications as mentioned previous sections; therefore, it is a well-known benchmark candidate for the alternative shear wall systems. The hypothetical steel thickness was determined by equating the bending stiffness of the GFRP to steel plates. The lateral load resistance of the infilled moment frames was investigated and presented in this section.

In the second part, three different plate thicknesses, 3.2 mm, 6.0 mm and 10 mm, and four different panel aspect ratios, 1/2, 1/1, 3/2 and 2/1, were parametrically investigated within the selected moment frames. The GFRP plate width is assumed 1000 mm for all the tested

moment frames while the height of the plates was varied.

4.1 Moment Frames

The test frame was designed to be a steel moment frame with rigid end connections owning lateral stiffness depending on the frame geometry. The frame opening had 1000 mm times 1000 mm a square area, and it was constant for all the cases. In the second part of this study, the panel height was redefined to investigate the different panel aspect ratios for moment frames. The size of columns and beams were identical, and double UPN beams were chosen as the main structural members in numerical analysis with rigid end connections. Two UPN beams were aligned back-to-back to construct the test frames in the FE models. Three different UPN beams from flexible to rigid (UPN50, UPN100 and UPN200) were investigated as the main moment frames to be stiffened with GFRP plates. These beams were modeled using BEAM 188 elements and the strong axis of all the beams were aligned to the loading direction, and the typical frame model is shown in Figure 3b with an infill GFRP shear plate model. The moment frame was loaded at the top beam in horizontal direction by the deflection-controlled method. The total shear load was calculated at the bottom of the plate and load tip deflection was recorded at the loading point. It was assumed that steel follows bi-linear isotropic hardening material model with 235 MPa yield stress and 200000 MPa elastic modulus.

In an experimental test set-up, double UPN beams can be preferable to wrap the perimeter of the plate on both sides by bolting or bonding, so the specimen can be loaded without eccentricity and fixed-fixed boundary condition preserved as presented in this study. In these FE models, the GFRP plate was assumed to be perfectly bonded to the steel frame. Therefore, the stiffness

contribution from the moment frame with and without GFRP plate was similarly accounted.

4.2 GFRP Plates

Pultruded composite sections are layered products where the different number of fiber layers can be rowed within the thickness. The number of layers within the plate can vary and depend on the products and manufacturers; nevertheless, five layers of fibers were counted within the 3.2 mm plate thickness, so the plate was modeled with five layers of fibers and each layer was about 0.63 mm thick. The number of layers were increased as the plate thickness was increased to keep the thickness of each single layer unchanged. GFRP plates were constructed using layered SHELL 181 elements in FE models. Lengthwise properties of GFRP plates were oriented 0° , 45° , and 90° angles in the moment frames and the lengthwise fiber directions for the modeled plates are shown in Figure 4. It may be expected that 0° and 90° angle fiber orientations in a plate show similar results in a square panel; however, tension field angle will yield different failure predictions and load capacities for 0° and 90° angle fiber orientations. The highest load capacity can be expected when 45° angle fiber orientation was aligned with tension field angle; however, it is not practical to locate tension field angle before any theoretical calculations. Even though slightly lesser load capacity can be attained by aligning the lengthwise fibers to the panel diagonal, it is more practical to apply 45° angle in real life structures. Nevertheless, the expected fracture mechanism for three different panels with three fiber orientations was addressed in the first part of the study as shown in Figure 4, and in the second part of the study only 45° angle fiber orientation was investigated with different panel aspect ratios.

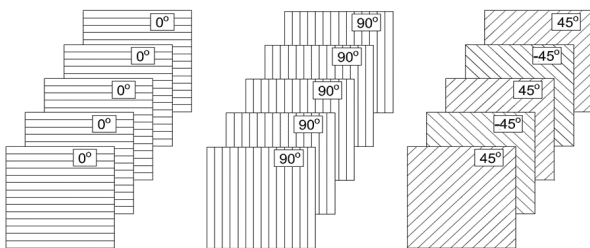


Figure 4. Fiber orientation angles within the tested GFRP plates.

The geometric nonlinearity is considered in FE models by providing an initial out-of-plane distortion to the GFRP plates. Most of the structural elements have some sort of geometrical imperfections that cause the secondary stresses. In those fabricated products, possible out-of-straightness exists before and after the installation of the GFRP plates. Different methods can be used to include the initial imperfections. The first

buckled mode shape of Eigen Buckling analysis was assigned to the plates. It was noted that some varied distortional ratios, 1/2000 and 1/500, did not show significant load capacity changes but yield different post buckling convergence issues for the considered thin GFRP plates. The assumed distortion was the 1/1000 of the plate heights, which conclude a unit distortion in the model for the square infill plates.

4.3 Steel Plates

Steel plate shear walls (SPSW) are commonly used in structural applications. In this study, SPSW is considered as a benchmark method in research of GFRP plate shear walls. The steel plate was modeled homogenous non-layered shell element. The mechanical properties were assumed identical to the moment frame where the plate has 235 MPa yield stress and 200000 MPa elastic modulus with elastic perfectly plastic bilinear material model. The hypothetical thickness of the steel plate was calculated 1.501 mm by equating the bending stiffness of the plates. Initial imperfections of the steel plates were included in FE analysis by employing the deformed shape of first Eigen Buckled mode; therefore, tension field action developed within the steel plates.

4.4 Mesh Study of the FE Model

In the developed FE model, meshing is an important step for the plate analysis where the buckling occurs, the fracture propagates in the tension and compression zones. Therefore, different element sizes were studied for the GFRP plates within the moment frames. The plate mesh topology was followed by the columns and beams. The results showed that the difference in the load-deflection results were in the decimal places for relatively fine meshes; 50 mm, 25 mm, and 10 mm element sizes. However, it can be said that the convergence of these element sizes in FE model slightly differs due to progressive fracture of the GFRP plates. In this study, 25 mm element size is chosen for analysis of all the FE models. Therefore, the meshed GFRP plates were represented at least with 1600 elements in 1000 mm x 1000 mm plate areas.

5. Test Results

5.1 Analytical Results of the Moment Frames

Approximate load capacities of the GFRP plate shear wall systems were obtained using the equivalent truss member method. The FE model results are only presented for 0° and 45° angle fiber oriented GFRP plates in Figure 5 and 6, respectively. Steel moment frames yielded before the rupture initiation of the GFRP plates. Initial lateral stiffnesses of the numerical models were in good agreement with total spring stiffness that was used in the analytical calculations when the and the

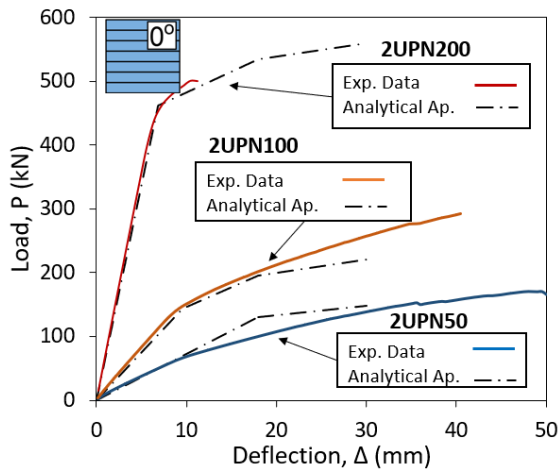


Figure 5. Load – deflection curve of the moment frames for 0° fiber orientation angle.

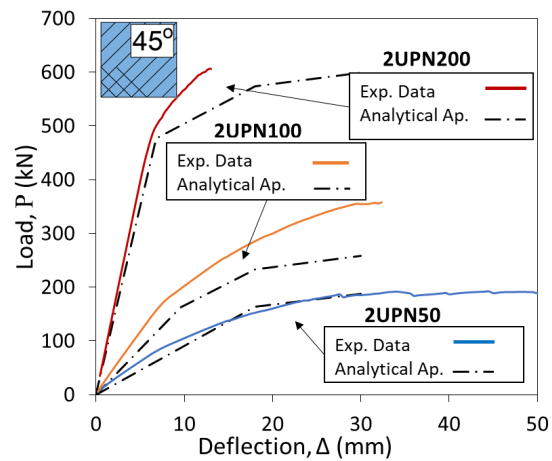


Figure 6. Load – deflection curve of the moment frames for 45° fiber orientation angle.

Table 1. Initial stiffness ratio of numerical and analytical calculations.

Moment Frames	GFRP Plate Orientation					
	90°			45°		
	0°	90°	45°	0°	90°	45°
	$E_i \text{ numerical} / E_i \text{ analytical}$			$P_u \text{ numerical} / P_u \text{ analytical}$		
2UPN 50	1.01	1.10	1.23	0.87	0.80	0.90
2UPN 100	1.06	1.09	1.27	1.01	1.01	1.07
2UPN 200	1.06	1.06	1.12	0.81	0.85	0.75

E_i: Initial Stiffness; P_u: Ultimate load capacity

lengthwise fiber oriented 0° angle as shown in Figure 5. Slight difference can be seen for the initial stiffness of the tested frames when the fiber was oriented 45° angle, latter can be seen in Figure 6. In Figure 5 and 6, after the steel frame yields, the lateral stiffness of that frame was neglected, and equivalent truss member stiffness resist the lateral load until the extreme fiber layers reached to critical failure stress. It was calculated that the moment frames reached about 21.8 mm lateral deflection until the first fiber rupture. The effective height of the section was recalculated after the first rupture of GFRP layers from top and bottom of the section. The GFRP section's loss was accounted by updating the effective elastic modulus and effective area of the GFRP plates for the second iteration. The second iteration was completed when the next unfailed extreme fiber reached its critical stress state. In other words, the residual stress capacity of the internal fibers was recalculated by an iterative approach until the critical stress was exceeded. The further iterations can be completed to obtain stiffness losses until the rupture of the last internal fiber, but the calculations were not considered after the second iteration.

The numerical difference between the initial stiffness and peak loads of the numerical and analytical calculations are presented as the ratio of the results in Table 1, respectively. The maximum initial stiffness ratio was 1.27 for the 2UPN 100 frame and the average ratio is about 1.21 for all three moment frames when the

plate oriented at 45° angle. When the fiber was oriented 0° and 90° angles, the average initial stiffness ratio is 1.07 for these moment frames as given in Table 1. Peak load ratios between the numerical and analytical calculations were presented in Table 1. The numerical results for the 2UPN 200 frame did not converge at the post buckling load capacities; therefore, the last step solutions were given as their peak load ratios in Table 1. The maximum peak load difference was calculated 0.75 for the non-converged solution of 2UPN 200 frame when the plate oriented at 45° angle. The average ratio can be calculated 0.89 for all the moment frames considering all the fiber orientations. This result showed that the analytically predicted peak loads were generally higher than the peak loads of the numerical results. Another analytical approach can be the inclusion of load drops at each fiber rupture. Once the fiber ruptures, the force needs to be balanced at the same deflection with equivalent adjusted stiffness and equivalent area which causes the load drop until the new stress equilibrium satisfied. However, this load drops were not included in the current analytical calculations, and the obtained results were found to be adequate to validate the numerical model results.

It should be noted that the error in these approximations can be calculated by assuming different failure definitions; therefore, initial failure criterion played an important role in these capacity predictions.

Table 2. Ultimate load capacity and load capacity increase of the moment frames.

Test Frames	Plate Thickness (mm)					
	--	1.501	3.175		3.175	
	P_{u_MF} (kN)	P_{u_SP} (kN)	$P_{u_FP_0^\circ}$ (kN)	$P_{u_SP} -$ $P_{u_FP_0^\circ}$	$P_{u_FP_45^\circ}$ (kN)	$P_{u_SP} -$ $P_{u_FP_45^\circ}$
2UPN 50	20.6	137	147	6.80%	187	26.74%
2UPN 100	91.3	259	282	8.16%	354	26.84%
2UPN 200	416	612	505	-21.19%	612	0.00%

MF: Moment frame, SP: Steel Plate Shear Wall, FP: GFRP Plate Shear Wall, Pu: Ultimate load capacity

Table 3. Initial stiffness and deflections of the moment frames at their initial yield points.

Moment Frames	Steel Plate		0° FRP Plate		45° FRP Plate	
	E_i (N/mm) [%]	Δ_i (mm) [%]	E_i (N/mm) [%]	Δ_i (mm) [%]	E_i (N/mm) [%]	Δ_i (mm) [%]
2UPN 50	42150 [4053]	3.5 [82]	7240 [613]	9.6 [50]	11167 [1000]	8.0 [58]
2UPN 100	64207 [638]	5.0 [52]	16689 [92]	8.0 [23]	22677 [161]	8.0 [23]
2UPN 200	138950 [123]	2.5 [60]	72090 [16]	6.1 [16]	79000 [27]	6.1 [16]

E_i : Initial stiffness, Δ_i : Lateral deflection

5.2 Numerical Results of the Square GFRP Plates

Lateral load resistance of steel moment frames was analyzed without GFRP infill plates, and these were called as the base frame performances. The base frames with double UPN (2UPN) 50, 100 and 200 beams reached about 19.2 mm, 10.4 mm, and 6.5 mm deflections at their 20 kN, 91 kN, and 416 kN peak lateral loads, respectively. These critical peak loads for the steel plates and initial rupture of the GFRP plates were given at peak loading Table 2. The 90° angle fiber orientation was omitted in Table 2 because 0° and 90° fiber angles produced similar load capacities.

The maximum load capacity gain was obtained when GFRP plate positioned with 45° angle fiber orientation. The stiffer moment frame reduced the relative load capacity increment for steel and GFRP plates. Only the load capacity of GFRP plate stayed below the steel plate's when the GFRP plate was oriented at 0° or 90° fiber angles in the most rigid steel frame. Therefore, the proper alignment of the lengthwise fiber angle can result more load capacity increment for GFRP plate than steel plate shear wall systems. On the other hand, elastic stiffness and post buckling stiffness of the steel plate shear walls were significantly superior to the GFRP plates for the considered moment frames. The increment for the initial stiffness and lateral deflections at failure over the base moment frames can be seen in Table 3. These deflections can be read as the story drift of a single-story frame and the reduction was a gain or vice versa for the recorded deflections at their failure points on the load-deflection curves. This showed that the hypothetical steel and GFRP plates can reduce the story drifts as low as 52% and 16%, respectively. These story drifts can be reduced more when the flexible moment frames were needed to be stiffened. Fiber orientation was another effective parameter for the reduction of the story drifts. The graphical representation of the

considered moment frames with steel and GFRP plates were plotted in Figure 7 to 9. A small difference was observed between the load deflection curves of 0° and 90° angle fiber oriented GFRP plates, and this difference became negligible when the lateral stiffness of the steel frame was increased. Theoretically, this difference can be attributed to the difference between the panel diagonal angle and tension field angle. Another difference was observed in the initiation and propagation of the GFRP fiber ruptures during the post yielding of the steel frames. The yield deflections were improved with flexible steel frame as can be seen in Figure 7, but this improvement gradually reduces as the lateral stiffness of the steel frame was increased as shown in Figure 9.

When the fiber angle was oriented parallel to the diagonal, 45°, the increase in lateral stiffness and load capacity were obtained. Hypothetical steel plates were provided around four times stiffer response than the GFRP plates in linear loading phase, and almost stable load capacity change observed during the post buckling phase. Toughness of the moment frames was defined in Table 4 with assumed deflection limits when the first rupture of GFRP was initiated; therefore, yielding of steel and progressive rupture of GFRP were excluded in these calculations. The total toughness of the GFRP plate shear walls with 0° fiber orientation was 32.4% below the toughness of steel plate. The fiber orientation at 45° angle for the GFRP plates improved the total toughness. The difference between the steel and GFRP plate shear walls was almost negligible, less than 1.0%, for 2UPN50 and 2UPN100 frames. However, the GFRP plate within the stiffer frame 2UPN200 showed 19.4% less fracture toughness than the steel plate shear wall system. Therefore, the stiffer moment frame requires thicker GFRP plate to reach the similar toughness of benchmark steel plate shear wall systems.

Table 4. Fracture toughness of the moment frames with infill plates

Test Frames	Plate Thickness (mm)					
	--	1.501	3.175		3.175	
	Deflection Cut-off, Δ_c (mm)	T_SP (kNmm)	T_FP_0° (kNmm)	T_SP - T_FP_0°	T_FP_45° (kNmm)	T_SP - T_FP_45°
2UPN 50	28	3274	2244	-45.9%	3254	-0.62%
2UPN 100	30	6808	5143	-32.4%	6825	0.25%
2UPN 200	13	6161	4570	-34.8%	5160	-19.40%

T: Fracture toughness, Δ_c : deflection state for toughness calculation, SP: Steel Plate Shear Wall, FP: GFRP Plate Shear Wall

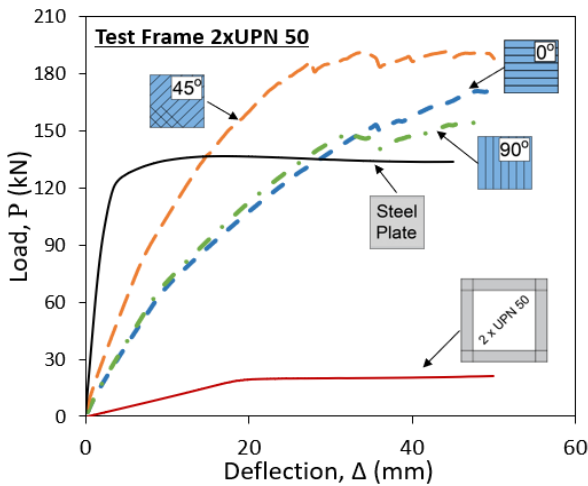


Figure 7. The load-deflection curve of 2UPN 50 moment frame with/without shear plates.

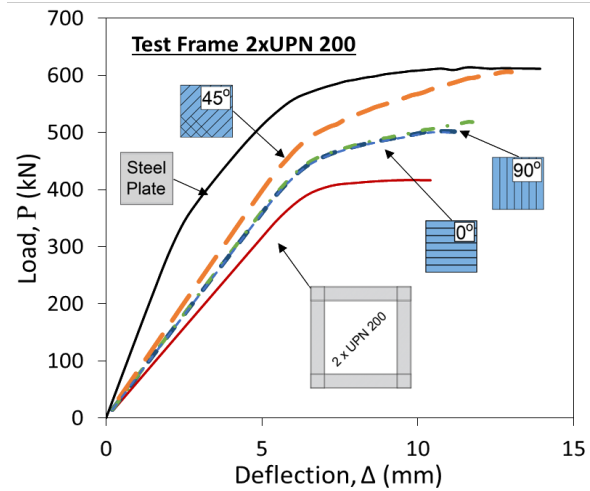


Figure 9. The load-deflection curve of 2UPN 200 moment frame with/without shear plates.

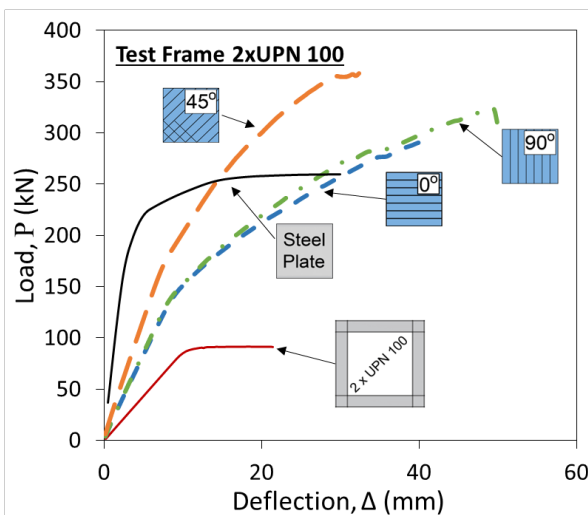


Figure 8. The load-deflection curve of 2UPN 100 moment frame with/without shear plates.

The averaged elastic equivalent strains along the tension and compression fields were recorded at the GFRP plates' peak load capacities. The solid and dashed lines represent the tension and compression field strains respectively in Figure 10 to 12. Strain readings were extracted only for the 45° GFRP plate orientation in this study.

The average of the experimentally obtained uniaxial failure strain was also plotted with a black dotted line in those figures to provide an approximate uniaxial failure strain.

The most straining effect can be seen in 2UPN 50 beams with the plate thickness of 3.2 mm as shown in Figure 10. Two ends of the tension field diagonal were strained the most in the 2UPN50 beam, and this straining effect was smaller around the middle of the tension field diagonal, which was about the center of the GFRP plate. Therefore, it was concluded that the initiation of the failure for the considered GFRP plate shear walls were the end connections of the moment frames. Compression and tension field diagonals cross each other at the center, and both shows an identical straining effect at the same location. That location is about the maximum straining location for the compression field diagonal and the strains become relatively negligible at the end of the compression field diagonal.

In a cyclic loading of a GFRP shear wall system, the four corner regions of the plate will be subjected to the more intensified stresses and needs to be protected for thinner plates to eliminate immature failures. As the plate thickness or the lateral stiffness of the steel frame

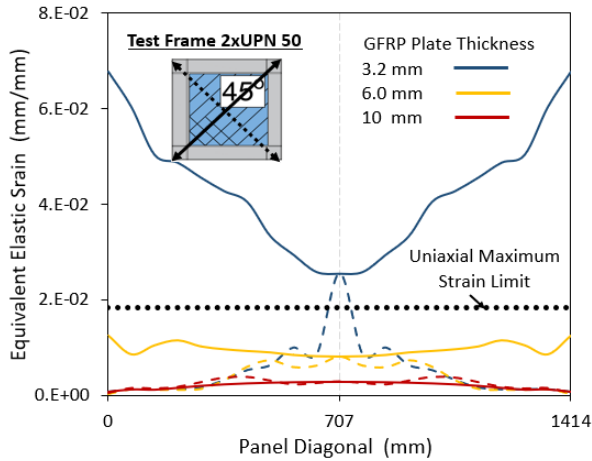


Figure 10. Tension (solid lines) and compression (dashed lines) field equivalent strains for 2UPN 50 frame.

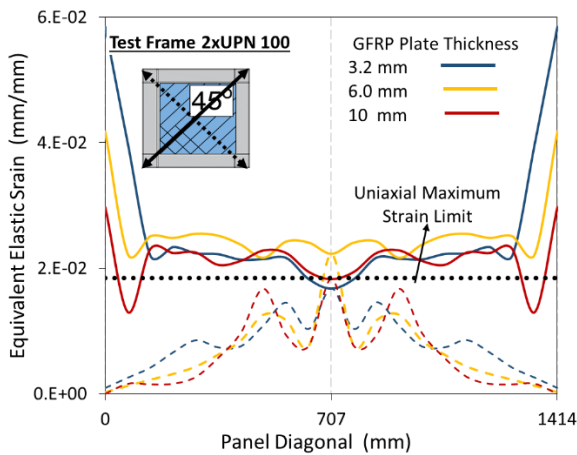


Figure 11. Tension (solid lines) and compression (dashed lines) field equivalent strains for 2UPN 100 frame.

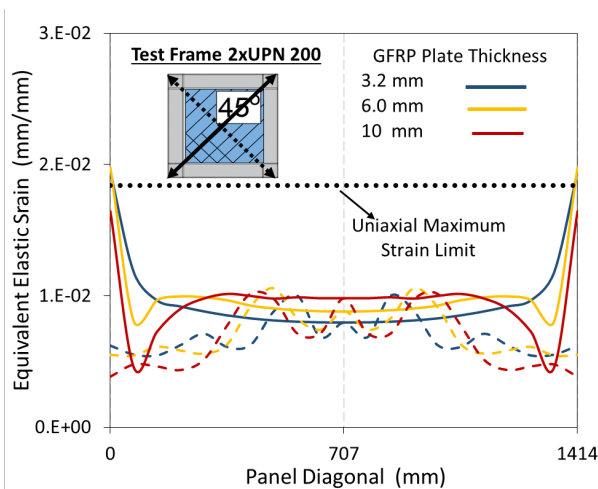


Figure 12. Tension (solid lines) and compression (dashed lines) field equivalent strains for 2UPN 200 frame.

increases, the straining action on the diagonals tends to reduce gradually as can be seen in Figure 11 and 12. The increased stiffness of the steel frame results more unified straining action on the GFRP plate up to their peak loads. It should be noted that the convergence of the load capacities may slightly alter the strain values at the peak loads; however, the equivalent strains with different steel frames and plate thicknesses provide the possible failure pattern of the GFRP plate. Therefore, the tension field action can be developed with relatively thicker plates and the straining action become more uniform along the plate diagonals.

The detailed study of the infill plated steel moment frames using either steel or GFRP plates showed that the tension field action was developed with the thin plates. Flexible moment frames were benefited more from the use of shear plates even though the full tension field action cannot be developed within the flexible frames [28]. The reduced story drifts delayed the yield of the moment frames, and the yield load capacity of those frames were also increased using the shear plates. However, the yield point of the rigid moment frames almost was not affected from the tension field action as shown in Figure 9.

5.3 Results of Different GFRP Panel Aspect Ratios

The different plate slenderness and panel aspect ratios of the GFRP plate shear wall systems were investigated, and their normalized peak load capacities are given in this section. Each GFRP plate shear wall frame's peak loads were normalized using its corresponding base frame's load capacity to be able present the relative load capacity ratios. In this section four different panel aspect ratios, panel height divided by panel width, were considered with three different GFRP plate thickness. These thicknesses created different plate slenderness within the considered moment frames. In this study, 1000 mm wide panel width was kept unchanged and panel height was varied to have the panel aspect ratio of 1/2, 1/1, 3/2 and 2/1. Three different thicknesses were selected considering the commercial availability of the GFRP plates and they were placed to be oriented at 45° angle within the moment frames. This angle was not guaranteed the best performance for some of the panel aspect ratios due to variation of the tension field angle according to the panel aspect ratios; however, 45° fiber orientation can be assumed one of the most practical approaches in the field applications. In other words, the lateral resistance of the GFRP plates can be increased some amount from the presented load capacity ratios when the lengthwise fiber angle was aligned with the theoretical tension field angles. Nevertheless, the presented results are still valid for the assumed GFRP plate orientation and that minimum and maximum angle difference is 0° and 7° for the 1/2 and 2/1 panel aspect ratios, respectively. The results were presented in Figure 13 to 15 with custom markers, and these markers

represent the panels in scale so the reader can easily follow the change in load capacity ratios for different panel aspect ratios. The customized black lines in the same figures represent the same GFRP plate thickness for different set of panel aspect ratios.

Typical two general results were concluded from the parametric results of the GFRP plate shear wall system. The first one is the increased plate slenderness reduces the load ratios, and the second is the increased plate thickness increases the load capacity ratios in all moment frames. Another common result for all the moment frames was that the normalized load capacity ratio was the highest for the largest panel aspect ratio within the same thickness category, and that normalized capacity ratios gradually decreases as the panel aspect ratio decreases. Finally, it can be concluded from the trend of these plots that the panel aspect ratio larger than 2/1 will not yield significant load capacity increase for the considered moment frames.

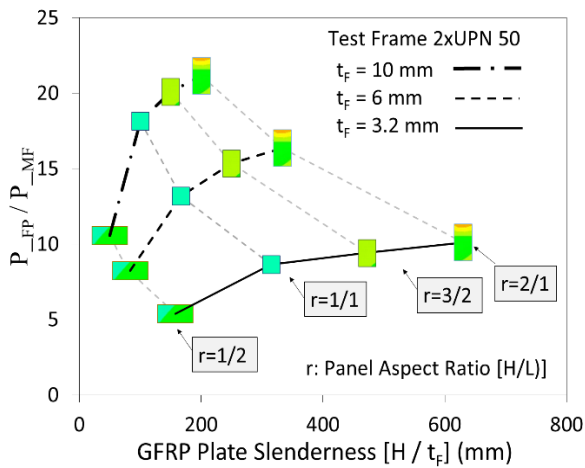


Figure 13. Plate slenderness effect with different panel sizes for 2UPN 50 moment frame

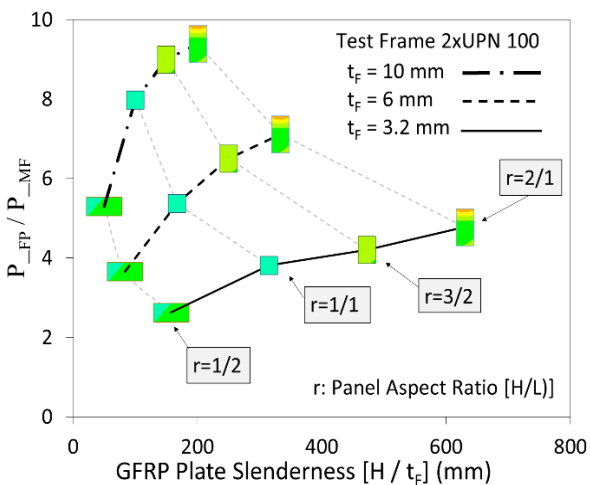


Figure 14. Plate slenderness effect with different panel sizes for 2UPN 100 moment frame

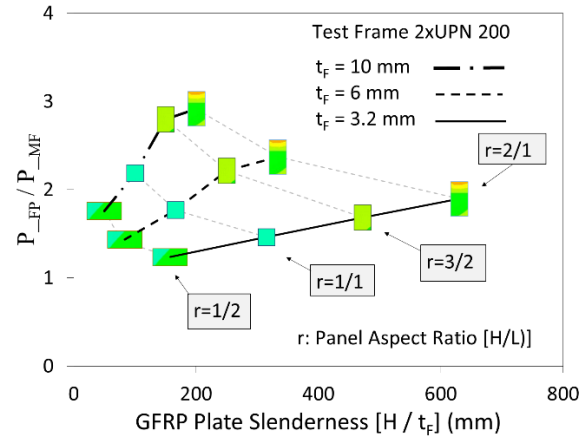


Figure 15. Plate slenderness effect with different panel sizes for 2UPN 200 moment frame

The higher load capacity ratios were obtained while stiffening the more flexible moment frames as described earlier for the square panel beams. The moment frame with 2UPN 50 beams can reach the load capacity ratio of 5 to 21 as the plate thickness ranges from 3.2 mm to 10 mm, respectively. The change in the capacity of that frame is shown in Figure 13. These load capacity ratios for the same thicknesses get decreased to the range of 2.6 and 9.2 when the 2UPN 100 beam was considered as the steel moment frame as shown in Figure 14. Finally, the load capacity ratios for the same thicknesses become narrowed down to 1.2 to 2.9 for the relatively rigid frame, 2UPN 200 beams in Figure 15, respectively.

5. Conclusions

The study aimed to enhance the lateral load capacity of a moment frame with an infill GFRP plates taking the advantage of the composite material properties. Commercially available thin GFRP plates were selected in this study. These plates can buckle before the critical shear load capacities so the full shear resistance cannot develop within the plate. Therefore, tension field action can develop after the plate buckling. The numerical models were first developed and then verified to study the performance of square GFRP plates in a moment frame. The material properties and failure criterion for the GFRP specimens was extracted from the experimental results of the three-point bending tests. An analytical method using an equivalent truss member stiffness was presented to approximate and verify the lateral load capacities of a single-story moment frames. As a result of the analytical formulation, not only the peak load capacities but also the load deflection history of the moment frames was presented in this paper. Hypothetical steel plate was defined instead of GFRP plates within the moment frames to compare the lateral response of two different materials. Finally, different plate thicknesses with different panel aspect ratios were

parametrically studied with the verified numerical models, and all related findings were listed below:

- Tension field action can develop in GFRP plates until the initial rupture. After that rupture, the degradation of fibers reduces the load capacities.
- The effectiveness of the GFRP plate is highly dependent on the base moment frame's lateral stiffness. The flexible moment frames produce the highest load capacity and initial stiffness increase or vice versa. The least load capacity and initial stiffness increments are about 21% and 16%, respectively, for the most rigid moment frame.
- The resistance of the tension field depends on the lengthwise and crosswise properties of the GFRP plates. The most gain can be attained when the GFRP plate's lengthwise direction is aligned with the tension field angle. The numerical study showed that the 45° angle fiber orientation showed the ultimate gain in this study.

However, it was found that even for the square plates, tension field angle slightly differs than 45°; therefore, 0° and 90° angle fiber orientations showed slight difference in their initial stiffness and peak load capacities.

- The hypothetical steel plate showed the most initial stiffness increase by 123% in this study. Following the steel plate yielding, there is flat post buckling zone obtained without rupture since the steel is modeled as elastic - perfectly plastic material. It can be concluded from the load deflection curves that the elastic energy stored in the steel plates was higher than the GFRP plates'. On the other hand, GFRP plate still weighs lighter than the hypothetical steel plate for the considered GFRP plate thicknesses.
- The numerical studies showed that the peak load capacities of the GFRP plates were either above or same as the steel plate's for the square moment frames. However, the initial stiffness of the steel plate was found 4 times more than the GFRP plate's.
- The approximated analysis provided an iterative analytical solution including the fiber failures. These formulations can be used to verify the numerical results.
- Considering the same plate thicknesses within the different panel aspect ratios, the largest panel aspect ratio, 2, showed the highest normalized load capacity increase than that of the others.
- When the panel aspect ratio of a frame was larger than 2, that panel was provided significant load capacity increase for the considered moment frames.

In summary, while the GFRP plates can be utilized to enhance the load capacity and reduce the relative story drifts, they can be as effective as the steel plates. The mechanical properties and light weight of the composite panels can be an alternative for steel or wood plate shear wall applications. This results courage the researchers to perform further experimental test to obtain static and cyclic performances of the GFRP plate shear walls.

Acknowledgments

Donation of GFRP materials by Reinforced Plastics, Inc. and technical support of the Department of Civil and Environmental Engineering at Louisiana State University are acknowledged.

Author's Contributions

Tuna Ülger: Drafted and wrote the manuscript, performed, and interpreted the whole experiments and analysis.

Ethics

There are no ethical issues after the publication of this manuscript.

References

- [1]. Frketic, J, Dickens, T, Ramakrishnan, S. 2017. Automated manufacturing and processing of fiber-reinforced polymer (FRP) composites: an additive review of contemporary and modern techniques for advanced materials manufacturing. *Additive Manufacturing*; 14: 69–86.
- [2]. Green, MF, Bisby, LA, Fam, AZ, Kodur, VK. 2006. FRP confined concrete columns: Behaviour under extreme conditions. *Cem. Concr. Compos.*; 28(10): 928–937
- [3]. Arghya, D, Bhattacharyya, SK. 2010. Investigation into the effect of bonding on FRP-wrapped cylindrical concrete columns. *J. Compos. Constr.*; 14(6): 706–719.
- [4]. Pham, TM, Hadi, MNS, Jim, Y. 2015. Optimized FRP wrapping schemes for circular concrete columns under axial compression. *J. Compos. Constr.*; 19(6): 4015015.
- [5]. Wang, Z, Wang, D, Smith, ST, Lu, D. 2012. Experimental testing and analytical modeling of CFRP-confined large circular RC columns subjected to cyclic axial compression. *Eng. Struct.*; 40: 64–74.
- [6]. Saadatmanesh, H, Malek, AM. 1998. Design guidelines for flexural strengthening of RC beams with FRP plates. *J. Compos. Constr.*; 2(4): 158–164.
- [7]. Elsanadedy, HM, Almusallam, TH, Alsayed, SH, Al-Salloum, YA. 2013. Flexural strengthening of RC beams using textile reinforced mortar – experimental and numerical study. *Compos. Struct.*; 97: 40–55.
- [8]. Rasheed, HA, Zaki, MA, Foerster, AS. 2022. Efficient bidirectional U-wrap system to anchor CFRP sheets bonded to reinforced concrete T-girders. *Structures*; 38: 226–236
- [9]. Van Den Einde, L, Zhao, L, Seible, F. 2003. Use of FRP composites in civil structural applications. *Construction and Building Materials*; 17(6): 389–403.
- [10]. Sonnenschein, R, Gajdosova, K, Holly, I. 2016. FRP composites and their using in the construction of bridges. *Procedia Engineering*; 161: 477–482.
- [11]. Alshurafa, S, Alhayek, H, Polyzois, D. 2021. Static characteristics of multicells jointed FRP tower with mass on its top. *Mechanics of Advanced Materials and Structures*; 28(3): 229–236.
- [12]. Wang, Y, Chen, G, Wan, B, Han, B, Ran, J. 2021. Axial compressive behavior and confinement mechanism of circular FRP-steel tubed concrete stub columns. *Composite Structures*; 256: 113082.

- [13]. Salim, HA, Davalos, JE, Qiao, P, Kiger, SA. 1997. Analysis and design of fiber reinforced plastic composite deck-and-stringer bridges. *Composite Structures*; 38(1): 295–307.
- [14]. Cheng, L, Karbhari, VM. 2006. New bridge systems using FRP composites and concrete: a state-of-the-art review. *Progress in Structural Engineering and Materials*; 8(4): 143–154.
- [15]. Oludare, O, Elias, T. 2019. In-plane shear characterization of composite GFRP-foam sandwich panels. *Journal of Composites for Construction*; 23(5): 4019034.
- [16]. Nateghi-Alahi, F, Khazaei-Poul, M. 2012. Experimental study of steel plate shear walls with infill plates strengthened by GFRP laminates. *Journal of Constructional Steel Research*; 78: 159–172.
- [17]. Edalati, SA, Yadollahi, Y, Pakar, I, Bayat, M. 2015. On the effect of GFRP fibers on retrofitting steel shear walls with low yield stress. *Earthquakes and Structures*; 8: 1453–1461.
- [18]. Petkune, N, Donchev, T, Hadavinia, H, Limbachiya, M, Wertheim, D. 2016. Performance of pristine and retrofitted hybrid steel/fibre reinforced polymer composite shear walls. *Construction and Building Materials*; 117: 198–208.
- [19]. Bach, D, Akhrawat, L. 2020. Optimization of fiber-reinforced polymer patches for repairing fatigue cracks in steel plates using a genetic algorithm. *Journal of Composites for Construction*; 24(2): 4020006.
- [20]. Ronny, P, Michel, B. 2009. Finite-element investigation and design recommendations for perforated steel plate shear walls. *Journal of Structural Engineering*; 135(11): 1367–1376.
- [21]. Azarafrooz, A, Shekastehband, B. 2020. Behavior of fully-connected and partially-connected multi-story steel plate shear wall structures. *Structural Engineering and Mechanics*; 76(3): 311–324.
- [22]. Mirmura, H, Akiyana, H. 1977. Load-deflection relationship on earthquake-resistant steel shear walls developed diagonal tension field. *Transactions of the Architectural Institute of Japan*; 260: 109–114.
- [23]. Vincent, C, Mohamed, E, Ruobo, C. 1993. Experimental study of thin steel-plate shear walls under cyclic load. *Journal of Structural Engineering*; 119(2): 573–587.
- [24]. Ramla, Q, Michel, B. 2019. Behavior of steel plate shear walls subjected to repeated synthetic ground motions. *Journal of Structural Engineering*; 145(4): 4019008.
- [25]. Deng, E-F, Zong, L, Wang, H-P, Shi, F-W, Ding, Y. 2020. High efficiency analysis model for corrugated steel plate shear walls in modular steel construction. *Thin-Walled Structures*; 156: 106963.
- [26]. Damghani, M, Wallis, C, Bakunowicz, J, Murphy, A. 2021. Using laminate hybridisation (CFRP-GFRP) and shaped CFRP plies to increase plate post-buckling strain to failure under shear loading. *Thin-Walled Structures*; 162: 107543.
- [27]. Lu, J, Zhang, H, Yu, S. 2021. Study on seismic behaviors of self-centering steel plate shear walls with slits. *Journal of Constructional Steel Research*; 185: 106878.
- [28]. Thorburn, LJ, Montgomery, CJ, Kulak, GL. Analysis of steel plate shear walls, Edmonton, Alberta, 1983.
- [29]. Dolan, JD, Foschi, RO. 1991. Structural analysis model for static loads on timber shear walls. *Journal of Structural Engineering*; 117(3): 851–861.
- [30]. Bryan, F, Andre, F. 2001. Cyclic analysis of wood shear walls. *Journal of Structural Engineering*; 127(4): 433–441.
- [31]. Ilg, P, Hoehne, C, Guenther, E. 2016. High-performance materials in infrastructure: a review of applied life cycle costing and its drivers – the case of fiber-reinforced composites. *Journal of Cleaner Production*; 112: 926–945.
- [32]. Bedford Reinforced Plastics. Bedford Structural Shapes. <https://bedfordreinforced.com/products/proseries/proforms/> (accessed at 13.10.2021).
- [33]. ANSYS Academic Research Mechanical, Release 15. Mechanical APDL Material Reference.
- [34]. ASTM D790. 2015. Standard Test Method for Flexural Properties of Unreinforced and Reinforced Plastics and Electrical Insulating Materials. West Conshohocken, PA, USA: ASTM International.

An Investigation on the Flexural and Thermo-mechanical Properties of CaCO₃/Epoxy Composites

S. Bahar Baştürk^{1*} 

¹ Faculty of Engineering, Metallurgy and Materials Engineering Department, Manisa Celal Bayar University

[*bahar.basturk@cbu.edu.tr](mailto:bahar.basturk@cbu.edu.tr)

*Orcid: 0000-0002-4027-1935

Received: 27 October 2021

Accepted: 9 May 2022

DOI: 10.18466/cbayarfbe1015351

Abstract

Present work focused on the flexural and thermo-mechanical characteristics of epoxy based composites filled with 3 different calcium carbonate (CaCO₃) concentrations: 1.5, 3 and 5 wt.%. Composite specimens were fabricated through conventional casting method and subjected to flexural test via 3 point bending fixture. Additionally, dynamic-mechanical analyzer (DMA) with single cantilever mode was used to reveal the thermo-mechanical responses of samples. The findings showed that the filler concentration increase led to the increase of storage modulus (E') for all specimens while the glass transition temperature (T_g) slightly decreased for 1.5 wt. % CaCO₃ filled epoxy composite. The 5 wt.% CaCO₃ loaded composite showed maximum E' and T_g values with 10% and 1.5% improvement, respectively. Based on flexural test results it was surprisingly found that, 1.5% wt. CaCO₃ addition attained the highest strength with ~30% improvement among all samples. However, 5 wt.% CaCO₃ introduced composites displayed the lowest mechanical performance due to the presence of agglomerates/tactoids, which was verified from SEM images as well.

Keywords: CaCO₃/epoxy composites, flexural properties, thermo-mechanical response

1. Introduction

Application of polymer matrix composite (PMC) materials are extending day by day depending on the demands required by several markets like energy, automotive, aviation, electronics and infrastructure [1]. Epoxy is the mostly preferred thermoset matrix in composites due to its remarkable properties such as improved dimensional stability, high abrasion resistance and superior chemical resistance. Epoxies generally include two components (resin and hardener), and they attain desired stiffness via curing process, which is the transition from liquid to solid form in diverse durations [2-4]. When fibers or fillers integrated with epoxy, the resultant composites show exceptional mechanical strength and stiffness properties. In literature, various powders with micron or nano size (e.g., wood fiber, rice hull, sawdust, graphene oxide, magnesium hydroxide) have been introduced as the reinforcement phase to produce polymer matrix composites. Fundamentally, those powders are categorized into three main groups: natural, synthetic, and organic [5-6]. A large number of fillers such as talc, silica, clay, mica and CaCO₃ are industrially available and utilized in many areas. Among

them, CaCO₃ is predominantly used because of its commercial abundance and low cost [7-9]. Mechanical, thermal and optical characteristics of polymers have been significantly enhanced with the addition of optimum CaCO₃ concentration. For instance, Techawinyutham et al. [5] investigated the performance of PP/CaCO₃ composites for 10, 20, 30 40 and 50 wt.% filler contents with and without maleic anhydride polypropylene (MAPP) introduction. They found that the strength values of composites decreased while tensile and flexural rigidities of the specimens increased. Azman et al. [10] examined the flexural responses of eggshell powder-ESP (as CaCO₃ source) filled epoxy composites loaded with 5, 10, 15 and 20 wt.% filler. Based on that study, 15 wt.% ESP concentration improved the modulus but led to lower strength as compared with neat epoxy. Kirboga et al. [11] developed biodegradable PHBV/CaCO₃ composites with 0.1-1 wt.% of CaCO₃ content and manufactured them by melt extrusion. According to their results, composite samples with 0.1wt.% CaCO₃ enhanced both storage and loss modulus values up to 76% and 175%, respectively. De Moura et al. [12] prepared composites by integrating 25 wt.% and

50 wt.% CaCO₃ and PU, separately. In that study, as the particle content increased, the tensile and flexural modulus of specimens increased while the strength values of composites improved only along out of plane direction.

Based on various studies referred above, it has been observed that nonidentical results were obtained with respect to filler concentration, particle form and size as well as experimental conditions. The main motivation of the present work is to reveal the effects of CaCO₃ filler on the flexural and thermo-mechanical characteristics of polymer composites. Indeed, the extended version of this study considers the utilization of low-cost micron size CaCO₃ powder with and without surface modification. However, as the first part, the content of the paper particularly covers the properties of composites including less amount unmodified CaCO₃ compared with literature [5,8,12]. Basically, CaCO₃ particles with 1.5, 3 and 5 wt.% concentration was dispersed in epoxy, casted into silicon molds and subjected to curing process. The produced composites were exposed to flexural test and dynamic mechanical analysis. Additionally, fractographic images of samples were evaluated to deeply understand the distribution of particles in the microstructure, which significantly affects the mechanical performance.

2. Materials and Methods

2.1. Materials

The thermoset epoxy matrix system consists of DTE 1200 resin and DTS 2110 hardener was purchased from Duratek™, Turkey. The calcium carbonate (CaCO₃) powder was provided by Merck™ with an average particle size of ~14 μm (d₅₀).

2.2. Preparation of Composites

In the present study, epoxy resin and micron sized CaCO₃ powder with 1.5, 3 and 5 wt.% were integrated with traditional casting method for composite production (see Figure 1). The required amount of DTE 1200 epoxy resin and CaCO₃ were blended firstly and dispersed in acetone for 3 hours. The mixture was dried at 80°C in the oven for 12 hours for acetone evaporation. Prior to casting, the DTS 2110 hardener was incorporated with mixture based on the manufacturer instructions and blended via magnetic stirrer for 30 minutes. Silicon moulds were filled with resultant composite mixture and kept into vacuum for minimizing void/bubble formation. Curing of samples were conducted at room temperature for 15 hours following a post-curing at 80 °C for 8 h. For simplicity, sample abbreviation adopted depending on filler volume fraction, e.g. 1.5CaCO₃-epoxy comp represents 1.5 wt.% CaCO₃ in epoxy matrix.

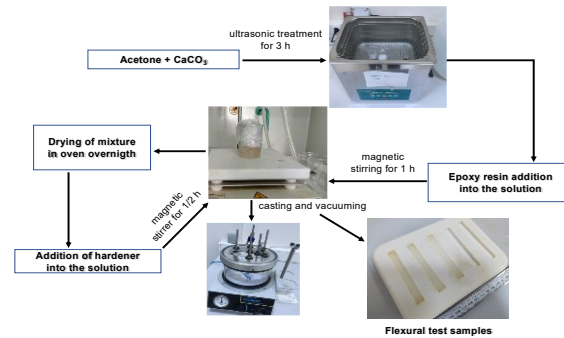


Figure 1: Preparation steps of flexural test samples.

2.3. Characterization of Composites

The X-ray diffraction (XRD) measurement of CaCO₃ powder was conducted via Panalytical Empyrean system with CuKα radiation ($\lambda = 1.540\text{\AA}$) in a wide range of 2θ ($10^\circ \leq 2\theta \leq 80^\circ$). The scanning speed of the diffractometer was fixed as 1°/min to disclose the crystalline properties and present phases. Flexural test of composites was performed in a universal mechanical test machine via three-point bending (3PB) fixture in accordance with ASTM D-790 standard [13] with a crosshead speed of 1.5 mm/min. Based on the standard, the full length was determined as 80 mm while the width (b) value of bending samples was determined as 14 mm. The thicknesses (d) of neat epoxy and the composite systems with 1.5%, %3 and %5 CaCO₃ content were measured as 4.23 ± 0.08 , 4.26 ± 0.12 , 4.21 ± 0.10 and 4.23 ± 0.14 , respectively.

Flexural strength ($\sigma_{flexural}$) and modulus ($E_{flexural}$) parameters were calculated based on the equations (2.1) and (2.2) given below where span length (L) was specified as 64 mm.

$$\sigma_{flexural} = \frac{3PL}{2bd^2} \quad (2.1)$$

$$E_{flexural} = \frac{L^3 m}{4bd^3} \quad (2.2)$$

The “ m ” is the slope of the tangent to the initial straight-line portion of the load-deflection curve and obtained from the 3PB tests.

In this study, the visco-elastic responses of structures were characterized by dynamic-mechanical analyser (DMA) under liquid nitrogen atmosphere via TA™ Instrument Q800. Through DMA measurements, the variation of storage modulus (E') and loss modulus (E'') of every sample were recorded from 40°C to 150°C at 1 Hz constant frequency. Single cantilever mode was chosen and the heating rate was determined as 5°C/min. The E' and E'' represent the stored and dispersed energy values of specimens, respectively. The ratio of those two parameters (E''/E') is calculated by the analyzer and provide the “tangent delta- $\tan\delta$ ” magnitude for each

temperature. Fracture surfaces of flexural test samples were investigated by scanning electron microscope (SEM) photographs taken by COXEM™ EM-30 Plus and Carl Zeiss 300 VP equipment.

3. Results and Discussion

3.1. XRD Results

Figure 2 shows the XRD patterns of as-received CaCO₃ powder in the 2θ range from 10° to 80°. The recorded diffraction peak locations, corresponding reflections, and calculated crystal size (or thickness) values of CaCO₃ powder are reported in Table 1. Debye–Scherrer equation is widely used to estimate the particle size of substances and expressed as in Eq. (3.1).

$$d = \frac{k\lambda}{\beta \cos\theta} \quad (3.1)$$

Table 1. Debye–Scherrer parameters for the calculation of CaCO₃ crystal size.

2θ (°)	Reflection Planes	FWHM (radian)	Crystal size-d (µm)
29.25	(104)	0.001469	5.84
35.82	(110)	0.001494	5.85
39.26	(113)	0.001452	6.07
43	(202)	0.001373	6.50
47.35	(018)	0.001586	5.71
48.34	(116)	0.001513	6.02

The d , k , λ , β and $\cos\theta$ represent the crystal size, Debye–Scherrer constant (0.9), X-ray wavelength (0.15406 nm) and line broadening (in radian) found from the full width at half maximum (FWHM) of sharp peaks and Bragg angle, respectively [14]. According to the calculations, CaCO₃ crystal size values ranged between 5.7 µm to 6.5 µm, which is yet to be verified from SEM photos. By considering the findings from XRD analysis and based on the literature [15-16], it is concluded that calcite is the dominant phase for this powder (see Figure 2).

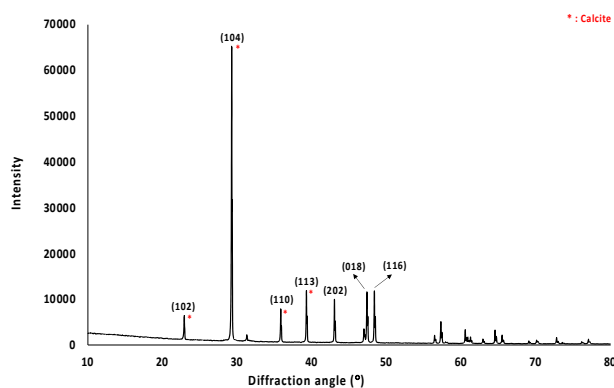


Figure 2. XRD patterns of CaCO₃.

3.2. Thermo-mechanical Results

The thermomechanical responses of CaCO₃/epoxy composites were determined via dynamic mechanical analyser (DMA) and the resultant graphs are shown in Figure 3 (a) to (c).

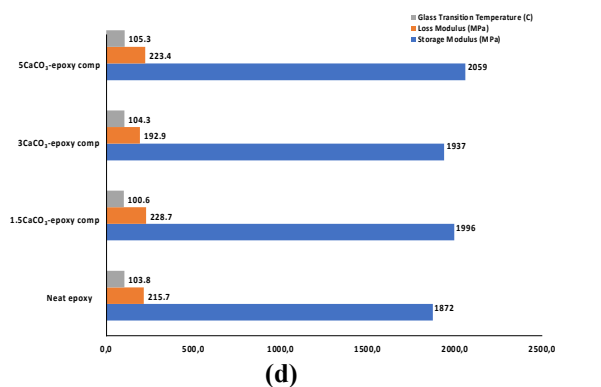
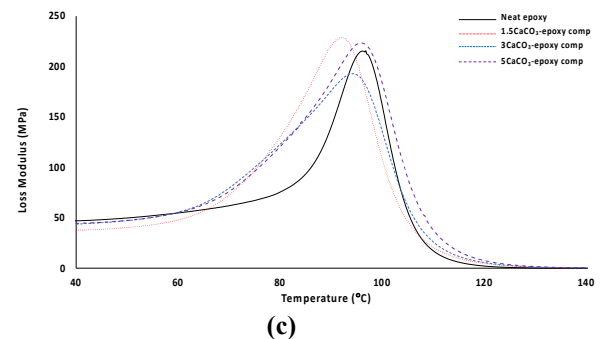
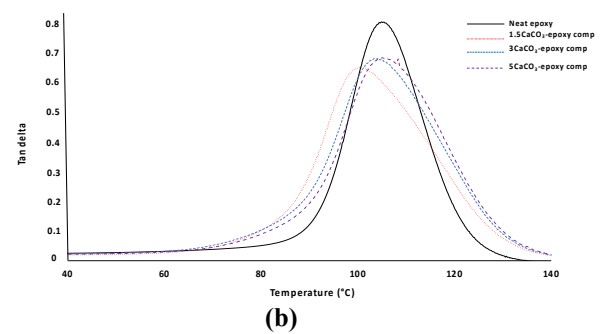
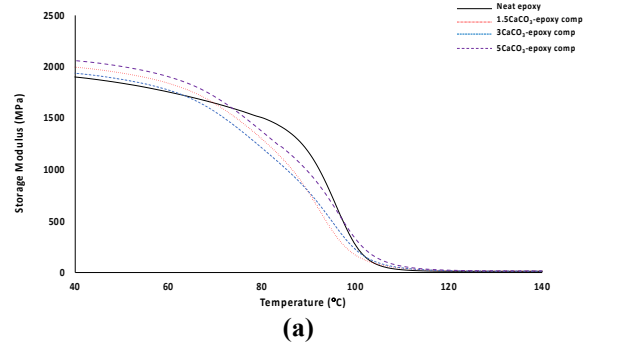


Figure 3. DMA results of CaCO₃/epoxy composites: a) E' -temperature variation, b) $\tan\delta$ -temperature variation, c) E'' -temperature variation, d) T_g , E' and E'' variation depending on CaCO₃ concentration at 40°C.

Based on the theory of DMA, storage modulus (E') represents the elasticity of the material while loss modulus (E'') indicates the viscous characteristics of samples. The ratio between E' and E'' is expressed as the damping factor ($\tan\delta$) and the peak point in $\tan\delta$ -temperature curve represents the glass transition temperature (T_g) of specimens [17]. Due to the temperature limitation and fluctuations during DMA analysis, the initial and final temperatures values were specified as 40°C and 140°C, respectively. The variations of glass transition temperature, storage modulus and loss modulus depending on CaCO_3 concentration are given as a different graph in Figure 3 (d). Storage modulus-temperature path generally follows three sequential sections: low temperature glassy zone, constricted steep decline zone and high temperature rubbery plateau [18]. All of those regions are available in Figure 3 (a) and as it is seen in the same figure that, at 40°C, the E' of pure epoxy exhibited the lowest value among all samples while the 5 wt. % filler loaded composite showed the highest storage modulus with 10% increase. Other two composites displayed close values for the same parameter at the same temperature. Therefore, increase of E' indicates the improved adhesion between filler and matrix. The rubbery plateau of the host matrix is apparently observed in Figure 3 (a), however, the addition of CaCO_3 led to the shrinkage of that plateau, as expected [17-18]. The increase in temperature caused to the enhancement of polymer chain mobility and resulted in the decrease of storage modulus, as in this study [18]. Based on Figure 3 (b), $\tan\delta$ parameter reduced with the introduction of CaCO_3 powder independent of its amount, which indicates an advanced interaction between composite components [19]. Additionally, composite samples exhibit broader $\tan\delta$ peaks that can be attributed to slower relaxation process due to matrix-filler interaction, as compared with pure epoxy [20].

The temperature corresponding to peak point of $\tan\delta$ gives T_g , whose variation provides essential information about the effectiveness of particle-polymer bonding. For instance in this work, the 5 CaCO_3 -epoxy composite exhibited maximum T_g (~1.5% \uparrow) that is slightly higher than unfilled epoxy. However, 1.5 wt. % filler addition decreased that parameter into some extent and this situation may be related with the amount of micron-sized filler that was insufficient for better interaction. It is also probable that nano-size CaCO_3 introduction with optimum content would result in higher glass transition temperature and/or storage modulus due to higher specific surface area of nano-particles [20]. Limited surface area of micron size filler considered in this study is presumably one of the main reasons for obtaining less effective results. In literature, Miranda et al. investigated [21] the thermo-mechanical characteristics of nano- CaCO_3 /epoxy composites for 1, 2.5 and 5 wt.% particle content. Based on that study, the 2.5 wt. % filler concentration provided the maximum

increase in T_g (from 137°C to 142°C with 5°C \uparrow) with respect to neat epoxy. Nonetheless, the E' values of those samples were lower than epoxy matrix up to 120°C. Baskaran et al. [22] examined unsaturated polyester/nano- CaCO_3 composites for 1, 3, 5, 7 and 9 wt. % powder content. According to their study, 5 wt. % nanoparticle introduced composite achieved both maximum glass transition temperature (from 90°C to 121°C with 31°C \uparrow) and storage modulus among other composites.

Loss modulus (E'') describes the heat energy loss because of the internal friction occurs in polymers and composites during sinusoidal dynamic loading [23]. As the temperature enhanced, whole samples reached a maximum value for E'' and then dramatically dropped to zero when the polymer chain mobility becomes extremely high (transition from glassy state to rubbery state). The increase of loss modulus points out an advanced interfacial bonding between matrix and filler due to the enhanced energy dissipation between them [3,23]. In this work, only 3 CaCO_3 -epoxy composite exhibited slightly lower E'' value, although its E' and T_g parameters were higher than host matrix.

3.3. Flexural Test Results

The effects of CaCO_3 content on the flexural properties of composites are presented in Figure 4 (a) and (b) with representative samples.

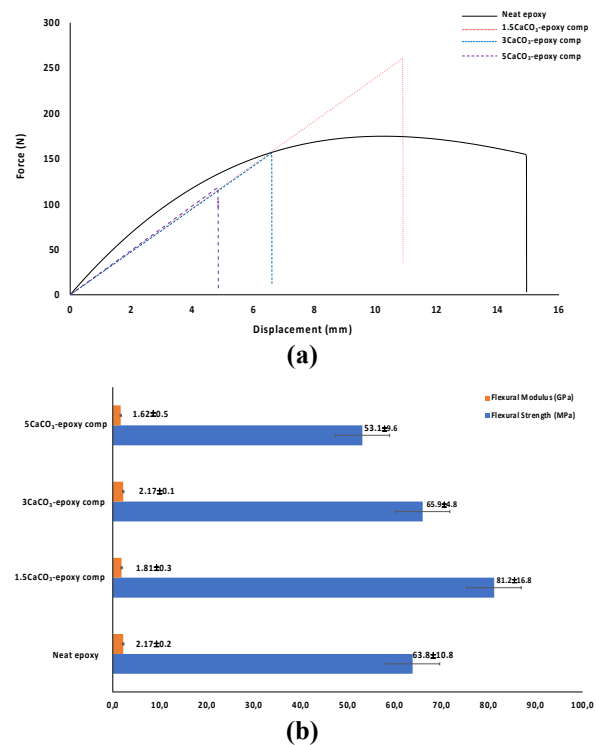


Figure 4. (a) Flexural force-displacement graph, (b) average flexural modulus and strength variation of CaCO_3 /epoxy composites depending on CaCO_3 concentration.

As obviously seen in that figure, addition of CaCO_3 resulted in the increase of brittle character and caused to the decrease of plasticity in composites (see Figure 4-a). The calculated mechanical parameters such as flexural strength and modulus are given in Figure 4 (b) with standard deviations. Based on that figure it is interestingly observed that, the 1.5% wt. CaCO_3 introduction achieved the maximum strength (81.2 MPa with ~30% improvement) but reduced the flexural modulus (1.81 GPa with 17% decline) as compared with neat epoxy. Additionally, the 3% wt. CaCO_3 showed slightly higher strength (65,9 MPa with 3% improvement) and modulus (2.18 GPa with 1% improvement) values than matrix material. However, 5 wt.% CaCO_3 loaded composites exhibited lowest mechanical properties due to the presence of agglomerates, which is yet to be confirmed from SEM images. It is probable that 5% wt. filler in the matrix was excessive in terms of optimum flexural properties while the other two concentrations facilitated better reinforcement-matrix interaction.

Suresha et al. [2] prepared the nano- CaCO_3 /epoxy composites for 1,3 and 5 wt.% particle content and according to that study, both stiffness and strength magnitudes of samples decreased under out of plane loading. Likewise, Yang et al. [24] investigated the cube-like CaCO_3 introduced epoxy composites and they found that 1.5 wt.% filler presence led to the maximum improvement in flexural properties. Eskizeybek et al. [25] integrated epoxy with 1, 2 and 3 wt.% nano- CaCO_3 powder and based on that research, 2 wt.% filler exhibited the maximum performance both in tensile and flexural loading.

3.4. Fractographic Analysis

The SEM images of CaCO_3 , neat epoxy and composites after flexural test are shown in Figure 5. The cubic morphology of CaCO_3 particles is apparently seen in Figure 5 (a) and it is also clear that those cubes in the photos show large size variations. The micron-size filler clusters form agglomerates and are present in the other figures as well. It is obvious that the 1.5 wt.% CaCO_3 loaded composite displayed rougher fracture surface than other composites (see Figures 5-c, 5-e and 5-g) that can be attributed to more energy absorption and relatively fine particle dispersion. Approximately 30% flexural strength improvement can be related with this situation occurred in the microstructure.

Additionally, pit formation is seen in the inset of Figure 5 (e) and this defect can be attributed to the detachment of filler from matrix material. As observed from the insets of Figure 5 (d), (f) and (h) that, the agglomerates thoroughly embedded in the microstructure, which points out an advanced bonding between epoxy and CaCO_3 . Despite this positive effect, filler concentration increase caused to the existence/increase of cluster

formation. In particular, non-homogeneous powder distribution was observed with the introduction of 3 wt.% and 5 wt.% CaCO_3 , which resulted in the reduction of stress transfer between matrix and reinforcement phase [17].

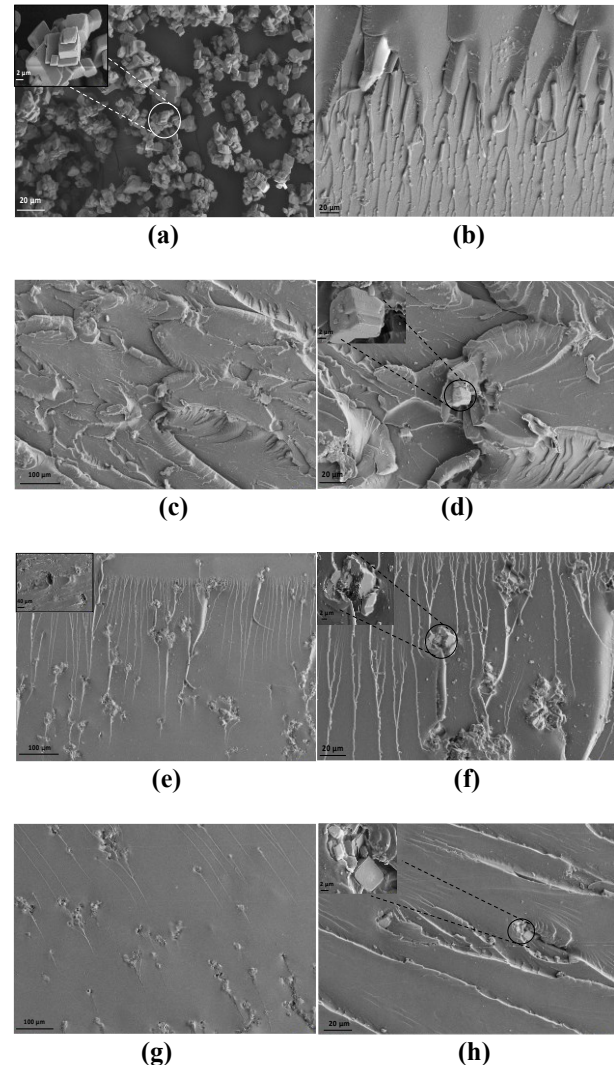


Figure 5. SEM images of a) neat CaCO_3 , b) neat epoxy, c) 1.5 CaCO_3 -epoxy composite (100 μm scale), d) 1.5 CaCO_3 -epoxy composite (20 μm scale), e) 3 CaCO_3 -epoxy composite (100 μm scale), f) 3 CaCO_3 -epoxy composite (20 μm scale), g) 5 CaCO_3 -epoxy composite (100 μm scale), h) 5 CaCO_3 -epoxy composite (20 μm scale).

4. Conclusions

In the context of the present study, cube shaped CaCO_3 particles with 1.5, 3 and 5 wt.% content was dispersed in epoxy medium. The samples fabricated with traditional casting technique were considered in terms of their thermo-mechanical and flexural responses via dynamic-mechanical analyzer (DMA) and three-point bending fixture, respectively. According to XRD

analysis, calcite was detected as the dominant phase in cubic CaCO_3 particles and the crystal size of powder was approximated between $5.7 \mu\text{m}$ to $6.5 \mu\text{m}$, which was also confirmed by SEM measurements. Based on DMA results, the 5 wt.% filler content provided the maximum values in terms of storage modulus (E') and glass transition (T_g) temperature. It was interestingly found that the 3 wt.% CaCO_3 presence resulted in the lowest loss modulus (E'') despite its improved E' and T_g values as compared with epoxy matrix. Flexural test results revealed that 1.5 wt. % CaCO_3 addition enhanced the strength parameter of about 30% while the modulus slightly decreased for the same concentration. The observations from SEM fracture images, it was concluded that, filler amount increase (for 3 wt. % and 5 wt. %) caused to the CaCO_3 agglomeration, which was evaluated as an indication for the reduced strength. To overcome that negative situation, it is planned to apply silane and/or oleic acid modification to filler in the second part of the study. With the introduction of a surface agent, hydrophilicity of calcite will probably decrease, which leads to better dispersity in the matrix.

Author's Contributions

S. Bahar Baştürk: Drafted and wrote the manuscript, performed, and interpreted the whole experiments and analysis.

Ethics

There are no ethical issues after the publication of this manuscript.

References

- [1]. Türkmen, İ, Köksal, N.S. 2013, Investigation of mechanical properties and impact strength depending on the number of fiber layers in glass fiber reinforced polyester matrix composite materials. *CBU Journal of Science*; 8(2): 17-30.
- [2]. Suresha, B, Varun, C.A, Indushekhara, N.M, Vishwanath, H.R, Venkatesh. 2019. Effect of Nano filler reinforcement on mechanical properties of epoxy composites. *IOP Conf. Series: Materials Science and Engineering*; 574, 012010.
- [3]. Ho, NM, Nguyen, TC, Tran, TTV, Nguyen, TD, Thai, H. 2021. Enhancement of dynamic mechanical properties and flame resistance of nanocomposites based on epoxy and nanosilica modified with KR-12 coupling agent. *Journal of Applied Polymer Science*; 138(29): 50685.
- [4]. Xian, Y, Kang, Z, Liang, X. 2021. Effect of nanodiamonds and multi-walled carbon nanotubes in thermoset hybrid fillers system: Rheology, dynamic mechanical analysis, and thermal stability. *Journal of Applied Polymer Science*; 138(21): 50496.
- [5]. Techawinyutham, L, Sumrith, N, Srisuk, R, Techawinyutham, W, Siengchin, S, Mavinkere Rangappa, S. 2021. Thermo-mechanical, rheological and morphology properties of polypropylene composites: Residual CaCO_3 as a sustainable by-product. *Polymer Composites*; 42(9): 4643.
- [6]. Poyraz, B, Eren, Ş, Subaşı, S. 2020. Filler type and particle distribution effect on compact properties of polymer composites. *CBU Journal of Science*; 17(1): 79-89.
- [7]. Kapusuz, D, Ercan, B. 2019. Calcium phosphate mineralization on calcium carbonate particle incorporated silk-fibroin composites. *CBU Journal of Science*; 15(3): 301-306.
- [8]. Tao, Y, Mao, Z, Yang, Z, Zhang, J. 2021. CaCO_3 as a new member of high solar-reflective filler on the cooling property in polymer composites, *Journal of Vinyl and Additive Technology*; 27(2): 275–287.
- [9]. Yao, J, Hu, H, Sun, Z, Wang, Y, Huang, H, Gao, L, Jiang, X, Wang, X, Xiong, C. 2021. Synchronously strengthen and toughen polypropylene using tartaric acid-modified nano- CaCO_3 . *Nanomaterials*; 11(10):2493.
- [10]. Azman, N.A.N, Islam, M.R, Parimalam, M. 2020. Mechanical, structural, thermal and morphological properties of epoxy composites filled with chicken eggshell and inorganic CaCO_3 particles. *Polymer Bulletin*; 77: 805–821.
- [11]. Kirboga, S, Öner, M, Deveci, S. 2021. Preparation and characterization of calcium carbonate reinforced poly(3-hydroxybutyrate-co-3-hydroxyvalerate) biocomposites. *Current Nanoscience*; 17(2): 266-278.
- [12]. De Moura A.P, Da Silva E.H, Dos Santos V.S. 2021. Structural and mechanical characterization of polyurethane- CaCO_3 composites synthesized at high calcium carbonate loading: An experimental and theoretical study. *Journal of Composite Materials*; doi:10.1177/0021998321996414.
- [13]. American Society for Testing and Materials, ASTM D790, 2004. Standard Test Methods for Flexural Properties of Unreinforced and Reinforced Plastics and Electrical Insulating Materials.
- [14]. Bokuniaeva, A.O, Vorokh, A.S. 2019. Estimation of particle size using the Debye equation and the Scherrer formula for polyphasic TiO_2 powder. *Journal of Physics: Conference Series*; 1410, 012057.
- [15]. Mallakpour, S, Khadem, E. 2017. Facile and cost-effective preparation of PVA/modified calcium carbonate nanocomposites via ultrasonic irradiation: Application in adsorption of heavy metal and oxygen permeation property. *Ultrasonics Sonochemistry*; 39: 430–438.
- [16]. Tran, H.V, Tran, L.D, Vu, H.D, Thai, H. 2010. Facile surface modification of nanoprecipitated calcium carbonate by adsorption of sodium stearate in aqueous solution. *Colloids and Surfaces A: Physicochemical and Engineering Aspects*; 366(1–3): 95–103.
- [17]. Menard, K.P. Dynamic Mechanical Analysis: A Practical Introduction, Second Edition (2nd ed.), CRC Press, 2008; pp 91.
- [18]. Panwar, V, Pal, K. Dynamic Mechanical Analysis of Clay-Polymer Nanocomposites. In *Clay-Polymer Nanocomposites*, 1st edn. Elsevier, New York, 2017, pp 413–441.
- [19]. Bashir, M.A. 2021. Use of Dynamic Mechanical Analysis (DMA) for Characterizing Interfacial Interactions in Filled Polymers. *Solids*; 2, 108-120.
- [20]. Fombuena, V, Bernardi, L, Fenollar, O, Boronat, T, Balart, R. 2014. Characterization of green composites from biobased epoxy matrices and bio-fillers derived from seashell wastes. *Materials and Design*; 57, 168–174.
- [21]. Miranda, T.B, Silva G.G. 2020. Hierarchical microstructure of nanoparticles of calcium carbonate/epoxy composites: thermomechanical and surface properties. *Express Polymer Letters*; 14:179–191.

- [22]. Baskaran, R, Sarojadevi, M, Vijayakumar, C.T. 2011. Mechanical and thermal properties of unsaturated polyester/calcium carbonate nanocomposites. *Journal of Reinforced Plastics and Composites*; 30(18):1549-1556.
- [23]. Mat Yazik, M.H, Sultan, M.T.H, Jawaid, M, Abu Talib, A.R, Mazlan, N, Md Shah, A.U, Safri, S.N.A. 2021. Effect of nanofiller content on dynamic mechanical and thermal properties of multi-walled carbon nanotube and montmorillonite nanoclay filler hybrid shape memory epoxy composites. *Polymers*; 13, 700.
- [24]. Yang, G, Heo, Y.-J, Park, S.-J. 2019. Effect of morphology of calcium carbonate on toughness behavior and thermal stability of epoxy-based composites. *Processes*; 7, 178.
- [25]. Eskizeybek, V, Ulus, H, Kaybal, H. B, Şahin, Ö. S, Avcı, A. 2018. Static and dynamic mechanical responses of CaCO₃ nanoparticle modified epoxy/carbon fiber nanocomposites. *Composites Part B: Engineering*; 140, 223–231.



Adventitious and Normal Respiratory Sound Analysis with Machine Learning Methods

Burcu Acar Demirci^{1*} , Yücel Koçyiğit² , Deniz Kızıllırmak³ , Yavuz Havlucu⁴ 

^{1,2} Manisa Celal Bayar University, Electrical and Electronics Engineering Department, Manisa, Türkiye

^{3,4} Manisa Celal Bayar University, Hafsa Sultan Hospital, Chest Disease Department, Manisa, Türkiye

* burcu.acar@cbu.edu.tr

* Orcid No: 0000-0002-7328-1267

Received: 1 October 2021

Accepted: 27 May 2022

DOI: 10.18466/cbayarfbe.1002917

Abstract

Computerized respiratory sound analysis systems provide vital information regarding the current condition of the lung. These systems, used by physicians for the diagnosis of various respiratory diseases, help to classify respiratory sounds. Since physicians have differing degrees of knowledge and experience, this can cause differences in diagnosis and therefore treatment. Well-calibrated machine learning tools can help physicians make more informed decisions. For this purpose, different machine learning classifiers and feature extraction models have been developed to classify respiratory sounds from healthy individuals and patients. In this study, the combinations of Empirical Mode Decomposition, Mel Frequency Cepstral Coefficients, and Wavelet Transform methods are used for feature extraction, and k -Nearest Neighbor, Artificial Neural Networks, and Support Vector Machines are used for classification. The highest accuracy has been achieved as 98.8% when Mel Frequency Cepstral Coefficient and k -Nearest Neighbor methods are used in combination.

Keywords: Respiratory sound, mel-frequency cepstral coefficient, empirical mode decomposition, k nearest neighborhood method.

1. Introduction

Respiratory diseases cause millions of premature deaths in the world [1]. Therefore, early detection of respiratory diseases is a crucial medical research area. Computed Tomography (CT), pulmonary function test, chest x-rays, and lung auscultation are effective methods for diagnosing respiratory diseases [2]. Auscultation is the most commonly used method for the capturing the sounds that occur in the internal organs such as circulatory and respiratory systems, examining the current status of systems, and diagnosing diseases of these systems. Pulmonary auscultation, a commonly used method for capturing the sounds that occur in the internal organs, is the most straightforward and cheapest method used in the diagnosis of respiratory diseases [3]. The method, carried out through classical stethoscopes, provides critical information to physicians to diagnose respiratory diseases. Despite these properties, it has many limitations. It is a subjective process that depends on the physician's hearing ability, experience, and skill to distinguish between various sound patterns [2].

Another limitation of the method is that classical stethoscopes have a frequency response that reduces frequency components of lung sound signals above 120 Hz and that the human auditory system is not sensitive to the remaining low-frequency band. In recent years, Computerized Respiratory Sound Analysis systems (CORSA) have been used to overcome these limitations, and classical stethoscopes have been replaced by electronic stethoscopes that reduce noise, increase the volume and allow recording. Electronic stethoscope auscultation devices have evolved from analog to digital, and it has enabled storage, analysis, and visualization in computer systems. Nevertheless, digital auscultation is not yet a mature and complete computational procedure [4].

Many studies aim to leverage digital auscultation from the point of data and algorithms. The sounds recorded in the memory of the stethoscope are analyzed with CORSA systems. The availability of CORSA systems has led to increased research in the field of lung sounds. Adventitious respiratory sounds associated with specific

disease were compared with normal respiratory sounds in many studies [5-13]. For example, Corbera *et al.* [5] focused on wheeze respiratory sound because of widespread asthma and aimed to detect significant differences between wheeze and healthy sounds. In this regard, the study focused on identifying wheezing attacks from spectrograms by applying the temporal and spectral continuity criteria to the previously detected peaks. Sezgin *et al.* [6] used two types of respiratory sounds: normal and patient. In this study, the decision process comprises three stages: the normalization process, the feature extraction process, and the classification process. In the feature extraction process, the features are determined with wavelet analysis; afterward, the optimum features are selected by dynamic programming. The classification process was made with Artificial Neural Networks (ANN). Maruf *et al.* [7] have developed CORSA systems consisting of four modules to detect crackle sounds automatically. A 100-2500 Hz bandpass filter was applied to respiratory sounds in the pre-processing module and in the feature extraction module preferred Wavelet Transform (WT). They identified the best four features in the feature selection module and classified them using Gaussian Mixture Model (GMM), Support Vector Machines (SVM) and ANN methods in the classification module. Lozano *et al.* [8] have suggested a different method for automatically diagnosing normal and wheezing sounds. Empirical mode decomposition-based methods have been used in the study. The proposed methods have eliminated the mode mixing problem of the Empirical Mode Decomposition (EMD) method and have offered high energy concentrations, high time, and high-frequency resolutions. The tests applied showed that the proposed Ensemble Empirical Mode Decomposition-Kay based Hilbert spectrum better results in wheezing sound detection.

The success of cepstral features in respiratory sound classification has inspired many studies [9], [10-12]. Palaniappan *et al.* [9] have used parenchymal pathology, obstructive pathology, and normal respiratory sounds. The Mel-Frequency Cepstral Coefficient (MFCC) method, a highly efficient feature extraction algorithm used in the processing of audio signals, was used in this study. The 13 cepstral coefficients obtained by MFCC have been classified using the k-Nearest Neighbors Algorithm (k-NN) and SVM. Sengupta *et al.* [10] suggested a new set of cepstral features to classify normal, wheeze, and crackle sounds by considering the achievement of cepstral features in the classification of speech sounds.

Liu *et al.* [11] have proposed examining the normal, wheeze, and crackle respiratory sounds in time, frequency, and cepstral domains. They extracted 46 features, and 6 crucial features were selected from the obtained features. GMM to classify these three respiratory sounds is proposed. Sunil and Ganesan [12]

have proposed an efficient method to classify normal and abnormal respiratory sounds. These sounds are analyzed by the MFCC and classified by the Adaptive Neuro-Fuzzy Inference System. Haider *et al.* [13] have suggested using auscultation and pulmonary function tests together in the study. A total of 39 features of respiratory sounds and 3 spirometry features were used. Various parametric and nonparametric tests have been conducted to determine the similarity level of the extracted features. Logistic Regression (LR), Decision Tree (DT), Discriminant Analysis (DA), SVM and k-NN have been used to classify normal and Chronic Obstructive Pulmonary Disease (COPD) respiratory sounds.

This study aims to diagnose normal and abnormal respiratory sounds similar to abovementioned studies. However, we used methods such as Empirical Mode Decomposition, and combined it with established classification methods to potentially identify the most accurate method. The success of the proposed method has been compared to frequency analysis and cepstral analysis. The cepstral and frequency analyses have been done by using MFCC and WT methods, respectively. Comparing the performances of different classifiers on the problem of classification of respiratory sounds in the literature is a common practice. It is also compared in classifiers such as ANN, k-NN, and SVM within this study's scope. The rest of the article's organization is as follows: Section 2 briefly describes the material and methods used in our study. It involves Respiratory Sound Acquisition, Preprocessing, Feature Extraction, and Classification Methods. Results and Discussion are presented in Section 3, and the Conclusions are presented in Section 4.

2. Materials and Methods

The rate, time, and sounds of respiratory are essential in diagnosing respiratory system diseases. Inspiration and expiration stages of respiratory sounds contain important information about the respiratory system. CORSA systems provide a new perspective on the detection and treatment of many diseases. Generally, the systems consist of two steps. Firstly, the crucial features of respiratory sounds are extracted. Secondly, these crucial features are used for detecting or classifying adventitious respiratory sounds [14]. Commonly preferred methods for feature extraction in the literature are MFCCs [9], spectral features [15], Fourier [16], The Autoregressive Model [17], and Wavelet coefficients [18]. For classification, algorithms such as ANN [19], SVM [20], GMM [11], k-NN [9], and LR models [13] are used. Figure 1 shows the block diagram for all system stages recommended in this study. The system is divided into four stages: the acquisition of respiratory sound, pre-processing, feature extraction, and classification.

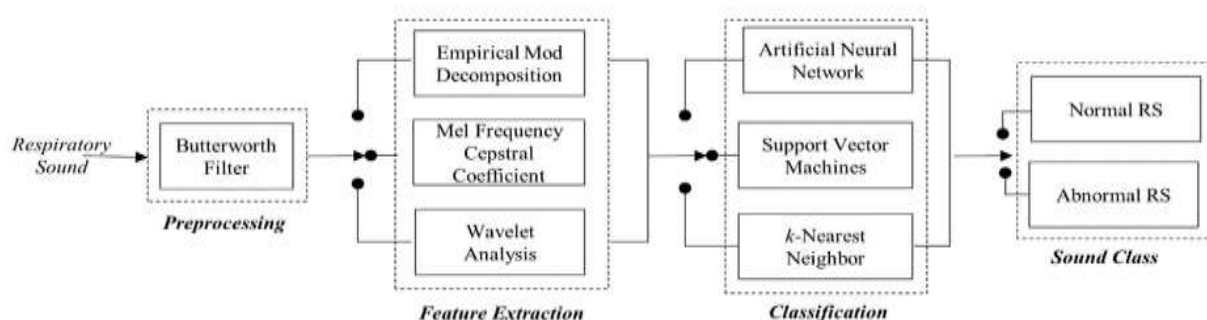


Figure 1. Block Diagram of the recommended system.

2.1 Respiratory sound acquisition

During the inspiration and expiration stage of respiration, vibrations occur as a result of rapid changes in gas pressure in the airways. Respiratory sounds occur when the vibrations pass through the lung tissue and reach the chest wall. Changes in vibration create sounds with a certain amplitude and frequency [21]. Respiratory sounds are divided into normal and adventitious (abnormal). Normal respiratory sounds are those are heard when there is no pathological airflow in the airways. Adventitious respiratory sounds are caused by pathological effects in the lungs or respiratory tract. A data set consisting of wheeze and rhonchi adventitious sounds and normal sounds was used in this study. The normal lung sounds are both louder and larger amplitude sounds during the inspiration stage than during the expiration stage. The signal frequency band of the sounds is between 150-1000 Hz [22]. Wheeze and rhonchus sounds are determined airway obstruction pathology. They are common signs of obstructive lung diseases like asthma or COPD. Wheeze respiratory sounds are musical, continuous, and coarse sounds commonly heard during the expiration stage as a result of high-speed airflow through narrowed airways [18]. Some parts of the respiratory tree must be narrowed or obstructed for the wheezing adventitious sound to occur. [23]. Rhonchus respiratory sounds are low-pitched and continuous sounds that result from obstruction or secretions in larger airways heard during the inspiration and expiration stage. According to the American Thoracic Society (ATS), wheezes have a dominant frequency of 400 Hz or more, while rhonchus has a dominant frequency of about 200 Hz or less, and the event is longer than 250 ms [1].

In this study, the Respiratory Sounds (RS) were recorded by specialist physicians in the Hafsa Sultan Hospital, Manisa Celal Bayar University. All records were obtained using Littmann 3200 Electronic stethoscope from 25 healthy and 25 patient volunteers treated in the clinic of respiratory medicine of the hospital. The study population was picked among the patients who have different demographic attributes and

lack previous comorbidities of the study population. Normal respiratory sounds were recorded by selecting 7 female and 18 male volunteers among volunteers who had never smoked or used tobacco products. Wheeze respiratory sounds were recorded from 12 volunteers, 4 females and 8 males, with asthma or COPD. Rhonchus breath sounds were recorded from 13 volunteers, 7 females and 6 males, with Pneumonia and Chronic bronchitis. Each volunteer was asked to breathe in and out of the mouth four times, and the recording was made to include four full breaths. Thus, 100 normal, 52 rhonchus, and 48 wheeze RS were obtained. All sounds sampled at a frequency of 11025 Hz were recorded by the auscultation protocol determined by specialist physicians. According to this protocol, sounds were recorded in a calm environment, with the patient sitting and loosening his/her posture muscles. The records are obtained from the most appropriate places for the maximum collection of data about patients' pathologies, as determined by the CORSA standard [24].

100 abnormal and 100 normal respiratory sounds were used in the study. The Hotelling T-squared statistical method [25] was used to evaluate the adequacy of the data numbers. Hotelling's T-squared statistical method is used to determine whether there is a significant difference between the two groups for multivariate samples. The F distribution can be a good approximation of the T-squared statistic distribution when the dimension of the data is less than the size of the samples. As shown in the table, the results of Hotelling's T-squared statistics revealed a significant difference in all coefficients for normal and abnormal respiratory sounds

Table 1. Hotelling's T- squared Test For Normal and Abnormal Respiratory Sounds.

	T^2	F	p Value
MFCC	551.779	F(78,121)=7.878	0.0000000000
EMD	141.140	F(30,169)=4.016	0.0000000038
WT	118.729	F(30,169)=3.378	0.0000002985

2.2 Pre-processing

Pre-processing aims to reduce background noise and improve the quality of recorded respiratory sounds [7]. When respiratory sounds are recorded, they are affected by low-frequency sounds such as muscles and heart sounds and high-frequency noises due to sudden movements. To avoid these effects, pre-filtering should be performed considering the dominant frequency range of the respiratory sounds. Various filters such as Butterworth, Chebyshev, and Elliptical filters of varying degrees have been tested for the study. The accuracy and success of the filtering have been inspected by experts listening to the recorded respiratory sounds, and the filter has been selected. In this study, are used a fourth-order bandpass Butterworth filter. The frequency range of this filter is 100-1800 Hz [26].

2.3 Feature extraction

The feature extraction process enables converting high-dimensional vectors to lower-dimensional vectors [16]. The properties of signals formed after pre-processing the respiratory sounds are analyzed simultaneously in the time, frequency, or time-frequency domain by feature extraction methods. In this study, some feature extraction methods such as EMD, MFCC, and WT are used. The coefficients of respiratory sounds are determined by using these methods. The coefficients obtained by feature extraction methods are not used directly. The feature vectors constructed with statistical parameters such as the standard deviation, variance, mean power, entropy, mode, and energy values of the coefficients are used instead of the coefficients. The novelty of the paper is the combination of the EMD method and statistical analysis methods for feature extraction.

2.3.1. Empirical mode decomposition

Many biomedical signals such as EEG signals, EMG signals, and respiratory sounds have a nonlinear and non-stationary structure. Wigner-Ville Transform, Short Time Fourier Transform, and WT are widely used to analyze these types of signals. New methods are being investigated due to different restrictions on each. EMD has been proposed as an alternative and appropriate tool for analyzing multicomponent nonlinear and non-stationary signals [27]. EMD is an adaptive and direct decomposition method. Unlike Fourier and WT analysis, it is unnecessary to have prior knowledge of the signal properties to select parameters in this analysis [20]. EMD allows the target signal is separated into Intrinsic Mode Functions (IMFs) listed from the high-frequency components to low-frequency components [28]. A sifting process based on the estimated upper and lower envelopes of the input signals is used to obtain the IMF. There are two conditions for the statements obtained as a result of the sifting process to

be IMF. First, the number of extrema and zero-crossings must be equal or differ by one at most in the whole data set. Second, the upper and lower envelopes' local average should be zero at any point [29].

The IMF components of $x(t)$ signal is obtained by the following algorithm: [28, 30]

1. Find the local minima and local maxima of $x(t)$
2. The maximum envelope $e_{\max}(t)$ is calculated using local maxima points with cubic spline interpolation. Similarly, minimum envelop $e_{\min}(t)$ is calculated using local minima.
3. The local average envelope is found by taking the average of the maximum and minimum envelope:

$$m_1(t) = [e_{\min}(t) + e_{\max}(t)]/2 \quad (1)$$

4. The local average envelope is removed from the original signal:

$$h_1(t) = x(t) - m_1(t) \quad (2)$$

5. Whether $h_1(t)$ to become an IMF is checked. If the conditions are met, it is considered $IMF_1(t) = h_1(t)$. If $h_1(t)$ is not an IMF, $h_1(t)$ is considered a new signal. The loop is repeated using $h_1(t)$ to create $h_2(t)$. If $h_2(t)$ is not an IMF, the stop criterion is calculated to end the elimination process. The formula for the stop criterion, SD, is set out below.

$$SD(i) = \sum_{t=0}^N \frac{|h_{i-1}(t) - h_i(t)|^2}{h_{i-1}^2(t)} \quad (3)$$

If $h_2(t)$ meets SD, $IMF_1(t) = h_2(t)$. If it does not meet the stop criteria, $h_2(t)$ is treated as a new signal. During steps 1-6, its operations on $h_2(t)$ are repeated to form $h_i(t)$ until $h_i(t)$ meets the requirements of the IMF or SD. It is calculated $IMF_1(t) = h_i(t)$.

6. $IMF_1(t)$ is formed. By subtracting $IMF_1(t)$ from $x(t)$ signal, a residual signal $r_1(t)$ is obtained. To find the next residual signal, $r_1(t)$ is considered the original signal, and steps 1-6 are repeated. When the process is completed, the original signal is composed of several IMF components and residual $r_n(t)$. And is expressed as follows;

$$x(t) = \sum_{i=1}^n IMF_i(t) + r_n(t) \quad (4)$$

IMF coefficients vary according to the state and frequency distribution of respiratory sounds. In the study, it has been observed that the amplitude of the IMF coefficients at Level 5 and beyond is very low and it has been determined that it contains redundant information. For this reason, 4 IMF coefficients are used. IMF coefficients of respiratory sounds obtained by the EMD method are given in Figure 2, Figure 3, and Figure 4.

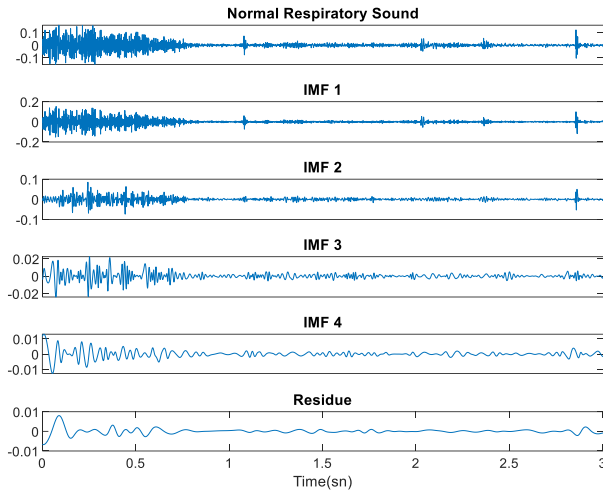


Figure 2. First 4 IMF coefficients and residue signal for Normal RS.

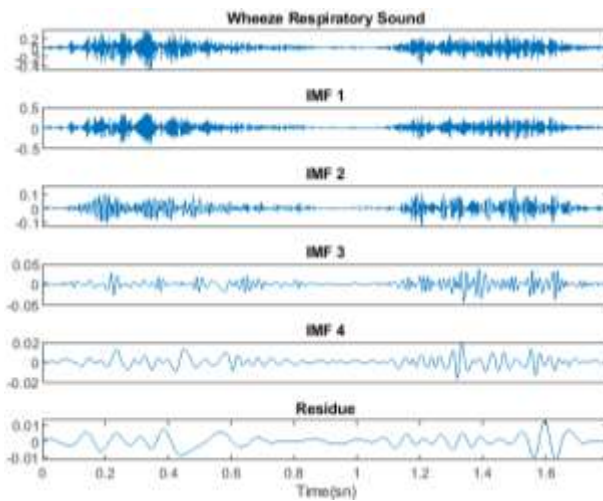


Figure 3. First 4 IMF coefficients and residue signal for Wheeze RS.

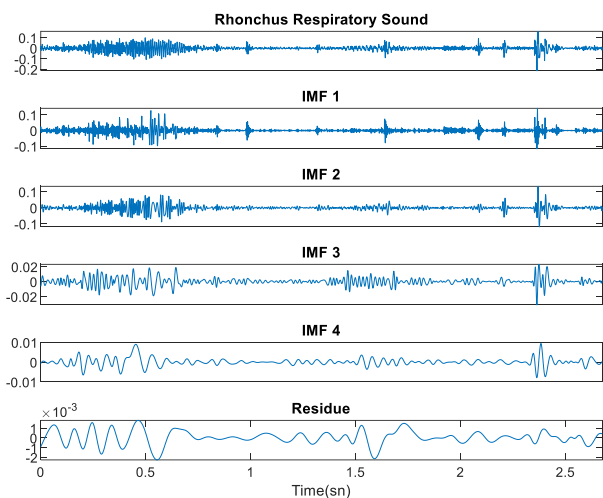


Figure 4. First 4 IMF coefficients and residue signal for Rhonchus RS.

2.3.2 Mel-frequency cepstral coefficient

MFCC is a highly effective feature extraction algorithm commonly used for automatic speech and speaker recognition [12]. This is because MFCC can distinguish speakers with high accuracy by imitating the frequency selectivity of the human ear. In addition, MFCCs are often preferred because they are much less affected by changes and sound wave structure.

In recent years, the MFCC method has been used in CORSA systems in many studies, and promising results have been obtained [31, 32]. The MFCC performs a nonlinear scaling, assuming that the audio signal's low-frequency components carry more critical information than the high-frequency components. MFCC analysis is similar to cepstral analysis, apart from frequency wrapping. In MFCC analysis, the frequency is wrapped according to the Mel-Scale [31]. There are several methods in the literature for calculating MFCC. Fast Fourier Transform (FFT) based method is one of the most commonly used methods among them. The block diagram of this method used to calculate the MFCC features is shown in Figure 5.

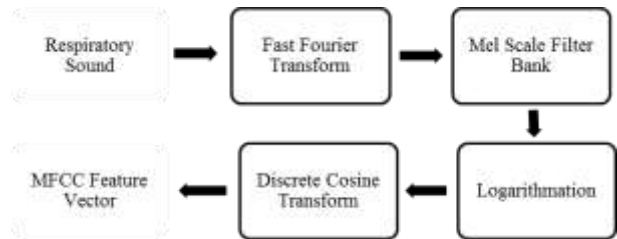


Figure 5. Block diagram used to calculate MFCC Features Vector.

In this method, firstly, FFT is applied to the windowed signal. A triangle bandpass filter bank known as a Mel-scale filter bank is applied to the obtained FFT spectrum. The Mel-Scale, designed based on the human hearing system, is based on mapping the actual frequency and the perceived pitch. This scale consists of linear ranges up to 1 kHz and logarithmic ranges after 1 kHz. The mapping of linear frequency to Mel-frequency is done by applying equation (5).

$$f_{\text{mel}} = 2595 * \log \left(1 + \frac{f_{\text{linear}}}{700} \right) \quad (5)$$

A logarithm process is applied to the signal filtered using a Mel-Scale filter bank. With this process, the sensitivity of the feature vectors to changes is reduced. Discrete cosine transform is applied to the logarithmic scale applied signal finally, and the signal is converted back to the time domain. Discrete cosine transform is applied to the logarithmic scale applied signal finally, and the signal is converted back to the time domain. Thus, MFCCs with the amplitude of the spectrum are obtained. In this study, 13 MFCCs are used to classify RS. The obtained results are presented in Figure 6, Figure 7, and Figure 8.

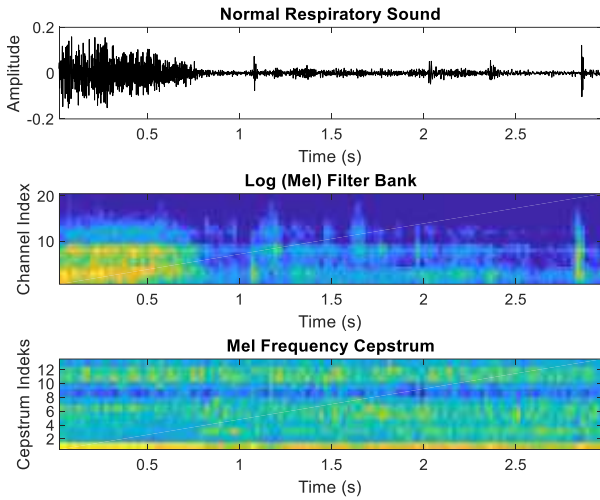


Figure 6. MFCCs of Normal RS.

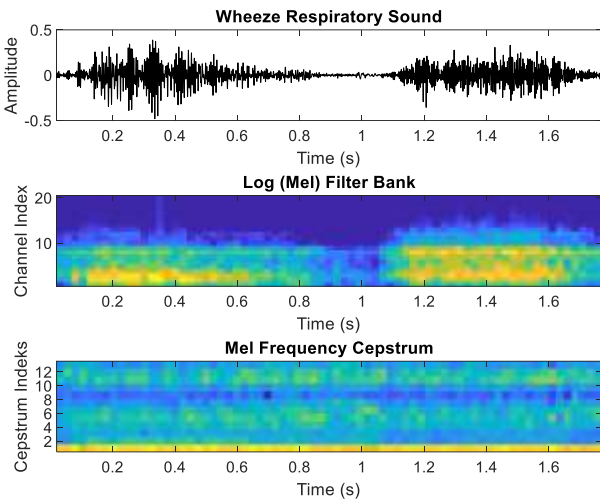


Figure 7. MFCCs of Wheeze RS.

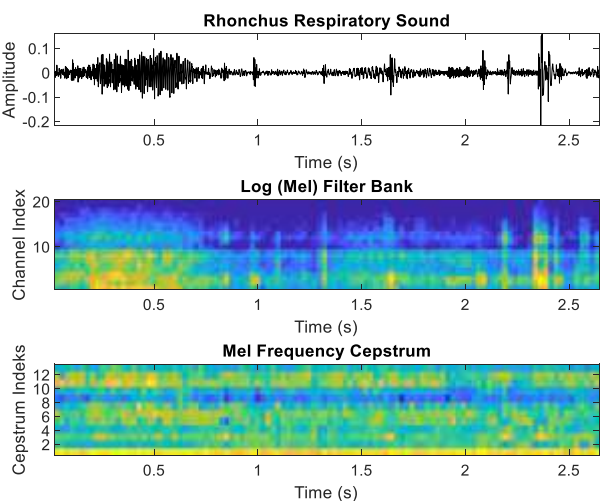


Figure 8. MFCCs of Rhonchus RS.

2.3.3 Wavelet transform

WT is a signal processing method used as an alternative to Fourier Transform (FT) [33]. FT is an analysis

method used to analyze stationary signals defined in the time domain, providing frequency information by examining the signal in the frequency domain. However, only frequency analysis is not sufficient for dynamic and non-periodic signals. WT is a commonly used method for non-stationary, nonlinear, and non-periodic signal analysis, such as lung sounds. With WT, the signal is defined in both the time domain and frequency domain, thus providing information on how the signal's frequency components vary with time. WT uses short window size when high-frequency information is essential, while long window size uses when low-frequency information is important [34].

In Discrete Wavelet Transform (DWT), the signal is separated into sub bands by passing through the high-pass filter (h) and low-pass filters (g) according to the determined level. Equation conditions that these filters must meet are as follows; [35]

$$G(z)G(z^{-1}) + G(-z)G(-z^{-1}) = 1 \quad (6)$$

$$H(z) = zG(-z^{-1}) \quad (7)$$

A sequence of filters with increasing length (indexed by i) can be obtained;

$$G_{i+1}(z) = G(z^{2^i})G_i(z) \quad (8)$$

$$H_{i+1}(z) = H(z^{2^i})G_i(z) \quad i=0, 1, \dots, i-1 \quad (9)$$

With the initial condition $G_0(z) = 1$. It is expressed as a two-scale relation in the time domain

$$g_{i+1}(k) = [g]_{\uparrow 2^i} g_i(k), h_{i+1}(k) = [h]_{\uparrow 2^i} g_i(k) \quad (10)$$

where the subscript $[\cdot]_{\uparrow m}$ indicates the up-sampling by a factor of m and k is the equally sampled discrete-time. The normalized wavelet and scale basis functions $\varphi_{i,l}(k)$, $\psi_{i,l}(k)$ can be defined as

$$\varphi_{i,l}(k) = 2^{\frac{i}{2}} g_i(k - 2^i l) \quad (11)$$

$$\psi_{i,l}(k) = 2^{\frac{i}{2}} h_i(k - 2^i l) \quad (12)$$

where the factor $2^{i/2}$ = inner product normalization, i = scale parameter and l = the translation parameter. The DWT decomposition can be described as

$$a_i(l) = x(k) * \varphi_{i,l}(k) \quad (13)$$

$$d_i(l) = x(k) * \psi_{i,l}(k) \quad (14)$$

a_i is approximation coefficient and d_i is detail coefficient. The approximation coefficients represent the lower frequency band, and the detail coefficients represent the higher frequency band.

These coefficients are used for the classification process in many signal processing applications. In the analysis of signals using DWT, the selection of the appropriate main wavelet function and the determination of the appropriate decomposition level are very important. The main wavelet function, which is one of the most important parameters of the wavelet transform, takes on the task of the window function in the Fourier transform. There are many main wavelet functions with different properties and uses. In previous studies on the application of DWT in respiratory sound analysis, Daubechies 8 (db8) main wavelet function was used and found to give good results. Therefore, db8 is also preferred in this study [18]. Another important parameter is the number of decomposition levels, determined according to the dominant frequency components of the signal. In the study, the number of decomposition levels is chosen to be 7. Thus, respiratory sounds are decomposed into detail coefficients D1-D7 and approximation coefficient A7. Since the frequency range of D3-D7 sub-bands carries important information, these sub-bands are preferred.

2.4 Classification

In CORSA systems, the classification stage comes after the feature extraction stage. For classification, are used k -NN, SVM, and ANN in this study. SVM and ANN classifiers have two stages training and testing. During the training stage, data from each RS class is introduced to the system as training data, and the system makes a distinction by class. Unknown sounds are analyzed during the test stage, and the most appropriate class is selected [19].

In the kNN classifier, which is instance-based learning, no training phase is required [36]. Samples divide into training and test samples. Training samples are multidimensional vectors, each with a class label. In the classification phase, unlabeled test vectors are labeled by taking into account the closest k training examples.

In classifier algorithms, the effects of model parameters on performance and the effects of these parameters on classifier capacity and complexity were observed, and the most suitable model parameters were determined. The parameters selected for each method are given in the relevant section. The classification performance of a classifier in medical tests depends on the ability to detect patients and healthy people. In this study, standard parameters such as sensitivity, specificity, and accuracy were used for performance evaluation. Sensitivity is the ratio of the number of correctly classified patients to the total number of patients, while specificity is the ratio of correctly classified healthy people to the total number of healthy people. Accuracy is the ratio of the number of sick and healthy people correctly classified to the total number of people [19].

2.4.1 Support Vector Machines

SVM method, based on statistical learning theory, was developed by Vladimir Vapnik in 1992. SVM, a supervised learning algorithm, is used to solve classification, regression analysis, and nonlinear function approach problems [37]. Provides high classification and high generalization performance in solving bioinformatics problems, text, voice, object, and image recognition problems [38].

SVM applies a useful learning algorithm to identify difficult-to-analyze patterns in complex data sets. In SVM, the objective is to create an n -dimensional hyperplane that optimally divides the data into different classes. It is also used to obtain the optimal limit of two data sets on a vector space, independent of the probability distributions of training vectors in sets. Like artificial neural networks, SVM models have a two-layer, feed-forward network structure that uses a sigmoid kernel function. Some of the commonly used kernel functions are RBF, linear, quadratic, and polynomial kernel. In this paper, second-order polynomial kernel functions are used.

2.4.2 k Nearest Neighbors Algorithm

k -NN is a supervised and nonparametric classification method that classifies data based on the proximity of training samples in the data set. This classification method finds the k nearest neighbors of unknown data between the dataset according to a distance equation. Then, it uses the majority vote approach to estimate the data label [39]. Distance equations such as Manhattan, Hamming, Euclidean, and Minkowski are used for distance calculation. In this study, the Euclidean distance equation was used to locate the nearest neighbor.

The basic steps to be applied for classification with the k -NN algorithm are as follows:

1. The number k is determined.
2. The new data is evaluated individually with all the data in the training data set, and the distances between them are calculated by distance functions.
3. The k data closest to the new data is selected.
4. The class to which most of the selected data belongs is determined, and the new data is assigned to this class.

In this study, the results were obtained for $k=1$ and $k=3$.

2.4.3 Artificial Neural Network

ANN is a topological structure created for a specific purpose inspired by the neuron functioning of the brain. The structure consisting of interconnected artificial neurons is widely used in various recognition,

prediction, and modeling fields, as well as the recognition and classification of biological signals. In ANN, learning is carried out with special training algorithms that imitate the learning mechanisms of biological systems [35].

In this study, various model trials were conducted while determining the ANN classifier model. In models with three hidden layers, the excess number of layers and the number of neurons in the layers increases the processing and learning ability of the artificial neural network but reduces the generalization ability of the network and causes overfitting. In models with a single hidden layer, the pattern in the data cannot be learned sufficiently and underfitting occurs. For this reason, a model with two hidden layers is preferred. Tests were made for the number of neurons in the network (45:45), (45:30), (30:15), (15:15) and (10:10). The most successful result (15:15) was obtained with the number of neurons and the hyperbolic tangent activation function. Backpropagation (BP) algorithm, which is the most frequently used training algorithm for multilayer feedforward networks, and Mean Error Squares the most frequently used performance function, are also preferred in this study. Levenberg–Marquardt learning algorithm, which creates a balanced system structure in the network structure and reduces the processing load, is preferred.

3. Results and Discussion

In this study, while classifying with the ANN method, 80% of the data was used for training and 20% for testing. While using SVM and k -NN methods for classification, training and test groups were determined by applying 10 cross-validations to the data. Besides, we have iterated the whole classification method 10 times, and average performance values have been calculated.

The sensitivity, specificity, and accuracy parameters obtained with the proposed system are recorded in Tables 2, 3, and 4. Table 2 includes a comparison of MFCC-based features, Table 3 EMD-based features, and Table 4 WT-based features with different classifiers. Each classifier has its advantages and disadvantages. The k -NN algorithm has advantages such as no training required, being easy to perform, being analytically tractable, adaptable to local information, and resistant to noisy training data. There are also disadvantages, such as the need for a high amount of memory space, and the processing load and cost increase significantly as the data set and attribute size increase [40]. This method is crucial to selecting the k value from the optimal value; as the k value decreases, more sensitive results were obtained. The major advantages of ANN over traditional statistical

techniques are that it requires fewer assumptions and can model nonlinear relationships depending on the choice of activation functions. Neural network models can learn to complex nonlinear relationships between independent and dependent variables, and they can make logical decisions in the face of similar events. The information is stored throughout the network, and some of the artificial nerve cells do not function, causing the loss of information. However, it has disadvantages, such as requiring excess computational overhead and having limited ability to identify possible causal relationships. Using trial and error in determining parameters such as the selection of activation function, the number of hidden layers, and neurons is one of the most significant disadvantages [41]. SVM models provide good scaling for high-dimensional data and can be used for both linear and nonlinear applications similar to artificial neural networks. Also, there is less risk of overfitting. But choosing the appropriate kernel function is not straightforward [42].

This study used ANN and SVM classifier models, determining the optimum selection of system parameters by trial-and-error methods creates a disadvantage. Furthermore, the fact that the data size is not too big and no training is required has provided an advantage for k -NN. The highest accuracy rate obtained using the MFCC and WT features were respectively 98.8% and 82.7% with the k -NN classifier. The highest accuracy rate achieved using the EMD features is 88.9% with the ANN classifier. Additionally, we observed that MFCCs provide the best results among all the feature extraction methods examined. MFCC analysis has been more successful in evaluating respiratory sounds because it is closer to the response of the human auditory system. MFCC can distinguish speakers with high accuracy by imitating the frequency selectivity of the human ear. The auditory perception-specific information captured by MFCCs reveals differences in respiratory sounds, and the use of these differences for diagnostic purposes has increased success. Providing a more successful analysis than FT and WT, the EMD method has been proven to have a mode mixing effect when applied to some respiratory sounds, as noted in earlier studies [20]. The mode mixing effect causes some frequency components of abnormal RS to occur in different IMFs, which has a negative effect on the success of the method.

The lack of large databases publicly available to develop algorithms and compare results is one of the field's most significant problems [4]. It is quite difficult to compare the performance of the studies due to different classifier models, different respiratory sounds classified, and different feature vectors used in the classification. Table 5 shows the results of the standard parameters of various studies in this field.

Table 2. Classification Result of MFCC Features.

<i>Classifier</i>	MFCC Features		
	<i>Sensitivity</i>	<i>Specificity</i>	<i>Accuracy</i>
<i>ANN</i>	100	97 ± 3.3	98.7 ± 1.6
<i>SVM</i>	97.7 ± 1.1	93.3 ± 1.1	95.7 ± 0.9
<i>k-NN (k=3)</i>	99.8 ± 0.6	93 ± 0.8	96.3 ± 0.6
<i>k-NN (k=1)</i>	99.5 ± 0.9	97.5 ± 0.8	98.8 ± 0.6

Table 3. Classification Result of EMD Features.

<i>Classifier</i>	EMD Features		
	<i>Sensitivity</i>	<i>Specificity</i>	<i>Accuracy</i>
<i>ANN</i>	93.5 ± 3.9	84 ± 6.3	88.9 ± 3.2
<i>SVM</i>	78.2 ± 2.1	77.1 ± 1.8	77.9 ± 1.6
<i>k-NN (k=3)</i>	81 ± 1.4	76.7 ± 1.8	79.1 ± 1.6
<i>k-NN (k=1)</i>	77.8 ± 1.8	74.3 ± 0.9	76.3 ± 1.2

Table 4. Classification Result of Wavelet Features.

<i>Classifier</i>	WAVELET Features		
	<i>Sensitivity</i>	<i>Specificity</i>	<i>Accuracy</i>
<i>ANN</i>	83 ± 7.4	74.5 ± 5.2	79 ± 3.7
<i>SVM</i>	77.9 ± 1.2	76.3 ± 1.6	77.3 ± 1.3
<i>k-NN (k=3)</i>	82.1 ± 1.5	80.5 ± 1.9	81.6 ± 1.6
<i>k-NN (k=1)</i>	83.2 ± 1	82 ± 1.2	82.7 ± 0.9

4. Conclusion

The CORSA systems provide vital information about the current state of the lung. The proposed system diagnoses the disease by separating the respiratory sounds as normal and abnormal. While EMD, MFCC, and WT feature extraction methods are used for disease diagnosis, ANN, SVM, and k-NN classifiers are used for classification. Since respiratory sounds are not stationary and linear, classical frequency analysis methods are not adequate in the analysis of these sounds. For extraction of good acoustic characteristics from respiratory sounds, it is required to examine these sounds over sufficiently short periods of time. WT and MFCC methods are preferred in this study because of enabling short-time analysis. MFCC is a representation of the short-time power spectrum of the sound signal. Signal cepstrum is obtained by inverse transforming of the logarithm of the signal spectral representation. The frequency bands in mel-frequency cepstral representation of the power cepstrum are equally spaced on the mel-scale approximating the human auditory perception.

EMD analyses are non-linear and non-stationary data without the assumption of linearity or short-time stationarity. EMD process does not involve a fixed basis but rather has a signal-specific approach to decompose the signal. The application of the EMD method for respiratory sounds is a quite new method. In the previous studies, IMF coefficients are obtained by using only the inspiration stage of respiration. In this study, both inspiration and expiration stages of respiration are used to obtain IMF coefficients. It is aimed to compare the EMD method with traditional feature extraction methods for respiratory sounds. In order to evaluate the performance of the coefficients obtained by different feature extraction methods, classification has been made with the statistical parameters. EMD method gives more successful results than the WT method. EMD provides lower success compared to the MFCC method because the MFCC analysis is more successful in assessing respiratory sounds as it is closer to the response of the human auditory system.

This comparative study shows that MFCC features are more successful in diagnosing respiratory sounds compared to the other features. The highest accuracy rate is obtained for the k-NN classifier with 98.8%.

Author's Contributions

Burcu Acar Demirci: Methodology, Software, Validation, Formal analysis, Data Curation, Writing-Original Draft, Visualization

Yücel Koçyiğit: Conceptualization, Funding acquisition, Writing-Review&Editing Draft, Supervision, Project administration

Deniz Kızıllırmak: Investigation, Resources, Data Curation

Yavuz Havlucu: Investigation, Resources, Supervision

Acknowledgments & Ethics

This study is supported by Manisa Celal Bayar University Scientific Research Project Coordination Unit [Project No. 2017-191]. Within this study's scope, the recording of respiratory data was performed with the approval of the ethics committee number 20.478.486, dated 20.10.2017

Table 5. Some Results obtained with CORSA Systems

Ref.	Analyzed: Sound/ Disorder	Dataset	Feature Extraction Method	Classification Method	Best Result
[5]	Normal, Wheeze	N:15 W:16	The Local Adaptive Wheezes Detection Algorithm (LAWDA)		Sensitivities: 71% - 100%
[6]	Normal, Abnormal	N:10 A:10	Wavelet Analysis	Artificial Neural Network	Accuracy: 98 %
[7]	Normal, Crackle	N:27 C:14	Wavelet Analysis	Artificial Neural Network Support Vector Machine Gauss Mixture Model	<u>GMM:</u> Accuracy: 97.56 % Sensitivity:92.85 % Specificity:100 %
[8]	Normal Abnormal	N:385 A:485	Ensemble Empirical Mode Decomposition	Support Vector Machine	Accuracy: 94.6 % Sensitivity:94.2 % Specificity:95 %
[9]	Normal, Obstruction, Parenchymal	N:17 O:26 P:25	Mel-Frequency Cepstral Coefficient	Support Vector Machine k-Nearest Neighbors	<u>k-NN:</u> Accuracy: 98.26 %
[10]	Normal, Wheeze, Crackle,	Total:30	Statistical Properties Of Cepstral Coefficients Based New Feature Set	Artificial Neural Network	Accuracy: 97.2 % Sensitivity:97.41 % Specificity:95.5 %
[11]	Normal, Wheeze, Crackle,	N: 20 W:20 C:20	Mel-Frequency Cepstral Coefficient	Gaussian Mixture Model	Accuracy: 98.4 %
[12]	Normal Abnormal	N:17 A:51	Mel-Frequency Cepstral Coefficient	Adaptive Neuro-Fuzzy Inference System	Accuracy: 97.25 % Sensitivity:99.37 % Specificity:95.3 %
[13]	Normal, COPD patient	N:25 P:30	Temporal, Spectral, and Spectra-temporal features (MFCC LPC, etc.)	Support Vector Machine k-Nearest Neighbors Logistic Regression Decision Tree and Discriminant Analysis	<u>SVM and LR:</u> Accuracy: 100 % Sensitivity:100 % Specificity:100 %
This Study	Normal Abnormal	N:100 A:100	Mel-Frequency Cepstral Coefficient Empirical Mode Decomposition Wavelet Analysis	Artificial Neural Network Support Vector Machine k-Nearest Neighbors	<u>MFCC + k-NN:</u> Accuracy: 98.8 % Sensitivity:99.5 % Specificity:97.5 % <u>EMD+ANN:</u> Accuracy: 88.9 % Sensitivity:93.5 % Specificity:84 %

References

- [1]. World Health Organization. The Top 10 Causes of Death n.d. <https://www.who.int/news-room/fact-sheets/detail/the-top-10-causes-of-death> (accessed March 20, 2020).
- [2]. Güler I, Polat H, Ergün U. 2005. Combining neural network and genetic algorithm for prediction of lung sounds. *Journal of Medical Systems*; 29:217–31. doi: 10.1007/s10916-005-5182-9.
- [3]. Polat H, Güler I. 2004. A simple computer-based measurement and analysis system of pulmonary auscultation sounds. *Journal of Medical Systems*; 28: 665–72. doi: 10.1023/B:JOMS.0000044968.45013.ce.
- [4]. Rocha BM, Filos D, Mendes L, Serbes G, Ulukaya S, Kahya YP, et al. 2019. An open access database for the evaluation of respiratory sound classification algorithms. *Physiological Measurement*; 40. doi:10.1088/1361-6579/ab03ea.
- [5]. Homs-Corbera A, Fiz JA, Morera J, Jané R. 2004. Time-Frequency Detection and Analysis of Wheezes During Forced Exhalation. *IEEE Transactions on Biomedical Engineering*; 51: 182–186. doi: 10.1109/TBME.2003.820359.
- [6]. Sezgin MC, Dokur Z, Olmez T, Korurek M. Classification of respiratory sounds by using an artificial neural network. *2001*



- Proceedings of the 23rd Annual EMBS International Conference, Istanbul, Turkey, 2001, pp. 697-699.* doi:10.1109/IEMBS.2001.1019035.
- [7]. Maruf SO, Azhar MU, Khawaja SG, Akram MU. Crackle separation and classification from normal respiratory sounds using Gaussian Mixture Model. *2015 IEEE 10th International Conference on Industrial and Information Systems, Sri Lanka, 2015, pp. 267-271* doi: 10.1109/ICIINFS.2015.7399022
- [8]. Lozano M, Fiz JA, Jané R. 2016. Performance evaluation of the Hilbert-Huang transform for respiratory sound analysis and its application to continuous adventitious sound characterization. *Signal Processing*; 120: 99–116. doi:10.1016/j.sigpro.2015.09.005.
- [9]. Palaniappan R, Sundaraj K, Sundaraj S. 2014. A comparative study of the svm and k-nn machine learning algorithms for the diagnosis of respiratory pathologies using pulmonary acoustic signals. *BMC Bioinformatics*; 15:223. doi:10.1186/1471-2105-15-223.
- [10]. Sengupta N, Sahidullah M, Saha G. 2016. Lung sound classification using cepstral-based statistical features. *Computers in Biology and Medicine*; 75: 118–29. doi: 10.1016/j.compbio.2016.05.013.
- [11]. Liu Y, Lin Y, Zhang X, Wang Z, Gao Y, Chen G, et al. Classifying respiratory sounds using electronic stethoscope. *2017 IEEE SmartWorld, Ubiquitous Intelligence & Computing, Advanced & Trusted Computing, Scalable Computing & Communications, Cloud & Big Data Computing, Internet of People and Smart City Innovation, San Francisco, CA, USA, 2017.* doi: 10.1109/UIC-ATC.2017.8397496
- [12]. Sunil NKB, Ganesan R. 2015. Adaptive neuro-fuzzy inference system for classification of respiratory signals using cepstral features. *International Journal of Applied Engineering Research*; 10 (28): 22121-22125.
- [13]. Haider NS, Singh BK, Periyasamy R, Behera AK. 2019. Respiratory sound based classification of chronic obstructive pulmonary disease: a risk stratification approach in machine learning paradigm. *Journal of Medical Systems*; 43: 255. doi: 10.1007/s10916-019-1388-0.
- [14]. Pramono RXA, Bowyer S, Rodriguez-Villegas E. 2017. Automatic adventitious respiratory sound analysis: A systematic review. *Plos One*; 12(5): 1-43. doi: 10.1371/journal.pone.0177926
- [15]. Bokov P, Mahut B, Flaud P, Delclaux C. 2016. Wheezing recognition algorithm using recordings of respiratory sounds at the mouth in a pediatric population. *Computers in Biology and Medicine*; 70 (2016): 40-50. doi:10.1016/j.compbio.2016.01.002.
- [16]. Bahoura M. Pattern recognition methods applied to respiratory sounds classification into normal and wheeze classes. 2009. *Computers in Biology and Medicine*; 39 (2009): 824-843. doi: 10.1016/j.compbio.2009.06.011
- [17]. Göğüş FZ, Karlık B, Harman G. 2016. Identification of pulmonary disorders by using different spectral analysis methods. *International Journal of Computational Intelligence Systems*; 9 (4): 595-611. doi:10.1080/18756891.2016.1204110
- [18]. Kandaswamy A, Kumar CS, Ramanathan RP, Jayaraman S, Malmurugan N. 2004. Neural classification of lung sounds using wavelet coefficients. *Computers in Biology and Medicine*; 34 (2004): 523-537. doi: 10.1016/S0010-274825(03)00092-1
- [19]. Oweis RJ, Abdulhay EW, Khayal A, Awad A. 2015. An alternative respiratory sounds classification system utilizing artificial neural networks. *Biomedical Journal*; 38 (2): 153-161. doi: 10.4103/2319-4170.137773.
- [20]. Lozano M, Fiz JA, Jane R. 2016. Automatic differentiation of normal and continuous adventitious respiratory sounds using ensemble empirical mode decomposition and instantaneous frequency. *IEEE Journal Of Biomedical And Health Informatics*; 20 (2): 486-497. doi: 10.1109/JBHI.2015.2396636
- [21]. Pasterkamp H, Kraman SS, Wodicka GR. 1997. State of the Art Respiratory Sounds Advances Beyond the Stethoscope. *American Journal of Respiratory and Critical Care Medicine*; 156(3): 974-987. doi: 10.1164/ajr-ccm.156.3.9701115.
- [22]. Palaniappan R, Sundaraj K, Ahamed N, Arjunan A, Sundaraj S. 2013. Computer-based respiratory sound analysis: a systematic review. *IETE Technical Review*; 30 (3): 248-256. doi: 10.4103/0256-4602.113524
- [23]. Dokur Z. 2009. Respiratory sound classification by using an incremental supervised neural network. *Pattern Analysis and Applications*; 12 (4): 309-319. doi: 10.1007/s10044-008-0125-y
- [24]. Sovijarvi ARA, Vanderschoot J, Earis JE. 2000. Standardization of computerized respiratory sound analysis. *European Respiratory Review*; 10 (77): 585.
- [25]. Ben Nouma B, Mitiche A, Ouakrim Y, Mezghani N. 2019. Pattern Classification by the Hotelling Statistic and Application to Knee Osteoarthritis Kinematic Signals. *Machine Learning and Knowledge Extraction*; 1 (3): 768-784. doi:10.3390/make1030045
- [26]. Vannuccini L, Earis JE, Heliştop P, Cheetham BMG, Rossi M et al. 2000. Capturing and preprocessing of respiratory sounds. *European Respiratory Review*; 10 (77): 616-620.
- [27]. Huang NE, Shen Z, Long SR, Wu MC, Shih HH et al. 1998. The Empirical Mode Decomposition and The Hilbert Spectrum for Nonlinear and Non-stationary Time Series Analysis. *Royal Society of London Proceedings Series A*; 454: 903-995. doi: 10.1098/rspa.1998.0193
- [28]. İçer S, Gengeç Ş. 2014. Classification and analysis of non-stationary characteristics of crackle and rhonchus lung adventitious sounds. *Digital Signal Processing*; 28 (2014): 18-27. doi: 10.1016/j.dsp.2014.02.001
- [29]. Hu X, Peng S, Hwang WL. 2012. EMD revisited: A new understanding of the envelope and resolving the model mixing problem in AM-FM signals. *IEEE Transactions on Signal Processing*; 60(3): 1075-1086. doi:10.1109/tsp.2011.2179650
- [30]. Deering R, Kaiser JF. The use of a masking signal to improve Empirical Mode Decomposition. *IEEE International Conference on Acoustics, Speech, and Signal Processing, Philadelphia, PA, USA, 2005.* doi:10.1109/icassp.2005.1416051
- [31]. Palaniappan R, Sundaraj K. Respiratory sound classification using cepstral features and support vector machine. 2013 IEEE Recent Advances in Intelligent Computational Systems, Trivandrum, India, 2013. doi:10.1109/raics.2013.6745460
- [32]. Aykanat M, Kılıç Ö, Kurt B, Saryal S. 2017. Classification of lung sounds using convolutional neural networks. *EURASIP Journal on Image and Video Processing*; 2017(1). doi: 10.1186/s13640-017-0213-2
- [33]. Rioul O, Vetterli M. 1991. Wavelets and Signal Processing. *IEEE Signal Processing Magazine*; 8 (4): 14-38. doi: 10.1109/79.91217
- [34]. Gengeç Ş. Akciğer Seslerinden İşaret İşleme Teknikleri Kullanılarak Özellik Çıkarma ve Sınıflandırma. Erciyes Üniversitesi, 2012. (in Turkish)

- [35]. Subasi A. 2007. EEG signal classification using wavelet feature extraction and a mixture of expert model. *Expert Systems with Applications*; 32 (4): 1084-1093. doi:10.1016/j.eswa.2006.02.005
- [36]. Reichert S, Gass R, Brandt C, Andres E. 2008. Analysis of Respiratory Sounds: State of the Art. *Clinical Medicine: Circulatory, Respiratory and Pulmonary Medicine*; 2008 (2): 45-58. doi: 10.4137/ccrpm.s530
- [37]. Vapnik VN. Statistical Learning Theory. New York: Wiley; 1998.
- [38]. Başer F, Apaydın A. 2015. Comparison Between Logistic Regression and Support Vector Machines for Classification Purposes. *Anadolu Üniversitesi Bilim ve Teknoloji Dergisi B- Teorik Bilimler*; 3 (2): 53-65 (in Turkish with an abstract in English) doi: 10.20290/btdb.67263.
- [39]. Naves R, Barbosa BHG, Ferreira DD. 2016. Classification of lung sounds using higher-order statistics: A divide-and-conquer approach. *Computer Methods and Programs in Biomedicine*; 129 (2016): 12-20. doi:36 10.1016/j.cmpb.2016.02.013
- [40]. Bhatia N, Vandana. 2010. Survey of Nearest Neighbor Condensing Techniques. *International Journal of Computer Science and Information Security*; 8 (2): 302-305.
- [41]. Tu J V. 1996. Advantages and disadvantages of using artificial neural networks versus logistic regression for predicting medical outcomes. *Journal of Clinical Epidemiology*; 49 (11):1225-1231. doi: 10.1016/s0895-4356(96)00002-9
- [42]. Özmen Ö, Khdr A, Avcı E. 2018. Sınıflandırıcıların kalp hastalığı verileri üzerine performans karşılaştırması. *Fırat Üniversitesi Mühendislik Bilimleri Dergisi*; 30(3): 153-159. (in Turkish with an abstract in English) doi:10.13140/rg.2.2.24732.95365.

Log-normal and Negative Binomial Distributions of DONUT Data

Çağın Kamışcıoğlu*¹ 

¹ Physics Engineering Department, Faculty of Engineering, Ankara University, Ankara, Türkiye

* gunescc@ankara.edu.tr

* Orcid: 0000-0003-2610-6447

Received: 24 August 2021

Accepted: 27 May 2022

DOI: 10.18466/cbayarfbe.986699

Abstract

Since charged particle multiplicity distributions provide important results about the interactions of particles it has been studied in various experiments so far. The analysis of multiplicity distributions, which can be easily obtained in experiments, is therefore very important. There are several parametric models to describe the charged particle multiplicity distributions in literature. Among them, log-normal distribution and negative binomial distribution are the most well-known parametric models. In this study, negative binomial and log-normal distributions are compared and tested in neutrino interactions produced in Direct Observation of Nu-Tau experiment. This analysis was carried out using the real experimental results of the Direct Observation of Nu-Tau experiment collaboration. The results of the analysis show that the neutrino data, reported by Direct Observation of Nu-Tau Collaboration, is well described by negative binomial and log-normal distribution. In terms of fit parameters, the χ/ndf value of the both distribution NBD and LND are close to unity but log-normal distribution data slightly better than negative binomial distribution.

Keywords: Negative binomial, log-normal, multiplicity.

1. Introduction

In particle physics experiments, the multiplicity distribution is an interesting parameter that can be easily obtained in the experiment, but it keeps information about the characteristics of the interaction. To reveal the nature of the interaction, it is necessary to understand the behavior of multiplicity distribution. Several measurements have been collected so far in many experiments at different energies and on different reactions to understand the behavior of charged particle multiplicity distributions. In particular, the shape of the multiplicity distribution is very important as it provides information about the particle production mechanism. Therefore, various theoretical, phenomenological models and rules are proposed to parameterize charged particle multiplicity distributions in the literature. However, results from experiments showed that some parametric models are more successful in describing the data and its energy dependence up to now [1-7].

Among the parametric models, log-normal distribution and negative binomial distribution are the most well-known parametric models, so this study focuses on these two models. The log normal distribution, is a statistical function has a longer tail, more peaked than

the negative binomial distribution. It is very common to encounter this distribution in nature. Therefore, it has been found to be applicable in a number of different fields like population ecology, income distribution in some economies and multi-particle production etc. [8,9].

The Log-Normal Distribution (LND) is defined as;

$$P(x) = \frac{1}{x\sqrt{2\pi s^2}} e^{-(\ln x - m)^2 / 2s^2} \quad (1.1)$$

and here m and s are the free parameters. When multi-particle production is analyzed, the log normal distribution arises in naturally so this leads an important and simple physical interpretation. In 1990, R. Szwed et al. has showed that, LND describes the e^+e^- multiplicity data very well [10,11]. Then, Apparatus for LEP PHysics (ALEPH) Collaboration proved that, LND gives a proper description of the charged particle multiplicity distribution of e^+e^- annihilation in 1991 [12]. In addition, the studies on of νp , $\bar{\nu} p$, and $\bar{p} p$ interactions showed that, charged particle multiplicity data can be parameterized by a log-normal distribution [11,13-15]. Although, the LND has been tested in many experiments, it has been studied very rarely in neutrino interactions.

To describe the charged particle multiplicity, the other parametric model is Negative Binomial Distribution (NBD) which is a statistical distribution and defined as;

$$P(n; k, \bar{n}) = \binom{\bar{n}+k-1}{\bar{n}} p^{\bar{n}} (1-p)^k \quad (1.2)$$

where k and \bar{n} are free parameters of the distribution with $p = (\bar{n}/k) / (1 + (\bar{n}/k))$. It is known that the first application was made to the cosmic-ray muon data by McKeown and Wolfendale in 1966 [16]. In 1985, the UA5 Collaboration obtained a remarkably good negative binomial fit in the $\bar{p}p$ collision and this made an overwhelming impression [17-19]. In the same year, it was shown that NBD describes the charged multiplicity distribution of e^+e^- annihilation excellently [20]. Similar results were obtained for the charged particle multiplicity distribution of μp and pp collisions [21,22]. Recently, The Oscillation Project with Emulsion-Tracking Apparatus (OPERA) Collaboration also tested the NBD distribution and published the result that NBD describes the charged particle multiplicity in neutrino interactions very well [6].

Previously, neutrino multiplicity data of Direct Observation of Nu-Tau (DONUT) experiment is compared and tested for KNO-G scaling and the validation of data has been shown [23]. In this study, charged particle multiplicity distribution of neutrino interaction produced in DONUT experiment is analyzed for NBD and LND. Although, these models have been tested in several experiments before, this is the first study for DONUT which is an emulsion based-neutrino experiment.

2. Experimental Data and Analysis

The DONUT experiment was designed to observe directly and study about $\nu_{\tau}CC$ interactions in the SPS Wide Band Neutrino Beam. For this purpose, a number of 800 GeV protons from the Tevatron collide into the beam dump so a prompt neutrino beam, composed of ν_{μ} (%60), ν_e (%35), ν_{τ} (%5) neutrinos with 53 GeV average energy, was created. Then charm particles (D_s) are produced and decay to an anti-tau neutrino and a tau lepton. The tau neutrino, produced in the decays of tau, travels 36 m to reach the emulsion target. The experiment used an emulsion/counter-hybrid-detector and the target was composed of nuclear emulsion as a three-dimensional tracking device. Because of its sub-micron accuracy and high spatial resolution, nuclear emulsion is a very powerful technique for the detection of short-lived tau particle. So, three emulsion target designs were used in the experiment. Each design had different plastic base layer and emulsion layer thickness, called as ECC200, ECC800 and Bulk type. The combination of emulsion designs intent to increase the amount of mass while increasing the precision for tau particle. The first design, (ECC 200) composed of 1 mm thick steel sheets interleaved with emulsions having 100

μm thick emulsion layers on both size 200 μm plastic base. The second design (ECC800) is the same as the first design, only the thickness of the plastic base is 800 μm . The bulk design consists of only 350 μm thick emulsion layers on both size of 90 μm plastic base without steel plates.

DONUT experiment collected data during 1997 and published first and the most important results in 2000. Thanks to the emulsion technology and the detector identified 578 neutrino interactions and the collaboration observed 9 $\nu_{\tau}CC$ events with background of 1.5 events. Based on these data, they announced the discovery of the tau particle in 2000 [24-27].

1. Negative Binomial and Log-normal Distributions

The NBD provides a convenient framework for multiplicity distributions with two free parameters. In fact, the two free parameters make NB distribution a highly flexible distribution [28,29]. In order to test negative binomial distribution, the data of located multiplicity distributions of charged particles produced in the DONUT experiment obtained directly from the ref [24] which is given in Figure 1.

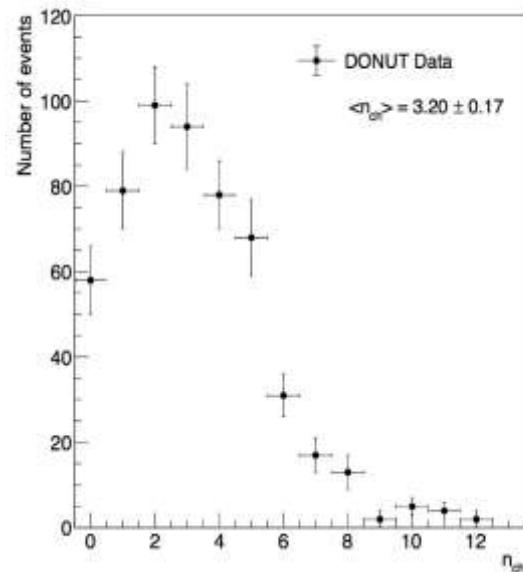


Figure 1. The located multiplicity distributions of charged particles produced in the DONUT experiment.

Then NBD fit applied to the $P(n)$ vs. n distribution of charged particles and the parameters \bar{n} and k are obtained from this fit directly. The fitting procedure was applied, using the χ^2 method, until the best fit was achieved. The data and superimposed fit line are given in Figure 2 and the values of parameters obtained from negative binomial fit is given in Table 1. It can be seen that the fit line shows good agreement with the data set.

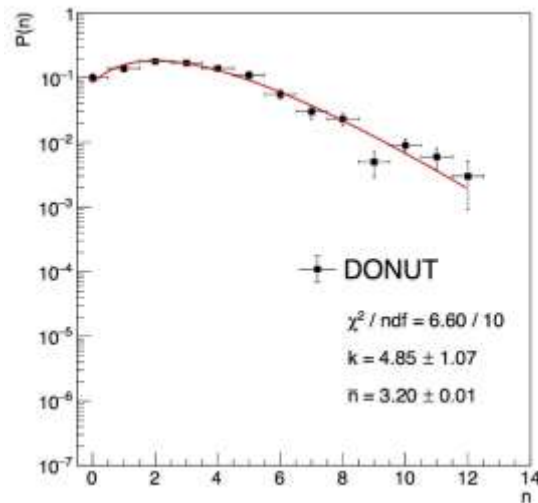


Figure 2. The data distribution with the negative binomial fit.

Another parametric model that is well known and has many applications in the literature is LND [30].

Since shape of charged multiplicity distributions is showed well described by LND, in this study LND fit applied to the data of located multiplicity distributions of charged particles produced in the DONUT experiment.

Table 1. The negative binomial fit results.

Applied Fit	\bar{n}	k	χ^2/ndf
Negative Binomial	3.20 ± 0.01	4.85 ± 1.07	6.60/10

The fitting procedure was applied, using the χ^2 method, until the best fit was achieved. The data and the resulting fit are shown in Figure 3 and fit parameters are given in Table 2. It is observed that, LND fit seen to be very good which reflects the shape of charged particle multiplicity distribution.

Table 2. The log-normal fit results.

Applied Fit	m	s	χ^2/ndf
Log-normal	1.80 ± 0.02	0.38 ± 0.01	8.52/10

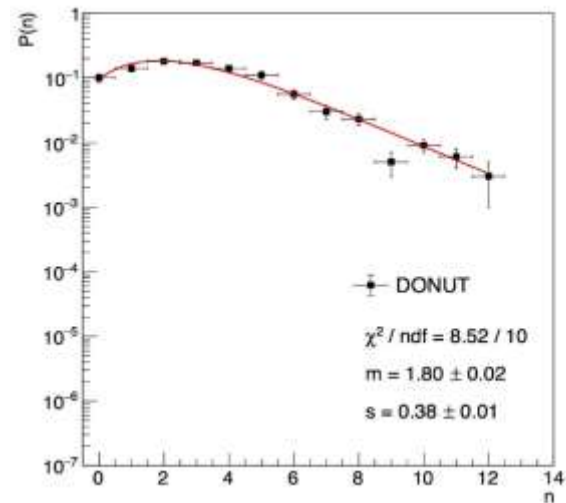


Figure 3. The data distribution with the log-normal fit.

3. Conclusion

In this study, the charged particle multiplicity data of DONUT experiment tested for two well-known parametric models which are log-normal distribution and negative binomial distribution. For the analysis, the real data directly obtained from the DONUT reference paper [24], NBD (1.1) and LND (1.2) fits were applied one by one until the best fit was achieved and the results are presented in the form of tables. It has been shown that, charged particle multiplicity distribution of DONUT experiment can be described in terms of the k and \bar{n} parameters of NBD and can be described in terms of m and s parameters of LND. Although both fit lines show good agreement with data, χ^2/ndf results shows that log-normal distribution gives a better description of data than the negative binomial distribution. The χ^2/ndf values of NBD and LND are close to unity, but the fit value of the lognormal distribution are relatively better for DONUT neutrino interactions. At the same time, the dependence of the free parameters on energy are reported in the tables for the neutrino interactions.

Author's Contributions

Çağın Kamaşcıoğlu: Drafted and wrote the manuscript, performed, and interpreted the whole experiments and analysis.

Ethics

There are no ethical issues after the publication of this manuscript.

References

- [1]. Ansorge RE., Åsman B., Burow L., Carlson P., DeWolf RS. et al, 1989. Charged Particle Multiplicity Distributions at 200-GeV and 900-GeV Center-Of-Mass Energy *Z. Journal of Physics C*; 43, 357. doi: 10.1007/BF01506531.
- [2]. Berger Ch., Lackas W., Raupach F., Wagner W., Alexander G. et al., 1978. A study of jets in electron positron annihilation into hadrons in the energy range 3.1 to 9.5 GeV (PLUTOColl.) *Physics Letters B*; 78,176. doi:10.1016/0370-2693(78)90377-5.
- [3]. Brandelik RW, Braunschweig K, Gather V, Kadansky K, Lübelsmeyer et al, 1980. (TASSOColl.) Rapid growth of charged particle multiplicity in high energy e^+e^- annihilations. *Physics Letters B*; 89 (3-4): 418-422. doi:10.1016/0370-2693(80)90156-2.
- [4]. Allen P, Blietschau J, Grassler H, Lanske D, Schulte R, et al, 1981. Multiplicity distributions in neutrino-hydrogen interactions. *Nuclear Physics B*; 181 (3): 385-402. doi:10.1016/0550-3213(81)90532-0.
- [5]. Kayis-Topaksu A, Öngentü G, Dantzig van R, Jong de M, Oldeman RGC et al., 2007. (CHORUS Coll.) Charged Particle Multiplicities in Charged-Current Neutrino and Anti-Neutrino Nucleus Interactions. *The European Physical Journal C*; 51: 775-785. doi:10.1140/epjc/s10052-007-0366-8.
- [6]. Agafonova N, Aleksandrov A, Anokhina A, Aoki S, Ariga A et al., 2018. (OPERA Coll.) Study of Charged Hadron Multiplicities in Charged-Current Neutrino-Lead Interactions in the OPERA Detector. *The European Physical Journal C*; 78: 62. doi:10.1140/epjc/s10052-017-5509-y
- [7]. Kamişcioğlu Ç., 2020. Study of KNO scaling in the emulsion based neutrino experiments. *Turkish Journal of Physics*; 44:222-228. doi: 10.3906/fiz-1912-12.
- [8]. Carius S. and Ingelman G., 1990. The log-normal distribution for cascade multiplicities in hadron collisions. *Physics Letters B*; 252:657. doi:10.1016/0370-2693(90)90500-6.
- [9]. Huberman BA. 1988. The Ecology of Computation. North Holland (March 15, 1988).342 pages.
- [10]. Szwed R., Wrochna G., Wroblewski AK., 1991. New AMY and DELPHI multiplicity data and the lognormal distribution. *Modern Physics Letters A*;6: 245-258. doi:10.1142/S021773239100021X.
- [11]. Szwed R., Wrochna G., Wroblewski AK., 1990. Genesis Of The Lognormal Multiplicity Distribution In The e^+e^- Collisions And Other Stochastic Processes. *Modern Physics Letters A*;5:1851-1870. doi:10.1142/S0217732390002110.
- [12]. Decamp D., Deschizeaux B, Goy C, Lees JP, Minard N et al., 1991. Measurement of the charged particle multiplicity distribution in hadronic Z decays. *Physics Letters B* 273(1-2):181-192. doi:https://doi.org/10.1016/0370-2693(91)90575-B.
- [13]. Jones GT, Jones RWL, Kennedy BW, Morrison DRO, Mobayyen MM. et al., 1992. Multiplicity distributions of charged hadrons in vp and charged current interactions. *Zeitschrift für Physik C Particles and Fields*. 54:45–54. doi:10.1007/BF01881707.
- [14]. Buskulic D, Casper D, Bonis DI, Decamp D, Ghez P et al., 1995. Measurements of the charged particle multiplicity distribution in restricted rapidity intervals. *Zeitschrift für Physik C Particles and Fields* 69:15–25. doi:10.1007/BF02907382.
- [15]. Acton PD, Alexander G, Allison J, Allport PP, Anderson KJ et al., 1992. A Study of charged particle multiplicities in hadronic decays of the Z0. *Zeitschrift für Physik C*. 53:539-554. doi:10.1007/BF01559731.
- [16]. MacKeown PK. and Wolfendale AW., 1966. The interpretation of the charge ratio of cosmic-ray muons. *Proceedings of the Physical Society*, 553. doi:10.1088/0370-1328/89/3/312.
- [17]. Alner, GJ, Alpgard K, Anderer P, Ansorge RE, Asman B. et al., 1985. Multiplicity distributions in different pseudorapidity intervals at a CMS energy of 540 GeV. *Physics Letters B*,160(1-3): 193-198. doi: 10.1016/0370-2693(85)91491-1.
- [18]. Alner, GJ, Alpgard K, Anderer P, Ansorge RE, Asman B. et al., 1985. A new empirical regularity for multiplicity distributions in place of KNO scaling. *Physics Letters B*;160(1-3): 199-206. doi: 10.1016/0370-2693(85)91492-3.
- [19]. Alner GJ, Ansorge RE, Asman B, Bockmann K, Booth CN et al., 1986. Scaling Violations in Multiplicity Distributions at 200-GeV and 900-GeV. *Physics Letters B*, 167:476-480. doi:10.1016/0370-2693(86)91304-3.
- [20]. Chew CK and Lim YK., 1985. Charged-particle multiplicity distributions in e^+e^- annihilation and negative binomial distributions. *Physics Letters B*,163(1-4):257-260. doi:10.1016/0370-2693(85)90233-3.
- [21]. Grosse-Oetringhaus JF, Reygers K., 2010. Charged-Particle Multiplicity in Proton-Proton Collisions. *Journal of Physics G* 37:083001. doi:10.1088/0954-3899/37/8/083001.
- [22]. Armeodo M., 1987. Comparison of multiplicity distributions to the negative binomial distribution in muon-proton scattering. *Zeitschrift für Physik C Particles and Fields*; 35:335–345. doi:10.1007/BF01570769.
- [23]. Kamişcioğlu Ç., 2021. Study of KNO-G scaling in neutrino interactions. *Modern Physics Letters A*. 36(9):2150062. doi:10.1142/S0217732321500620.
- [24]. Kodama K, Ushida N, Andreopoulos C, Saoulidou N, Tzanakos G et al., 2008. Final tau-neutrino results from the DONUT experiment. *PHYSICAL REVIEW D*;78:052002. doi: 10.1103/PhysRevD.78.052002.
- [25]. Kodama K, Saoulidou N, Tzanakos G, Baller B, Lundber B et al., 2002. Detection and analysis of tau-neutrino interactions in DONUT emulsion target. *Nuclear Instruments and Methods in Physics Research A*. 493:45–66. doi:10.1016/S0168-9002(02)01555-3.
- [26]. Kodama K, Ushida N, Andreopoulos C, Saoulidou N, Tzanakos G et al., 2001. Observation of tau neutrino interactions. *Physics Letters B*; 504: 218–224. doi:10.1016/S0370-2693(01)00307-0.
- [27]. Kodama K, Andreopoulos C, Giokaris N, Saoulidou N, Tzanakos G et al., 2004. Identification of neutrino interactions using the DONUT spectrometer. *Nuclear Instruments and Methods in Physics Research A*;516 :21–33. doi:10.1016/j.nima.2003.07.035.
- [28]. Kittel W., De Wolf EA, 2005. Soft multihadron dynamics. World Scientific Press.
- [29]. Szwed R. 1986. Proceedings of the XVII international symposium on multiparticle dynamics. pp. 663.
- [30]. Wroblewski AK, 1990. High-energy physics. Proceedings, 25th International Conference. pp. 125. Singapore.



Synthesis of Poly(azomethine) Containing Sulfonic Acid Unit Oxygen and Sulphur Bridged: Investigation of Its Thermal, Optical and Electrochemical Properties

Elif Karacan Yeldir^{1*} 

¹Çanakkale Onsekiz Mart University, Faculty of Sciences and Arts, Department of Chemistry, Polymer Synthesis and Analysis Lab. 17020, Çanakkale, Türkiye

* elifkaracan@comu.edu.tr

* Orcid: 0000-0001-8638-1198

Received: 9 February 2022

Accepted: 27 May 2022

DOI: 10.18466/cbayarfbe.1070592

Abstract

In this study, a poly(azomethine) compound (SBP) containing sulfur and oxygen bridge was obtained from 4,4'-[thiobis(4,1-phenyleneoxy)]dibenzaldehyde (DBA) and 4,4'-diamino-2,2'-biphenyl sulfonic acid from condensation reaction. Structural, optical, electrochemical and morphological analyzes of the obtained polymeric material were performed. Structural characterizations were performed from 1H-NMR and FT-IR spectra. Optical properties were determined in the UV-Vis spectrum and the optical band gap was calculated as 3.63 eV. Electrochemical properties were investigated by cyclic voltammetry (CV) and HOMO-LUMO and electrochemical band gap values were calculated. In addition, with the help of Gel Permeation Chromatography (GPC), the average molecular mass was found 5050 Da. Thermogravimetric analysis (TGA) results showed that the thermal degradation of SBP occurred in four steps and the maximum mass loss was at 391 °C. The surface analysis of the obtained polymeric material was investigated with scanning electron microscope (SEM) and it was determined that the surface was rough.

Keywords: Schiff base, poly(azomethine), sulphanilic acid, electrochemical band gap, thermal analysis.

1. Introduction

The imine compound form the reaction of a carbonyl and an amine compound under suitable conditions is called Schiff base [1]. These compounds, first synthesized by Hugo Schiff, are highly researched substances due to their relatively easy synthesis, obtained compounds having wide range of colors and high thermal and mechanical features [2–4]. With the polycondensation of two reagents with diamine and dicarbonyl groups, long-chain poly(imine), also known as poly(azomethine) compounds, are obtained [5,6]. Due to their high conjugation, poly (azomethine) compounds generally have improved optical, electrochemical, thermal and mechanical properties. In this way, they have a wide application network [7–9]. In addition, these compounds allow the design of materials that can tune their properties in the desired direction, due to the diversity of monomers [10]. Poly(azomethine) features could be improved by changing the colors, conductivity or solubility with various organic and inorganic dopants such as m-cresol,

methane sulfonic acid, SnCl₂ [11–13]. 10-Camforsulfonic acid was doped into a poly(azomethine) compound obtained in a study by Iwan et al., and its solubility was improved with photovoltaic parameters for solar cell application [14].

Among the dopant materials used, especially sulfonic acid derivatives have an important place due to the increase in solubility, high conductivity and thermal stability and flexibility they bring to the material [15,16]. In fact, it has been reported that a fluorene-based poly(azomethine) acquires photoluminescence and electroluminescence properties when only sulfonated polystyrene is added to the compound and its protonation is increased [17]. In addition, sulfonic acid groups are also used in active catalyst systems, dyes, detergents and surfactants [18–21].

In this study, it was aimed to obtain a poly(azomethine) compound with especially high thermal resistance. In the light of this information, a dialdehyde compound (DBA) was obtained by bromine elimination from 4-

Bromobenzaldehyde and 4,4'-thiodiphenol; and a Schiff base polymer (SBP) was synthesized from 4,4'-diamino-2,2'-biphenyl sulfonic acid and DBA by Schiff base reaction. After the synthesized DBA and SBP were characterized, their optical, electrochemical, thermal and surface properties were investigated.

2. Materials and Methods

2.1. Materials

4-Bromobenzaldehyde, 4,4'-thiodiphenol, 4,4'-diamino-2,2'-biphenyl sulfonic acid, K_2CO_3 , para-toluensulfonic acid (PTSA) used as reagents and catalyst in the study and solvents dimethyl sulfoxide (DMSO), methanol and dimethylacetamide (DMA) were obtained from Merck Co (Germany). All chemicals and solvents were used without further purification.

2.2. Synthesis of DBA

DBA was obtained by bromine elimination reaction by using 4-bromobenzaldehyde instead of 4-iodobenzaldehyde using the method given in the literature [22]. 1.091 g (0.005 mol) of 4,4'-thiodiphenol was dissolved in 15 mL of DMA in a 100 mL three-necked flask. 1.382 g (0.01 mol) of K_2CO_3 was weighed and added to the flask. It was stirred for 1 hour at $150^\circ C$ under reflux in Ar atmosphere. Then, 2 g (0.01 mol) of 4-bromobenzaldehyde was weighed into a beaker and 6.5 mL of DMA was dissolved. The mixture was added

dropwise to the flask. After 12 hours of reaction at $150^\circ C$, the product was precipitated in ice water and filtered. It was dried in a vacuum oven at $50^\circ C$ for 12 hours. The reaction scheme is shown in Figure 1A.

2.3. Synthesis of SBP

Weighed 0.670 g (0.0015 mol) of synthesized DBA and 0.516 g (0.0015 mol) of 4,4'-diamino-2,2'-biphenylsulfonic acid. The weighed substances were added into a 100 mL three-necked round bottom flask and it was dissolved in 20 mL of DMA. As a catalyst, PTSA 0.285g (0.0015 mol) was weighed and 2 mL of toluene was added by dissolving and mixed. After stirring under an argon atmosphere at $150^\circ C$ for 4 hours, it was cooled under an argon atmosphere at room temperature for 9 hours. The product was precipitated with methanol and washed with methanol to remove unreacted materials, dried in a vacuum oven at $50^\circ C$ for 3 hours. The reaction scheme is given in Figure 1B.

1H NMR (DMSO- d_6 , δ , ppm): 9.76 (s, terminal -CHO), 8.10 (s, -SO₃H), 7.81 (s, -C=N), 7.49 (d, Hd), 7.41 (d, Hb), 7.16 (s, Hf), 7.11 (d, He), 7.05 (d, Hc), 6.90 (s, terminal -NH₂), 6.67 (d, Ha).

^{13}C NMR (DMSO- d_6 , δ ppm): 191.51 (terminal -CHO), 166.36 (-C=N-) and 116.74, 119.17, 122.10, 126.28, 127.91, 128.62, 138.11, 146.43, 147.12, 157.14, 162.97 (Ar-C).

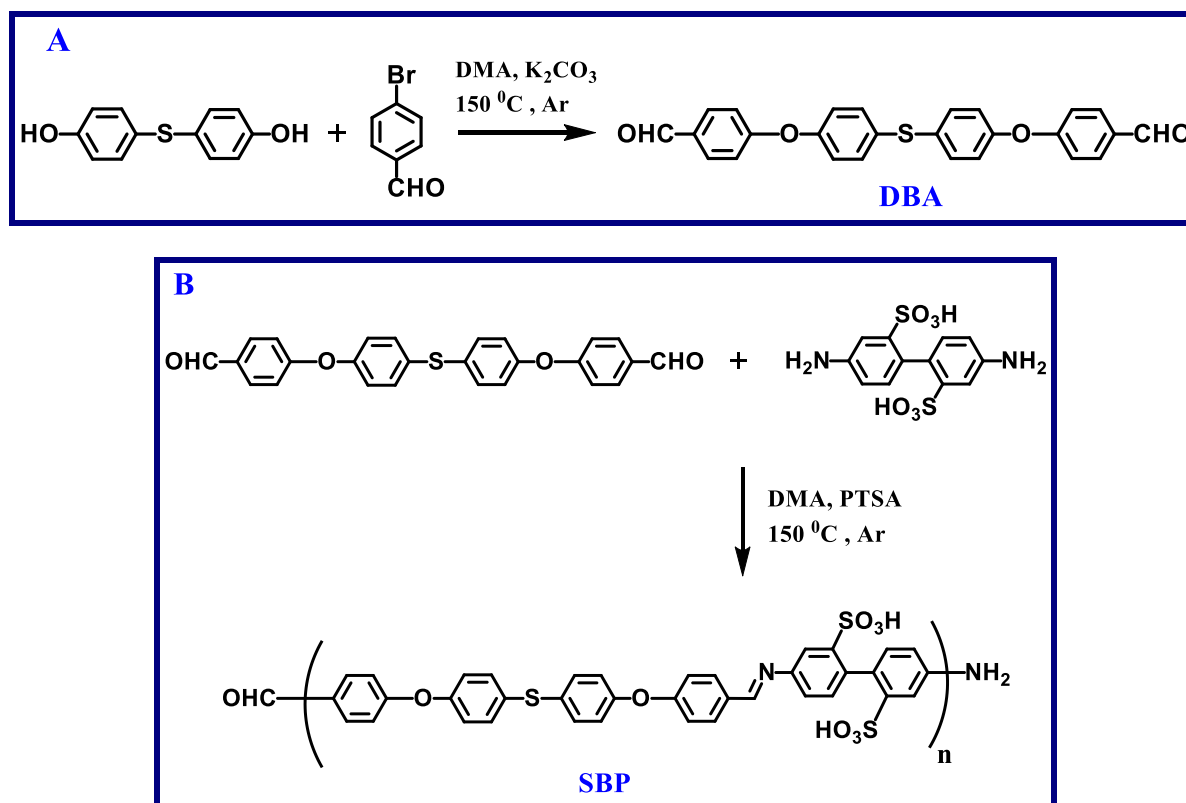


Figure 1. Reaction scheme of a) DBA and b) SBP synthesis.

2.4. Characterization techniques

The FT-IR spectrophotometer used for the structural analysis of the obtained DBA and SBP is a Perkin Elmer Spectrum-One instrument with ATR sampling accessory. Spectra were obtained in the range of 4000-400 cm^{-1} at room temperature. $^1\text{H-NMR}$ and $^{13}\text{C-NMR}$ techniques were used in nuclear magnetic resonance spectrophotometer analysis, which is another structural characterization. $^1\text{H-NMR}$ (400 MHz, DMSO, SiMe_4 internal standard) and $^{13}\text{C-NMR}$ (100.6 MHz, DMSO, SiMe_4 internal standard) spectra were obtained using the solutions of the samples in DMSO using Bruker AC FT-NMR instrument.

Optical properties of the obtained materials were examined with Analytikjena Specord 210 Plus UV-Vis spectrophotometer device. Spectra were obtained from solutions of DBA and SBP prepared in DMA at room temperature in the range of 280-800 nm.

The electrochemical character of DBA and SBP was analyzed by cyclic voltammetry (CV). Voltamograms were obtained with a CH instruments 660 C electrochemical Analyzer (CH Instruments, Texas, USA) at room temperature and using 0.1 M tetrabutylammonium hexafluorophosphate (TBA) as the electrolyte solution. A triple electrode system (Ag reference electrode, Pt counter electrode and glassy carbon working electrode) was used. After the film of SBP dissolved in DMF was prepared by casting solution on a glass slide surface, the measurement of solid state conductivity was made with a two-probe Keithley 2400 Electrometer.

The thermal stability of the samples was examined with the Perkin Elmer Sphire Differential Scanning Calorimetry device, which measures the mass loss with an increase of 10 $^\circ\text{C}$ per minute in a nitrogen atmosphere. The molecular weight of the polymer (SBP) was determined by gel transmission chromatography-light scattering (GPC-LS) analysis with the Malvern Viscotek GPC Dual 270 max system with a refractive index detector (RID) and 8.00 mm x 300 mm dual column. The column temperature was 55 $^\circ\text{C}$. DMF at a flow rate of 1.0 mL min^{-1} was used as eluent including 40 mM LiBr. In order to examine the surface properties of the polymeric material, after the samples were subjected to gold and carbon coating, JEOL SEM-7100-EDX scanning electron microscope was used.

3. Results and Discussion

3.1. Structural Analysis

DBA, a dibenzaldehyde compound obtained from the bromine elimination reaction from 4,4'-thiodiphenol and bromo-benzaldehyde, was examined by FTIR

spectroscopy. In a study by Culhaoğlu and Kaya [22], the FT-IR spectra of this synthesized substance were compared and it was observed that the spectra were compatible with each other. FT-IR spectra of synthesized DBA and SBP are shown in Figure 2. The characteristic -C=O vibration of the aldehyde group in the structure of DBA was observed at 1685 cm^{-1} and the -C-O-C- vibration arising from the oxygen bridge in the structure was observed at 1227 cm^{-1} . In the spectrum of SBP obtained as a result of polymerization of DBA with 4,4'-diamino-2,2'-biphenylsulfanic acid, a derivative of sulfanilic acid, the characteristic imine (-C=N-) vibration, originating from the Schiff base, was observed at 1601 cm^{-1} . In addition, aromatic -C-H vibrations in the structure of SBP appeared at 3116 cm^{-1} and 3045 cm^{-1} , aromatic C=C vibrations at 1593 cm^{-1} and 1573 cm^{-1} , and -C-O-C- vibration at 1221 cm^{-1} . The disappearance of the carbonyl vibration of the aldehyde and the amine vibration of the 4,4'-diamino-2,2'-biphenylsulfanic acid observed in DBA in the SBP formed as a result of the polymerization reaction, and the emergence of the vibration peak of the imine is an indication of the formation of the Schiff base polymer.

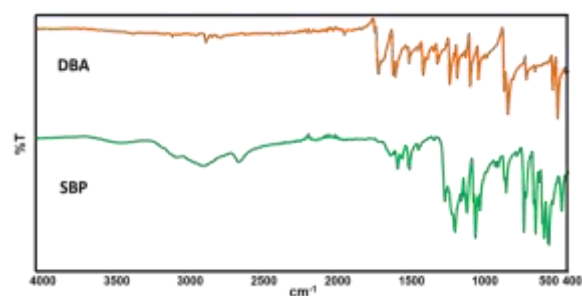


Figure 2. FT-IR spectra of DBA and SBP.

A poly(azomethine) compound, SBP, was obtained after the reaction of the carbonyl group of the dibenzaldehyde compound DBA and the amine group of 4,4'-diamino-2,2'-biphenylsulfanic acid, which is a sulfanilic acid derivative, with the presence of PTSA catalyst. $^1\text{H-NMR}$ spectra were taken and shown in Figure 3. The signal seen at 7.81 ppm in the $^1\text{H-NMR}$ spectrum belongs to the characteristic imine proton formed as a result of the reaction of the amine and carbonyl. The proton signals of the terminal aldehyde and terminal amine at the ends of the polymer chain formed as a result of polymerization were observed in the spectrum at 9.76 ppm and 6.90 ppm, respectively. The acid protons from the sulfanilic acid in the SBP chain corresponded to the singlet signal seen at 8.10 ppm. Also, the signals seen in the spectrum at 7.49 ppm, 7.41 ppm, 7.16 ppm, 7.11 ppm, 7.05 ppm and 6.67 ppm belonged to Hd, Hb, Hf, He, Hc and Ha on the aromatic ring, respectively.

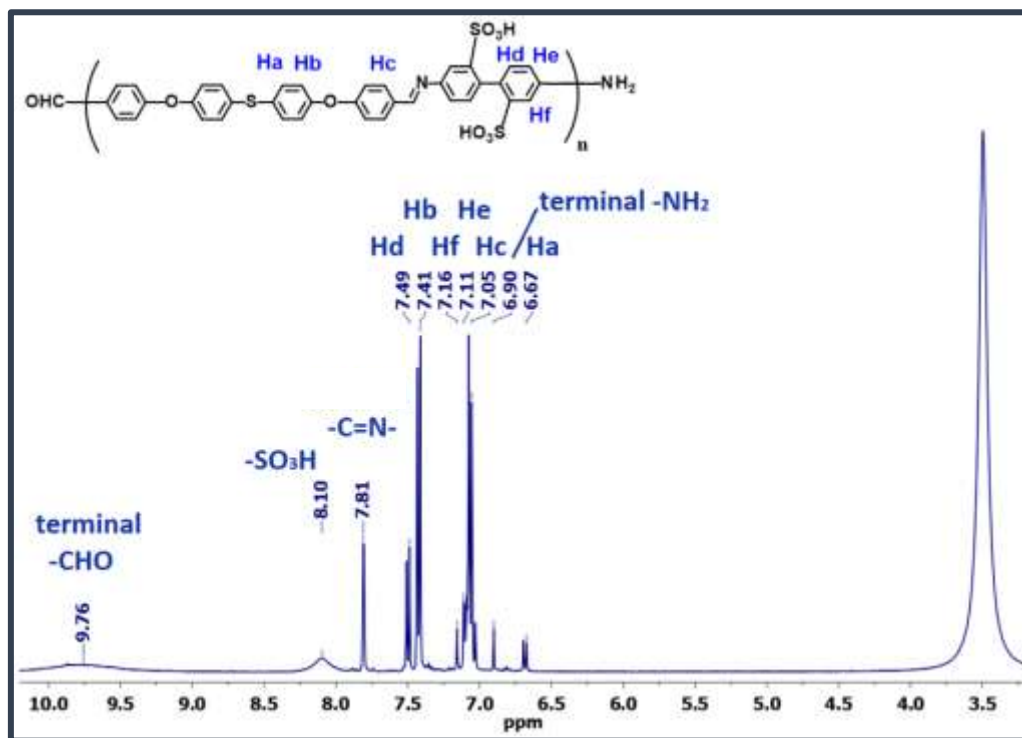


Figure 3. ¹H-NMR spectrum of SBP.

3.2. Optical Analysis

The optical properties of the synthesized DBA and SBP were investigated by UV-Vis Spectroscopy and the spectra obtained from the solutions prepared in DMA are shown in Figure 4. In the spectrum of DBA, a shoulder shape observed at 289 nm was observed, which is caused by the electronic transitions of $\pi \rightarrow \pi^*$ phenyl groups in the structure. When the spectrum of SBP, a Schiff base polymer, is examined, a peak belonging to the characteristic imine group $n \rightarrow \pi^*$ electronic transition is observed at 312 nm. The optical properties of the synthesized DBA and SBP were investigated by UV-Vis Spectroscopy and the spectra obtained from the solutions prepared in DMA are shown in Figure 4. In the spectrum of DBA, a shoulder shape observed at 289 nm was observed, which is caused by the electronic transitions of $\pi \rightarrow \pi^*$ phenyl groups in the structure. When the spectrum of SBP, a Schiff base polymer, is examined, a peak belonging to the characteristic imine group $n \rightarrow \pi^*$ electronic transition is observed at 312 nm. The most important reason for the expansion of this signal is the increased conjugation in the polymeric structure.

3.3. Electrochemical analysis

Electrochemical properties of DBA and SBP were investigated by cyclic voltammetry. The voltammograms obtained in the electrolyte solution at room temperature and in an argon atmosphere

between +1600 mV and -1600 mV are given in Figure 6. Reduction potential (E_{red}) and oxidation potential (E_{ox}) of DBA and SBP were obtained from voltammograms. From these obtained E_{ox} and E_{red} values, HOMO - LUMO energy levels and

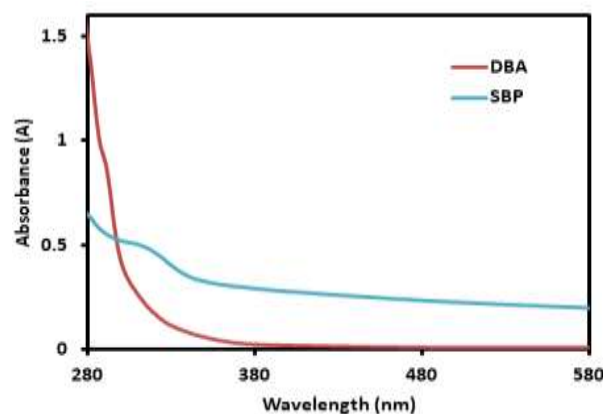


Figure 4. UV-Vis Spectra of DBA and SBP.

electrochemical band gap (E'_g) were calculated with the help of the formulas given in the literature[24,25]:

$$E_{HOMO} = -(4.39 + E_{ox}) \quad (1)$$

$$E_{LUMO} = -(4.39 + E_{red}) \quad (2)$$

$$E'_g = E_{LUMO} - E_{HOMO} \quad (3)$$

From voltammograms, E_{ox} and E_{red} values were found to be +0.86 V and -0.94 V for DBA, and +1.27 V and -1.09 V for SBP, respectively. E_{HOMO} , E_{LUMO} and E'_g values were calculated in the light of the formulas given above and -5.25 eV, -3.45 eV and 1.80 eV for DBA; for SBP, it was calculated as 5.66 eV, -3.30 eV and 2.36 eV, respectively. As a result of the polymerization, it was observed that the E'_g value increased due to the increased conjugation.

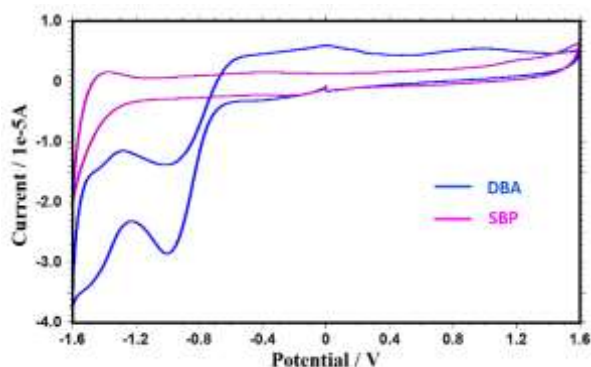


Figure 5. Voltammograms of DBA and SBP.

3.4. Conductivity of SBP

The conductivity measurement of SBP was made with the aid of a film formed on the glass surface using the casting method. After the analysis using the two-probe technique, the conductivity value of SBP was calculated as 2.35×10^{-10} S/cm. Since it was stated in the studies that the conductivity values of undoped poly(azomethine) compounds were generally observed in the range of $1 \times 10^{-9} - 1 \times 10^{-11}$ S/cm, the result was found to be compatible with previous studies[22]. Therefore, it turned out that the conductivity of the obtained SBP was low.

3.5. Thermal stability analysis

The thermal properties of the obtained polymer SBP were investigated by TGA and TGA-DTG-DTA curves are given in Figure 6. Accordingly, it was observed that the mass loss was 9.92% when heated up to 105°C, and this loss was due to the organic solvent and moisture in the sample. It was found that decomposition took place in four steps, except for moisture loss, and the total mass loss was 98.74%. The temperatures at which maximum mass loss

occurred in each step were found as 303 °C, 391 °C, 436 °C and 513 °C. As a result of heating at 1000 °C, the amount of residue was calculated as 1.26%. According to DTA analysis, exothermic peak was observed at 442°C due to mass loss.

The thermal stability of some of the poly(azomethine) studies, which were similar to the SBP obtained within the scope of the study, were given in Table 1. Accordingly, the thermal stability of the SBP obtained especially thanks to the sulfonic acid and thioether groups was found to be higher when compared to the reference studies [2,6,8].

3.6. Molecular weight and morphology of SBP

The molecular weight of the obtained polymer SBP was determined by gel permeation chromatography (Figure 7). Four types of molecular weight values were calculated from the GPC analysis results: Number average molecular weight (M_n), weight average molecular weight (M_w), peak average molecular weight (M_p) and Z average molecular weight (M_z). Accordingly, M_n , M_w , M_p and M_z values of SBP were calculated as 5050, 5150, 5000 and 5200 Da, respectively. Accordingly, it was revealed that the new material obtained was at the level of oligomers. In addition, the polydispersity index (PDI) calculated from the ratio of M_w to M_n and expressed as the width of the molecular weight distribution was found to be 1.020.

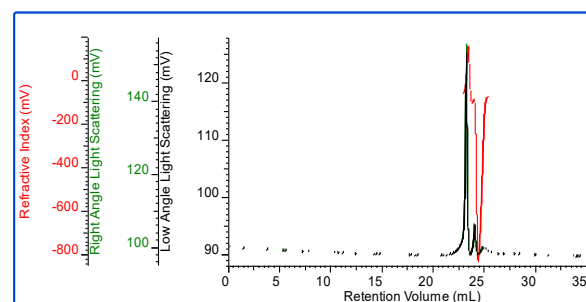


Figure 7. GPC analysis of SBP synthesis.

The structural properties of the obtained polymer were investigated by scanning electron microscopy (SEM). The SEM images given in Figure 8 showed that the obtained polymer SBP had an agglomerated structure. When the magnification was increased, the particles were found to have an irregular shape.

Table 1. Comparison of SBP with similar studies in references.

Polymers	Properties of polymer	Degradation temperature	Ref
Thiosemicarbazide base polymer	Thermally stable polymers	270 °C	2
Poly(phenoxy-imine)s	Photovoltaic properties	155 – 185 °C	6
Poly(azomethine)	Antimicrobial properties	230 – 335 °C	8
SBP	Thermally stable polymers	303 – 513 °C	in the study

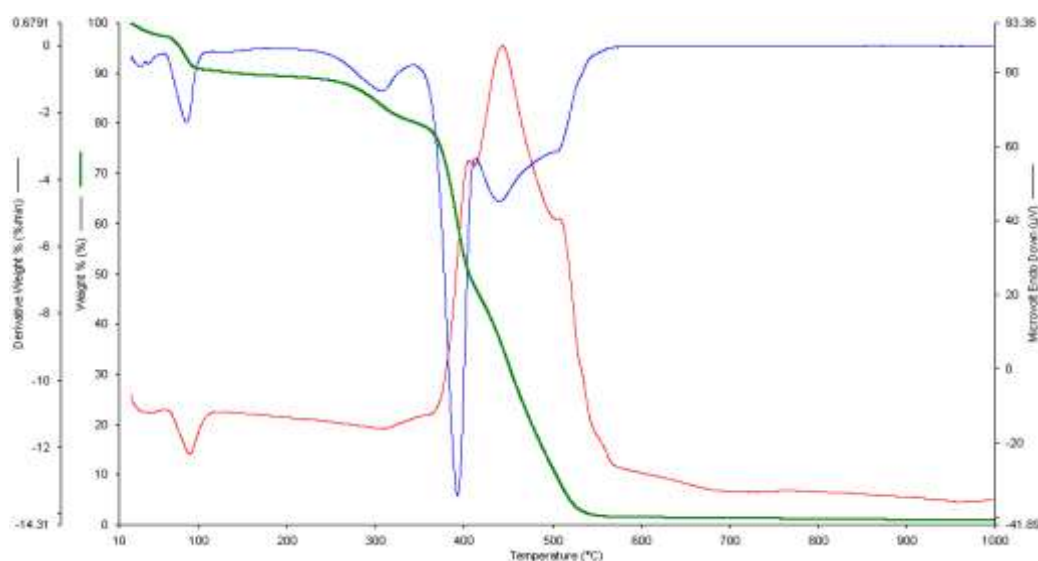


Figure 6. TGA-DTA-DTG curves of SBP.

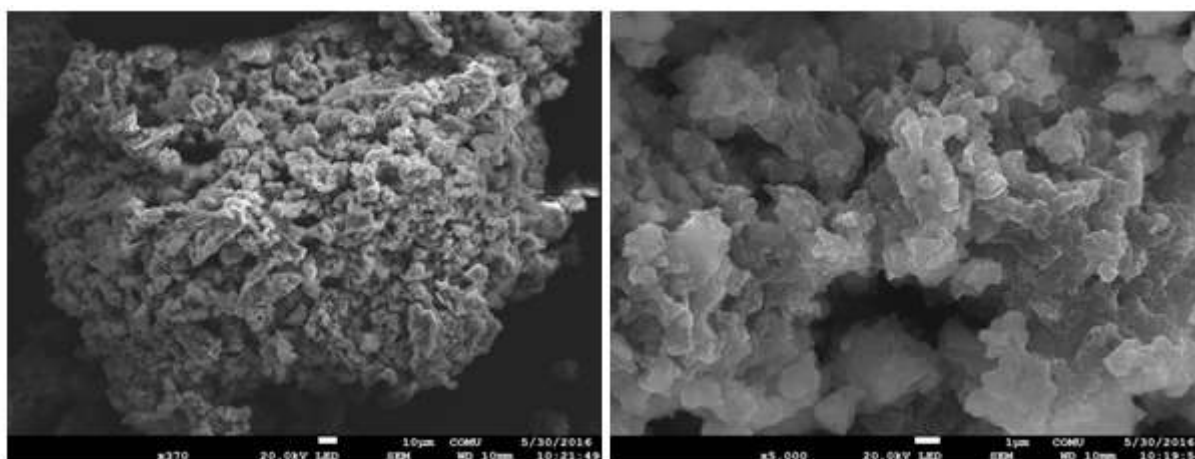


Figure 8. SEM images of SBP.

4. Conclusion

A dialdehyde compound (DBA) was synthesized by bromine elimination reaction using 4-bromobenzaldehyde from 4,4'-thiophenol, and characterized by FT-IR. SBP in poly(azomethine) structure was obtained by reaction of Schiff base from sulfonic acid derivative 4,4'-diamino-2,2'-biphenyl sulfonic acid and obtained DBA, and the structure of this unique polymer was elucidated by ¹H-NMR, ¹³C-NMR and FT-IR. Optical properties of both synthesized materials were examined by UV-Vis spectroscopy and E_g values were calculated. Depending on the imine group in the structure of SBP, the $n \rightarrow \pi^*$ transition was observed at 312 nm and the E_g value was calculated as 3.62 eV. E'_g values were calculated from the electrochemical properties of DBA and SBP examined by CV, and were

calculated as 1.80 eV and 2.36 eV, respectively, and it was revealed that this difference was due to the conjugate structure of the polymer. Also the conductivity of the SBP was measured and it was found that the 2.35×10^{-10} S/cm value and the electrical conductivity were very low.

The molecular weight of the obtained SBP was determined by GPC and it was found that the number average molecular mass was 5050 Da. It was found that SBP, which was found to be thermally stable, decomposed in four steps and the residual amount was 1.26% after heating at 1000 °C. In addition, it was determined by SEM images that the polymeric material had a rough surface.



Author's Contributions

Elif Karacan Yeldir: Made whole experiments and analyzed of results for the article. Drafted and wrote the manuscript.

Ethics

There are no ethical issues after the publication of this manuscript.

References

- [1]. Kamaci, UD, Kamaci, M, Peksel, A. 2017. Thermally Stable Schiff Base and its Metal Complexes: Molecular Docking and Protein Binding Studies. *Journal of Fluorescence*; 27: 805–817.
- [2]. Mighani, H. 2020. Schiff Base polymers: synthesis and characterization. *Journal of Polymer Research*; 27 (6): 168.
- [3]. Puchtler, H, Meloan, SN. 1981. On Schiff's bases and aldehyde-fuchsin: A review from H. Schiff to R.D. Lillie. *Histochemistry*; 72: 321–332.
- [4]. Nitschke, P, Jarzabek, B, Vasylieva, M, Honisz, D, Malecki, JG, Musiol, M, Janeczek, H, Chaber, P. 2021. Influence of chemical structure on thermal, optical and electrochemical properties of conjugated azomethines. *Synthetic Metals*; 273: 116689.
- [5]. Grigoras, M, Catanescu, CO. 2004. Imine oligomers and polymers. *Journal of Macromolecular Science: Part C: Polymer Reviews*; 44: 131–173.
- [6]. Kaya, İ, Aytan, B, Şenol D. 2018. Syntheses of poly(phenoxy-imine)s anchored with carboxyl group: Characterization and photovoltaic studies. *Optical Materials*; 78: 421–431.
- [7]. Karacan Yeldir, E, Erdener, D, Kaya, İ. 2022. Synthesis and characterization of a pyrene-based Schiff base and its oligomer: Investigation of fluorescent Cr³⁺ probe. *Reactive and Functional Polymer*; 170: 105097.
- [8]. Yılmaz Baran, N, Saçak, M. 2018. Preparation of highly thermally stable and conductive Schiff base polymer: Molecular weight monitoring and investigation of antimicrobial properties. *Journal of Molecular Structure*; 1163: 22–32.
- [9]. Avci, A, Kamaci, M, Kaya, I, Yildirim, M. 2015. Synthesis of Novel crosslinked Poly(azomethine-urethane)s: Photophysical and thermal properties. *Materials Chemistry and Physics*; 163: 301–310.
- [10]. Guo, Z, Sun, P, Zhang, X, Lin, J, Shi, T, Liu, S, Sun, A, Li, Z. 2018. Amorphous Porous Organic Polymers Based on Schiff-Base Chemistry for Highly Efficient Iodine Capture. *Chemistry - An Asian Journal*; 13: 2046–2053.
- [11]. Iwan, A. 2015. An overview of LC polyazomethines with aliphatic-aromatic moieties: Thermal, optical, electrical and photovoltaic properties. *Renewable and Sustainable Energy Reviews*; 52: 65–79.
- [12]. Jarzabek, B, Weszka, J, Hajduk, B, Jurusik, J, Domanski, M, Cisowski, J. 2011. A study of optical properties and annealing effect on the absorption edge of pristine- and iodine-doped polyazomethine thin films. *Synthetic Metals*; 161: 969–975.
- [13]. Marin, L, Perju, E, Damaceanu, MD. 2011. Designing thermotropic liquid crystalline polyazomethines based on fluorene and/or oxadiazole chromophores. *European Polymer Journal*; 47: 1284–1299.
- [14]. Iwan, A, Boharewicz, B, Tazbir, I, Filapek, M. 2015. Enhanced power conversion efficiency in bulk heterojunction solar cell based on new polyazomethine with vinylene moieties and [6,6]-phenyl C61 butyric acid methyl ester by adding 10-camphorsulfonic acid. *Electrochimica Acta*, 159: 81–92.
- [15]. Iwan, A, Sek, D. 2008. Processible polyazomethines and polyketanils: From aerospace to light-emitting diodes and other advanced applications. *Progress in Polymer Science*; 33: 289–345.
- [16]. Bhadra, J, Madi, NK, Al-Thani, NJ, Al-Maadeed, M.A. 2014. Polyaniline/polyvinyl alcohol blends: Effect of sulfonic acid dopants on microstructural, optical, thermal and electrical properties. *Synthetic Metals*; 191: 126–134.
- [17]. Jung, SH, Lee, TW, Kim, YC, Suh, DH, Cho, HN. 2003. Synthesis and characterization of fluorene-based poly(azomethines). *Optical Materials*; 21: 169–173.
- [18]. Wolska, J, Stawicka, K, Walkowiak-Kulikowska, J. 2021. Sulfonic-acid-functionalized polymers based on fluorinated methylstyrenes and styrene as promising heterogeneous catalysts for esterification. *Materials Chemistry and Physics*; 273: 125132.
- [19]. Hassan, MM. 2021. Energy-efficient dyeing of wool fabrics with sulfonic acid derivatives of aniline by oxidation polymerization. *Sustainable Materials and Technologies*; 29: e00290.
- [20]. Elibal, F, Gumustekin, S, Ozkazanc, H, Ozkazanc, E. 2021. Poly(N-methylpyrrole) with high antibacterial activity synthesized via interfacial polymerization method. *Journal of Molecular Structure*; 1242: 130712.
- [21]. Thangarasu, R, Dharmalingam, K, Ramasundaram, S, Elangovan, T, Balasundaram, ON, Pathak, TK. 2021. The role of polymeric surfactants on morphology and volatile organic compounds sensing efficiency of tennis bat like vanadium pentoxide nanorod. *Journal of Environmental Chemical Engineering*; 9: 105683.
- [22]. Çulhaoğlu, S, Kaya, I. 2015. Synthesis , Characterization , Thermal Stability and Conductivity of New Schiff Base Polymer Containing Sulfur and Oxygen Bridges. *Polymer(Korea)*; 39: 225–234.
- [23]. Kaya, I, Kolcu, F. 2018. Polymerization of Chrysoidine with chemical and enzymatic oxidative preference: Synthesis, characterization, and spectroscopic study. *Polymers for Advanced Technologies*; 29: 2515–2528.
- [24]. Olgun, U, Dikmen, Z, Çetin, H, Arıcan, F, Gülfe, M. 2022. Synthesis, optical dye properties and band gap energies of silver hydroxy-aryl thiazolo[5,4-d]thiazole complexes. *Journal of Molecular Structure*; 1250: 131816.
- [25]. Kaya, I, Karacan Yeldir, E. 2021. Comparative study on oxidative and enzyme catalyzed oxidative polymerization of aminophenol compound containing dihalogen. *Journal of Polymer Research*; 28: 1–16.

Phylogenetic Analysis of Mosquito (Diptera: Culicidae) Species with Mitochondrial Cytochrome Oxidase Subunit 1 Gene Distributed in Kocaeli

Fikriye Polat^{1*} , Serkan Dede² 

¹ Kocaeli University, Faculty of Education, Department of Mathematics and Science Education, Kocaeli, Türkiye

² Kocaeli University, Faculty of Arts and Science, Department of Biology, Kocaeli, Türkiye

* fikriyepolat@gmail.com

* Orcid: 0000-0002-5414-2501

Received: 8 October 2021

Accepted: 22 May 2022

DOI: 10.18466/cbayarfb.1007398

Abstract

Mosquitoes, which are in the Culicidae family and have blood-sucking properties, infect humans and animals with many diseases. The present study, it was aimed to detect the mosquito species spreading in Kocaeli province based on the DNA barcoding method. DNA isolation was performed using the samples of mosquitoes collected in the Kocaeli province between June 2017 and September 2018. Then, Polymerase Chain Reaction (PCR) and DNA sequence analysis were performed using universal primers of the mitochondrial COI gene. The sequences in FASTA format obtained with the Chromas program were compared with those of other mosquito species in the world through the NCBI-BLAST database. For phylogenetic analysis, the sequences were uploaded into the MEGA X program, and phylogenetic trees were created in the Maximum Likelihood method, Tamura-Nei Model (Tamura & Nei, 1993), Bootstrap 1000. Among mosquitoes collected in this study, 7 species belonging to *Aedes*, *Anopheles*, *Culiseta* and *Culex* genera were identified and characterized as *Aedes geniculatus* (n = 10), *Aedes albopictus* (n = 7), *Anopheles funestus* (n = 1), *Anopheles plumbeus* (n = 1), *Culiseta longiareolata* (n = 1), *Culex torrentium* (n = 1) and *Culex pipiens* complex sp. (n = 33). Within them, *Culex pipiens* complex sp. was found as the dominant species in Kocaeli. In conclusion, this study is the first molecular research of mosquito species spreading in Kocaeli which provides records to GenBank.

Keywords: *Aedes*, *Anopheles*, *Culex*, *Culiseta*, COI

1. Introduction

Mosquitoes are in the Culicidae family in the Nematocera suborder belonging to the Diptera order, and they are the only member within the family that have blood-sucking properties [1]. Pathogens transmitted by mosquitoes to animals and humans are arbovirus, helminths, and protozoa.

63 mosquito species have been found so far in Turkey. 12 of these species belong to *Anopheles* (*An.*), 16 to *Culex* (*Cx.*), 5 to *Culiseta* (*Cs.*), 26 to *Aedes* (*Ae.*), 2 to *Coquillettidia*, 1 to *Orthopodomyia* and 1 to *Uranotenia* (2). In Turkey, two studies revealing the characterization of *Cx. pipiens* complex members by genotyping have drawn attention [2, 3]. Günay (2) accomplished the characterization and barcoding of mitochondrial COI gene region of species including *Cx. (barraudius) modestus*, *Cx. laticinctus*, *Cx. mimeticus*,

Cx. perexiguus, *Cx. pipiens*, *Cx. pipiens* form *molestus*, *Cx. quinquefasciatus*, *Cx. theileri*, *Cx. torrent*, *Cx. tritaeniorhynchus*, and *Cx. hortensis* which had been determined that they belonged to the *Culex* genus by morphological analysis and distributed in the border of Turkey. In addition, Şahingöz Demirpolat et al. [4] investigated the *Cx. pipiens* complex and *Cx. torrentium* species based on the COI sequences in mosquito samples collected from the province of Kayseri. In the study performed by Öter and Tüzer [5], in total 992 of 1085 female mosquitoes were determined as *Cx. pipiens*, 32 were *Cs. longiareolata*, *An. maculipennis* (22), *An. claviger* (18), *Cs. annulata* (13), *Ae. vexans* (3), *Cx. hortensis* (3), and *Ochlerotatus* (2) based on morphological identification [5]. In the study performed by Çetin and Yanıkoğlu (2004), six mosquito species were identified based on morphological characters in Antalya [6]. These were *Cx. pipiens* Linnaeus, 1758, *Cx. martini* Medschid, 1930, *Cx. deserticola*

Kirkpatrick, 1924, *Ochleratus caspius* Pallas, 1771, *An. superpictus* Grassi, 1899, and *Cs. longiareolata* Macquart, 1838. They pointed out *Cx. pipiens* as the dominant species. Demirci et al. [7] made a study of SNP for 11 different gene regions belonging *Cx. theileri* from northeastern Turkey and created the first record for that type.

Topluoğlu et al. [8], in their study conducted in Sanlıurfa, collected the larvae and determined species as *Ansacharovi* (84%), which is a vector for malaria, and *Anopheles superpictus* (41%) based on morphological features. As of today, in the world, there are 531 *Anopheles* species of mosquitoes, 481 of them are known officially while 50 have not been named yet [9]. So far, 10 species belonging to that group have been identified in Turkey [8]. Öter et al. [5] made the molecular identification of *Ae. albopictus* using the COI barcode gene in Thrace region. In a study on morphological species identification of mosquitoes seen prevalently in the Felahiye district of Kayseri, 32.1% of 305 mosquitoes were found to be *Ae. vexans* and 67.9% were *Cx. pipiens* [10].

Kuçlu and Dik (2018) determined the mosquito fauna in the Western Black Sea Region (Bartın, Bolu, Karabük, Düzce, Zonguldak, Kastamonu) and identified 13 mosquito species belonging to the genera *Aedes*, *Anopheles*, *Culex* and *Culiseta*. They also morphologically identified *Ae. caspius*, *An. maculipennis*, *Cx. theileri* and *Cx. pipiens* which were dominant species. In a study conducted by Sarıkaya et al. [12] on refugee migration routes involving 17 provinces, 6 genera and 22 species were identified namely *Anopheles*, *Aedes*, *Coquillettia*, *Culex*, *Culiseta* and *Uranotaenia*.

When we investigated previous research in the northern region of Turkey, there were some considerable studies such as the molecular analysis of *Ae. albopictus* in the Western Thrace and the Eastern Black Sea region (Artvin, Hopa, Rize, Trabzon, Beğendik and İğneada) [5, 13], the detection of mosquito species seen in Istanbul [14], and the morphological determination of the mosquito species distributed in the Western Black Sea [11]. The distribution and species of mosquitoes have been determined from the study of these regions, from Western Thrace to the Eastern Black Sea Region, however, among these studies, there has been no study specifically focusing on Kocaeli situated in the Marmara region of Turkey.

The present study, has aimed to determine the species of mosquitoes at the molecular level based on the COI gene barcoding method in Kocaeli, where no detailed research has been conducted so far. We believe that this study would contribute additional information to the literature which is valuable for effective vector control management.

2. Materials and Methods

2.1. Collection of Samples

Mosquitoes were collected from 4 different locations in the Kocaeli province (Table 1) between June 2017 and September 2017 by selecting forest areas, resting places, and water edges with the help of mouth aspirators. The altitude values for the locations are 0-260 m for Izmit, 78-314 m for Derince, 223-232 m for Başiskele, and 464-823 m for Kartepe, respectively. The collected 54 adult mosquitoes were kept at -20°C in 70% ethyl alcohol until DNA isolation.

2.2. DNA Isolation-Polymerase Chain Reaction-DNA Sequencing

DNA isolation was performed using the Macherey-Nagel (Genomic DNA from insects, NucleoSpin DNA Insect, Catalog number 740470.50) following the procedures recommended by the company. DNA concentrations of the samples were measured using the Qubit 2.0 Fluorometer kit (Invitrogen, America). Primers for COI gene were as follows: 5'-GGTCAACAAATCATAAAGATATTGG-3' (forward) and 5'-TAAACTTCAGGGTGACCAAAAAATCA-3' [15]. 5x FIREPol Master Mix (Solis BioDyne) was used to prepare the PCR reaction mixture. The PCR reaction mix consisted of 6 µl 5x Master Mix, 0.5 µl 10 µM primer (sense), 0.5 µl 10 µM primer (antisense), 2 µl mold DNA. Bidistilled water was added to 30 µl for the PCR mixture of the gene region. PCR steps were involved: 5 min at 94°C (pre-denaturation), 35 cycles at 95°C for 60 s (denaturation), 60 s at 55 °C (annealing), 60 s at 72°C (extension), and 7 min at 72°C (final extension). The amplified COI gene PCR products were then for 30 minutes at 100 volts in 1,5% agarose gel electrophoresis and visualized with a UV transilluminator by using Safe-T staining (ethidium bromide alternative).

PCR products were purified by BM Lab using ExoSAP-ITTM PCR Product Cleanup Reagent (Thermo Fisher Scientific, USA) kit procedures. Sequence analysis was performed in the Macrogen Netherlands laboratory using the ABI 3730XL Sanger Sequencer (Applied Biosystems, Foster City, CA) and the forward and reverse primers of the COI gene.

2.3. Phylogenetic Analysis

The DNA sequences were visualized using the Chromas (Version: 2.6.5) program, and the sequences were recorded separately in the FASTA format with the Chromas program. The forward and reverse complement readings of the sequences were compared by aligning them with the ClustalW program [16]. The COI gene regions for all mosquito samples were deposited into the Genbank.

The similarities of the COI sequences of the same mosquito species with the sequences registered in the NCBI database (Table 2) were compared and used in

the phylogenetic tree. For evolutionary analysis, MEGA X [17] program was executed and modeling methods, genetic distance matrices, nucleotide compositions, nucleotide pair frequencies, substitution matrices for DNA barcode gene sequences of the samples were determined. Phylogenetic trees were created in the Maximum Likelihood method, Tamura-Nei Model [18], Bootstrap 1000.

3. Results

In this study, the coordinate and altitude information of the four districts in Kocaeli where mosquito samples were collected are shown in Table 1. The COI fragments belonging to the collected mosquitoes were analyzed by amplifying them three times, to obtain the highest quality sequence, and deposited in GenBank.

Phylogenetic analysis of the COI fragments for the sequences obtained from both the 4 populations of this study and other genera and mosquito species of Genbank enabled us to identify 7 species belonging to the genera *Culex*, *Aedes*, *Anopheles*, and *Culiseta* (Table 2). Findings for each species will be discussed separately.

3.1. *Aedes geniculatus*

9 out of 10 samples were obtained from Kartepe (MH392201, MH392202, MH392203, MH392204, MH392205, MH463069, MK713997, MK713999, MK714000), and 1 of them was from İzmit (MK713998). When the G-C ratios of *Ae. geniculatus*

were examined, it was found that the values varied between 31.2% and 32.3%. When considered together with the outgroups, the average G-C ratio was determined as 31.6% (17, 18). The average genetic distance among mosquitoes belonging to the genus *Aedes* was 0.017 (1.7%) (Data not shown here).

These results showed the values within the appropriate range of variation that could be seen among individuals representing the same species. The phylogenetic tree created at 0.0100 scale for *Ae. geniculatus* species is shown in Figure 1.

3.2. *Aedes albopictus*

Seven out of 17 *Aedes* genera mosquitoes were identified as *Ae. albopictus* as a result of the COI barcode gene examination (MK714010, MK714007, MK714003, MK713991, MK714006, MK714008, MK714009). When the G-C ratios of the samples were examined, it was determined that the values of *Ae. albopictus* varied between 30.7% and 32.5%. When considered together with the outgroups, the average G-C ratio was found as 32.3% (17, 18). The intra-species variation rate was determined as 0.16%. The lowest genetic distance was found to be 0, and the highest genetic distance was 0.0016. It is seen that different branches and clades are also separated from the 1000-repetitive bootstrap phylogenetic tree constructed with the sequences of other *Aedes* species obtained from GenBank (Figure 2).

Table 1. Mosquito species distributed in four different districts of Kocaeli (n: frequency, m: meter, Lon.: Longitude, Lat.: Latitude).

Districts		İzmit	Derince	Başiskele	Kartepe
Geo. Details (Lon., Lat.)		40.760071,29.928734	40.771936,29.816591	40.640383,29.938674	40.682336,30.136046
		40.822020,29.924783	40.834515,29.903672	40.639618,29.938382	40.656733,30.146763
Altitude (m)		0-375	78-315	223-232	464-823
Genus	species				
<i>Culex</i>	<i>pipiens complex</i> <i>sp</i> (n=33)	26	5	2	-
	<i>torrentium</i> (n=1)	-	-	1	-
<i>Aedes</i>	<i>geniculatus</i> (n=10)	1	-	-	9
	<i>albopictus</i> (n=7)	2	3	2	-
<i>Anopheles</i>	<i>funestus</i> (n= 1)	-	-	1	-
	<i>plumbeus</i> (n=1)	1	-	-	-
<i>Culiseta</i>	<i>longiareolata</i> (n=1)	1	-	-	-
Total (n=54)		31	8	6	9

Table 2. Accession numbers of mosquito species obtained from NCBI for use in phylogenetic trees for the COI DNA barcode gene.

Species	Accession numbers	Species	Accession numbers	Species	Accession numbers
<i>Ae. geniculatus</i>	KM258304.1	<i>An. funestus</i>	MK300232.1	<i>Cx. quinquefasciatus</i>	KF407473.1
<i>Ae. japonicus</i>	FJ641869.1	<i>An. funestus</i>	MH299888.1	<i>Cx. pipiens molestus</i>	FN395171.1
<i>Ae. notoscriptus</i>	MG242508.1	<i>An. eiseni</i>	MF172271.1	<i>Cx. torrentium</i>	KJ401313.1
<i>Ae. albopictus</i>	MH817529.1	<i>An. darlingi</i>	JF923693.1	<i>Cx. pipiens pallens</i>	KC407754.1
<i>An. funestus</i>	KJ522832.1	<i>An. annulipes</i>	MG712534.1	<i>Cx. hortensis</i>	KJ012068.1
<i>An. funestus</i>	MK300231.1	<i>An. plumbeus</i>	KM258215.1	<i>Cx. pipiens</i>	KM258167.1

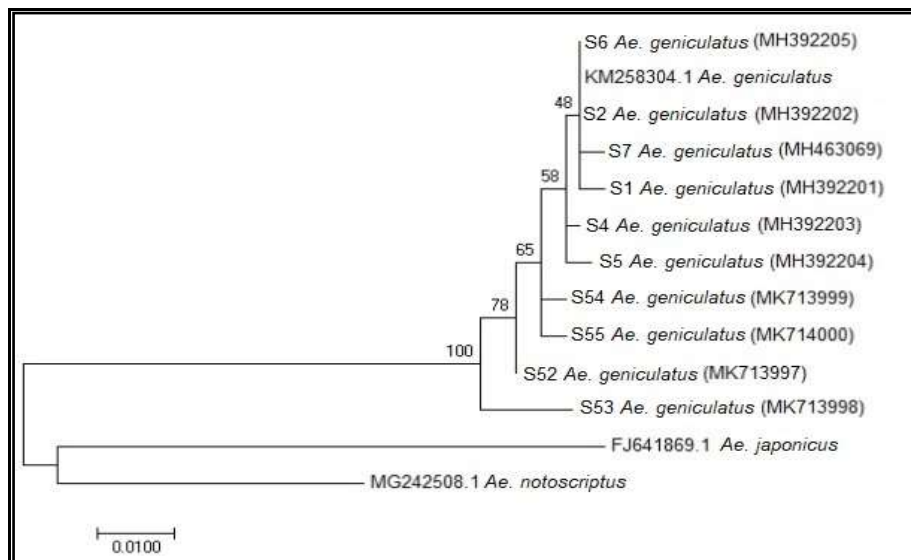


Figure 1. Molecular phylogenetic tree created by ML method for the COI gene region of *Aedes geniculatus*.

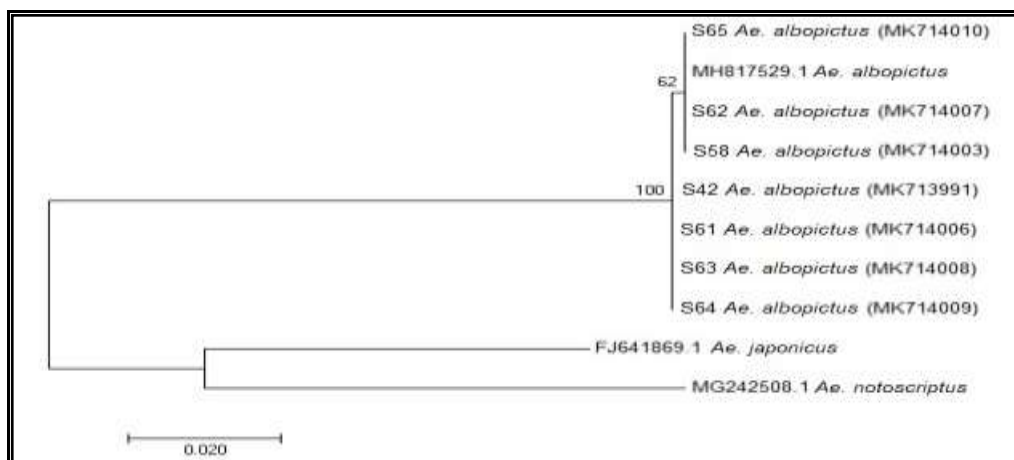


Figure 2. Molecular phylogenetic tree created by ML method for the COI gene region of *Aedes albopictus*

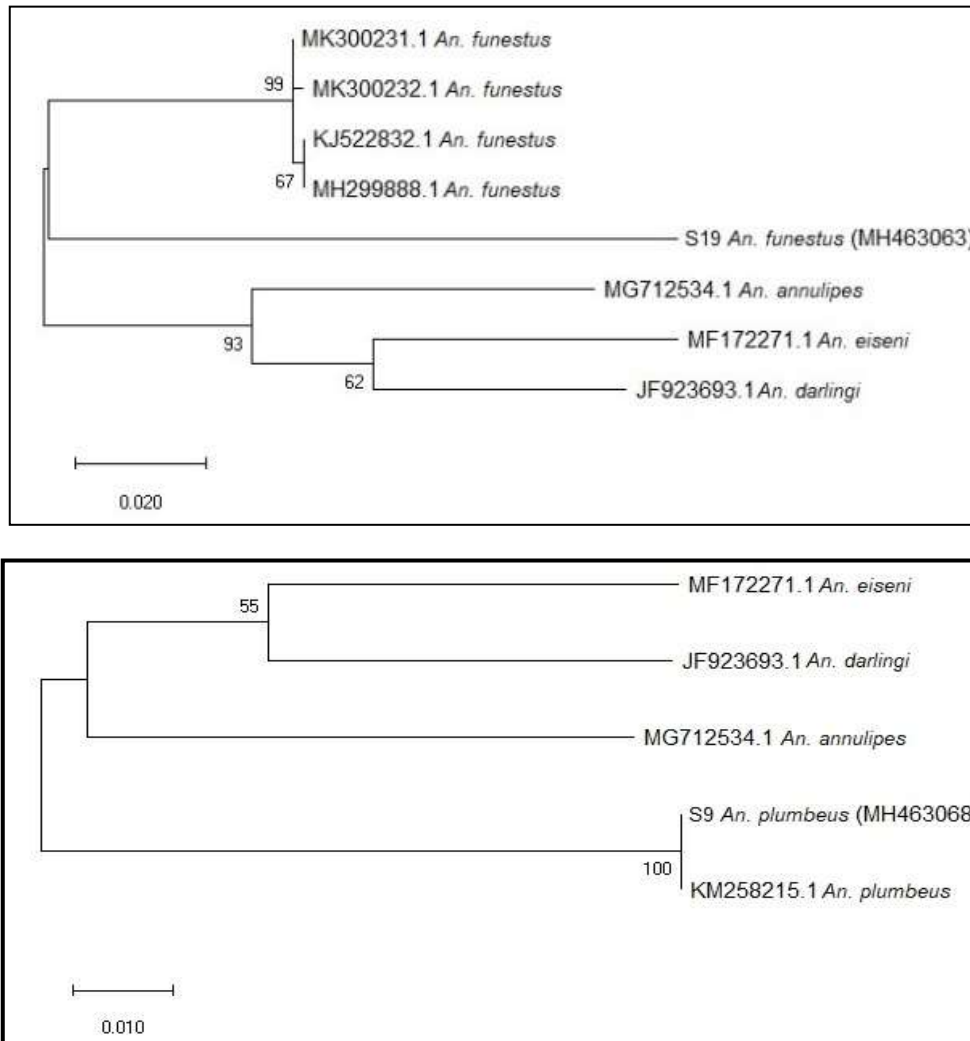


Figure 3. Molecular phylogenetic tree created by ML method for the COI gene region of *Anopheles funestus* (S19 MH463063) (upper) and *Anopheles plumbeus* (S9 MH463068) (below).

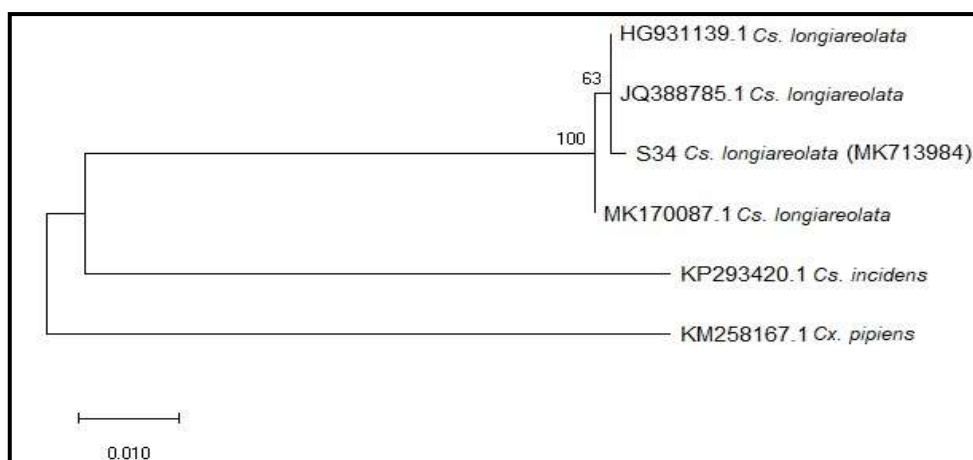


Figure 4. Molecular phylogenetic tree created by ML method for the COI gene region of *Culiseta longiareolata*.

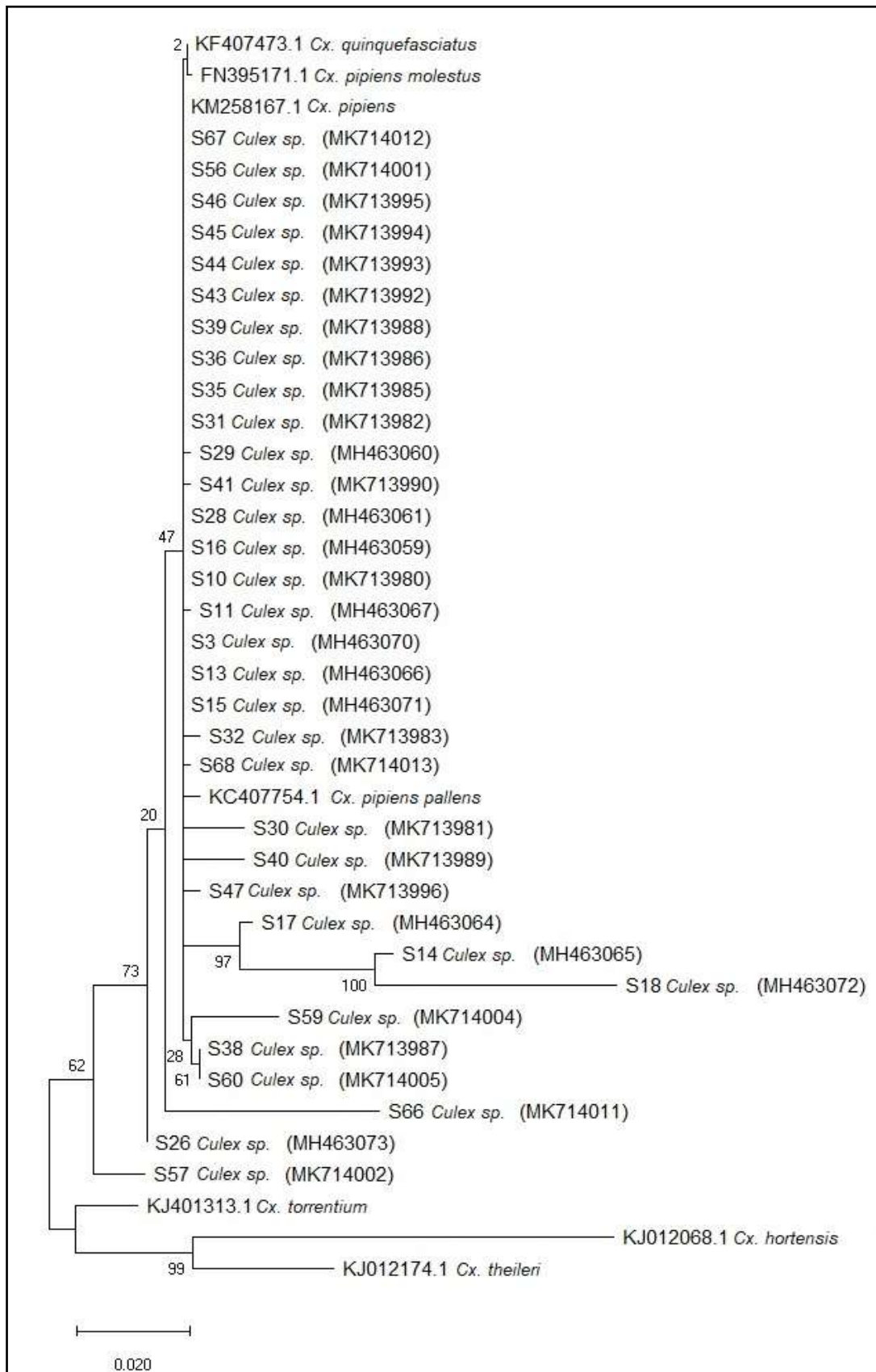


Figure 5. Molecular phylogenetic tree created by ML method for the COI gene region of *Cx. pipiens* complex *sp.*

3.3. *Anopheles funestus* and *Anopheles plumbeus*

One of the samples in Izmit was identified as *An. plumbeus* while in Başıskele *An. funestus* was found. When the G-C rates of *An. plumbeus* were examined, its ranged varied between 29.79% and 32.37%. When considered together with the outgroups, the average G-C ratio was determined as 31.09% [17, 19]. On the other hand, *An. funestus* was determined to vary between 29.86% and 34.99% in terms of G-C content [17, 18]. Phylogenetic trees obtained at 1000 bootstrap values are shown in Figure 3.

3.4. *Culiseta longiareolata*

As a result of the COI gene analysis one sample from Izmit was determined as *Cs. longiareolata* (MK713984). When the sequences belonging to other *Cs. longiareolata* species of the world were obtained from GenBank to be compared with the samples of our study, it was determined that the conserved region in the COI gene region was 99.69% and the variable region was 0.31%. In the pairwise genetic distance matrix created based on the Tamura 3-parameter model, the average genetic distance between mosquitoes belonging to the genus *Culiseta* was found to be 0.0554 (5.54%). The lowest genetic distance of *Cs. longiareolata* species was found to be 0, and the highest genetic distance was 0.0031 (0.31%). The phylogenetic tree created in 0.010 scale is shown in Figure 4.

3.5. *Culex species complex*

As a result of COI analysis, from mosquito species collected, 26 in Izmit, 5 in Derince, and 2 in Başıskele were determined as *Cx. pipiens* complexes. In addition,

1 sample in Başıskele was identified as *Cx. torrentium*. When the G-C rates of 33 *Cx. pipiens* complex *sp.* samples were examined, it was found that they varied between 30.70% and 32.25%. When considered together with the outgroups, the average G-C ratio was determined as 31.25% (Tamura & Nei, 1993; Kumar et al., 2018). Sequence data were deposited in GenBank (MH463070, MK713980, MH463067, MH463066, MH463065, MH463071, MH463059, MH463064, MH463072, MH463073, MH463061, MH463060, MK713981, MK713982, MK713983, MK713985, MK13983, MK713985, MK13983, MK713993, MK713994, MK713995, MK713996, MK714001, MK714002, MK714004, MK714005, MK714011, MK714012, MK714013). KM258167.1 (*Cx. pipiens*), KF407473.1 (*Cx. quinquefasciatus*), FN395171.1 (*Cx. pipiens molestus*), KJ401313.1 (*Cx. torrentium*), KC407754.1 (*Cx. pipiens pallens*), KJ012068.1 (*Cx. hortensis*) and KJ012174.1 (*Cx. theileri*) were chosen as the outgroups to the phylogenetic tree. The average genetic distance between mosquitoes belonging to the genus *Culex* was found to be 0.0137 (1.37%). The phylogenetic tree created at 0.020 scale is shown in Figure 5.

3.6. *Culex torrentium*

When 1 *Cx. torrentium* (MH463062) obtained from Başıskele was evaluated together with the outgroups selected from GenBank, it was found that there were differences in 2 nucleotides (0.31%) on a region with 634 base pairs long, and the genetic distance between mosquitoes of the same breed was 0.018 (1.8%). The phylogenetic tree created at 0.0050 scale is shown in Figure 6.

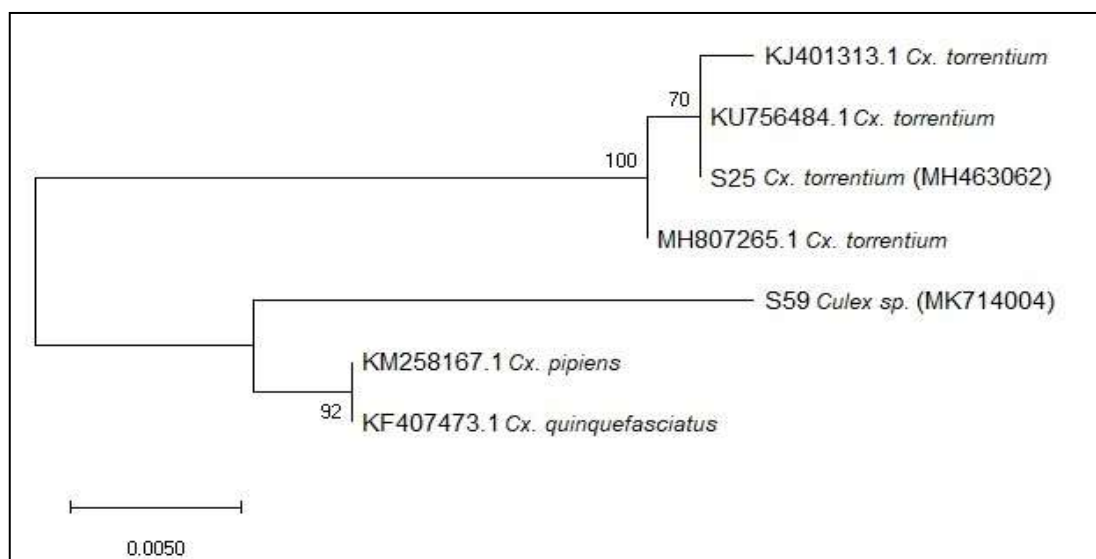


Figure 6. Molecular phylogenetic tree created by ML method for the COI gene region of *Cx. torrentium*.

4. Discussion and Conclusion

Considering that *Aedes*, *Anopheles*, and *Culex* mosquitoes are vectors for many important diseases, detailed information is needed on distribution and epidemiology of these mosquito species [4]. Studies on mosquitoes in Turkey have been generally based on morphology. Despite this, there have also been studies at the molecular level on the detection of mosquito species in recent years [2, 5, 6, 10, 20].

Mosquitoes belonging to the *Culex* genus are common in all climate types in our country. In our study, 34 out of 54 mosquitoes consist of two species belonging to the genus *Culex*. One of them belonged to *Cx. torrentium* and the others to the *Cx. pipiens* complex mosquitoes. Mosquitoes of the *Cx. pipiens* complex include species named as *Cx. pipiens form molestus*, *Cx. pipiens form pipiens* and *Cx. quinquefasciatus*. Unfortunately, these sibling species, whose identifications were difficult regarding morphology, could not be detected separately with the COI barcode gene in our study either. In the BLAST application of the NCBI genome database, the % similarity rates of these sibling species were almost the same. In our opinion, the COI barcode gene is not strong in distinguishing *Cx. pipiens* complex species. Thus, in the study by Laurito et al. [21] on *Culex* species in Argentina and Brazil using the COI gene, they pointed out that they were able to define species at the rate of 69%, but the remaining could be misidentified or not be identified. Şahingöz Demirpolat et al. [4] sampled 1052 female mosquitoes in their field study and analyzed 315 of them morphologically with diagnostic keys. As a result, they determined that 311 samples showed *Cx. pipiens* band profiles with ACE-2 and CQ11 microsatellite analysis. The remaining 4 samples were found to be hybrids of *Cx. pipiens form pipiens* and *Cx. pipiens form molestus* by microsatellite analysis (4).

In a study for molecular identification of the *Cx. pipiens* subspecies, the number of TG dinucleotide repeats in the microsatellite CQ11 region were compared [22]. Since there is no *Cx. torrentium* species in North America, the technique used in the study was effective in separating for *Cx. pipiens* s.s., *Cx. pipiens form molestus*, and *Cx. quinquefasciatus*. However, another study conducted in England reported that it would be insufficient to diagnose the above-mentioned species in the genus *Culex* with the COI DNA barcode gene and CQ11 region, and therefore it was shown that these genes could not be used for screening in Europe [23].

According to Morçişek et al. [24], although *Cx. pipiens* and *Cx. quinquefasciatus* are two different species in terms of physiology and behavior, they found the interspecific genetic sequence difference was 0.2%. However, it has been suggested that in most Diptera species, greater than 2% sequence divergence in the

COI gene is a threshold level for species limitation [25, 26].

Although there are some specific limitations in the use of DNA-based methods in the identification and classification of species, it has significant advantages compared to the use of conventional taxonomic methods. This sensitive method can be used in routine labs, and can make a more accurate and powerful diagnosis. The COI is the slowest changing region of all mitochondrial protein-encoding genes and is generally a good molecular tool in evolutionary genetic and interspecific and intraspecific variability studies [24]. However, as can be seen in this study, the COI gene was not effective in distinguishing *Cx. pipiens* sibling species.

Cx. pipiens, and *Cx. torrentium* are two morphologically similar sister species. When the *Cx. torrentium* (S25-MH463062) from our study was compared with the *Cx. torrentium* species from the study by Günay et al. [27] (KJ012236, KJ012242, and KJ012238) the similarity rate was found to be 100%. Likewise with *Cx. torrentium* samples recorded in data banks from different countries (KJ401313.1 (Denmark), HF562557.1 (Germany), KU756484.1 (Austria), and MH807265.1 (Austria)) the similarity rates were found to be quite distinctive and between 99.84% and 100%. With the present study, the first records for the *Cx. pipiens* complex and *Cx. torrentium* species in Kocaeli were created with the COI barcode gene.

Ae. geniculatus, which we recorded in the NCBI genome database, showed a similarity between 99-100% compared with the those from other countries. For *Ae. geniculatus*, which can be adapted to the waters accumulating in tree hollows during pre-adult periods [2] and has been registered previously in the Antalya, Bursa, Rize, Samsun, Edirne and Kırklareli provinces in Turkey [2, 28, 29], our study also determined it at the molecular level based on the COI gene region in Kocaeli and stored to NCBI-Nucleotide.

When the records in GenBank were compared, the similarity rate of the 7 *Ae. albopictus* we identified was between 99.8-100%. *Ae. albopictus*, known as the Asian Tiger Mosquito, has the potential to transmit approximately 32 viruses such as Dengue fever, Zika virus, Japanese encephalitis, Yellow fever, Western equine encephalitis, Venezuelan equine encephalitis [29]. Öter et al. [30] was the first to identify the *Ae. albopictus* species based on the DNA barcoding method in Kashan and Ipsala from the Thrace Region in Turkey. It was also detected in the Eastern Black Sea [31], the Black Sea coasts of the Thrace region and some districts of the European side in Istanbul, and registered to GenBank [2, 29]. In a study based on morphology, it was reported that *Ae. albopictus* specimen was found for the first time in Izmit-Kocaeli in August 2018 [32].

In our study carried out between June 2017 and September 2018, we also detected the same type of mosquito sample by using the COI barcode gene in 3 different locations in Kocaeli and recorded its information in the gene database. In a study conducted by Tuna Türkozan [13] using mitochondrial ND5 and COI genes, this mosquito species was detected in a large region including the Eastern Black Sea and the Thrace region. Then, in our study, it was also detected in a small region between mentioned areas and its first record at the molecular level was created by us. Therefore, it can be stated that *Ae. albopictus* is a mosquito species spreading along the Black Sea coast based on the data obtained from both this study and a study reported by Türkozan (2020).

An. plumbeus specimen with accession number MH463068 was 100% similar to the Belgian specimen, *An. plumbeus* with access number KM258215.1. *An. funestus* specimen, accession number MH463063 was slightly weaker supported by NCBI-registered species, at approximately 88%. It showed 87.81% similarity with the Kenya sample with the access number MK300231 and 87.71% with the American sample with the access number KJ522832.1. Unfortunately, we could not find any sample registered in GenBank from Turkey for *An. funestus*, so we did not have the opportunity to make a comparison. *An. plumbeus* has been reported to be found in forest areas up to 1200 m above sea level [33]. In our study, *An. plumbeus* was obtained at 225 m above sea level, while *An. funestus* was at 341 m in the forest area.

Cs. longiareolata, a vector for brucellosis, avian influenza and West Nile encephalitis, can be found in many areas such as swamps, septic tanks, and drainage channels, although it is found in similar habitats to *Culex* mosquitoes. Although it is known to be zoophilic, it is rarely fed with human blood [34]. According to the analysis results of *Cs. longiareolata* from NCBI BLAST, it was found to be 99.69%-99.85% similar to samples with access numbers JQ388785.1, MK170087.1, and HG931139.1. In a thesis study conducted by Günay [2] in 2015, mosquitoes belonging to the *Cs. longiareolata* species of the *Allotheobaldia* subgenus obtained from different cities were studied and 13 haplotypes within this species were determined. The first COI registration at Genbank for *Cs. longiareolata*, which was also found in Kocaeli, was achieved with this study.

In this study, the mitochondrial COI barcode gene was used. This barcode gene has high discriminatory power for *Aedes*, *Anopheles*, and *Culiseta* species, whereas it is effective for only one *Cx. torrentium* within *Culex* species. It was not possible to distinguish the sibling species belonging to the *Cx. pipiens* complex by using this DNA barcode gene. Knowing which barcode genes should be used for the definitive identification of vector

mosquitoes at the molecular level and species basis will enable us to reach practical information more easily. For this reason, to researchers who wish to study the phylogenetics of mosquito species, we suggest that they can try the following nuclear genes: IGS (Intergenic Spacer), ITS1 (Internal Transcribed Spacer 1), mitochondrial protein-coding regions ND1 (NADH dehydrogenase 1), ND2 (NADH dehydrogenase 2), COII (Cytochrome Oxidase Subunit 2), and cytb (cytochrome b apoenzyme).

As a result, from a total of 54 mosquito samples collected in Kocaeli between June 2017 and September 2018, 7 species belonging to 4 genera were identified with a molecular analysis based on the mitochondrial COI barcode gene. With this study, the first molecular records for the mosquito species in Kocaeli were created. The limitation of the study might be sample size which was relatively small.

Acknowledgement

Additional thanks to Ela Gök for proofreading this article.

Author's Contributions

Fikriye Polat: Drafted and wrote the manuscript, performed the experiment and result analysis.

Serkan Dede: Collection of mosquitoes, experimental study, DNA extraction, PCR.

Ethics

This study does not present any ethical concerns.

References

1. Kettle DS (1995). Medical and veterinary entomology. 2nd ed., CAB International, Wallingford, UK.
2. Günay F (2015). Türkiye sivrisinek faunası üzerine DNA barkodlama yöntemiyle moleküler analizler. Doktora Tezi, Hacettepe Üniversitesi, Fen Bilimleri Enstitüsü, Ankara.
3. Ergunay K, Gunay F, Erisoz Kasap O, Oter K, Gargari S, Karaoglu T, Tezcan S, Cabalar M, Yildirim Y, Emekdas E, Alten B and Ozkul A (2014). Serological, molecular and entomological surveillance demonstrates widespread circulation of West Nile Virus in Turkey. *PLoS Neglected Tropical Diseases*; 8, e3028.
4. Şahingöz Demirpolat G, İnci A, Yıldırım A, Düzlü Ö, Önder Z (2018). Kayseri yöresinde *Culex pipiens* biyotipleri ve *Culex torrentium*'un real time PCR ile araştırılması ve moleküler karakterizasyonu, *Ankara Üniversitesi Veterinerlik Fakültesi Dergisi*; 65 (3), 253-259.
5. Öter K, Tüzer E (2014). İstanbul'da sivrisinek türlerinin (Diptera: Culicidae) kompozisyonu. *İstanbul Üniversitesi Veterinerlik Fakültesi Dergisi*; 40 (2), 249-259.
6. Çetin H, Yanıkoğlu A (2004). Antalya kentinde bulunan sivrisinek (Diptera: Culicidae) türleri, üreme alanları ve baskın tür *Culex pipiens* L.'in bazı özellikleri. *Türk Entomoloji Dergisi*; 28, 283-294.

7. Demirci B, Lee Y, Lanzaro GC, Alten B (2012). Identification and characterization of single nucleotide polymorphisms (SNPs) in *Culex theileri* (Diptera: Culicidae). *Journal of Medical Entomology*; 49(3), 581-588.
8. Topluoğlu S, Karasartova D, Karaer ZK, Taylan-Özkan A (2020). Şanlıurfa yöresindeki anofel larvalarının morfolojik tanımlanması ve üreme alanlarının fiziksel ve ekolojik özelliklerinin araştırılması. *Türk Hijyen ve Deneysel Biyoloji Dergisi*; 77(2), 207-216.
9. URL1-Harbach RE. Genus *Anopheles* Meigen, 1818. Mosquito Taxonomic Inventory, 2015. <http://mosquito-taxonomic-inventory.info/genus-anopheles-meigen-1818#> (Access Date: 02/08/2021)
10. Bişkin Z, İnci A, Yıldırım A, Düzülü Ö (2010). Kayseri'nin Felahiye yöresinde yaygınlık gösteren sivrisinek (Diptera: Culicidae) türleri. *Sağlık Bilimleri Dergisi*; 19(2), 133-139.
11. Kuclu O, Dik B (2018). Mosquito (Diptera: Culicidae) fauna of Western Black Sea Region of Turkey. *Türkiye Parazitoloji Dergisi*; 42(2), 138-43.
12. Sarıkaya Y, (2017). Türkiye-Suriye sınırında yer alan mülteci kampları çevresinde ve mülteci göç yolları üzerindeki sivrisinek (Diptera: Culicidae) türlerinin tespit edilmesi. Yüksek Lisans Tezi, Hacettepe Üniversitesi, Fen Bilimleri Enstitüsü, Ankara.
13. Tuna Türkozan S (2019). Türkiye'de *Aedes* (*Stegomyia*) *albopictus* (Scue, 1894)'un populasyon genetiği ve ekolojik niş modellenmesi. Yüksek Lisans Tezi. Aydın Adnan Menderes Üniversitesi, Fen Bilimleri Enstitüsü, Aydın.
14. Öter K (2007). İstanbul'da görülen sivrisinek türlerinin tespiti. Doktora Tezi. İstanbul Üniversitesi, Sağlık Bilimleri Enstitüsü, İstanbul.
15. Ortman BD, Bucklin A, Pages F, Youngbluth M (2010). DNA barcoding the medusozoa using mtCOI. *Deep-Sea Research II*; 57(24-26), 2148-2156.
16. URL-2: <https://www.genome.jp/tools-bin/clustalw> (Access Date: 10/31/2019)
17. Kumar S, Stecher G, Li M, Knyaz C, Tamura K (2018). MEGA X: molecular evolutionary genetics analysis across computing platforms. *Molecular Biology and Evolution*; 35(6), 1547-1549.
18. Tamura K (1992): Estimation of the number of nucleotide substitutions when there are strong transition-transversion and G + C-content biases. *Molecular Biology and Evolution*; 9(4), 678-687.
19. Tamura K, Nei M (1993): Estimation of the number of nucleotide substitutions in the control region of mitochondrial DNA in humans and chimpanzees. *Molecular Biology and Evolution*; 10(3), 512-526.
20. Korkmaz S, Yıldırım A, Düzülü Ö, Çiloğlu A, Önder Z, İnci A (2016). Kayseri yöresinden toplanmış *Culex pipiens* komplekse ait sivrisinek (Diptera: Culicidae) örneklerinin kan beslenme identifikasyonu. *Türkiye Parazitoloji Dergisi*; 40, 199-204.
21. Laurito M, Oliveira TM, Almirón W.R, Sallum MAM, (2013). COI barcode versus morphological identification of *Culex* (*Culex*) (Diptera: Culicidae) species: a case study using samples from Argentina and Brazil. *Memorias do Instituto Oswaldo Cruz*; 108(suppl 1), 110-122.
22. Shaikevich EV, Vinogradova E., Bouattour A, Almeida APG (2016). Genetic diversity of *Culex pipiens* mosquitoes in distinct populations from Europe: contribution of *Culex quinquefasciatus* in Mediterranean populations. *Parasites Vectors*; 9, 47.
23. Danabalan R, Ponsonby DJ, Linton YM (2012). A critical assessment of available molecular identification tools for determining the status of *Culex pipiens* s.l. in the United Kingdom. *Journal of the American Mosquito Control Association*; 28(4 suppl), 68-75.
24. Morçişek B, Gocmen Taskin B, Doğaç E, Doğaroğlu T, Taskin V (2018). Evidence of natural *Wolbachia* infections and molecular identification of field populations of *Culex pipiens* Complex (Diptera: Culicidae) mosquitoes in Western Turkey. *Journal of Vector Ecology*; 43(1), 44-51.
25. Hebert PD, Cywinska A, Ball SL, deWaard JR (2003). Biological identifications through DNA barcodes. *Proceeding Biological Sciences/The Royal Society*; 270(1512): 313-321.
26. Hebert, PD, Ratnasingham S, J.R. deWaard JT (2003). *Barcoding animal life: COI divergences among closely allied species. Proceeding Biological Sciences/The Royal Society*; 270: S96-S99.
27. Günay F, Alten B, Simsek F, Aldemir A, Linton YM (2015). Barcoding Turkish *Culex* mosquitoes to facilitate Arbovirus Vector incrimination studies reveals hidden diversity and new potential vectors. *Acta Tropica*; 143, 112-120.
28. Şahin, İ (1984). Antalya ve çevresindeki sivrisinekler (Diptera: Culicidae) ve filariose vektörü olarak önemleri üzerinde araştırmalar. II. Sivrisinek Faunasını Belirlemek Amacıyla Yapılan Çalışmalar. *Doğa Bilimleri Dergisi* A2, 8: 385-396.
29. Şakacı Z (2018). Edirne merkez ilçesinde vektöriyel öneme sahip sivrisinek (Diptera: Culicidae) türlerinin araştırılması, Yüksek Lisans Tezi, Trakya Üniversitesi, Fen Bilimleri Enstitüsü, Edirne.
30. Öter K, Günay F, Tüzer E, Linton YM, Bellini R, Alten B (2013). First record of *Stegomyia albopicta* in Turkey determined by active ovitrap surveillance and dna barcoding. *Vector Borne and Zoonotic Diseases*; 13(10), 753-761.
31. Akiner MM, Demirci B, Babuadze G, Robert V, Schaffner F (2016). Spread of the invasive mosquitoes *Aedes aegypti* and *Aedes albopictus* in the Black Sea Region increases risk of Chikungunya, Dengue, and Zika Outbreaks in Europe. *PLoS Neglected Tropical Diseases*; 10(5), e0004664.
32. Şakacı Z (2021). Contribution to mosquito (Diptera: Culicidae) fauna of Sakarya province and the first record of the invasive vector *Aedes albopictus* (Skuse, 1894) for Kocaeli province. *BAUN Fen Bilimleri Enstitüsü Dergisi*; 23(1), 10-21.
33. Schaffner F, Thiéry I, Kaufmann C, Zettor A, Lengeler C, Mathis A, Bourgoin C (2012). *Anopheles plumbeus* (Diptera: Culicidae) in Europe: a Mere Nuisance Mosquito or Potential Malaria Vector? *Malaria Journal*, 11, 393.
34. Muslu H (2009): Manisa bölgesinde saptanan sivrisinek türleri (Diptera: Culicidae) ve bunların vektöriyel önemleri. Yüksek Lisans Tezi, Celal Bayar Üniversitesi, Fen Bilimleri Enstitüsü, Manisa.

The Quasi Parallel Curve of a Space Curve

Fatma GÜLER^{1*} 

¹ Department of Mathematics, Arts and Sciences Faculty, Ondokuz Mayıs University, Samsun, Turkey

* f.guler@omu.edu.tr

* Orcid: 0000-0002-5107-8436

Received: 22 June 2021

Accepted: 9 January 2022

DOI: 10.18466/cbayarfbe.955974

Abstract

A parallel or offset curve is defined as a curve whose points are a fixed distance from a given curve. These curves are not parallel transport. Often, it has a more complex mathematical structure than the first curve. Offset curves are important in numerically controlled machining, for example, where a biaxial machine defines the shape of the cut made with a round cutting tool. In this study, the quasi parallel curve is defined with the help of the quasi frame of a given curve. According to all selections of the projection vector, the quasi frame equations of this curve are expressed in terms of the quasi elements of the given curve. The curvatures of the quasi parallel curve were obtained depending on the quasi curvatures of the main curve. The study was supported by examples. The examples confirm that the quasi parallel curve is not parallel transport.

Keywords: Space curves, parallel curves, Frenet frame, q-frame

1. Introduction

Curves are the building blocks of differential geometry. The study of special curves has an important place in the theory of curves. A parallel curve or offset is defined as a curve whose points are at a constant normal distance from a given curve. Some of the offset curves that have been subject to many studies are involute evolute offsets, Bertrand offsets, Mannheim offsets curves. The authors studied Mannheim partner curves [1, 2]. The offset surface of a surface is at a constant distance from the surface. The offset surface appears as the expansion or contraction of the main surface. The authors are define Bertrand offset ruled surfaces and investigate the developable ruled surface conditions of these surfaces, [3]. In [4], They using networks of bicubic patches for approximating the offsets to general piecewise parametric surfaces. In [5,6], the authors are define the Mannheim offsets and the involute-evolute offsets of ruled surfaces. Offset surfaces are also seen in other subjects, [7,8]. Parallel curves are important, for example, in numerically controlled machining, where a two-axis machine defines the shape of the cut made with a circular cutting tool. The authors investigated motion of parallel curves and surfaces in Euclidean 3-space, [9]. The Frenet frame defined on the curve gives the properties of the curve. Alternative frame definitions are available in the literature for cases where the Frenet

frame cannot be defined. Rotation minimizing frame, which is among the most important of these, was defined by bishop, [10]. In [11], they defined a new frame for a space curve called as the q-frame. This frame can be defined even along a line. They They obtain some conditions for the given curve to be the inextensible flows of curves using the q-frame, [12]. The authors have researched the translation surfaces using q-frame, [13]. In [14] by using directional quasi fields, they obtain new optical conditions of quasi magnetic Lorentz flux. The authors have found relations between the motion of curves according to q-frame and the motion of their spherical image,[15]. In this paper, we define parallel curve using the q-frame of a curve and obtain its q-frame and q-curvature according to q-frame of given curve. Also, the study was supported by examples.

2. Materials and Methods

Let $\alpha : I \rightarrow \mathbb{R}^3$, $s \rightarrow \alpha(s)$ be a unit speed curve.

The orthonormal frame $\{T(s), N(s), B(s)\}$ is called the Frenet frame of the curve α , where

$T(s)$, $N(s)$, $B(s)$ are the unit tangent, the principal normal and the binormal vector fields of α , respectively, and they are defined by

$$\begin{aligned} T(s) &= \alpha'(s), \\ N(s) &= \alpha''(s)/\|\alpha''(s)\|, \\ B(s) &= T(s) \times N(s). \end{aligned} \quad (2.1)$$

The curvature $\kappa(s)$ and torsion $\tau(s)$ of α are given by $\kappa(s) = \|\alpha''(s)\|$, $\tau(s) = \langle N'(s), B(s) \rangle$. Then the famous Frenet formula is,

$$\begin{bmatrix} T'(s) \\ N'(s) \\ B'(s) \end{bmatrix} = \begin{bmatrix} 0 & \kappa(s) & 0 \\ -\kappa(s) & 0 & \tau(s) \\ 0 & -\tau(s) & 0 \end{bmatrix} \begin{bmatrix} T(s) \\ N(s) \\ B(s) \end{bmatrix}. \quad (2.2)$$

The q-frame $\{T, N_q, B_q, k\}$ of the curve $\alpha(s)$ is given by

$$T = \frac{\alpha'(s)}{\|\alpha'(s)\|}, \quad N_q = \frac{T \times k}{\|T \times k\|}, \quad B_q = T \times N_q, \quad (2.3)$$

where k is the projection vector.

If T and k are parallel, then the projection vector can be $k = (1, 0, 0)$ or $k = (0, 1, 0)$ or $k = (0, 0, 1)$, [11].

The relationship matrix between the Frenet frame $\{T, N, B\}$ and the q-frame $\{T, N_q, B_q, k\}$ of the curve $\alpha(s)$ is given by

$$\begin{bmatrix} T \\ N_q \\ B_q \end{bmatrix} = \begin{bmatrix} 1 & 0 & 0 \\ 0 & \cos\theta & \sin\theta \\ 0 & -\sin\theta & \cos\theta \end{bmatrix} \begin{bmatrix} T \\ N \\ B \end{bmatrix}, \quad (2.4)$$

where the angle θ between the principal normal N and quasi-normal N_q vectors. The first-order angular variation of the q-frame may be expressed as

$$\begin{bmatrix} T' \\ N'_q \\ B'_q \end{bmatrix} = \begin{bmatrix} 0 & k_1 & k_2 \\ -k_1 & 0 & k_3 \\ -k_2 & -k_3 & 0 \end{bmatrix} \begin{bmatrix} T \\ N_q \\ B_q \end{bmatrix}, \quad (2.5)$$

where $k_1 = \kappa \cos \theta$, $k_2 = -\kappa \sin \theta$, $k_3 = d\theta + \tau$ are the q-curvatures of the curve $\alpha(s)$, [11]

2. Results and Discussion

Definition: The quasi parallel curve or q-parallel curve $\bar{\alpha}(\bar{s})$ of a unit speed curve $\alpha(s)$ is defined by as

$$\bar{\alpha}(\bar{s}) = \alpha(s) + dB_q(s) \quad (3.1)$$

where d is a nonzero real constant, $s = s(\bar{s})$ is the arc length of $\alpha(s)$ and $B_q(s)$ is q-binormal vector fields of the curve $\alpha(s)$, and

$$\Omega = ds/d\bar{s} = 1/\sqrt{(1-dk_2)^2 + (dk_3)^2}.$$

If the derivative is taken from Eq. (3.1) according to the arc length s and using Eq. (2.5), then the tangent vector \bar{T} of q-parallel curve $\bar{\alpha}(\bar{s})$ is

$$\bar{T} = \Omega(1-dk_2)T - d\Omega k_3 N_q. \quad (3.2)$$

The q-normal vector \bar{N}_q and q-binormal vector \bar{B}_q of q-parallel curve $\bar{\alpha}(\bar{s})$ are

$$\bar{N}_q = \frac{\bar{T} \times k}{\|\bar{T} \times k\|}, \quad \bar{B}_q = \bar{T} \times \bar{N}_q, \quad (3.3)$$

where k is the projection vector.

Using Eqs. (3.1) and (3.3), we can write as follows corollaries.

Corollary 1. If chosen the projection vector $k = (1, 0, 0)$, then the relationship between the q-frame $\{\bar{T}, \bar{N}_q, \bar{B}_q\}$ of q-parallel curve $\bar{\alpha}(\bar{s})$ and the q-frame $\{T, N_q, B_q\}$ of the curve $\alpha(s)$ is given by

$$\begin{aligned} \bar{T} &= \bar{k}_1 T - \bar{k}_2 N_q \\ \bar{N}_q &= \bar{k}_2 B_q \\ \bar{B}_q &= -\bar{k}_2^2 T - \bar{k}_1 \bar{k}_2 N_q \end{aligned}, \quad (3.4)$$

where $\bar{k}_1 = \Omega(1-dk_2)$, $\bar{k}_2 = d\Omega k_3$.

Corollary 2. If chosen the projection vector $k = (0, 1, 0)$, then the relationship between the q-frame

$\{\bar{T}, \bar{N}_q, \bar{B}_q\}$ of q-parallel cuve $\bar{\alpha}(\bar{s})$ and the q-frame $\{T, N_q, B_q\}$ of the curve $\alpha(s)$ is given by

$$\begin{aligned} \bar{T} &= \bar{k}_1 T - \bar{k}_2 N_q \\ \bar{N}_q &= \bar{k}_1 B_q \\ \bar{B}_q &= -\bar{k}_1 \bar{k}_2 T - \bar{k}_1^2 N_q \end{aligned} \quad (3.5)$$

where $\bar{k}_1 = \Omega(1 - dk_2)$, $\bar{k}_2 = d\Omega k_3$.

Corollary 3. If the projection vector $k = (0, 0, 1)$, then the relationship between the q- frame

$\{\bar{T}, \bar{N}_q, \bar{B}_q\}$ of q-parallel cuve $\bar{\alpha}(\bar{s})$ and the q-frame $\{T, N_q, B_q\}$ of the curve $\alpha(s)$ is given by

$$\begin{aligned} \bar{T} &= \bar{k}_1 T - \bar{k}_2 N_q \\ \bar{N}_q &= -\bar{k}_2 T - \bar{k}_1 N_q \\ \bar{B}_q &= -(\bar{k}_1^2 + \bar{k}_2^2) B_q \end{aligned} \quad (3.6)$$

where $\bar{k}_1 = \Omega(1 - dk_2)$, $\bar{k}_2 = d\Omega k_3$.

Example 1: The unit speed helix curve

$\alpha(s) = \left(\frac{3}{5} \sin s, \frac{3}{5} \cos s, \frac{4}{5} s\right)$ (Figure 1., blue), has

the following q-frame

$$\begin{aligned} T &= \left(\frac{3}{5} \cos s, -\frac{3}{5} \sin s, \frac{4}{5}\right) \\ N_q &= (-\sin s, -\cos s, 0) \\ B_q &= \left(\frac{4}{5} \cos s, -\frac{4}{5} \sin s, -\frac{3}{5}\right) \end{aligned}$$

where the projection vector is $k = (0, 0, 1)$.

The q-parallel curve $\bar{\alpha}(\bar{s})$ of the curve $\alpha(s)$ is

$$\bar{\alpha}(\bar{s}) = \left(\frac{32}{5} \cos s + \frac{3}{5} \sin s, \frac{3}{5} \cos s - \frac{32}{5} \sin s, \frac{4}{5} s - \frac{24}{5}\right)$$

where $d=8$, (Figure 1., red).

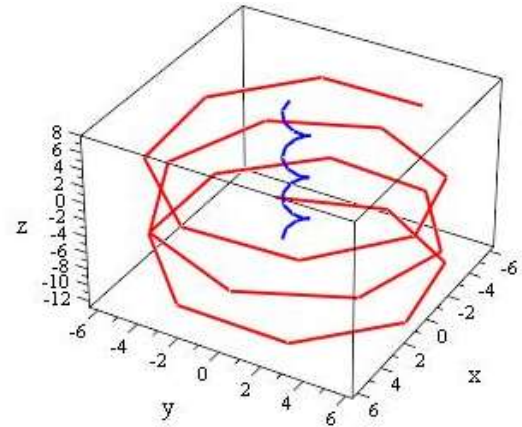


Figure 1. The helix curve and its q-parallel curve.

Example 2 : The curve $\alpha(s) = (s^3, s, s^2)$ (Figure 2., blue), has the following q-frame

$$\begin{aligned} T &= \frac{1}{\sqrt{9s^4 + 4s^2 + 1}}(3s^2, 1, 2s) \\ N_q &= \frac{1}{\sqrt{9s^4 + 1}}(1, -3s^2, 0) \\ B_q &= \frac{1}{\sqrt{(9s^4 + 4s^2 + 1)(9s^4 + 1)}}(6s^3, 2s, -9s^4 - 1) \end{aligned}$$

where the projection vector is $k = (0, 0, 1)$.

The q-parallel curve $\bar{\alpha}(\bar{s})$ of the curve $\alpha(s)$ is

$$\bar{\alpha}(\bar{s}) = \left(s^3 + \frac{48}{\sqrt{(9s^4 + 1)(9s^4 + 4s^2 + 1)}}, s + \frac{16s}{\sqrt{(9s^4 + 1)(9s^4 + 4s^2 + 1)}}, s^2 - \frac{8(9s^4 + 1)}{\sqrt{(9s^4 + 1)(9s^4 + 4s^2 + 1)}} \right)$$

where $d=8$, (Figure 2., red).

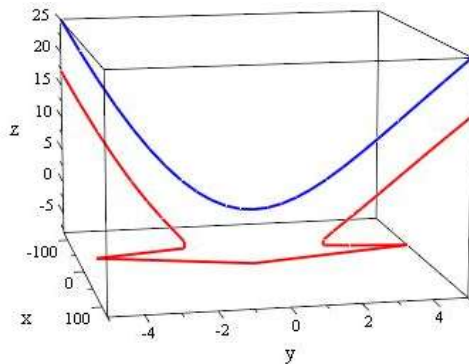


Figure 2. The curve $\alpha(s)$ and its q-parallel curve.

Example 3: The curve

$$\alpha(s) = \left(\frac{4}{5} \cos s, 1 - \sin s, -\frac{3}{5} \cos s \right)$$

(Figure 3., blue), has the following q-frame

$$T = \left(-\frac{4}{5} \sin s, -\cos s, \frac{3}{5} \sin s \right)$$

$$N_q = \left(-\frac{3}{5}, 0, -\frac{4}{5} \right),$$

$$B_q = \left(-\frac{4}{5} \cos s, -\frac{7}{25} \sin s, -\frac{3}{5} \cos s \right)$$

where the projection vector is $k = (0, 1, 0)$.

The q-parallel curve $\bar{\alpha}(\bar{s})$ of the curve $\alpha(s)$ is

$$\bar{\alpha}(\bar{s}) = \left(-\frac{36}{5} \cos s, 1 - \frac{19}{5} \sin s, -\frac{33}{5} \cos s \right)$$

where $d=10$, (Figure 3, red).

References

- [1] Wang, F., Liu, H., 2007. Mannheim partner curves in 3-Euclidean space. *Mathematics in Practice and Theory*, vol. 37, no. 1, pp. 141-143.
- [2] Liu, H., Wang, F., 2008. Mannheim partner curves in 3-space, *Journal of Geometry*, vol. 88, no. 1-2, pp. 120-126.
- [3] Ravani, B., Ku, T. S., 1991. Bertrand Offsets of ruled and developable surfaces, *Comp. Aided Geom.Design*, (23), No. 2.
- [4] R.T. Farouki, 1986. The approximation of non-degenerate offset surfaces, *Computer Aided Geometric Design*, Volume 3, Issue 1, Pages 15-43, ISSN 0167-8396.
- [5] Orbay, K., Kasap, E., Aydemir, I, 2009 .Mannheim Offsets of Ruled Surfaces, *Mathematical Problems in Engineering*, Volume, Article ID 160917.
- [6] Kasap E, Yüce S, Kuruoğlu N. 2009. The involute-evolute offsets of ruled surfaces. *Iranian J Sci Tech Transaction A*; 33: 195-201.
- [7] Güler, F., Bayram, E., & Kasap, E. 2018. Offset surface pencil with a common asymptotic curve. *International Journal of Geometric Methods in Modern Physics*, 15(11), 1850195.

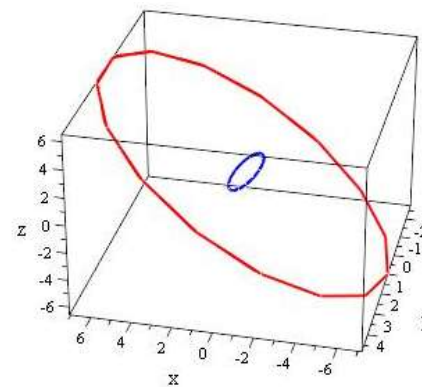


Figure 3. The curve $\alpha(s)$ and its q-parallel curve.

3. Conclusion

The parallel or offset curve points is a curve with a fixed distance from a given curve which are not parallel transport. In this study, we defined the q-parallel curve of a given curve. The equations of the q- frame of the q-parallel curve were obtained according to q-frame of given curve. Also, the curvatures of q-parallel curve are obtain. It was supported by the examples given that the q-parallel curve is not a parallel transport of the main curve.

Author's Contributions

Fatma Güler: Drafted and wrote the manuscript.

Ethics

There are no ethical issues after the publication of this manuscript.

- [8] Güler, F. 2021. Offset Trajectory Planning of Robot End Effector and its Jerk with Curvature Theory. *International Journal of Computational Methods*, 18(10), 2150050.
- [9] Aldossary, M. T., & Gazwani, M. A.2020. Motion of Parallel Curves and Surfaces in Euclidean 3-Space R3. *Geometry-math-journal.ro*.
- [10] Bishop, Richard L. 1975. There is more than one way to frame a curve. *American Mathematical Monthly* : 246-251.
- [11] Dede, M., Ekici, C., & Tozak, H. 2015. Directional tubular surfaces. *International Journal of Algebra*, 9(12), 527-535.
- [12] Baş, S., & Körpınar, T. 2018. Directional Inextensible Flows of Curves by Quasi Frame. *Journal of Advanced Physics*, 7(3), 427-429.
- [13] Tozak, H., Dede, M., & Ekici, C. 2020. Translation surfaces according to a new frame. *Caspian Journal of Mathematical Sciences (CJMS)*, 9(1), 56-67.
- [14] Körpınar, T., Demirkol, R. C., Körpınar, Z., & Asil, V. 2021. New magnetic flux flows with Heisenberg ferromagnetic spin of optical quasi velocity magnetic flows with flux density. *Revista Mexicana de Física*, 67(3 May-Jun), 378-392.
- [15] Yazla, A., & Sariaydin, M. T. 2020. On Surfaces Constructed by Evolution According to Quasi Frame. *Facta Universitatis, Series: Mathematics and Informatics*, 605-619.

Effects of Zinc oxide Nanoparticles (ZnO NPs) on Hemocyte Types of *Galleria mellonella*

Ata Eskin^{1*} 

¹Department of Plant and Animal Production, Avanos Vocational School Of Fine Arts, Nevşehir Hacı Bektaş Veli University, Nevşehir, Türkiye

* ataeskin@nevsehir.edu.tr

* Orcid: 0000-0002-7953-654X

Received: 31 August 2021

Accepted: 27 May 2022

DOI: 10.18466/cbayarfbe.989240

Abstract

In this study, 70 nm-sized and nanorod-shaped ZnO NPs concentrations (0.5, 1, 2.5, 5, and 10 µg/10 µl) was force-fed to fourth instar (110 ± 20 mg) *Galleria mellonella* (Lepidoptera: Pyralidae) larvae. The effects of ZnO NPs on plasmatocyte, granulocyte, spherulocyte, prohemocyte, oenocytoid, and coagulocyte numbers in hemolymph of *G. mellonella* larvae was determined. Results showed that treating *G. mellonella* with 10 µg/10 µl ZnO NPs significantly decreased spherulocytes numbers, whereas numbers of plasmatocyte, granulocyte, prohemocyte, oenocytoid, and coagulocyte numbers did not differ significantly when compared to the control group after 24 h force feeding treatment. There was a statistically significant difference between the experimental groups in the prohemocyte numbers of larvae that exposed to 1 and 5 µg/10 µl ZnO NPs.

Keywords: *Galleria mellonella*, Hemocyte Type, Nanoparticle, Zinc Oxide.

1. Introduction

Nanomaterials are material arrangements at a scale of about 1 to 100 nanometers in length that have unique features because of their size [1]. Different sizes and diameters of nanomaterials are frequently used in a variety of industrial fields because of the rapid development of nanotechnologies [2]. Zinc oxide Nanoparticles (ZnO NPs), because of their absorption of UV light, their catalytic, antimicrobial, semiconducting, the use of nanoparticles in consumer products is currently increasing [3]. Because of such intensive use of nanoparticles, reliable methods for predicting any associated toxicity are important [4]. Today, there are some studies on nanoparticle toxicity that have been carried out using model experimental organisms with force-feeding method [5-8]. With force-feeding method, the changes that occur in the larvae after the material used in the experiment can be reliable and timing of the changes taking place is possibly [9]. *Galleria mellonella* L. (Lepidoptera: Pyralidae) larvae are a good model for carrying out toxicity studies [10]. Additionally, *G. mellonella* is a very inexpensive insect species which can be

produced in large numbers under laboratory conditions. In our previous study, we determined the lethal concentration values of ZnO NPs on the fourth instar *G. mellonella*, effects of different ZnO NPs concentrations (0.5, 1, 2.5, 5 µg/10 µl) on the hemocyte counts, and the percentage of dead cells of larvae with two different methods [5]. Also, transmission electron microscopy image, lethal concentration 50 (LC₅₀) values of ZnO NPs, and the percentage of dead cells of force fed *G. mellonella* larvae after 24 h the treatments have been described by us [5]. But the objective of the present study is to evaluate the effect of nanorod-shaped ZnO NPs on hemocyte types in *G. mellonella*. For this purpose, the effects of the ZnO NPs (0.5, 1, 2.5, 5, and 10 µg/10 µl/larva) was tested in the hemolymph of *G. mellonella* larvae after ZnO NPs exposure by the force-feeding method. In addition, a different ZnO NP (10 µg/10 µl ZnO NP) concentration was additionally tested for the first time with this study.

2. Materials and Methods

2.1. Insects

Different life stages (egg, larvae, and pupae) of *G. mellonella* were obtained from the infested midrib of the wax combs.

2.1.1. Insect diet

The collected samples were placed and reared with wax combs in jars (1 l capacity). The eggs laid by the adult moths who had emerged were also collected. The first stage larvae hatched from the eggs were again placed and reared with wax combs in jars (1 l capacity). The control (untreated) and experiment group larvae (NP treated) were reared in dark conditions at 27 ± 4 °C with $60 \pm 5\%$ relative humidity. All insect rearing cultures and experimental studies of NPs were studied at Avanos Vocational School of Fine Arts Avanos, Nevşehir, Turkey. Fourth instar (110 ± 20 mg) *G. mellonella* larvae were used in all, force-feeding studies [5].

2.2. Chemicals and Materials

The nanoparticle used in this study is a commercial product of Alfa Aesar (Zinc oxide, NanoShield®, 70 nm, ZN-3008C, 50% in H₂O, colloidal dispersion with cationic dispersant, Karlsruhe, Germany). Other materials used in the experiment are distilled water, 29 gauge micro-fine insulin syringe, ultrasonic bath sonicator (Isolab, Turkey), 20 ml plastic containers, giemsa stain solution (Bertek Chemistry, Lot no: P260417), filter paper (Grade 4, Whatman, Dia. 150 mm), Swift SW380T microscope (China), and Swift microscope camera (China) [5].

2.3. Force-Feeding Treatment

Firstly, stock concentrations of ZnO NPs (0.5, 1, 2.5, 5, and 10 µg/µL) were prepared. Then, they were sonicated for 10 min of duration with a bath-type sonicator [5]. 110 ± 20 mg weighed larvae were force-fed with 10 µL of the homogenized ZnO NPs concentrations (0.5, 1, 2.5, 5, and 10 µg/µL) or 10 µL distilled water with a micro-fine insulin syringe (29 gauges) [5, 11]. Postforce-feeding treatment, each larva was kept in a sterile plastic box (20 ml) without natural wax in dark conditions at 26 ± 3 °C with $60 \pm 5\%$ relative humidity. Hemocyte types and numbers in the hemolymphs of the control and experimental group larvae were determined by a giemsa staining method for 24 h post force-feeding treatment.

2.4. Use of Giemsa to Stain Hemocytes for Classification by Light Microscope

The dye-staining steps of the insect hemocytes were carried out at room temperature based on [7] with some modifications as follows. Giemsa stain was diluted 1:4 with distilled water. The diluted stain solution was filtered by whatman paper. Larvae were drilled from the first segment on the back of the head with a fine needle, and 5 µL hemolymph was taken with a micropipette. Hemolymph was smeared onto clean and dry slide immediately. Slides were incubated in 96% ethanol for 5 min. Afterwards, it was waited until the ethyl alcohol completely evaporated from the slides. Then a giemsa protocol was applied. The diluted giemsa solution was dropped onto the slides and the dye was allowed to stain the hemocytes for 15 min. The slides were washed in distilled water for 2 min. Finally, the slides dried for 15 min at room temperature, and then they mounted on a coverslip with entellan. 200 hemocytes were randomly selected in each slide. Each slide was scanned under a light microscope (Swift SW380T, China) at a magnification of 1000x with a Swift microscope camera (China). The types of these selected hemocytes (plasmacyte, granulocyte, spherulocyte, prohemocyte, oenocytoid, and coagulocyte) were classified (Figure 1) and counted separately according to [12, 13]. Five larvae were examined for each experimental group and were replicated three times. A total of 18.000 hemocytes were examined one by one at random, and the type of each hemocyte was determined and counted. The significance levels of differences between the control and experimental groups were determined separately for each type of hemocytes.

2.5. Statistical Analysis

IBM-SPSS (Version 20.0) was used for mean numbers of plasmacyte, granulocyte, spherulocyte, prohemocyte, oenocytoid, and coagulocyte analysis of *G. mellonella*. The parametric Tukey test was used for when data were normally distributed [14].

3. Results and Discussion

3.1. Hemocyte Types

The hemocytes were classified into six morphotypes, as plasmacyte (Figure 1.a), granulocyte (Figure 1.b), spherulocyte (Figure 1.c), prohemocyte (Figure 1.d), oenocytoid (Figure 1.e), and coagulocyte (Figure 1.f).

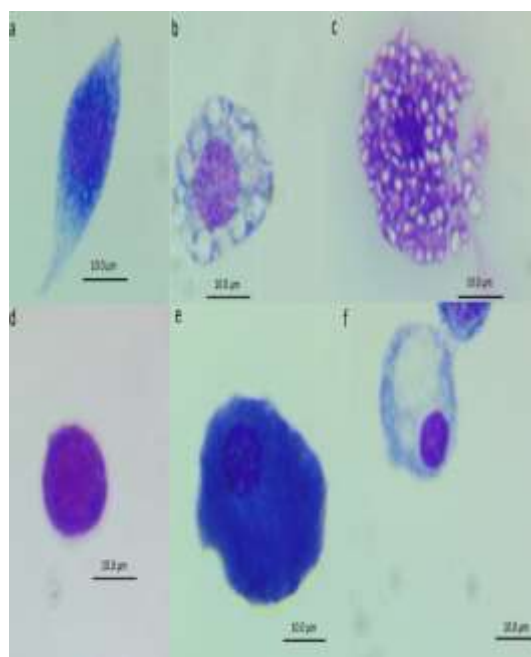


Figure 1. Types of hemocytes in *Galleria mellonella* larvae stained with Giemsa; a. plasmatocyte, b. granulocyte, c. spherulocyte, d. prohemocyte, e. oenocytoid, f. coagulocyte (measure bar: 10 µm; X100).

When we summarize the morphology and functions of the counted and typed hemocytes; plasmatocyte, granulocyte, spherulocyte, prohemocyte, oenocytoid, and coagulocytes are types of hemocytes that can be found in *G. mellonella* and some insect species [12, 13]. Granulocytes and plasmatocytes are the only hemocytes adhering to foreign organisms, so they can participate in phagocytosis, encapsulation and nodulation [15, 16]. Plasmatocytes are usually spindle-shaped (10-20 µm) or round (about 10 µm in diameter) (Figure 1.a) [17]. Granulocytes are highly nonameboid, round or oval cells, 12-16 µm in diameter, with a central nucleus that is often masked by large numbers of granules, 1-1.5 µm in diameter (Figure 1.b) [17]. Spherulocytes are responsible for the synthesis and transportation of mucopolysaccharidic components of the cuticle. They are ovoid or round cells of varying sizes (9-25 µm in length and 5-10 µm in width) and usually larger than granulocytes (Figure 1.c) [15-17]. Prohemocytes are considered stem cells, capable of mitotic division and specialized hemocyte differentiation [15, 16]. Prohemocytes are small, round to oval cells with a thin cytoplasmic margin, about 6-13 µm in diameter (Figure 1.d) [17]. Oenocytoids contain the cytoplasmic form of phenol oxidase, do not adhere to foreign bodies. They are small to large, thick, oval, spherical or elongated cells of highly variable sizes and shapes (16-54 µm or more) (Figure 1.e) [15, 16]. Coagulocytes generally range from small to large cells (3-30 µm long), spherical, transparent, fragile, and combine the characteristics of granulocytes and oenocytoids [17, 18].

3.2. Effects of (ZnO NPs) on Hemocytes Types of *G. mellonella*

The effects of ZnO NPs on mean numbers of plasmatocyte, granulocyte, spherulocyte, prohemocyte, oenocytoid, and coagulocyte in hemolymph of *G. mellonella* larvae was given in Table 1 below. Microscopic observations indicated that plasmatocytes were the most frequent hemocyte type. Also, plasmatocytes, granulocytes, and spherulocyte are the most numerous cells in the hemolymph of *G. mellonella* (Table 1). Coagulocytes were the least seen hemocyte type among hemocyte types. The mean numbers of six different hemocyte types according to the lowest and highest values in the table were as follows: 102.2 (1 µg/10 µl ZnO NPs) to 111.73 (5 µg/10 µl ZnO NPs) for plasmatocytes, 60.46 (5 µg/10 µl ZnO NPs) to 76.53 (10 µg/10 µl ZnO NPs) for granulocytes, 9.93 (10 µg/10 µl ZnO NPs) to 18.2 (control group) for spherulocytes, 4.73 (1 µg/10 µl ZnO NPs) to 11.13 (5 µg/10 µl ZnO NPs) for prohemocytes, 1.40 (10 µg/10 µl ZnO NPs) to 2.53 (1 µg/10 µl ZnO NPs) for oenocytoids, 0.46 (control and 0.5 µg/10 µl ZnO NPs) to 1.13 (10 µg/10 µl ZnO NPs) for coagulocytes. When evaluated in terms of the response of different hemocytes to the ZnO NPs exposure to the density of hemolymph, no statistically significant difference was observed between the control and experimental groups, except for the spherulocytes population (Tukey Test, Plasmatocyte: F: 0.534; df: 5; sig: 0.750, Granulocyte: F: 1.874; df: 5; sig: 0.108, Spherulocyte: F: 2.421; df: 5; sig: 0.042, Oenocytoid: F: 0.857; df: 5; sig: 0.514, Coagulocyte:

F: 0.981; df: 5; sig: 0.434) (Table 1). The mean number of spherulocytes significantly decreased 1.83 times in larvae exposed to the highest concentration of ZnO NPs (10 µg/10 µl) when compared to the control group. The mean number of *G. mellonella* larval prohemocytes that exposed to 5 µg/10 µl ZnO NPs

was 2.35 times higher than the larvae exposed to 1 µg/10 µl ZnO NPs concentration (Table 1). This 2.35-fold increase in prohemocyte mean was statistically significant (Tukey Test, Prohemocyte: F: 3.069; df: 5; sig: 0.014) (Table 1).

Table 1. Effects of ZnO NPs on mean numbers of plasmatocyte, granulocyte, spherulocyte, prohemocyte, oenocytoid, and coagulocyte in hemolymph of *Galleria mellonella* larvae (Mean ± Standard Error).

Concentrations of ZnO NPs (µg/10 µl)	Plasmatocyte (Mean ^b ± SE) ^c	Granulocyte (Mean ^b ± SE) ^c	Spherulocyte (Mean ^b ± SE) ^c	Prohemocyte (Mean ^b ± SE) ^c	Oenocytoid (Mean ^b ± SE) ^c	Coagulocyte (Mean ^b ± SE) ^c
0 ^a	110.26 ± 4.22 ^a	62.6 ± 4.86 ^a	18.2 ± 2.49 ^a	6.73 ± 0.98 ^{ab}	1.73 ± 0.38 ^a	0.46 ± 0.27 ^a
0.5	107.33 ± 5.3 ^a	70.73 ± 4.1 ^a	11.33 ± 1.8 ^{ab}	8.2 ± 1.81 ^{ab}	1.93 ± 0.57 ^a	0.46 ± 0.23 ^a
1	102.2 ± 4.9 ^a	76.4 ± 5.56 ^a	13.13 ± 1.83 ^{ab}	4.73 ± 0.86 ^a	2.53 ± 0.47 ^a	1 ± 0.35 ^a
2.5	111.4 ± 5.27 ^a	64.4 ± 5.15 ^a	14.73 ± 1.65 ^{ab}	6.33 ± 1.05 ^{ab}	2.26 ± 0.50 ^a	0.86 ± 0.37 ^a
5	111.73 ± 5.18 ^a	60.46 ± 6.37 ^a	13.13 ± 1.85 ^{ab}	11.13 ± 1.97 ^b	2.33 ± 0.39 ^a	1.20 ± 0.29 ^a
10	106 ± 5.43 ^a	76.53 ± 4.49 ^a	9.93 ± 1.19 ^b	5 ± 0.98 ^a	1.40 ± 0.37 ^a	1.13 ± 0.38 ^a

a "0" control group. b Values are the means of three replicates with 5 larvae. c The difference between groups with different letters in the same column is statistically significant.

It has been reported by [19] that ZnO NPs cross the gut barrier in the lepidopter species *Bombyx mori* (Lepidoptera: Bombycidae). They demonstrated that ZnO NPs can reach the hemolymph and their subsequent interaction and/or uptake by the circulating hemocytes therein. Besides, they showed that a decrease in the percentage of prohemocyte and an increase in the percentage of granulocytes and plasmatocytes [19]. This may be the reason why the lowest mean prohemocyte number and the highest granulocyte mean number were observed at 1 and 10 µg/10 µl ZnO NPs concentrations in our study (Table 1). In a study tested with Nomolt insecticide on *Schistocerca gregaria* Forskal (Orthoptera: Acrididae), it was determined that spherulocytes were the most sensitive cells to the Nomolt whereas the oenocytoids showed the least affected cells [20]. Similarly, spherulocytes were significantly the most sensitive hemocyte type to nanorod-shaped 10 µg/10 µl ZnO NP concentration when compared to the control group in the present study for *G. mellonella* larvae (F: 2.421; df: 5; sig: 0.042) (Table 1) due to their fragile structure (Figure 1.c) [20]. In addition, the mean number of oenocytoids did not differ statistically between the control and experimental groups (Table 1). In other words, the mean number of the oenocytoids was not significantly affected by ZnO NPs. Plasmatocytes and granulocytes are the most predominant hemocytes in *G. mellonella* [21, 22]. In our study, firstly, plasmatocytes and then granulocytes were found to be denser in control and experimental group larvae (Table 1). And the mean number of the plasmatocyte and granulocyte did not

differ statistically between the experimental and control group (Table 1). The effects of nanorod-shaped ZnO NPs on differential hemocyte count have not previously been studied. However, in another consistent study, [23] studied the effects of metyrapone on differential count in *Spodoptera littoralis* (Boisd) (Lepidoptera: Noctuidae). They observed that the proportion of plasmatocytes and granulocytes did not significantly change from days 4 to 7. As observed in our study, the fact that there is no significant change in plasmatocyte and granulocyte values of the insect immune response until the first 7 days after exposure to a foreign substance makes it more understandable. On a kind of stimulus, a labile cell resembling a platelet, the coagulocyte frees clotting factors in the surrounding hemolymph [24]. They are specialized for clotting [25]. [26] noted that the differential hemocyte counts (DHC) of coagulocytes can be affected by the titre of ecdysone in the last larval stage of *Heliothis armigera* Hübner (Lepidoptera: Noctuidae) [26, 27]. The reason why there was no significant increase or decrease in the number of coagulocytes at 24 h may be due to the ecdysone hormone level in fourth instar *G. mellonella* larvae (Table 1). Finally, the reason for the significant fluctuations seen in spherulocyte and prohemocytes in this study may have arisen from the toxic effects that occur as a result of the interaction of zinc oxide NPs with these hemocyte types in the hemolymph. Possible toxic interactions are summarized by [5, 28-30]. According to them, when compared to typical zinc forms, ZnO NPs have been shown to permeate into cells. After being taken in by the cells, they might

cause membrane architecture to deteriorate. The cytotoxicity in the cells is caused by their particle breakdown, zinc release into the media, or absorption by the cells [28-30].

Conclusion

The aim of this study was to determine the effects of nanorod-shaped ZnO NPs on hemocytes types of *G. mellonella* L. For this purpose, different concentrations of ZnO NPs were force-fed to fourth instar larvae. The toxic effects of ZnO NPs on plasmatocyte, granulocyte, spherulocyte, prohemocyte, oenocytoid, and coagulocyte numbers in hemolymph of *G. mellonella* larvae was studied. As a result of the study, it was understood that treating *G. mellonella* with 10 µg/10 µl ZnO NPs significantly decreased spherulocytes numbers. But mean numbers of plasmatocyte, granulocyte, prohemocyte, oenocytoid, and coagulocyte numbers did not differ significantly when compared to the control group after 24 h force-feeding treatments.

Author's Contributions

Ata Eskin: Drafted and wrote the manuscript, performed the experiment and result analysis.

Ethics

There are no ethical issues after the publication of this manuscript.

References

[1]. Miller, JC, Ruben S, Jose Miguel Represas-Cardenas, and Griffith K. The handbook of nanotechnology: Business, policy, and intellectual property law. John Wiley & Sons, 2004.

[2]. Tuncsoy, B, & Mese, Y 2021. Influence of titanium dioxide nanoparticles on bioaccumulation, antioxidant defense and immune system of *Galleria mellonella* L. *Environmental Science and Pollution Research*, 1-9.

[3]. Mir, AH, Qamar, A, Qadir, I, Naqvi, AH, & Begum, R 2020. Accumulation and trafficking of zinc oxide nanoparticles in an invertebrate model, *Bombyx mori*, with insights on their effects on immuno-competent cells. *Scientific reports*, 10(1), 1-14.

[4]. Moya-Andérico, L, Vukomanovic, M, del Mar Cendra, M, Segura-Feliu, M, Gil, V., José, A & Torrents, E 2021. Utility of *Galleria mellonella* larvae for evaluating nanoparticle toxicology. *Chemosphere*, 266, 129235.

[5]. Eskin, A, Öztürk, Ş, & Körükçü, M 2019. Determination of the acute toxic effects of zinc oxide nanoparticles (ZnO NPs) in total hemocytes counts of *Galleria mellonella* (Lepidoptera: Pyralidae) with two different methods. *Ecotoxicology*, 28(7), 801-808.

[6]. Eskin, A, Altinkaynak, C, Merve, T & Özdemir, N 2020. Fluorescent copper phosphate nanoflowers: a novel toxicity investigation study based on *Tenebrio molitor* Linnaeus, 1758 (Coleoptera: Tenebrionidae) larvae. *Bitlis Eren Üniversitesi Fen Bilimleri Dergisi*, 9(3), 975-984.

[7]. Eskin, A, & Bozdoğan, H 2021. Effects of the copper oxide nanoparticles (CuO NPs) on *Galleria mellonella* hemocytes. *Drug and Chemical Toxicology*, 1-11.

[8]. Eskin, A, Ekremoglu, M, Altinkaynak, C, & Özdemir, N 2021. Effects of organic-inorganic hybrid nanoflowers' framework on hemocytes and enzymatic responses of the model organism, *Galleria mellonella* (Lepidoptera: Pyralidae). *International Journal of Tropical Insect Science*, 1-12.

[9]. Matha, V, & Áček, Z (1984). Changes in haemocyte counts in *Galleria mellonella* (L.) (Lepidoptera: Galleriidae) larvae infected with *Steinernema* sp. (Nematoda: Steinernematidae). *Nematologica*, 30(1), 86-89.

[10]. Champion, OL, Wagley, S, & Titball, RW 2016. *Galleria mellonella* as a model host for microbiological and toxin research. *Virulence*, 7(7), 840-845.

[11]. Ramarao, N, Nielsen-Leroux, C, Lereclus, D 2012. The insect *Galleria mellonella* as a powerful infection model to investigate bacterial pathogenesis, *Journal of Visualized Experiments*, 70: 4392.

[12]. Shaban, HE, Helal, IB, Shamseldean, MM, & Seif, AI 201. Defensive reactions of *Periplaneta americana* (Blattodea: Blattellidae) adults against *Steinernema* Sp. 2d (Rhabditida). *The Egyptian Society of Experimental Biology*, 6(2): 263-271.

[13]. Blanco, LAA, Crispim, JS, Fernandes, KM, de Oliveira, LL, Pereira, MF, Bazzolli, DMS, & Martins, GF 2017. Differential cellular immune response of *Galleria mellonella* to *Actinobacillus pleuropneumoniae*. *Cell and Tissue Research*, 370(1), 153-168.

[14]. IBM-SPSS Statistics for Windows. 2011. Version 20.0. Elsevier, London, UK. IBM Corp. Released. Armonk, NY: IBM Corp.

[15]. Ribeiro, C, Brehélin, M, 2006. Insect hemocytes: What type of cell is that? *Journal of Insect Physiology*. 52, 417-429.

[16]. Mizerska-Dudka, M, & Andrejko, M 2014. *Galleria mellonella* hemocytes destruction after infection with *Pseudomonas aeruginosa*. *Journal of Basic Microbiology*, 54(3), 232-246.

[17]. Gupta, A 1979. Insect Hemocytes: Development, Forms, Functions and Techniques. Cambridge: Cambridge University Press. doi:10.1017/CBO9780511759987.

[18]. Arnold, JW 1974. The hemocytes of insects, pp. 201-54. In M. Rockstein (ed.). *The Physiology of Insecta*, Vol. 5, 2nd ed. Academic Press, New York.

[19]. Mir, AH, Qamar, A, Qadir, I, Naqvi, AH, & Begum, R 2020. Accumulation and trafficking of zinc oxide nanoparticles in an invertebrate model, *Bombyx mori*, with insights on their effects on immuno-competent cells. *Scientific Reports*, 10(1), 1-14.

[20]. Teleb, SS 2011. Effect of Nomolt on differential and total haemocytes in the desert locust *Schistocerca gregaria* Forskal (Orthoptera: Acrididae). *Journal of American Science*, 7(11), 479-484.

[21]. Tojo S, Naganuma F, Arakawa K, Yokoo S 2000. Involvement of both granular cells and plasmatocytes in phagocytic reactions in the greater wax moth, *Galleria mellonella*. *Journal of Insect Physiology*, 46:1129-1135.

[22]. Pereira, TC, De Barros, PP, Fugisaki, LRDO, Rossoni, RD, Ribeiro, FDC, De Menezes, RT, ... & Scorzoni, L 2018. Recent advances in the use of *Galleria mellonella* model to study immune responses against human pathogens. *Journal of Fungi*, 4(4), 128.

[23]. Gelbič, I, Stráčeková, J, & Berger, J (2006). Influence of metyrapone on the morphology of hemocytes of the Egyptian cotton



leafworm *Spodoptera littoralis* (Boisd.). *Zoological Studies*, 45(3), 371-377.

[24]. Bohn, H 1986. Hemolymph clotting in insects. *Immunity in Invertebrates*, 188-207.

[25]. Brehélin, M and Zachary, D, 1986. Insect haemocytes: a new classification to rule out the controversy. *In Immunity in Invertebrates* (pp. 36-48). Springer, Berlin, Heidelberg.

[26]. Essawy, M, A Maleville, and M. Brehélin. 1984. Evolution of haemogram during the larval development (last instar) of *Eliothis armigera*. *Invertebr Immunol Conf* 17-29 Sept 1984, Montpellier, France." *Dev Comp Immunol*.

[27]. Pathak, JPN 1986. Haemogram and its endocrine control in insects. *In Immunity in Invertebrates*, pp. 49-59. Springer, Berlin, Heidelberg, 1986.

[28]. Xia T, Kovoichich M, Liang M, Madler L, Gilbert B, Shi H, Yeh JI, Zink JI, Nel AE 2008. Comparison of the mechanism of toxicity of zinc oxide and cerium oxide nanoparticles based on dissolution and oxidative stress properties. *ACS Nano* 2:2121–2134.

[29]. De Berardis B, Civitelli G, Condello M, Lista P, Pozzi R, Arancia G, Meschini S 2010. Exposure to ZnO nanoparticles induces oxidative stress and cytotoxicity in human colon carcinoma cells. *Toxicology and Applied Pharmacology* 246:116–127.

[30]. Zhang X, Wang Z, Mao L, Dong X, Peng Q, Chen J, Tan C, Hu R 2017. Effect of ZnO nanoparticle on cell viability, zinc uptake efficiency, and zinc transporters gene expression: a comparison with ZnO and ZnSO₄. *Czech Journal of Animal Science*, 62(1):32–41.

The Anatomical Characteristics of *Salvia* (section *Aethiopsis*) From Mardin and Their Taxonomic Implications

Fatma Mungan Kılıç^{1*} , Murat Kılıç¹ 

¹ Department of Crops and Animal Production, Mardin Artuklu University, 47200 Mardin, Artuklu, Türkiye

* fatmamungankilic@artuklu.edu.tr

* Orcid: 0000-0001-6858-3458

Received: 3 November 2021

Accepted: 7 April 2022

DOI: 10.18466/cbayarfbe.1018553

Abstract

In this study, 4 *Salvia* species found in the *Aethiopsis* section distributed in the province of Mardin in the Southeast of Turkey between the years 2018-2021 were analyzed comparatively in terms of anatomy. Transverse sections taken from the roots, stems, leaves, and petioles of the taxa were examined under a light microscope. *Salvia brachyantha* ssp. *brachyantha*, *Salvia montbretii*, *Salvia palaestina*, and *Salvia syriaca* taxa were analyzed anatomically. *S. montbretii* and *S. syriaca* species were analyzed in detail for the first time anatomically. In the anatomical examinations, it was observed that the root, stem, leaf, and petiole structures of the taxa were similar, but the shapes and sizes, in addition to the tissue layer and pith row numbers, were different. As a result, anatomical characters provide important information in the differentiation of species.

Keywords: Anatomy, Mardin, *Salvia*, taxonomic implication, Turkey

1. Introduction

Salvia L. genus, which constitutes our research subject, is one of the richest members of the Lamiaceae family, which is popularly known as “sage”. Because it is rich in essential oils, aromatic and phenological compounds and secondary metabolites from most of the species belonging to the family; It is used in medicine, pharmacy, food, cosmetics, and perfumery. The family is a very large family with 236 genera, and 7.534 species in World [1]. In our country, there are 45 genera, 546 species, and 731 taxa In Turkey, 89 species and 94 taxa were defined in Flora of Turkey and 45 of them were recorded as endemic [2]. According to recent studies in our country, the number of *Salvia* species is 99 *Salvia* species, 52 (52%) of which are endemic [3]. Although the number of studies on this genus has increased in recent years, studies on the anatomical features of this genus are limited [4-12].

The anatomical characters of most of the *Salvia* species have not been studied so far. For example, *S. montbretii*, *S. suffruticosa*, and *S. syriaca* have not been studied in detail anatomically. This study aims to give a detailed account of anatomical characteristics of the *S. brachyantha* ssp. *brachyantha*, *S. montbretii*, *S. palaestina*, *S. syriaca* taxa of spreading in Mardin. The anatomical significance of these findings is also

discussed with the previous studies on section *Aethiopsis*. In addition, our aim with this research is to introduce *Salvia* species with a wide range of uses and to contribute to the Flora of Turkey in this direction, as well as contribute the literature for the usability of anatomy studies in taxonomy.

2. Materials and Methods

The study area is on the Tigris and Euphrates basin in southeastern Anatolia, eastern Batman, and Şırnak, west Şanlıurfa, north of Diyarbakır, in the south surrounded by Syrian soil Mardin, with a surface area of 8.891 km² [13] (Figure 1). Mardin is located in the Iran-Turan Phytogeographical Region, within the C8 square according to the Grid classification system applied by Davis [14]. The Mediterranean, terrestrial, and desert climates in the region, and the height between the mountain and lowland sections at 600-800 m have resulted in increased plant diversity.

This study was carried out on *Salvia* populations collected from Artuklu, Kızıltepe, Mazıdağı, and Midyat districts of Mardin province between 2018-2021 (Table I). Plant collection studies were carried out between May and September, which are the flowering periods of *Salvia* species. Davis's Flora of Turkey [14] and The checklist of Flora of Turkey (Vascular Plants)

[2] were used to determine plant species. Collected specimens were stored in falcon tubes in 70% alcohol for use in anatomical studies and examined. Cross-sections were taken from the root, stem, leaf, and petiole parts of the plants manually with the help of a razor, the preparations were prepared by staining with safranin-fast green, and their photographs were taken by examining them under a microscope with an imaging system [15]. As a result of the examination of these

preparations, anatomical features showing similarities and differences between taxa were determined. Photographs made with a light microscope were made with an Isolab brand microscope in the Department of Crops and Animal Production at Mardin Artuklu University. The biometric measurement of tissue and cells of root, stem, leaf, and petiole are given in Table 2, 3, 4, 5.

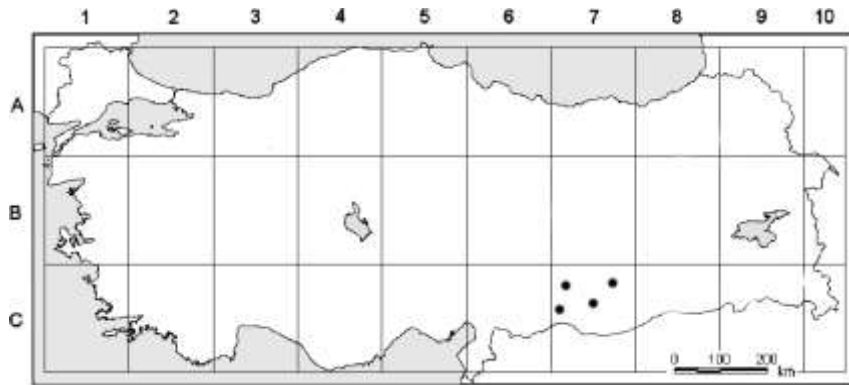


Figure 1. Distribution map of sect. *Aethiopsis* taxa (.)

Table1. *Salvia* taxa used for anatomical studies and collected localities.

Species	Collection areas and habitat	Collector's number
<i>S. brachyantha</i> ssp. <i>brachyantha</i>	Turkey, C8 Mardin: Artuklu, Sultanköy Village	M.Kılıç, F.Mungankılıç 226
<i>S. montbretii</i>	Turkey, C8 Mardin: Artuklu, Hamzabey Village, Sultanköy Village Turkey, C8 Mardin: Midyat, Eskimidyat Village	M.Kılıç, F.Mungankılıç 209, 217
<i>S. palaestina</i>	Turkey, C8 Mardin: Artuklu, Yenişehir Village, Dara Village, Eskikale Village, Hamzabey Village Turkey, C8 Mardin: Kızıltepe, Uluköy Village Turkey, C8 Mardin: Mazıdağı, Ömürlü Village, Kebapçı Village Turkey, C8 Mardin: Midyat, Eskimidyat Village	M.Kılıç, F.Mungankılıç 206, 207, 209, 213
<i>S. syriaca</i>	Turkey, C8 Mardin: Artuklu, Sultanköy Village Turkey, C8 Mardin: Mazıdağı, Enginköy Village Turkey, C8 Mardin: Midyat, Cumhuriyet Village	M.Kılıç, F.Mungankılıç 210, 212, 238

3. Results and Discussion

Transverse sections taken from the root, stem, leaf, and petiole of the plants were analyzed in detail and the obtained results are outlined below. The taxa are given in alphabetical order.

3.1. Root anatomical characteristics

Salvia brachyantha subsp. *brachyantha* (Bordz.) Pobed: The periderm was a crushed thick layer of large cells and fragmented in section. Parenchymatous cells under the periderm were multi-layered and under it, there are several layers of phloem. Cambium was unclear. In the

xylem, besides the large tracheas, tracheids and xylem parenchyma have lignified walls. Pith rays consist of 3-5 rowed narrow cells. As the xylem occupies the pith, it is very narrow (Figure 2, Table 2).

Salvia montbretii Bentham: The periderm was a thick layer that was crushed and fragmented in cross-section. Beneath the periderm is the multi-layered parenchymal cells, and below the parenchyma, several layered phloem. Cambium was unclear. In the xylem, besides the large tracheas, tracheids and xylem parenchyma have lignified walls. Pith rays consist of 1-3 rowed narrow cells. The xylem covering the pith region is very narrow (Figure 2, Table 2).

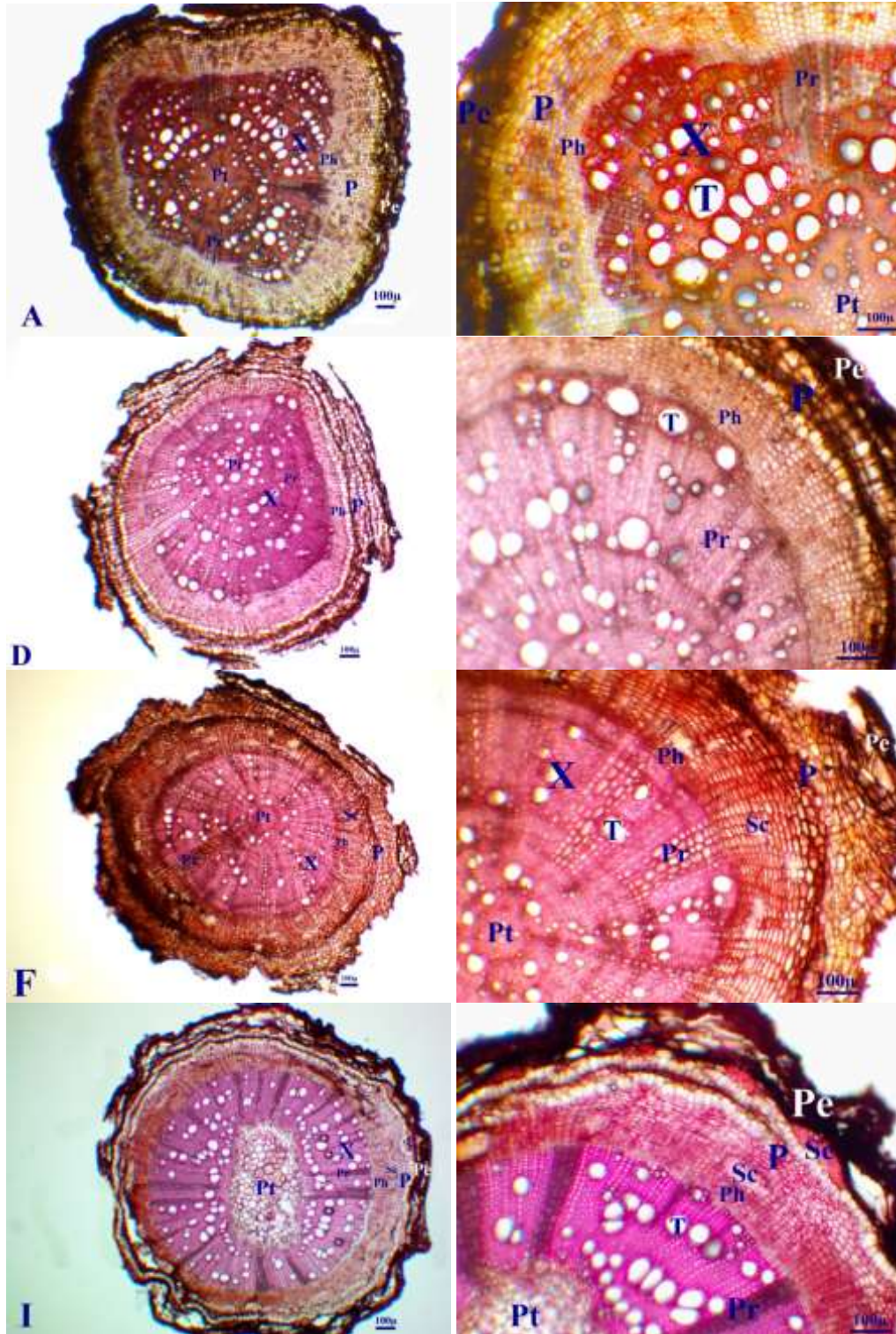


Figure 2. Root anatomical structure of investigated sect. *Aethiopsis* taxa. A. *Salvia brachyantha* subsp. *brachyantha*. D. *S. montbretii*. F. *S. palaestina*. I. *S. syriaca*. Pe: Periderm, P: Parenchyma, Sc: Sclerenchyma, Ph: Phloem, X: Xylem, Pr: Pith ray, T: Trachea, Pt: Pith region.

Table 2. Comparative anatomical measurements root tissues of investigated sect. *Aethiopsis* taxa.

Species	Tissue	Width (μ)		Length (μ)	
		Min.–Max.	Mean \pm S.D.	Min.–Max.	Mean \pm S.D.
<i>S. brachyantha</i> ssp. <i>brachyantha</i>	Periderm	24,04–52,11	36,43 \pm 7,35	33,14–72,68	52,17 \pm 9,97
	Parenchyma	17,63–53,29	35,86 \pm 9,30	17,89–32,39	24,27 \pm 4,06
	Trachea	10,12–34,40	20,98 \pm 7,61	9,30–36,42	23,28 \pm 9,05
	Pith	3,48–8,27	5,68 \pm 1,37	6,30–11,33	8,89 \pm 1,29
<i>S. montbretii</i>	Periderm	19,75–50,46	34,10 \pm 9,00	13,49–30,53	20,27 \pm 5,55
	Parenchyma	16,85–56,12	33,90 \pm 9,39	9,85–58,40	31,62 \pm 16,38
	Trachea	12,90–33,37	20,93 \pm 6,13	11,74–37,20	19,98 \pm 7,08
	Pith	3,74–9,82	6,32 \pm 1,81	4,61–10,92	7,61 \pm 1,93
<i>S. palaestina</i>	Periderm	11,86–59,87	36,07 \pm 13,61	7,91–44,28	19,95 \pm 10,83
	Parenchyma	12,39–36,79	24,04 \pm 6,95	8,62–20,64	13,64 \pm 3,28
	Trachea	14,21–50,50	30,39 \pm 10,85	15,65–56,82	34,28 \pm 11,19
	Pith	12,78–36,57	22,26 \pm 7,19	9,87–41,63	22,69 \pm 9,07
<i>S. syriaca</i>	Periderm	21,25–75,27	42,37 \pm 16,47	10,38–35,33	19,09 \pm 6,88
	Parenchyma	8,37–36,94	21,16 \pm 7,17	5,06–19,01	11,43 \pm 4,30
	Trachea	17,69–49,55	37,17 \pm 9,18	17,17–74,08	42,47 \pm 14,70
	Pith	6,84–22,49	14,62 \pm 4,25	7,83–43,57	20,82 \pm 9,65

S.D.: Standard Deviation

3.2. Stem anatomical characteristics

Salvia palaestina Bentham: The periderm was a thick layer that was crushed and fragmented in cross-section. Beneath the periderm is the multi-layered parenchymal cells, and below the parenchyma, several layered sclerenchyma. There are multi-layer of phloem under sclerenchyma groups. Cambium was unclear. In the xylem, besides the large tracheas, tracheids and xylem parenchyma have lignified walls. Pith rays consist of 2-8 rowed narrow cells. The xylem covering the pith region is wider than other taxa (Figure 2, Table 2).

Salvia syriaca L.: The periderm was a thick layer that was crushed and fragmented in cross-section. At the junction of the periderm and parenchyma, there are intermittent sclerenchyma groups in places. Besides, under the parenchyma, there are sclerenchyma cells in groups in places. There are multi-layer of phloem under sclerenchyma groups. Cambium was unclear. In the xylem, besides the large tracheas, tracheids and xylem parenchyma have lignified walls. Pith rays consist of 2-6 rowed narrow cells. The xylem covering the pith region is narrow (Figure 2, Table 2).

In all taxa were stem clearly quadrangular in the cross-section. The epidermis, single-layered, was formed by oval, square, and nearly rectangular cells and they are covered by a thin layer of cuticle.

Salvia brachyantha subsp. *brachyantha* (Bordz.) Pobed: The epidermis is seen that the dimensions of opposite corners are close to each other. There are glandular and eglandular hairs on the epidermis. Under the epidermis, there are 6-7 rows of collenchyma cells concentrated at the corners and 3-4 rows of these cells below it. The collenchyma layers consist of ovoidal and quadrilateral cells walls. Parenchyma, formed by parenchymatous, cubic, and oval cells was 3-7 rowed at the edges and 4-5

rowed at the corners. 3-5 rows of sclerenchyma were located on the vascular bundles. The phloem is of 5-7 rows. Below the 5-7 rows of phloem is an indistinct cambium. Xylem part was larger than the phloem part. The trachea is arranged quite regularly. In the center, there is the pith region, which covers a large area. The cells in the pith region are polygonal or orbicular parenchymatous cells that grow towards the center and form triangular spaces between them (Figure 3, Table 3).

Salvia montbretii Bentham: The epidermis is seen that the dimensions of opposite corners are close to each other. There are glandular and eglandular hairs on the epidermis. Under the epidermis, there are 5-6 rows of collenchyma cells concentrated at the corners and 1-3 rows of these cells below it. The collenchyma layers consist of oval, square, and quadrilateral cells walls. Parenchyma, formed by parenchymatous, formless, cubic and oval cells was 4-5 rowed at the edges and 5-6 rowed at the corners. 3-5 rows of sclerenchyma were located on the vascular bundles. The phloem is of several rows. Below the several rows of phloem is an indistinct cambium. Xylem part was larger than the phloem part. The trachea is arranged quite regularly. In the center, there is the pith region, which covers a large area. The cells in the pith region are polygonal or orbicular parenchymatous cells that grow towards the center and form triangular spaces between them (Figure 3, Table 3).

Salvia palaestina Bentham: The epidermis is seen that the dimensions of opposite corners are close to each other. There are many single or multicellular glandular hairs on the epidermis cells. Under the epidermis, there are 7-8 rows of collenchyma cells concentrated at the corners and 3-4 rows of these cells below it. The collenchyma layers consist of oval, square, and quadrilateral cells walls. Parenchyma, formed by parenchymatous, cubic, and oval cells was 1-2 rowed at

the edges and 2-3 rowed at the corners. 3-5 rows of sclerenchyma were located on the vascular bundles. The phloem is of several rows. Below the several rows of phloem is an indistinct cambium. Xylem part was larger than phloem part. The trachea are arranged quite regularly. In the center, there is the pith region, which

covers a large area. The cells in the pith region are polygonal or orbicular parenchymatic cells that grow towards the center and form triangular spaces between them (Figure 3, Table 3).

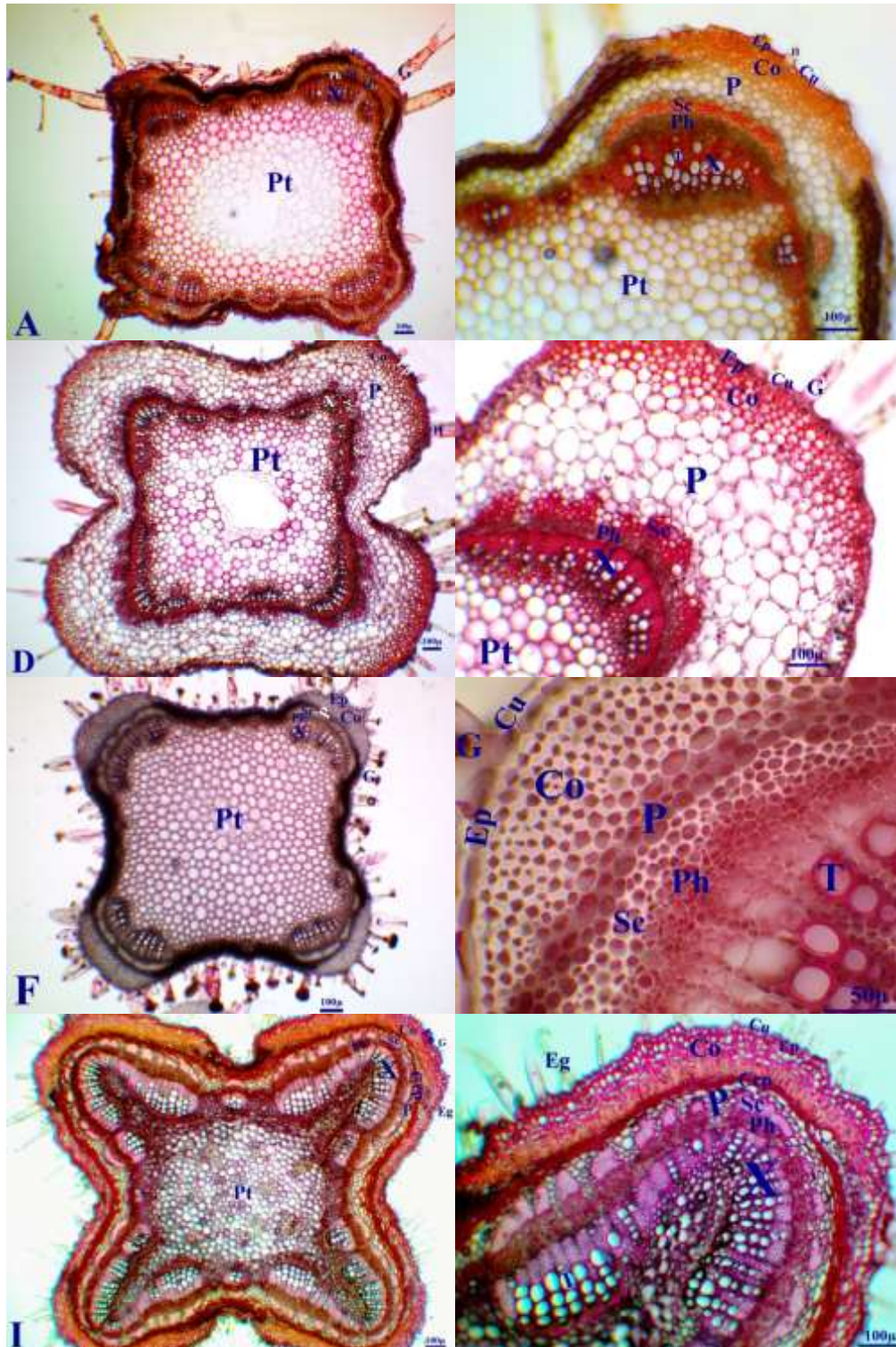


Figure 3. Stem anatomical structure of investigated sect. *Aethiopsis* taxa. A. *Salvia brachyantha* subsp. *brachyantha*. D. *S. montbretii*. F. *S. palaestina*. I. *S. syriaca*. G: Glandular hair, Eg: Eglandular hair, Ch: Compound hair, H: Hair,

Cu: Cuticle, Ep: Epidermis, Co: Collenchyma, Crp: Crushed parenchyma, P: Parenchyma, Sc: Sclerenchyma, Ph: Phloem, X: Xylem, T: Trachea, Pt: Pith region.

Table 3. Comparative anatomical measurements stem tissues of investigated sect. *Aethiopsis* taxa.

Species	Tissue	Width (μ)		Length (μ)	
		Min.–Max.	Mean \pm S.D.	Min.–Max.	Mean \pm S.D.
<i>S. brachyantha</i> ssp. <i>brachyantha</i>	Cuticle	–	–	2,11–6,78	4,04 \pm 1,28
	Epidermis	11,36–26,45	17,91 \pm 4,23	10,52–32,59	16,78 \pm 4,98
	Collenchyma	11,52–30,31	19,32 \pm 5,73	11,26–28,52	18,92 \pm 5,70
	Parenchyma	16,52–45,00	30,17 \pm 8,50	12,46–34,56	20,82 \pm 8,51
	Phloem	3,35–13,94	7,84 \pm 2,48	2,91–8,75	5,35 \pm 1,75
	Trachea	11,78–31,98	20,37 \pm 5,70	14,40–35,25	22,75 \pm 4,99
	Pith	25,34–93,50	53,96 \pm 22,44	16,73–98,58	47,94 \pm 23,78
<i>S. montbretii</i>	Cuticle	–	–	3,19–8,45	5,72 \pm 1,21
	Epidermis	10,71–31,29	19,18 \pm 5,28	9,49–27,92	17,32 \pm 4,63
	Collenchyma	7,16–25,93	16,01 \pm 5,28	8,47–25,77	14,79 \pm 4,96
	Parenchyma	14,94–69,79	38,59 \pm 17,74	14,09–77,72	33,34 \pm 15,72
	Phloem	8,64–18,82	13,20 \pm 3,15	4,79–11,83	8,70 \pm 1,88
	Trachea	15,80–54,18	31,05 \pm 9,69	14,00–45,09	26,85 \pm 9,42
	Pith	33,33–134,67	76,25 \pm 29,80	33,42–138,39	74,17 \pm 31,75
<i>S. palaestina</i>	Cuticle	–	–	4,14–7,88	6,15 \pm 1,00
	Epidermis	9,07–27,24	19,26 \pm 5,11	6,35–18,19	10,54 \pm 2,95
	Collenchyma	5,30–15,95	10,12 \pm 3,27	4,25–11,34	7,16 \pm 2,22
	Parenchyma	6,74–24,32	14,40 \pm 4,36	5,05–17,66	10,76 \pm 3,09
	Phloem	2,90–10,19	6,08 \pm 1,90	2,40–7,00	4,03 \pm 1,29
	Trachea	12,72–35,44	24,95 \pm 5,57	13,83–36,57	26,10 \pm 6,76
	Pith	30,57–80,91	51,06 \pm 13,26	26,49–91,53	53,77 \pm 17,10
<i>S. syriaca</i>	Cuticle	–	–	3,85–8,22	6,21 \pm 1,28
	Epidermis	7,94–26,75	17,60 \pm 5,33	5,50–21,94	12,03 \pm 4,66
	Collenchyma	10,50–27,31	18,18 \pm 4,42	7,76–26,73	15,46 \pm 4,77
	Parenchyma	11,37–44,57	28,30 \pm 10,41	6,98–46,21	23,92 \pm 10,70
	Phloem	5,77–12,19	8,22 \pm 1,90	4,42–10,81	7,28 \pm 2,16
	Trachea	5,66–39,58	22,05 \pm 9,69	5,32–39,91	21,58 \pm 10,13
	Pith	9,86–39,16	27,30 \pm 8,75	8,53–41,41	26,29 \pm 10,39

Salvia syriaca L.: The epidermis is seen that the dimensions of opposite corners are close to each other. There are glandular and eglandular hairs on the epidermis. Most of them are eglandular made up of one to or multicellular. Under the epidermis, there are 6-8 rows of collenchyma cells concentrated at the corners and 6-8 rows of these cells below it. The collenchyma layers consist of oval, square, and rectangular cells walls. Parenchyma, formed by parenchymatous, formless, cubic, and oval cells was 3-4 rowed at the edges and 1-3 rowed at the corners. 4-5 rows of sclerenchyma were located on the vascular bundles. The phloem is of several rows. Below the several rows of phloem is an indistinct cambium. Xylem part was larger than the phloem part. The trachea is arranged quite regularly. In the center, there is the pith region, which covers a large area. The cells in the pith region are polygonal or orbicular parenchymatous cells that grow towards the center and form triangular spaces between them (Figure 3, Table 3).

3.3. Leaf anatomical characteristics

In all taxa were stomata present on both surfaces of the leaf (amphistomatic type) and stomata are diacytic type.

Salvia brachyantha subsp. *brachyantha* (Bordz.) Pobed: There is a thin cuticle layer around the single-layered epidermis. Epidermis cells are oval or nearly rectangular. The epidermis is usually composed of single or multicellular long glandular hairs. Leaf mesophyll consists of palisade and spongy parenchyma cells. The leaf is bifacial. Palisade parenchyma cells were cylindrical in 2-3 rows, whereas spongy parenchyma cells were circular or polygonal in 2-3 rows. The adaxial surface is convex around the midrib area. Below the adaxial surface are 1-2 rows of collenchyma. Vascular bundles are collateral. The arcuate vascular bundle is surrounded by parenchyma cells. Just below the parenchyma is the xylem consisting of the trachea and tracheids. Phloem is 3-4 rows and is located below the xylem. The axial surface is convex, with 2-3 rows of collenchyma underneath (Figure 4, Table 4).

Salvia montbretii Bentham: The epidermis formed by oval and nearly rectangular cells. It is covered by a thin cuticula. There are many glandular and eglandular hairs on the epidermis cells. Most of them are eglandular made up of one or multicellular. Palisade parenchyma cells were 2-3 rowed and cylindrical, whereas spongy parenchyma cells were 1-2 rowed oval and polygonal in shape. Mesophyll type is bifacial. The adaxial surface is slightly convex around the median vein area. 2-3 rows

of collenchyma are found below the adaxial surface. The vascular bundles are collateral. The arcuate vascular bundle is surrounded by parenchyma cells. Just below the parenchyma are the trachea and the xylem consisting of tracheids. The phloem is several layers and

is located below the xylem. The abaxial surface is convex and located below it there are 3-4 rows of collenchyma (Figure 4, Table 4).

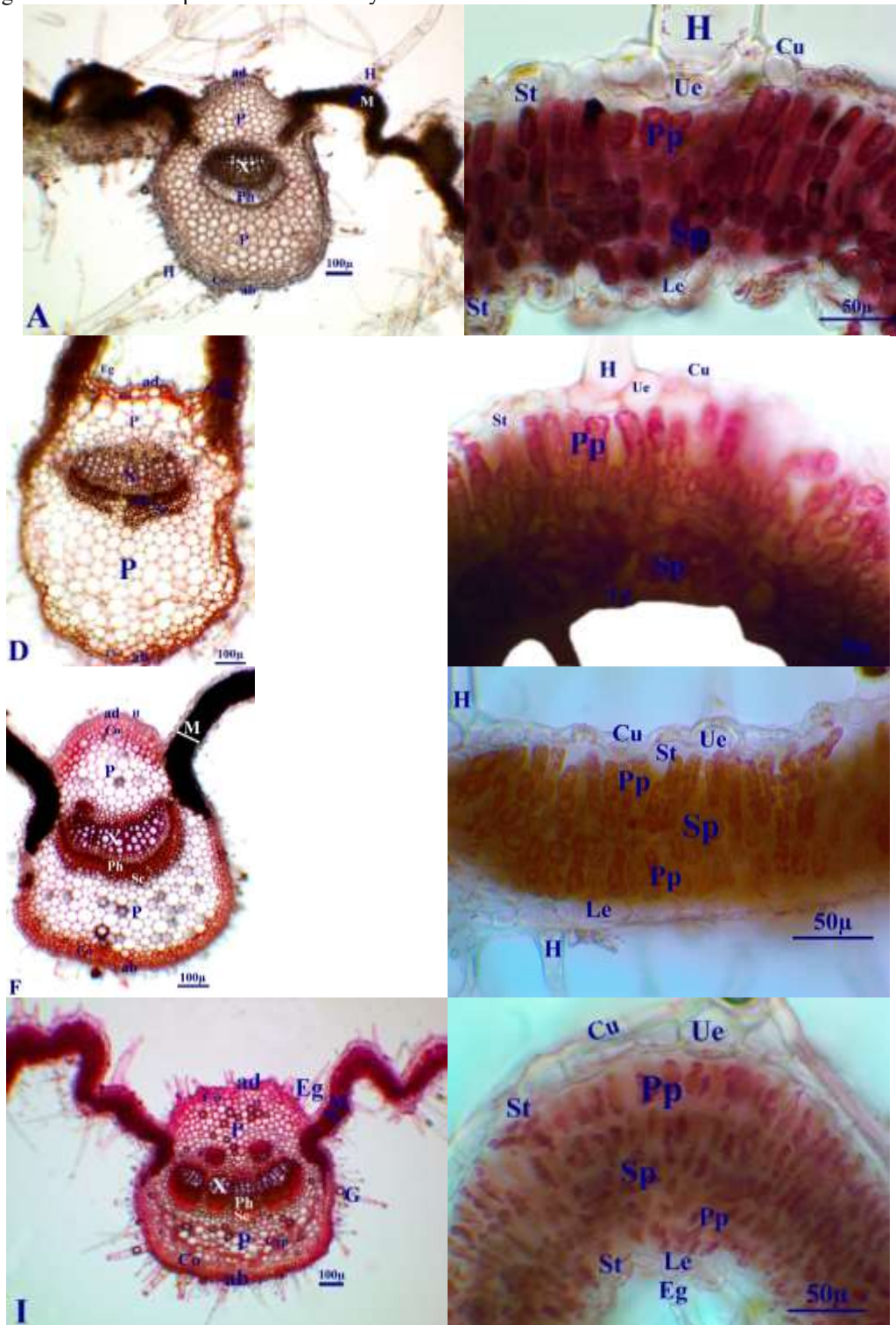


Figure 4. Leaf anatomical structure of investigated sect. *Aethiopsis* taxa. A. *Salvia brachyantha* subsp. *brachyantha*. D. *S. montbretii*. F. *S. palaestina*. I. *S. syriaca*. G: Glandular hair, Eg: Eglanular hair, Ch: Compound hair, H: Hair, M: Mesophyll layer, ad: Adaxial surface, Co: Collenchyma, Crp: Crushed parenchyma, P: Parenchyma, X: Xylem,

Ph: Phloem, ab: Abaxial surface, Ue: Upper epidermis, Le: Lower epidermis, Pp: Palisade parenchyma, Sp: Spongy parenchyma, Hp: Hypodermis, St: Stomata.

Table 4. Comparative anatomical measurements leaf tissues of investigated sect. *Aethiopsis* taxa.

Species	Tissue	Width (μ)		Length (μ)	
		Min.–Max.	Mean \pm S.D.	Min.–Max.	Mean \pm S.D.
<i>S. brachyantha</i> ssp.	Cuticle	–	–	1,92–5,72	3,66 \pm 0,96
	Upper epidermis	12,47–40,91	22,16 \pm 6,56	9,39–34,56	20,78 \pm 7,18
<i>brachyantha</i>	Palisade parenchyma	9,63–15,95	12,14 \pm 2,00	19,68–32,89	27,13 \pm 3,33
	Spongy parenchyma	10,87–16,65	12,83 \pm 1,41	12,17–23,37	17,89 \pm 2,56
	Mesophyll layer	–	–	86,17–205,58	118,70 \pm 35,79
<i>S. montbretii</i>	Lower epidermis	10,14–33,22	22,65 \pm 6,49	10,23–23,97	17,31 \pm 4,16
	Cuticle	–	–	0,72–2,53	1,34 \pm 0,63
	Upper epidermis	7,76–35,41	16,28 \pm 6,25	6,86–17,68	12,13 \pm 3,23
	Palisade parenchyma	8,62–17,18	13,35 \pm 2,18	29,41–58,13	42,97 \pm 8,15
	Spongy parenchyma	9,00–25,65	15,07 \pm 4,37	8,56–24,16	16,34 \pm 4,10
<i>S. palaestina</i>	Mesophyll layer	–	–	73,31–146,53	113,79 \pm 17,36
	Lower epidermis	7,94–29,48	16,85 \pm 5,97	6,75–19,17	13,48 \pm 4,19
	Cuticle	–	–	3,29–7,67	4,85 \pm 1,06
	Upper epidermis	9,11–47,62	20,66 \pm 9,63	6,63–29,15	14,62 \pm 6,10
	Palisade parenchyma	7,16–17,23	11,09 \pm 2,58	15,88–31,68	25,57 \pm 4,44
	Spongy parenchyma	8,58–18,19	10,96 \pm 2,14	9,71–20,91	13,99 \pm 2,66
<i>S. syriaca</i>	Mesophyll layer	–	–	98,53–248,14	168,63 \pm 52,79
	Lower epidermis	7,00–37,79	21,09 \pm 8,12	6,99–27,09	15,74 \pm 4,89
	Cuticle	–	–	3,74–8,17	5,80 \pm 1,29
	Upper epidermis	7,44–41,41	22,98 \pm 8,42	5,86–32,51	17,70 \pm 8,03
	Palisade parenchyma	6,96–15,08	10,06 \pm 1,90	15,29–40,52	27,92 \pm 5,82
<i>S. syriaca</i>	Spongy parenchyma	7,47–13,65	10,13 \pm 1,66	7,38–20,40	13,48 \pm 2,99
	Mesophyll layer	–	–	60,25–215,14	129,55 \pm 42,63
	Lower epidermis	3,80–31,72	9,08 \pm 6,02	5,54–18,02	9,13 \pm 3,37

Salvia palaestina Benthams: The epidermis formed by oval and nearly rectangular cells. It is covered by a thin cuticula. There are many glandular and eglandular hairs on the epidermis cells. Most of them are eglandular made up of one and multicellular. Palisade parenchyma cells are elongated rectangular, 2-3 rowed above and 1-2 rowed below. The spongy parenchyma cells are 1-2 rowed with large intercellular spaces. Mesophyll type is equifacial. The adaxial surface is convex around the median vein area. 2-3 rows of collenchyma are found below the adaxial surface. The vascular bundles are collateral. The arcuate vascular bundle is surrounded by parenchyma cells. Just below the parenchyma are the trachea and the xylem consisting of tracheids. The phloem is several layers and is located below the xylem. The abaxial surface is slightly convex and located below it there are 4-5 rows of collenchyma (Figure 4, Table 4).

Salvia syriaca L.: The epidermis formed by oval and nearly rectangular cells. It is covered by a thin cuticula. There are many glandular and eglandular hairs on the epidermis cells. Most of them are eglandular made up of one and multicellular. Palisade parenchyma cells are elongated rectangular or cylindrical, 2-3 rowed above and 1-2 rowed below. The spongy parenchyma cells are 1-2 rowed with large intercellular spaces. Mesophyll type is equifacial. The adaxial surface is slightly convex around the median vein area. 2-3 rows of collenchyma are found below the adaxial surface. The vascular bundles are collateral. The arcuate vascular bundle is surrounded by parenchyma cells. There are crushed

parenchymal cells between the parenchyma layer. Just below the parenchyma are the trachea and the xylem consisting of tracheids. The phloem is several layers and is located below the xylem. The abaxial surface is slightly convex and located below it there are 1-2 row of collenchyma (Figure 4, Table 4).

3.4. Petiol anatomical characteristics

Salvia brachyantha subsp. *brachyantha* (Bordz.) Pobed: In the cross-section of the petiole, it is anatomically similar to the midrib of the leaf. There is a thin cuticle layer around the single layer of the epidermis. Epidermis cells are similar in size, almost rectangular. There are many glandular and eglandular hairs on the epidermis cells. Most are glandular, consisting of 1-3 cells. Collenchyma cells are in 2-4 rows. Just below is the parenchymatic tissue covering a very large area. Parenchyma cells have a polygonal or nearly circular shape with pronounced triangular spaces between them. The median vascular tissue is inseparable or discrete in the center of the parenchymatic cells. There are well-developed, small vascular bundles at both corners of the petiole. The phloem contains bundles of sclerenchyma. Phloem tissue consists of several rows of cells. Trachea cells are arranged regularly in the xylem tissue (Figure 5, Table 5).

Salvia montbretii Benthams: In the cross-section of the petiole, it is anatomically similar to the midrib of the leaf. There is a thin cuticle layer around the single layer

of the epidermis. Epidermis cells are similar in size, oval, and nearly rectangular. There are many glandular and eglandular hairs on the epidermis cells. Most are glandular, consisting of 1-3 cells. Collenchyma cells are in 1-3 rows. Just below is the parenchymatic tissue covering a very large area. Parenchyma cells have a polygonal or nearly circular shape with pronounced triangular spaces between them. The median vascular

tissue is inseparable in the center of the parenchymatic cells. There are undeveloped, small vascular bundles at both corners of the petiole. The phloem contains bundles of sclerenchyma. Phloem tissue consists of several rows of cells. Trachea cells are arranged regularly in the xylem tissue (Figure 5, Table 5).

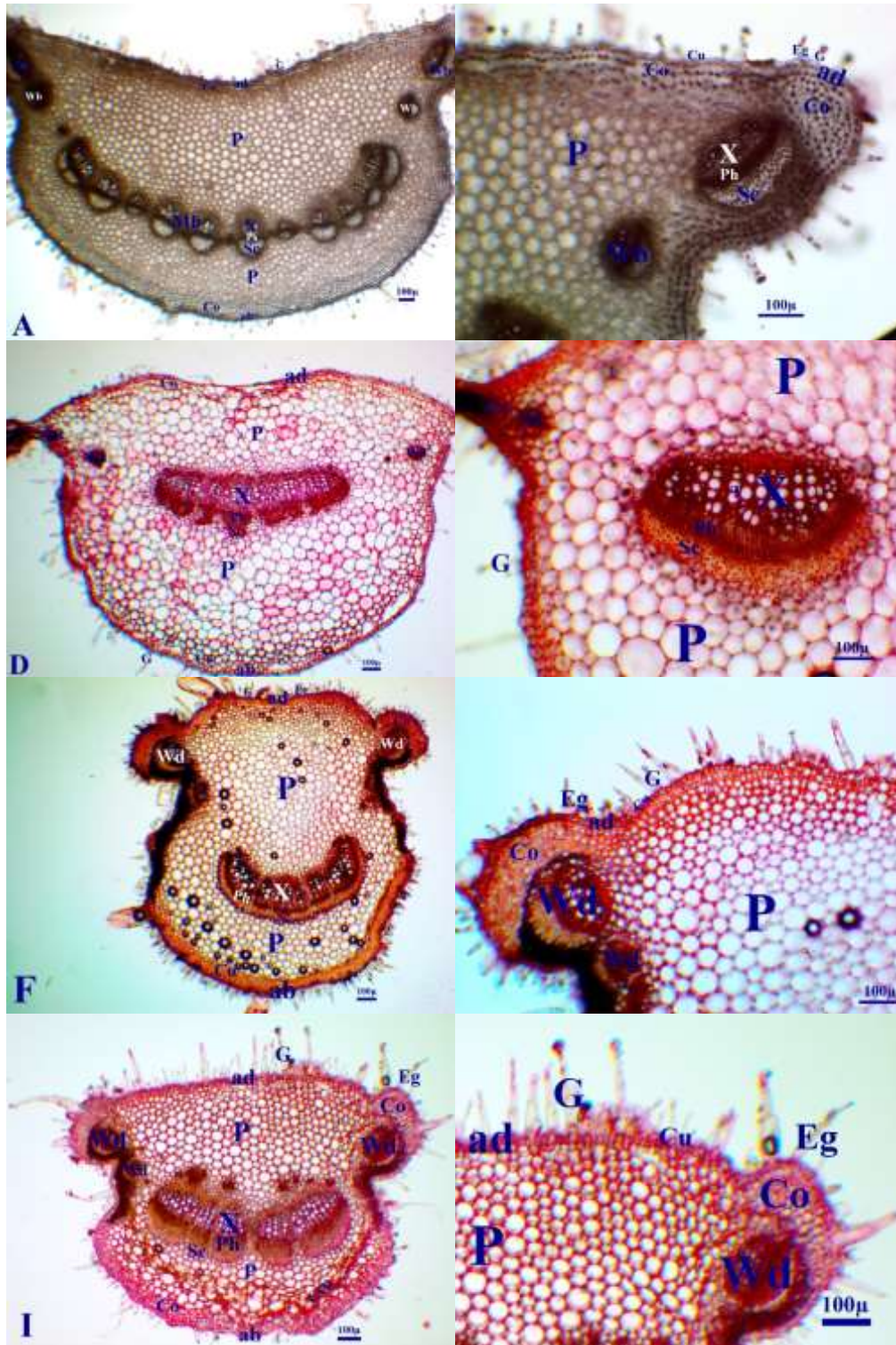


Figure 5. Petiole anatomical structure of investigated sect. *Aethiopsis* taxa. A. *Salvia brachyantha* subsp. *brachyantha*. D. *S. montbretii*. F. *S. palaestina*. I. *S. syriaca*. G: Glandular hair, ad: Adaxial surface, Co: Collenchyma, Crp: Crushed parenchyma, P: Parenchyma, X: Xylem, Ph: Phloem, Sc: Sclerenchyma, Mb: Median bundle, Wb: Wing bundle, ab: Abaxial surface, Cu: Cuticle, Eg: Eglanular hair.

Table 5. Comparative anatomical measurements petiol tissues of investigated sect. *Aethiopsis* taxa.

Species	Tissue	Width (μ)		Length (μ)	
		Min.–Max.	Mean \pm S.D.	Min.–Max.	Mean \pm S.D.
<i>S. brachyantha</i> ssp. <i>brachyantha</i>	Cuticle	–	–	3,32–6,28	4,53 \pm 0,85
	Adaxial epidermis	8,55–18,12	12,00 \pm 2,84	11,94–19,86	14,86 \pm 1,95
	Parenchyma	18,96–52,34	33,41 \pm 9,58	23,27–54,63	37,61 \pm 8,42
	Trachea	8,15–32,70	19,50 \pm 6,18	5,48–39,82	20,10 \pm 9,30
	Phloem	6,82–14,92	10,95 \pm 2,43	3,81–8,79	5,45 \pm 1,27
	Abaxial epidermis	12,18–23,25	17,61 \pm 3,53	12,70–16,74	14,70 \pm 1,13
<i>S. montbretii</i>	Cuticle	–	–	1,69–5,08	3,30 \pm 0,91
	Adaxial epidermis	7,15–20,35	14,48 \pm 3,36	8,14–21,01	12,48 \pm 3,45
	Parenchyma	34,55–96,79	63,26 \pm 16,94	34,51–83,64	53,96 \pm 15,39
	Trachea	12,50–25,64	18,83 \pm 3,80	11,03–24,99	17,62 \pm 4,42
	Phloem	5,00–13,03	8,79 \pm 2,20	3,60–12,36	6,39 \pm 2,18
	Abaxial epidermis	12,77–26,22	20,21 \pm 4,04	11,13–25,39	16,93 \pm 3,96
<i>S. palaestina</i>	Cuticle	–	–	3,96–6,83	5,24 \pm 0,83
	Adaxial epidermis	4,04–13,18	10,04 \pm 2,31	5,01–15,20	10,06 \pm 2,40
	Parenchyma	16,19–79,33	46,11 \pm 22,73	17,43–80,22	43,33 \pm 20,88
	Trachea	8,56–29,98	17,67 \pm 5,85	10,18–29,56	19,70 \pm 5,90
	Phloem	4,84–10,89	8,79 \pm 1,72	3,02–7,98	4,82 \pm 1,28
	Abaxial epidermis	7,91–23,05	13,52 \pm 4,41	6,63–16,89	11,70 \pm 2,99
<i>S. syriaca</i>	Cuticle	–	–	3,98–9,13	6,44 \pm 1,29
	Adaxial epidermis	7,08–27,24	15,20 \pm 5,16	7,61–25,28	13,44 \pm 4,08
	Parenchyma	22,82–82,70	50,44 \pm 19,46	17,44–62,54	39,02 \pm 14,44
	Trachea	11,31–35,14	27,23 \pm 6,41	10,48–41,66	29,82 \pm 8,36
	Phloem	3,21–9,34	6,36 \pm 1,78	3,66–9,96	6,10 \pm 1,69
	Abaxial epidermis	8,90–21,70	16,09 \pm 3,84	7,18–21,42	12,22 \pm 4,21

Salvia palaestina Benth: In the cross-section of the petiole, it is anatomically similar to the midrib of the leaf. There is a thin cuticle layer around the single layer of the epidermis. Epidermis cells are similar in size, oval, square, and nearly rectangular. There are many glandular and eglandular hairs on the epidermis cells. Most are eglandular, consisting of multicellular. Collenchyma cells are in 2-4 rows. Just below is the parenchymatic tissue covering a very large area. Parenchyma cells have a polygonal or nearly circular shape with pronounced triangular spaces between them. The median vascular tissue is inseparable in the center of the parenchymatic cells. There are well-developed, small vascular bundles at both corners of the petiole. The phloem contains bundles of sclerenchyma. Phloem tissue consists of several rows of cells. Trachea cells are arranged regularly in the xylem tissue (Figure 5, Table 5).

Salvia syriaca L.: In the cross-section of the petiole, it is anatomically similar to the midrib of the leaf. There is a thin cuticle layer around the single layer of the epidermis. Epidermis cells are similar in size, oval, square, and nearly rectangular. There are many glandular and eglandular hairs on the epidermis cells. Most are eglandular, consisting of multicellular. Collenchyma cells are in 4-5 rows. Just below is the parenchymatic tissue covering a very large area.

Parenchyma cells have a polygonal or nearly circular shape with pronounced triangular spaces between them. There are crushed parenchymal cells between the parenchyma layer. The median vascular tissue is inseparable in the center of the parenchymatic cells. There are well-developed, small vascular bundles at both corners of the petiole. The phloem contains bundles of sclerenchyma. Phloem tissue consists of several rows of cells. Trachea cells are arranged regularly in the xylem tissue (Figure 5, Table 5).

In this research, 4 *Salvia* species found in the *Aethiopsis* section distributed through Mardin-Turkey, were comparatively investigated in terms of their anatomy. The anatomical measurements of the root, stem, leaf, and petiole are shown in Tables II, III, IV, and V, respectively. The *Salvia* taxa used in our study belong to the *Aethiopsis* sections. In this section, we will compare it with the studies on this section.

Metcalf and Chalk [16], regarding the root anatomy of the Lamiaceae family, stated that the pith rays of the roots consist of 2-12 or more rows of cells. The pith rays of *Salvia limbata* C.A., *S. palaestina* Benth (sect. *Aethiopsis*) respectively consist of 2-6, 1-8(-10) rowed cells [17]; *S. brachyantha* (Bordz.) Pobed., *S. montbretii* Benth (sect. *Aethiopsis*)) respectively consist of 1-8, (1-)3-15 rowed cells. Our studies on the

cross-sections of the roots of *S. brachyantha* ssp. *brachyantha*, *S. montbretii*, *S. palaestina*, *S. syriaca* revealed that the taxa comprise respectively 3-4, 1-3, 2-8, 2-8 rowed ray cells. The number of lines of pith rays is a taxonomically important feature for distinguishing sections of the genus [8].

Stem anatomy features of the Lamiaceae; square stem, the shape of the vascular bundle, the location of collenchyma, the swollen or non-swollen shape of corners, and presence or absence [1]. In this study, we found the same anatomical features in the stem cross-section. Kahraman [18] has examined the stem anatomy of *Salvia* species. It can be seen that some data obtained by Kahraman [18] were similar to the results of our study. However, while the collenchyma was reported by Kahraman [18] to be 1-10 layers at the corners, 1-4 layers at the edges, and also the parenchyma contains 1-15 layers, we have found they to respectively consist of 5-10, 1-8, and 1-10 layers. In addition, Kahraman and Doğan [17] have examined the stem anatomy of *S. palaestina* species, while the parenchyma was reported to be 4-7 layers, we have found it to consist of 1-3 layers.

The leaf mesophyll of *Salvia* species is entirely parenchymatic and the midrib is surrounded by collenchymatous cells [16]. According to the mesophyll structure, the leaves of *S. palaestina*, *S. syriaca* are equifacial but other all species had bifacial mesophylls. This of *S. palaestina* [17] are equifacial. The palisade parenchyma had three-five rows in *S. palaestina*, *S. syriaca* and two-three rows in the other species. It can be seen that the data obtained by Kahraman [18] regarding the anatomy of the leaf of *S. brachyantha* is the same but other species are different from our study. The structure of palisade parenchyma in the leaf anatomy of *Salvia* species can't be used as a helpful key for distinguishing the species. The structure of vascular bundles in the leaf anatomy of *Salvia* species can be used as a helpful key for distinguishing the species [8]. In the midrib of *Salvia* taxa, there are one or two large vascular bundles or absent on sides. It can be seen that the data obtained by Kahraman [18] regarding the anatomy of the vascular bundles of *S. montbretii* and *S. palaestina* are different but other species compatible with our study. Besides, Kahraman and Doğan [17] have examined the leaf anatomy of *S. palaestina* species, while the vascular bundles were reported to be single in the center, we have found it to same.

The structure of the petiole shows differs between the genera and species. Helpful anatomical characters of the petiole can be determinable in the specified taxonomical structures of some species [19]. According to Metcalfe and Chalk [16], the vascular bundles in the petiole of the Lamiaceae family are very important as a diagnostic feature. In the petiole of *Salvia* taxa, there is a single

and lobed large bundle and there are two or three small subsidiary bundles in petiolar wings.

S. cyanescens, as indicated by Kahraman [18], has two broad vascular bundles in the middle of the petiole and two-four small bundles in its wings, *S. limbata* [17] has a four broad vascular bundle in the center of the petiole and eight small lateral bundles, four small bundles in its wings, *S. sclarea* [20] has two large bundles in the center and three small bundles in the wings, and *S. blepharochlaena* [4] has one large bundle in the center and two small bundles in the wings.

4. Conclusion

The examined taxa show the anatomical features of the Lamiaceae family. Different and similar anatomical features of taxa have been stated.

In conclusion, the anatomical characters (such as the number of ray rows in the root, vascular bundles in the stem, mesophyll structures in the leaf, the shape of the midrib, and the presence of sclerenchyma tissue in the petiole) we found in the cross-sections of the taxa we examined are not only for the standardization and revision of these characters. Besides, it is also important in terms of contributing to the definitions and distinctions of the examined taxa.

Acknowledgements

We wish to thank Scientific Investigation Project to Coordinate of Mardin Artuklu University (Project No. MAÜ.BAP.18.KMYO.043) for financial support.

Author's Contributions

Fatma Mungan Kılıç: Conducted the field work. Wrote and gave comments to the manuscript.

Murat Kılıç: Conducted the field work and anatomical analysis. Wrote and gave comments to the manuscript. Authors read and approved the final version of the manuscript.

Ethics

Conflict of Interest The authors declare that they have no conflict of interest.

Research involving Human Participants and/or Animals Not applicable.

Informed consent Not applicable.

References

- [1]. Garner, C. 2017. Hallmark Features of Stem Anatomy in the Family Lamiaceae. University of South Carolina, Senior Theses. pp 126. https://scholarcommons.sc.edu/senior_theses/156.
- [2]. Güner, A. Aslan, S, Ekim, T, Vural, M, Babaç, MT. 2012. The checklist of Flora of Turkey (Vascular Plants). Flora Araştırmaları

Derneği ve Nezahat Gökyiğit Botanik Bahçesi Yayını (in Turkish), İstanbul, Turkey. ISBN: 978- 605-60425-7-7.-7.

[3]. Celep, F, Kahraman, A, Atalay, Z, Doğan, M. 2014. Morphology, anatomy, palynology, mericarp and trichome micromorphology of rediscovered Turkish endemic *Salvia quzelii* (Lamiaceae) and their taxonomic implications. *Plant Systematics and Evolution*; 300: 1945-1958. doi:10.1007/s00606-014-1020- 1.

[4]. Özkan, M, Özdemir, C, Soy, E. 2007. Morphology, Anatomy, Hair and Karyotype Structure of *S. blepharochlaena* Hedge and Hub.-Mor. (Lamiaceae), Endemic to Turkey. *Pakistan Journal of Biological Sciences*; 10(6): 893-898.

[5]. Baran, P, Özdemir, C, Aktaş, K. 2008. The Morphological and Anatomical Properties of *Salvia argentea* L. (Lamiaceae) in Turkey. *Research Journal of Agriculture and Biological Sciences*; 4(6): 725-733.

[6]. Aktaş, K, Özdemir, C, Özkan, M, Akyol, Y, Baran, P. 2009. Morphological and anatomical characteristics of *Salvia tchihatcheffii* endemic to Turkey. *African Journal of Biotechnology*; 8(18): 4519-4528. doi: 10.5897/AJB09.1041.

[7]. Anačkov, G, Božin, B, Zorić, L, Vukov, D, Mimica-Dukić, N, Merkulov, L, Lgić, R, Jovanović, M, Boža, P. 2009. Chemical Composition of Essential Oil and Leaf Anatomy of *Salvia bertolonii* Vis. and *Salvia pratensis* L. (Sect. *Plethiosphace*, Lamiaceae). *Molecules*; 14: 1-9. doi:10.3390/molecules14010001.

[8]. Kahraman, A, Celep, F, Doğan, M. 2010. Morphology, anatomy, palynology and nutlet micromorphology of *Salvia macrochlamys* (Labiatae) in Turkey. *Biologia*; 65(2): 219-227, Section Botany. doi: 10.2478/s11756-010-0013-y.

[9]. Kowalczyk, AP, Raman, V, Galal, AM, Khan, IA, Siebert, DJ, Zjawiony, JK. 2014. Vegetative anatomy and micromorphology of *Salvia divinorum* (Lamiaceae) from Mexico, combined with chromatographic analysis of salvinorin A. *Journal of Natural Medicines*; 68: 63-73. doi:10.1007/s11418-013-0769-9.

[10]. Özdemir, A, Özdemir, AY, Yetisen, K. 2016. Statistical Comparative Petiol Anatomy of *Salvia* sp. *Planta Daninha*; 34(3): 465-474. <https://doi.org/10.1590/s0100-83582016340300007>.

[11]. Nejadhabibvash, F, Chiyaneh, ER, Pirzad, A. 2017. Anatomy of *Salvia limbata* in Relation to Altitudinal Gradient in West Azerbaijan (Iran). *International Journal of Horticultural Science and Technology*; 4(2): 205-216. doi:10.22059/ijhst.2017.208537.127.

[12]. Gürdal, B, Yeşil, Y, Akalın, E, Tan, N. 2019. Anatomical features of *Salvia potentillifolia* Boiss. & Heldr. ex Benth. and *Salvia nydeggeri* Hub.-Mor. (Lamiaceae). *Istanbul Journal of Pharmacy*; 49 (3): 186-190.

[13]. Demir, MM. 2010. Mardin City. Msc Thesis, Istanbul University, İstanbul, Turkey.

[14]. Davis, PH. 1965-1985. Flora of Turkey and the East Aegean Islands. Edinburgh University Press, Edinburgh, England, Vol. 1-9.

[15]. Bozdağ, B, Kocabaş, O, Akyol, Y, Özdemir, C. 2016. A New Staining Method for Hand-Cut in Plant Anatomy Studies. *Marmara Pharmaceutical Journal*; 20: 184-190. doi: 10.12991/mpj.20162044231.

[16]. Metcalfe, CR, Chalk, L. 1972. Anatomy of the Dicotyledons II. Clarendon Press, Oxford.

[17]. Kahraman, A, Doğan, M. 2010. Comparative study of *Salvia limbata* C.A. and *S. palaestina* Benth (sect. *Aethiopsis* Benth, Labiatae) from East Anatolia, Turkey. *Acta Botanica Croatica*; 69(1): 47-64.

[18]. Kahraman, A. 2011. Morphology, Anatomy And Systematics of The Genus *Salvia* L. (Lamiaceae) In East And Southeast Anatolia, Turkey. Phd Thesis, Middle East Technical University, Ankara, Turkey.

[19]. Akcin, ÖE, Özyurt, MS, Şenel, G. 2011. Petiole anatomy of some Lamiaceae taxa. *Pakistan Journal of Botany*; 43: 1437-1443.

[20]. Özdemir, C, Şenel, G. 1999. The morphological, anatomical and karyological properties of *Salvia sclarea* L. *Turkish Journal of Botany*; 23: 7-18.

Chemical Inferences Drawn From Basalt Volcanic Pumice

Ruhan Benlikaya^{1*} , Mehmet Kahrıman² 

¹ Balıkesir University, Dept. of Secondary Science and Mathematics Education, Balıkesir, Türkiye

² Private Tunafen Anatolian High School, Ankara, Türkiye

*ruhan@balikesir.edu.tr

*Orcid: 0000-0002-1731-8846

Received: 9 September 2021

Accepted: 27 May 2022

DOI: 10.18466/cbayarfbe.993131

Abstract

The idea to conduct this study came out with the purpose of responding to two questions concerning the Kula Geopark. The questions were as follows: how the wettability of the natural pumice sample with spongy structure taken from this site is and how it can be altered. With this end in view, firstly the pumice samples were characterized by X-ray Fluorescence Spectroscopy, Fourier Transform Infrared Spectroscopy and Scanning Electron Microscopy analyses. Next, after observing super hydrophilic nature of the pumice with porous structure containing various metal oxides, the samples were coated with copper stearate dispersion using a spraying method. And then the wettability properties of the copper stearate-treated samples were determined via contact angles. Given the data obtained, the wettability phenomena of these samples were discussed in terms of wettability models.

Keywords: Contact angle, Cassie Baxter, Volcanic pumice, Wenzel, Wettability.

1. Introduction

Pumice is a silicate-based, spongy-looking rock formed after volcanic activities. It can be found in a variety of colors from white to gray, red and brown to black. Turkey has 2.2 billion tons of pumice reserves [1]. There are important pumice deposits in the provinces of Manisa, Kayseri, Van, Bitlis, Ağrı, Osmaniye and Nevşehir [2]. The Kula Volcano of the youngest volcanic activity in Manisa is one of 14 volcanoes in our country. Nearly 80 volcanic edifices are located on the North flank of the Alaşehir Graben, Manisa [3]. The area of the Kula Volcano extends 15 km and 40 km in the north-south direction and in the west-east direction, respectively. In 2013, the volcanic field was accepted as the first geopark in Turkey by UNESCO and the 58th in Europe as Gürsoy et al. stated [4].

Quaternary volcanism in the Kula region started approximately 2 million years ago. This volcanism occurred due to the stress tectonics that started in the Pliocene in Western Anatolia. It is suggested that the mentioned volcanism is related to the rifting (tensions) that probably caused the formation of the Alaşehir graben in the region [5]. The common eruption products of these volcanoes are mostly alkaline type of pyroclastic materials such as basaltic lava flows, tephra

and slag. Basaltic lava flows and pyroclastic cones form the most common forms of volcanic relief in the Kula volcanic field, which is one of the youngest examples of volcanic topography in Anatolia [5].

There have been many studies on various applications of modified/coated/natural volcanic pumice samples in mainly two fields: construction industry (cement replacement material [6] and heat-insulating material [7]) and water/wastewater/soil/air treatment (production of hybrid catalyst [8], removal of various substances such as cadmium [9], natural organic matter [10], selenium [11], disinfection by-product precursors [12], lead and copper ions [13], etc. from at least one of these medium). In some of these studies, the volcanic pumice samples supplied from the Kula region have also been used [10-13]. However, there is no study on the wettability of the pumice samples. The aim of this study is to characterize the volcanic pumice at the Kula region and to discuss wetting phenomena of the pumice samples in terms of wettability models by changing its surface property.

1.1 Theory

Surface wettability is the ability of a solid surface to maintain contact with a liquid as a result of competing

of adhesion and cohesion forces. The wettability of solid surface depends strongly on both its chemical composition and surface morphology. The slope of the line drawn tangent to the liquid drop from the intersection of solid, liquid and air (vapor) phases between a solid surface and a liquid drop on this solid surface is defined as the "contact angle" [14]. To explain the geometry of the surfaces repelling water and oil, mainly 3 different mathematical approximation models are widely used: Young, Wenzel and Cassie-Baxter, of which schematics are shown in Figure 1.

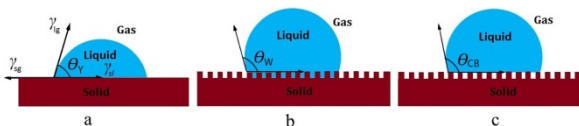


Figure 1. A droplet in the Young state on a smooth solid surface (a), collapsed in the Wenzel state (b), suspended in the Cassie-Baxter state (c).

The first equation and the most basic theory for wettability (1805) is Young's equation which explains the static contact angle (θ_Y) of the liquid on the solid surface having a homogeneous, smooth, and infinite flat ideal rigidity. Surface tension among the interfaces of solid-liquid, liquid-gas and solid-gas is balanced according to the equation (1.1) on horizontal direction, the model of which is given in Figure 1a.

$$\cos\theta_Y = (\gamma_{sg} - \gamma_{sl})/\gamma_{lg} \quad (1.1)$$

In this equation, γ_{sg} , γ_{sl} and γ_{lg} represent interface tensions of solid-gas, solid-liquid, and liquid-gas, respectively [14]. The contact angle of a liquid drop on the solid surface depends on equilibrium between cohesive forces (γ_{lg}) in the liquid and adhesive forces (γ_{sg} and γ_{sl}) between the pairs (s-l and s-g) in Young's equation.

Wenzel (1936) revealed that surface roughness (r) can significantly alter the contact angle of water; its model can be seen in Figure 1b. Drops become sticky to the surface when the liquid fully wets it as a result of penetrating to the grooves of rough surface on solid [15]. The existence of a rough structure at a solid surface causes an increase in the real superficial area of this surface. This makes that the actual solid-liquid contact area is larger than the apparent geometric contact area. Thus, hydrophobicity/hydrophilicity of the surface increases depending on geometry. The equation of the contact angle (θ_W) in Wenzel view is given in the equation (1.2) as

$$\cos\theta_W = r \cdot \frac{\gamma_{sg} - \gamma_{sl}}{\gamma_{lg}} = r \cdot \cos\theta_Y \quad (1.2)$$

where r is the roughness factor, representing the ratio of the actual area on rough surface to apparent geometry

area. The r factor will enhance the hydrophobicity/the hydrophilicity when the value of θ_Y is more/less than 90° [15, 16].

The roughness effect on the behavior of the drop on the surface was explained by Cassie-Baxter (1944). Unlike Wenzel, wetting is assumed to be heterogeneous in this model, Figure 1c. The contact area between liquid and solid is minimized due to air trapped in the surface voids by the liquid, while the one between liquid and air is maximized. Thus, liquid is forced to form spherical drops [16]. Depending upon Young's equation, the relationship between Cassie-Baxter contact angle (θ_{CB}) and θ_Y can be given with the equation (1.3) below

$$\cos\theta_{CB} = f \cdot (\cos\theta_Y + 1) - 1 \quad (1.3)$$

where f is the ratio of solid-liquid interface contact area and actual surface area under droplet within the unit area [14, 16]. In Cassie impregnating model, droplet penetrates completely or partially through the gaps between microstructures while not penetrate or only partially penetrates to the nanostructures [17, cited in 15]. This model can be thought of as an intermediate state between Wenzel and Cassie-Baxter models [17]. The wetted area in the model is greater than the Cassie-Baxter state. Considered f value for Cassie impregnating model according to (Eq. 1.3), the value is found as 16% (for $\theta_{CB}=140^\circ$). It means that greater than 84% of the water droplet is in contact with substrate while the other is on air [16].

2. Materials and Methods

The volcanic pumice samples were collected from the Geopark region, given in Figure 2a. There are two types of pumice as acidic and basic. The commonly used acidic pumice is light colored, whereas the basic one is dark colored [2]. It could be said that the pumice stone in Figure 2b is basic. All the chemicals in this study were analytical grade and used without further purification. Copper acetate and stearic acid were supplied by Sigma Aldrich and Chem Pure, respectively. Ethanol was from Merck. As shown in the literature, surfaces are given water repellency by means of various chemicals for low-surface energy modification, such as long alkyl chain thiols and fatty acids, aluminum and zirconium compounds, paraffin-based propellants, proteins, metal complexes, stearic acid compounds, fluorocarbons, silicone-based propellants, etc. [14]. Copper stearate (CSA) dispersion was used to give the property of hydrophobicity to the surface of the pumice in this study. For this aim, 0.75 grams of copper acetate was dissolved in 100 ml of ethyl alcohol. Considering the stoichiometric ratio between copper acetate and stearic acid, 2.37 grams of stearic acid (SA) was dissolved in 100 ml of ethyl alcohol. The SA solution was then added slowly to the copper acetate solution at 60°C as stated in the previous

study [18]. The surfaces of the volcanic pumice samples cut via scroll saw were covered using a spray bottle containing the resulting dispersion and allowed to dry in the oven. The pumice sample covered with CSA is abbreviated as the CSA-pumice. In order to examine whether there is any effect of spray times (STs) on the contact angles of the CSA-pumice samples, the surfaces of the pumice samples were covered with spraying the CSA dispersion 2, 5, 10 and 20 times.

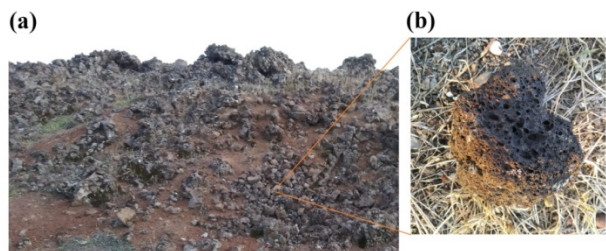


Figure 2. Photographs of the region (a) where the samples were taken in the Geopark region and a representative sample of the pumice stone (b).

2.1 Characterization

X-ray Fluorescence (XRF) spectroscopy analysis was made by Rigaku ZSX Primus II. Scanning Electron Microscopy (SEM) observations were carried out with QUANTA 400F Field Emission SEM after the samples were coated with Pd-Au on carbon film. Attension Theta Lite was used for contact angle measurements by creating a sessile drop from a liquid droplet at room temperature. The drop volume was approximately 10 μL . To determine whether contact angles are affected or not from the porous structure/STs of the CSA-pumice samples, five measurements were made at the regions of different porous structures on the samples. Fourier Transform Infrared Spectroscopy (FTIR) analyses of the CSA-pumice sample and the CSA dispersion were carried out using Perkin Elmer Spectrum Two in the range of 400–4000 cm^{-1} with ATR technique.

3. Results and discussion

3.1 Characterization of the volcanic pumice samples

Figure 3 shows XRF pattern of the pumice sample. Table 1 illustrates that SiO_2 is the major component (~43.0%) with about 18.80% Al_2O_3 , determined depending on the pattern. In addition, various metal oxides (>1%) have been found in the structure of the pumice such as iron, calcium, sodium, potassium, magnesium and titanium oxides. This composition shows that the pumice has a polar character and tends to interact well with water via mainly dipole-dipole and ion-dipole interactions.

The strong peak around 1000 cm^{-1} in the FTIR spectrum (Figure 4) of the CSA-pumice in powder form corresponds to Si–O stretching vibrations. A twin peak between 2950 and 3600 cm^{-1} may show the existence of Cu co-planarity during Cu salt formation [19].

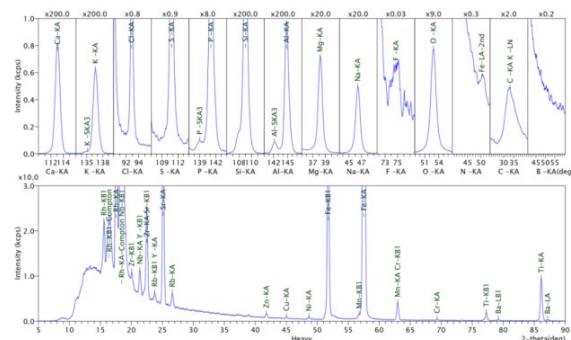


Figure 3. XRF pattern of the volcanic pumice sample.

Table 1. Chemical composition of the volcanic pumice determined by XRF.

No	Comp.	Result (% wt)	Det. limit	Intensity	w/o normal
1	SiO_2	43.0	0.0181	331.707	36.049
2	Al_2O_3	18.8	0.0113	194.629	15.742
3	Fe_2O_3	8.53	0.0053	269.248	7.149
4	CaO	7.77	0.0045	162.443	6.511
5	Na_2O	5.59	0.0155	9.766	4.685
6	CO_2	5.41	0.2154	0.756	4.532
7	K_2O	4.35	0.0033	124.059	3.649
8	MgO	3.11	0.0103	13.892	2.605
9	TiO_2	1.82	0.0115	9.354	1.524
10	P_2O_5	0.860	0.0030	12.055	0.721
11	MnO	0.185	0.0336	0.816	0.155
12	Cl	0.161	0.0033	1.127	0.135
13	SrO	0.139	0.0012	40.433	0.116
14	SO_3	0.130	0.0025	1.424	0.109
15	BaO	0.0874	0.0263	0.203	0.073
16	ZrO_2	0.0293	0.0069	2.251	0.024
17	Cr_2O_3	0.0187	0.0055	0.262	0.016
18	Nb_2O_5	0.0150	0.0016	5.253	0.013
19	Rb_2O	0.0106	0.0012	2.989	0.009
20	ZnO	0.0105	0.0018	0.896	0.009
21	NiO	0.0104	0.0023	0.518	0.009

The -CH stretchings of stearic acid in the spectrum of the CSA-pumice are seen in the range of 2800–2950 cm^{-1} . The peaks at 1589 and 1467 cm^{-1} were assigned to asymmetric and symmetric vibrations of the carboxylate group [20] due to the formation of copper stearate ($\text{Cu}^{2+} + 2\text{CH}_3(\text{CH}_2)_{16}\text{COOH} \rightarrow \text{Cu}[\text{CH}_3(\text{CH}_2)_{16}\text{COO}]_2 + 2\text{H}^+$) in other study. These peaks are also seen at 1586 and 1515 cm^{-1} in the spectrum of the CSA-pumice. In addition, the observation of the small peak at 1691 cm^{-1} and of the shoulder at 1634 cm^{-1} for C=O vibrations could show the residue of stearic acid molecules/stearate ions interacting differently with $\text{Cu}^{2+}/\text{Si-O}$ groups on the surface of the CSA-pumice.

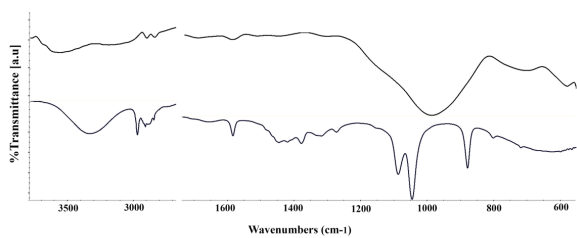


Figure 4. FTIR spectra of the CSA-pumice and the CSA dispersion in ethanol from top to down.

The FTIR spectrum of the CSA dispersion involves some peaks [-OH (3335 cm^{-1}), C=O ($1658, 1586\text{ cm}^{-1}$), C-O ($1047, 1088\text{ cm}^{-1}$), C-H ($2840\text{-}2980\text{ cm}^{-1}$) etc.] belonging to the interactions between ethanol and stearic acid molecules. The FTIR measurements confirm covering of the pumice sample surface with mainly CSA.

The SEM images of the pumice sample at different magnifications were given in Figures 5a-d. The images provide a better view of the pores/cavities that cannot be/can be seen with the naked eye and the rough structure throughout the surface as well as rod-like structures.

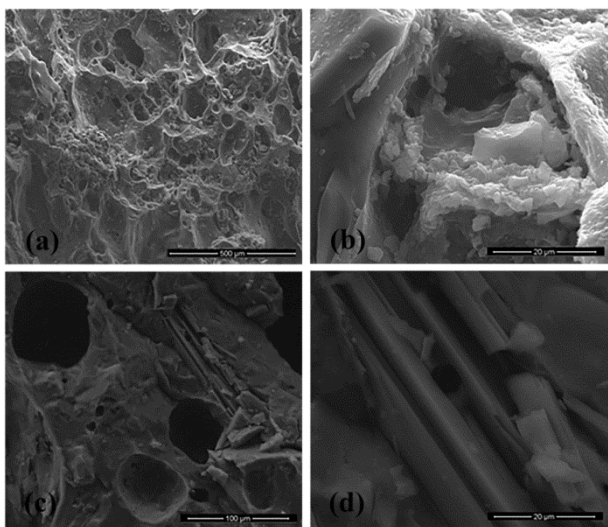


Figure 5. SEM images of the pristine pumice sample at different magnifications

Figure 6 shows SEM images of the CSA-pumice sample totally covered by the CSA dispersion. This coating has bur thorny flower-like morphology. In this morphology, thorny parts could involve mainly stearate groups when Cu^{+2} ions have been in the center of the flower. The size of a flower is about $15\text{-}20\text{ }\mu\text{m}$. Different morphologies for SA coating have been observed in the literature depending on the treatment method, the treatment duration and the properties of pristine surface.

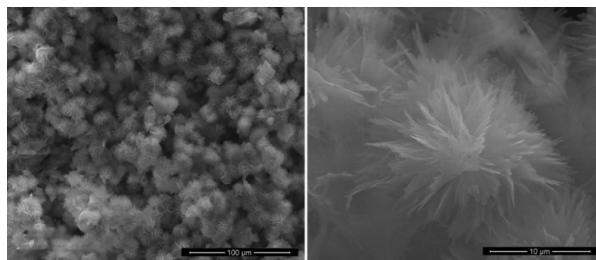


Figure 6. SEM images of the CSA-pumice sample at different magnifications

The formations of micro flowers of a diameter less than $5\text{ }\mu\text{m}$ (1 min) and of a rose-petal-like micro structured morphology (10 min) were observed from 1 min to 60 min in electrochemical modification of aluminum alloy in Cu/SA solutions [20]. The distribution of micro-nano flowers at anodic surface of the copper electrode after 1.5 h was seen in other study [21]. SEM image of super hydrophobic and super oleophilic poly(urethane) (PU) sponge prepared by facile dip coating in SA solution and subsequent heat treatment involved the micro/nanoscale SA protrusion with folding edges [22].

3.2 Wettability

Contact angle measurement is the main method in order to characterize the wettability of surfaces. When a water droplet forms a spherical shape, and the real contact between the adhered droplet and a surface is very small, a high contact angle (CA) occurs on the surface. In order for a surface to be super hydrophobic it must have a CA higher than 150° . In hydrophobic surface, the water drop will bead up with a CA greater than 90° . The wettable surfaces on which a water droplet tends to spread have a low CA value. Truly super hydrophilic surfaces possess roughness factors greater than one, and water spreads completely over them, which will have CA less than 5° . The drop will have a CA of less than 90° on hydrophilic surface [23-25].

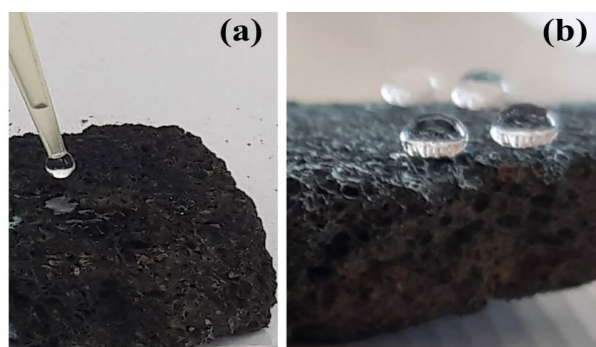


Figure 7. Wettability of the pristine pumice (a) and the CSA-pumice (b)

Figure 7 shows wettability of the pristine and the CSA-pumice samples.

When water is dropped on the pristine pumice (Figure 7a), which has a rough structure and contains a large amount of metal oxide in its structure, water spreads completely and spreads over the entire surface by filling the pores/cavities of the rough surface. This shows that the pristine pumice has super hydrophilic nature, which suggests being in the Wenzel state. In the case of the CSA-pumice, it is observed in Figure 7b that the water drop remains on the sample, presenting a non-sticking behavior. The pores in Figure 5 and Figure 7a may be getting smaller and more hydrophobic after being covered with CSA, nearly filled with the flowers (Figure 6). More air could be trapped between the flowers in the pores on the CSA-pumice surface. The trapped air and the CSA coating repel water drops and prevent them from spreading over the surface.



Figure 8. Sample images of water droplet CA measurements for the CSA-pumice sample (2 STs) from 141° to 117°.

Table 2. Summary of measured CA values for the CSA-pumice samples with different STs.

STs	CA values (°)
2	141, 131, 128, 121, 117
5	128, 121, 114, 111, 109
10	126, 116, 109, 108, 105
20	126, 121, 117, 112, 108

Sample images of the CA measurements are shown in Figure 8. The biggest CA value has been determined as 141° during the measurements taken from the regions of different porosity of the CSA-pumice sample covered with 2STs. The images imply that the CSA treatment imparted hydrophobic surfaces to the pumice samples. Yu et al. stated that the droplet is in the Cassie-Baxter state for hydrophobic textured surfaces generally only partially wetted [26]. The CA values in Table 2 show that the samples with different STs have different CAs in the same sample depending on the size of porosity. Chau et al. also stated that to obtain meaning and reproducible contact angle values of real samples is difficult due to the surface property changing with many factors such as surface roughness, heterogeneity, particle size, and particle shape [27]. For these reasons it may not be possible to explain the effect of STs on the CAs due to quite different CA values observed for each sample depending on heterogeneous porous structures of the pumice samples even if the highest CA value belongs to the sample with 2 STs. In another study, a decrease in CA was observed with an increase in concentration of SA after 4 wt% in the case of SA-coated PU. This was attributed to the exposure of

hydrophilic parts of SA molecules due to the hydrophobic association of long alkyl chain between the SA coating fixed to the PU sponge surface and the SA molecules, which were excessively absorbed at high SA concentration [22]. The CA value of the monolayer of SA obtained on mica by vapor exposure was 20°. Hydrophobicity was reached only when a thicker multilayer SA film (85° CA) was obtained in the study which involved the preparation of thin films of SA on mica by sublimation in air [28]. It is known that the CA values of flat surfaces even if coated with any material decreasing surface energy cannot exceed 120°.

Xu et al. [29] fabricated non-flaking 3D porous super hydrophobic frame with a pore size of less than 400 µm on copper foam substrates. Hierarchical micro-/nano-structures on the surfaces were obtained by immersing of the foams in ethanolic stearic acid solution at room temperature for about 4 days. The resulting material with the self-assembly CSA formation on Cu foam presented super hydrophobicity CA of 156°. In other studies that electrochemical modification was used for CSA/SA coating of any metal surface with/without etching, 162° [25] and ≈150° [15, 21] CA values were observed. The CA values increased from ~125 to 151° depending on SA concentration from about 0.2 wt% to 4 wt%, and then decreased to about ~147° in a study involving the PU sponge coated with SA [22]. The SA modification of the copper meshes/sheets caused 110° CA, after being abraded mechanically via SiC sandpaper various grits [30]. As seen in the literature, the differences between these CAs could also arise from the differences in surface chemical composition, porosity of the substrate, treatment methods and durations.

The techniques used in order to fabricate super hydrophobic surface usually involves two steps: roughening of the surface via etching chemically or mechanically to obtain micro-nano roughness and then modification of the surface to lower the surface energy [21]. The first step is not necessary when the volcanic pumice is used due to its rough morphology. Thus, using the volcanic sample as a starting material could be time-saving and inexpensive. However, the wide range of porous structures on the CSA-pumice surface may cause hydrophobicity instead of super hydrophobicity. The construction of the surface micro topography has great influence on the hydrophobic surfaces as Li et al. stated [30].

Wenzel's and Cassie-Baxter's equations help us to understand wettability properties of solid surfaces by accounting for their roughness and chemical structures. However, Erbil stated that much of the data in the literature are inconsistent with these theories and "modified forms" of Cassie's equations could be more convenient than others [31]. In our case, Cassie impregnating model may be used for the CSA-pumice

sample involving the microstructures (the flowers) of about 15 μm on heterogeneous pores/cavities at its surface, possible macro/micro gaps between this microstructures depending on the size of pores/cavities and micro/nano gaps between the thorns of the flower. A water droplet may penetrate partially into the macro/micro gaps while not penetrate to the nano gaps. However, Chau et al. suggested to examine the detailed nature of the surfaces and to characterize the surfaces to the smallest possible scale instead of trying to fit experimental data to idealized models in order to understand wetting phenomena of real surfaces. Thus, it may be possible to scale upwards to extract macroscopically verifiable data [27].

4. Conclusion

This study involves firstly the characterization of volcanic pumice samples from the Kula region. As can be seen from XRF and SEM analyses, the pumice samples consist of various oxides and have porous morphology. Having about 0° CA and facilitating water penetration into their pores quickly, the pristine pumice sample exhibits super hydrophilicity. Also as part of the study, the sample was treated with the CSA dispersion to see the effect of the treatment on wettability. In order to examine the effects of the treatment on the surface of the pristine one, the CSA-pumice sample has been examined via FTIR, SEM and CA measurements. The transformations in surface property and morphology of the pristine pumice with the CSA treatment have been shown via FTIR and SEM analyzes, respectively. The CA measurements have confirmed the change in the surface property of the pumice with the treatment from super hydrophilic to hydrophobic. The CSA-pumice samples have yielded CA values from 105° to about 141° due to their hydrophobic surfaces, the varying sizes of pores on their surface and various STs.

The wettability properties of the pristine and the treated pumice samples were tried to be explained in this study, depending upon their surface properties and the wettability models. The pristine pumice and the CSA-pumice samples may conform to Wenzel and Cassie impregnating models, respectively. Our next goal is to clarify how the spray coating with CSA influences on its surface porosity and roughness by examining the pore size distributions of the same pumice sample before and after coating with the CSA dispersion. It can be also examined whether reducing the SA concentration and covering the pristine pumice samples with various silanes will alter the results of this study.

Author's Contributions

Ruhan Benlikaya: Drafted and wrote the manuscript, assisted in analytical analysis on the structure, supervised the experiment's progress, and result analysis.

Mehmet Kahrıman: Performed the experiment, helped in result analysis.

Acknowledgement

Thanks to METU Central Laboratory for XRF and SEM analyses and to Zeynep Bıcıl, Balıkesir University for CA measurements.

Ethics

There are no ethical issues for the publication of this manuscript.

References

- [1]. Dünyada ve Türkiye'de Pomza, Maden ve Teknik Arama Müdürlüğü. <https://www.mta.gov.tr/v3.0/sayfalar/bilgi-merkezi/maden-serisi/pomza.pdf> (accessed at 10.02.2021)
- [2]. Çimen, Ö, Dereli, B, Keleş, E. 2020. Comparison of the effect of pumice of three different regions to high plasticity clay. *BEU Journal of Science*; 9(1): 427-433.
- [3]. Grütznert, T, Prelević, D, Akal, C. 2013. Geochemistry and origin of ultramafic enclaves and their basanitic host rock from Kula Volcano, Turkey. *Lithos*; 180-181: 58-73.
- [4]. Isik-Gürsoy, D, Uğurlu, E, Oldeland, J. 2018. Plant communities, diversity and endemism of the Kula Volcano, Manisa, Turkey. *Plant Biosystems*; 150(5): 1046-1055.
- [5]. Demir, T, Aytaç, A. 2019. Recommendation of three new geosites that are internationally significant in terms of geo-heritage within the territory of the Kula UNESCO Global Geopark. *Mediterranean Journal of Humanities*; 9: 125-140.
- [6]. Hossain, KMA. 2004a. Properties of volcanic pumice based cement and lightweight concrete. *Cement and Concrete Research*; 34: 283-291.
- [7]. Hossain, KMA. 2004b. Potential use of volcanic pumice as a construction material. *Journal of Materials in Civil Engineering*; 16 (6): 573-577.
- [8]. Maleki, A, Gharibi, S, Valadi, K, Taheri-Ledari, R. 2020. Pumice-modified cellulose fiber: An environmentally benign solid state hybrid catalytic system for the synthesis of 2,4,5-triarylimidazole derivatives. *Journal of Physics and Chemistry of Solids*; 142: 109443.
- [9]. Alemayehu, E, Lennartz, B. 2009. Virgin volcanic rocks: Kinetics and equilibrium studies for the adsorption of cadmium from water. *Journal of Hazardous Materials*; 169: 395-401.
- [10]. Kitis, M, Kaplan, S, Karakaya, E, Yiğit, N, Civelekoglu, G. 2007. Adsorption of natural organic matter from waters by iron coated pumice. *Chemosphere*; 66: 130-138.
- [11]. Yiğit, NO, Tözüm Akgül S. 2012. Removal of selenium species from waters using various surface-modified natural particles and waste materials. *Clean (Weinh)*; 40 (7): 735-745.
- [12]. Kaplan Bekaroğlu, S, Yiğit, N, Karanfil, T, Kitis, M. 2010. The adsorptive removal of disinfection by-product precursors in a high-sua water using iron oxide-coated pumice and volcanic slag particles. *Journal of Hazardous Materials*; 183: 389-94.

- [13]. Yayayürük, O, Erdem Yayayürük, A, Koçak, Ç, Koçak S. 2017. Lead and copper removal using Kula volcanics from environmental waters. *Separation Science and Technology*; 52(17): 2777-2787.
- [14]. Erayman, Y, Korkmaz, Y. 2017. Süperhidrofob Tekstil Yüzeylerin Florsuz Bileşikler Kullanılarak Sol-Jel Yöntemi ile Modifikasyonu. *Tekstil ve Mühendis*; 24: 105: 41-52.
- [15]. Bahrami, H, Ahmadi, B, Saffari, H. 2017. Preparing superhydrophobic copper surfaces with rose petal or lotus leaf property using a simple etching approach. *Material Research Express*; 4: 055014.
- [16]. Jiaqiang, D, Jin, Y, Deng, Y, Zuo, W, Zhao, X, Han, D, Peng, Q, Zhang, Z. 2018. Wetting models and working mechanisms of typical surfaces existing in nature and their application on superhydrophobic surfaces: A review. *Advanced Materials Interfaces*; 5: 1701052–1701091.
- [17]. Ebert, D, Bhushan, B. (2012) Wear-resistant rose petal-effect surfaces with superhydrophobicity and high droplet adhesion using hydrophobic and hydrophilic nanoparticles. *Journal of Colloid and Interface Science*; 384: 182-188.
- [18]. Keyf, S. 2019. Responce surface with Box-Benhken design for hydrophobic copper stearate synthesis. *European Journal of Science and Technology*; (16): 834-840.
- [19]. Anbarasan, R, Palanikumar, S, Devi, AA, Chen, P-H, Tung, KL. 2019. Characterization and application of Cu based superhydrophobic catalyst. *Progress in Natural Science*; 29 (4): 371-378.
- [20]. Xu, N, Sarkar, D, Chen, X, Zhang, H, Tong W. 2016. Superhydrophobic copper stearate/copper oxide thin films by a simple one-step electrochemical process and their corrosion resistance properties. *RSC Advances*; 6: 35466-35478.
- [21]. Huang, Y, Sarkar, D, Chen, XG. 2010. A one-step process to engineer superhydrophobic copper surfaces. *Materials Letters*; 64: 2722-2724.
- [22]. Wang, J, Zheng, Y. 2017. Oil/water mixtures and emulsions separation of stearic acid-functionalized sponge fabricated via a facile one-step coating method. *Separation and Purification Technology*; 181: 183-191.
- [23]. Koch, K, Barthlott, W. 2009. Superhydrophobic and superhydrophilic plant surfaces: An inspiration for biomimetic materials. *Philosophical Transactions of the Royal Society A: Mathematical, Physical and Engineering Science*; 367: 1487-1509.
- [24]. Drelich, J, Chibowski, E, Meng, DD, Terpilowski, K. 2011. Hydrophilic and superhydrophilic surfaces and materials. *Soft Matter*; 7: 9804–9828.
- [25]. Simpson JT, Hunter, SR, Aytug, T. 2015. Superhydrophobic materials and coatings: A review. *Reports on Progress in Physics*; 78: 086501.
- [26]. Yu, D, Doh, S, Kwak, H, Kang, H-C, Ahn, HS, Park, HS, Moriyama, K, Kim, MH. 2015. Wetting state on hydrophilic and hydrophobic micro-textured surfaces: Thermodynamic analysis and X-ray visualization. *Applied Physics Letters*; 106: 171602.
- [27]. Chau, TT, Bruckard, W, Koh, PTL, Nguyen, A, 2009. A review of factors that affect contact angle and implications for flotation practice. *Advances in colloid and interface science*; 150: 106-115.
- [28]. Sauthier, G, Segura, J, Fraxedas, J, Verdager, A. 2014. Hydrophobic coating of mica by stearic acid vapor deposition. *Colloids and Surfaces A: Physicochemical and Engineering Aspects*; 443: 331–337.
- [29]. Xu, J, Cao, Y, Ji, X, Yan, Y. 2013. Fabrication of non-flaking, superhydrophobic surfaces using a one-step solution-immersion process on copper foams. *Applied Surface Science*; 286: 220-227.
- [30]. Li, Y, Yang, S, Chen, Y, Zhang D. 2020. Hydrophobic and anti-fouling performance of surface on parabolic morphology, *International Journal of Environmental Research and Public Health*; 17 (2) 644: 1-11.
- [31]. Erbil, HY. 2014. The debate on the dependence of apparent contact angles on drop contact area or three-phase contact line: A review. *Surface Science Reports*; 69: 325-365.